Alma Mater Studiorum – Università di Bologna

DOTTORATO DI RICERCA IN

CHIMICA

Ciclo XXXII

Settore Concorsuale: CHIM/03

Settore Scientifico Disciplinare: 03/B1

ORGANIC AND INORGANIC NANOPARTICLES FOR IMAGING AND SENSING IN WATER

Presentata da: Valeria Caponetti

Coordinatore Dottorato
Prof. Aldo Roda

Supervisore
Prof. Marco Montalti

Esame finale anno: 2020

Table of Contents

Abstract

Nanotechnology is a new emerging field that involves many disciplines, including chemistry, materials science, medicine, electronics, environmental protection etc ... Nanotechnology aims at the design, synthesis, characterization and application of materials and devices on the nanoscale. Nanoparticles are defined as materials with the three dimensions in the space less than 100 nm. They possess chemical, biological, mechanical, electronic and magnetic properties hugely different from the corresponding macroscopic materials. Their peculiarities depend on the reduced size, shape, composition and interface, all aspects that can be controlled during the synthesis. Moreover, nanoparticles can act as platforms for assemble well-defined multifunctional structures able to perform varied tasks as drug delivery, sensors and contrast agent for bioimaging. Nanoparticles can be made by inorganic materials, as transition metals or silica, and by soft materials as molecular dye or organic polymers.

In the currently work a wide range of nanoparticles have been designed, synthesized and characterized for various purposes. In chapter 4 we propose simple and cheap strategy to develop multi-stimuli sensitive perylene diimide (PDI) molecules to create new smart materials by self-assembly. PBI has been chosen as a platform because is a well-known fluorophore, stable and with a high emission quantum yield that decreases considerably when the fluorophore aggregates.

Fluorescence is a powerful tool for mapping biological events in real-time with high special resolution. To achieve high sensitivity ultra-bright probes are needed as a huge number of fluorophores assembled in a single nanoparticle. Unfortunately, assembly results in fluorescence quenching because of short-range intermolecular interaction. In chapter 5 we report synthesis of designed molecule that self-assemble in nanoparticles in biocompatible environment without any dramatic decrease of fluorescence brightness. In chapter 6 a similar work has been repeated with commercial fluorophores.

Detection of chemical and biological agents plays a fundamental role in environmental and biomedical sciences. Among the various investigation techniques, luminescence based are the most sensitive and selective. For investigation of biological systems are indicated luminescent sensors working in correspondence of the biological window in NIR region. Gold nanocluster offer a suitable platform for multi-functionalization with a wide range of organic or biological ligands for the selective binding and detection of small molecules and biological targets. Gold nanocluster with diameter lower than 2 nm show detectable light emission in NIR region. In

chapter 7 small gold nanocluster functionalised with seven thiols in has been studied in presence active pharmaceutical ingredient (API).

Another interesting material is melanin. Melanin is an abundant and heterogeneous biopigment found ubiquitously in many livings being. Melanin plays an exemplary role as a radioprotector, thanks to its broad band absorption spectrum, its ability to convert 90% of absorbed light and free radical scavenger into heat. There are many sources in nature from which it is possible to extract melanin. Nevertheless, this operation has drawbacks. In fact, to date no extraction technique has been found that guarantees not to affect the properties of melanin in its natural environment. Therefore, researchers have sought alternative ways to obtain synthetic materials that reproduce the most interesting characteristics of melanin.

Currently the best candidate is polydopamine (PDA), a black insoluble material produced by oxidative polymerization of dopamine under alkaline conditions.

The unique characteristics of melanin, conferring antioxidant and radio- and photo-protective properties, are mostly due to the presence of unpaired electrons in the structure that results in a stable free radical property. We can suppose that increasing stable free radicals on melanin corresponds in increase the intrinsic free radical scavenging ability and consequently radioprotective effects. The presence of heavy transition metal, as Fe(III) and Mn(III) can contribute to increase the intrinsic melanin free radical scavenging ability, at the basis of radiation protection activity. Indeed, when Fe(III) and Mn(III) meets a free electron it can catch them reducing respectively at Fe(II)and Mn(II). In chapter eight we try to increase melanin radiation protection activity both increasing number of stable free radicals and introducing oxidative ion transition metal. We have chosen Fe(III) and Mn(III) to increase oxidative ability and Zn(II), that do not possess oxidative ability as reference. We used 4-amino-TEMPO to increase number of stable free radicals.

Acknowledgements

Prof. Marco Montalti, Dr. Jeannette Manzi, Dr. Gloria Guidetti, Dr. Andrea Cantelli, Arianna Menichetti, Moreno Guernelli, Dr. Marco Villa, Dr. Marianna Marchini, Dr. Francesco Romano, Dr. Francesco Palomba, Amedeo Agosti, Benedetta Del Secco, Liviana Mummolo, Alessandro Gradone, Ewelina Kuna, Lorenzo Casimiro, Martina Canton, Matteo Cingolani, Sara Angeloni, Giacomo Morselli, Prof Nathan Gianneschi, Dr. Chris Forman Dr. Claudia Battistella, Dr. Or Berger, Dr. Karthikeyan Gnanasekaran, Dr. Hao Sun, Naneki Collins-McCallum, Zofia Siwicka, Brittney Williams, Prof. Fabrizio Mancin.

Chapter 1: Introduction

1.1 Supramolecular chemistry

Supramolecular chemistry has been defined as the field of "chemistry of molecular assemblies and of intermolecular bond" or "chemistry of non-covalent bond"[1]. Supramolecular chemistry embraces organic and inorganic chemistry for precursors synthesis, physical and computational chemistry to understand properties and behaviour of supramolecular systems[2]. The first supramolecular systems observed were the host-guest system. They are formed by two molecules participating in a complex event to build a supramolecular structure. Usually the host is a large molecule, such as an enzyme or a synthetic cyclic compound, with a defined binding site. The binding site is the region where non-covalent interaction with the host happens. The guest could be an ion or a small molecule. Concepts at base of host-guest chemistry are recognitions and selectivity[3]. Fisher introduced them with the *lock and key* image, where geometric shape and size of guest are complementary to the host as shown in Fig.1.1.

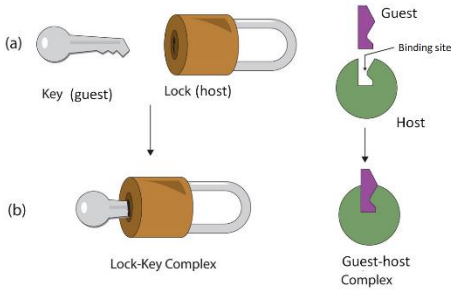

Fig.1.1 Schematic representation of a) the key (guest) and the lock (host); b) The lock-key and host-guest complex

There are other elements that contribute in incrementing stability in supramolecular complexes, as the positive cooperativity[4]. It occurs when host species with multiple binding site covalently connected forms a more stable host-guest complex than a similar system with not joined sites. Another decisive element is the host preorganisation, i.e. host geometry does not require a significant conformational change to bind a guest in the most stable way possible. A common example of preorganisation principle is the increased stability of ring-based host complexes compared to acyclic analogues. This is called the macrocyclic effect[5]. Indeed, when a linear host wraps around a guest, it loses many freedom degrees, as consequence the entropy of the system decreases. A free macrocyclic host does not have such conformational freedom, so the entropy decrease is limited.

An important characteristic of supramolecular systems is the stability of the complex in solution. To evaluate the host-guest affinity, binding constant, *K*, has been introduced and is defined as

$$K = \frac{[HG]}{[H][G]}$$

where [H] is host concentration, [G] is guest concentration and [HG] is complex concentration. To measure binding constant, it can be used any experimental technique that produces information about host-guest complex concentration as function of separated host and guest concentrations. Titrations are the more indicated experiments[6]. The most suitable can be chosen according to the characteristics of the system in question. For example, for macrocycles with tertiary amine, that can be protonated, protonation constant can be determined with a simple acid-base titration[7]. Another strategy is the isothermal titration calorimetry[8]. In this technique heat enthalpy, is measured as function of added guest or host concentration. If a fluorescent species is involved in the equilibrium fluorescence titration can be applied[9]. When complex or free host or guest possess a characteristic absorption band can be chosen[10].

Supramolecular systems are also formed by molecules, similar in size, that have complementary functionalities and interact to build more complex supramolecular species. The phenomenon is termed self-assembly and is the spontaneous equilibrium between two or more molecular components to produce an aggregate with a structure that is dependent only on the intrinsic information contained within the chemical building blocks[11]. Reversibility is a key feature in self-assembly and this permit them to correct mistakes in the supramolecular structure to achieve the most thermodynamically stable product. Self-assembled systems can be classified according to the diversity of interactions involved. Single-interactions self-assembly refers to systems where only one kind of interaction is present. Palladium/amine square in a classic example[12]. More often interactions of various nature are involved in self-assembly, termed multiple-interaction self-assembly. In this case, self-assembly progress is dominated by the most stabilising interactions in a descending hierarchy. For example, metal-ligand complexes may form initially and then combine into a larger architecture via hydrogen bonds[13]. When in self-assembly process it is possible recognise distinct steps, it is called hierarchical assembly[14]. If the order of steps cannot be inverted is a linear hierarchy.

Formation of new interactions in self-assembly building is an enthalpically favourite process. However, formation of aggregate species has an entopic cost for the freedom degree lost by system. But the release of solvent molecules that were previously interacting with building block can reduce the entropic penalty. This is called solvophobic effect[2].

Self-assembly has attracted much interest from researchers in the last decades because ubiquitous in nature. In biological systems innumerable non-covalent interactions bring to highly complex architectures, that permit them to accomplish their tasks. It must be

remembered, however, that final product of self-assembly represent the thermodynamic minimum of the system and mistakes can be corrected during the aggregation process. With this strategy errors or unwanted bioproducts can be avoid and biological process are characterized by high selectivity results. Reproducibility is a vital aspect because any deviation could have disastrous consequences. For example, many serious diseases, such as BSE, diabetes and Alzheimer's Disease, are caused by the misfolding of proteins into toxic, aggregated β-sheet fibrils[15]. Proteins are linear macromolecules, composed of typically 200–300 amino acid residues held together through peptide bonds Cit. This covalent sequence is referred to as the primary protein structure. In biological environment linear backbone undergo folding upon itself in secondary and tertiary structures. Some of them can join with other proteins in larger aggregates termed quaternary structure, as reported in Fig.1.2.

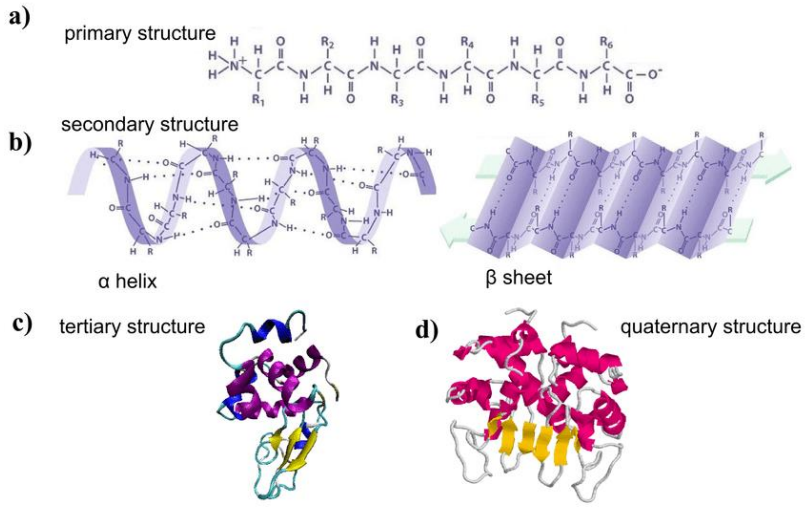

Fig.1.2 Schematic proteins self-assembly[16].

Proteins represent biological examples of hierarchical assemblies. Indeed, the tertiary structure cannot be obtained until the secondary structure has been assembled and similarly the quaternary structure cannot assemble until the tertiary folding is complete. Often self-assembly process is helped by species that are not involved in the final structure. For example, there are 'molecular chaperones' that protect protein until it is folded, to avoid that it may associate with other molecules rather than with itself. This is an example of assisted self-assembly. The observation and study of such marvellous systems at the base of life pushed researchers in trying to imitate nature and develop new materials for high tasks.

Over time the concept of self-assembly has been expanded to incorporate systems that do not fit into the first definition. Thus, subclasses have been created including assembly process that may require help, such as *templation*, or contain non reversible steps to complete aggregation[2]. The first subclass is called directed self-assembly and includes templated synthesis of

supramolecular aggregate. The most common example is the metal-directed self-assembly. Indeed, metal ions owns unique features that permit them to act as template for high predictable systems. Their well-defined coordination chemistry is the key for synthesis of regular geometric structure, high convergence, fast and facile formation of the final product, inherent defect-free assembly, great directionality and great versatility. Thus, metal-directed self-assembly has been widely used to synthesize supramolecular species with novel topological structures, such as cages[17], polyhedrons[18], ladders, racks[19], and helicates. The latter are coordination compounds displaying double- and triple helical structures that remember biological structure of DNA and collagen. A simple helicate is shown in Fig 1.3. The ligand (2, 2′:6′, 2′′ :6′′, 2′′′-quaterpyridine) is forming a double helicate using tetrahedral Cu(I) ions as templates[20].

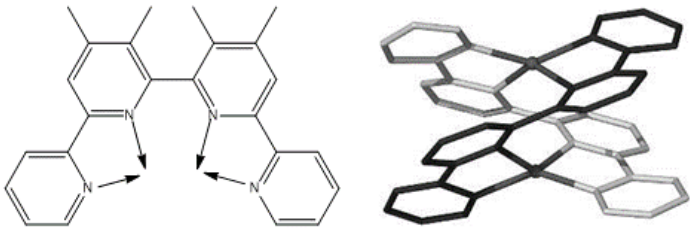

Fig.1.3 A simple example of a double-stranded helicate templated by tetrahedral Cu+ ions. The bidentate binding sites of the quaterpyridine ligand are shown by arrows.

Self-assembly with post-modification is another important subclass is. Here are contained systems that undergo synthetic alterations after the self-assembly step. Mechanical interlocking of molecules is an attractive strategy for supramolecular complex building. Mechanical interlocking means that two or more species are intertwine each other to form a single entity, i.e. are topologically linked and a covalent bond breakage is necessary to separate the individual units. Interlocking structures have interesting physical properties or the potential for them. An example of self-assembly with post-modification are catenanes: mechanically interlocked macrocycles. Catenanes can be templated via hydrogen bonding between the component parts or by using metal-mediated synthesis. An example is shown in Fig.1.4, where Cu(I) ion acts as a tetrahedral auxiliary linker between two substituted phenanthroline units, forming a self-assembled intermediate which can be reacted to form a catenane[21].

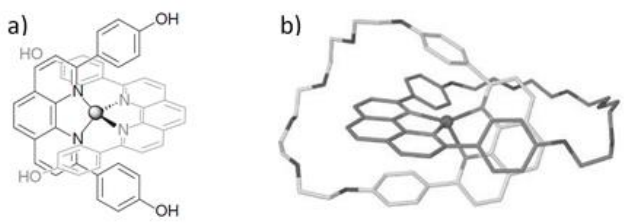

Fig.1.4 The Cu(i) ion acts as a linker between two phenol-substituted phenanthroline units, forming a self-assembled intermediate which can be reacted to form a catenane

Three rings ca be mutually interlocked without any catenane-like connections in the Borromean rings. The molecular graph of Borromean rings is shown in in Fig.1.5 and there are no two rings sharing a link[22].

Fig.1.5 Representations of Borromean rings:(a) the molecular graph; (b) three-dimensional view.

Rotaxane is an example of self-assembly with post-modification are, that consist in a macrocyclic where a linear molecule inserted as thread. The ends of the axel are capped to trap the ring. Apparently, rotaxanes cannot be described as topologically connected species as it is possible to pull the ring off the axel. However, in practice the macrocyclic ring cannot usually be removed without breaking any covalent bond[23].

Over the years, researchers have found more and more strategies for the synthesis and development of new materials based on the knowledge acquired in the field of supramolecular chemistry. One of the most surprising results was the discovery of nanomaterials.

1.2 Nanotechnology and Nanomaterials

In the last century the idea of manipulating matter at ever lower levels emerged more and more. The first exponent in this field was Feynman who with his famous speech *"There's Plenty of Room at the Bottom"* opened the way to a revolutionary approach to the design and production of materials. The challenge promoted by Feynman was matter manipulating at an extremely small scale, the level of molecules and atoms, i.e., the nanoscale. This event is considered by many to be the beginning of nanotechnology. Nanotechnology is the science of nanomaterials, i.e. materials with dimensions between about 1 and 100 nm. The first approach for nanotechnological devices preparation was the top-down approach[2]. It consists in breaking-down materials using techniques developed by solid state physicists called microfabrication. This term contains all various kinds of lithography. To make things smaller, scientists generally start by coating a substrate and cutting features into the coating. For example, a large block of silicon wafer can be reduced to smaller components by cutting, etching and slicing down to a desired size or shape. The most common microfabrication technique is photolithography, the

use of UV light as a pattern source. This technique contains an intrinsic limit, since it is not possible to overcome a resolution equal to $\lambda/2$, where λ is the wavelength of the source. More and more energetic sources can be used to reduce the lambda value, but this is related to an increase in the costs of the instruments used[24]. Very soon researches understood that to evolve in nanotechnology a paradigm change was needed. Drexler first introduced the idea of building nanomaterials atom-by-atom in 1980s. His goal was to build molecular assemblers capable of constructing objects at any scale, atom by atom[25]. His vision soon proved to be impractical[26], but the idea of developing nanomanipulation remained. The advent of nanoscale precision imaging tools allowed the nanomanipulation to move forward. Among the new techniques, scanning probe microscopes has emerged to be a unique tool for materials structuring and patterning with atomic and molecular resolution[27].

Scanning probe microscopes utilize nanoscale proximal probes that directly interact with samples and piezoelectric actuator that drives the probe with nanoscale precision.

The first time atoms had been precisely positioned on a flat surface, scanning tunnelling microscope was used to arrange 35 individual xenon atoms on a substrate of chilled crystal of nickel to spell out the three letter of the company IBM[28], as shown in Fig.1.6.

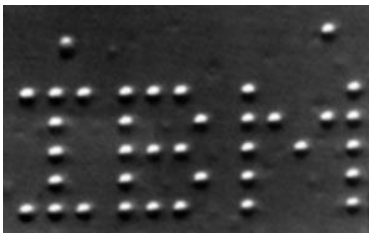

Fig.1.6 35 individual xenon atoms on a substrate of chilled crystal of nickel arranged with scanning tunnelling microscope to spell out the three letter of the company IBM

Despite remarkable progresses on nanomanipulation, this approach is not suitable for making large quantities of functional nanoscale materials. Free atoms resulted highly reactive and difficult to generate and handle. Instead molecules exhibit distinct properties making them more convenient building blocks than atoms. Indeed, they possess specific shape and reactivity that can be tuned to meet any need. Rational design of molecular allowed to leave great and expensive equipment to arrange building blocks in the space with nano-precision. It is enough to exploit the natural tendency of molecules to self-assembly. Therefore, it is natural that the knowledge and skills learned in the field of the chemistry of self-assembly have played a central role in the development and realization of nanoscale architectures[29]. Moreover, in a chemical approach about an Avogadro's number nano architecture are synthetized contemporaneously. Nanochemistry has permitted synthesis of a large range of nanomaterials. Today is still missing

a single internationally accepted definition for nanomaterials. Indeed, in the legislation of European Union and USA are present in different definitions[30].

For example, the Environmental Protection Agency refers to nanomaterials as, "Materials that can exhibit unique properties dissimilar than the equivalent chemical compound in a larger dimension"[31]. According to The US Food and Drug Administration "nanomaterials have at least one dimension in the range of approximately 1 to 100 nm and exhibit dimension dependent phenomena"[32]. Similarly, The International Organization for Standardization has described nanomaterials as a "material with any external nanoscale dimension or having internal nanoscale surface structure"[33]. European Commission describes the term *nanomaterial* is described as "a manufactured or natural material that possesses unbound, aggregated or agglomerated particles where external dimensions are between 1–100 nm size range"[34]. The lack of a general and universally recognized definition is due to the continuous growth and evolution of the field. In this chapter we will try to take a quick look at some of the most interesting nanomaterials. This list is in no way intended to be exhaustive of all existing nanomaterials. A good starting point are nanodevice. Nanodevice are made by linked molecular components with identifiable properties intrinsic to each component. Molecular building blocks can carry out the purpose for which they were created when they are connected in a nanoarchitecture, often with covalent bonds[2]. Since the execution of the nanodevice goals proceed through intercomponent processes, we can consider these macromolecules as supramolecular systems regardless the nature of the connectivity between components. In general, supramolecular devices are addressed by supplying the molecule with chemical, electrical or electromagnetic energy. If photoactive moieties (groups that can absorb or emit light) are involved in the device architecture, the system is called photochemical device. The key point in the design of photochemical devices is presence of sub-units, bound in a well-defined and controllable arrangement. Incident electromagnetic radiation excites an absorption moiety of the supramolecular system, changing the electronic interactions among the different components. Photophysical devices have been engaged for solar energy conversion. The key photophysical steps of solar energy harnessing are absorption of light which drives an initial electron–hole separation; cascade electron/hole transfer to the periphery of the system creating an independently reactive electron/hole pair and independent redox reactions at each site. A practical system should include a chromophore that absorbs sunlight, and electron donor and electron acceptor moieties, which are pre-organized in a way that permits the control of their electronic and steric interactions and therefore the rates and yields of electron transfer[35] An example is the antenna of four zinc porphyrin moieties, linked

to an artificial reaction center made up of a porphyrin electron donor joined to a fullerene acceptor, as shown in Fig.1.7 Excitation of any zinc porphyrin of is followed by energy transfer to the free base porphyrin. The resulting excited state donates an electron to the fullerene to generate an energetic charge-separated state[36].

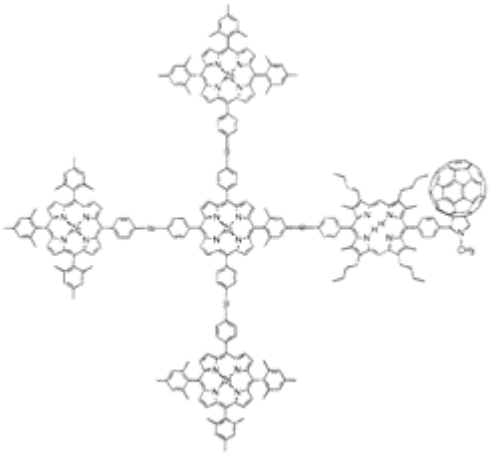

Fig.1.7 Photochemical device four zinc porphyrin moieties, linked to an artificial reaction center made up of a porphyrin electron donor joined to a fullerene acceptor

Mimicking biological devices is an interesting goal. For example, muscle in the human body are activated with complex process initiated by a potential travelling down a motor neuron. This stimulation is a mechanism that puts our limbs into automatic action to carry out a task. To mimic biological energizing process that activates a device a molecule needs to be able to change shape upon stimulation. Ionic electroactive polymers are promising mimic of biological muscles. Ions movement causes the material bending. The complex is an example of thermodynamic self-assembly Indeed, complexation is reversible and after ion removal polymers regain their initial conformation. A chemical example of a prototype ion-triggered molecular muscle is the extended terpyridyl ligand. In the free state, the ligand adopts an extended conformation. Upon binding Pb^{2+} ions, it a coiled structure is formed[37], as reported in Fig.1.8.

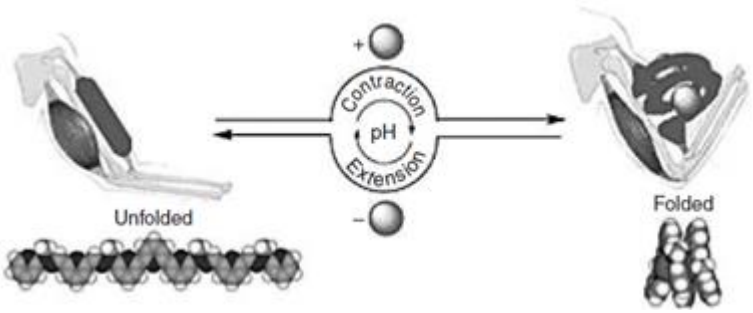

Fig.1.8 Ionic electroactive polymers in extended and contracted conformation. They mimic muscle in the human body

Nanochemistry has developed also new and fascinating nanomaterials, i.e. materials with at least one dimension between 1 and 100 nm. According this definition it is possible to divide the

nanomaterials into classes according to the number of dimensions that fall within the nanometric range. For example, sheet or thin films can extend in width and length for micro and macro-metric distances. But they can have a nanometric thickness. In this case they are considered two-dimensional structure. Graphene is one of the most attractive examples of this class. Graphene is a single atomic plane of graphite, sufficiently isolated from its environment to be considered freestanding. It is shown in Fig.1.9.

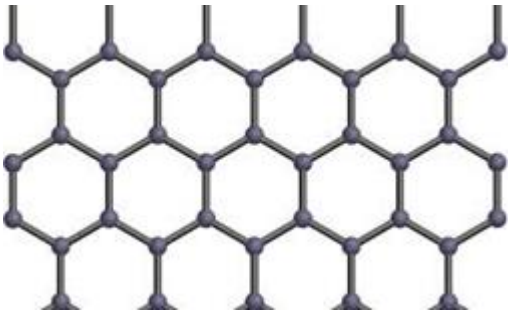

Fig.1.9 Structure of graphene[38]

Long-range π-conjugation in graphene yields extraordinary thermal, mechanical, and electrical properties, which have long been the interest of many theoretical studies and more recently became an exciting area for experimentalists[39]. The first surprising fact about graphene is its only existence because two-dimensional crystals were thought to be thermodynamically unstable at finite temperatures. In no time he has climbed all the rankings, proving to be a material with almost infinite resources. Indeed, it is the thinnest[40] known material in the universe and the strongest ever measured[41]. Its charge carriers exhibit giant intrinsic mobility[42], have zero effective mass and can travel for micrometres without scattering at room temperature[43]. Graphene can sustain current densities six orders of magnitude higher than that of copper[44], shows record thermal conductivity[45] and is impermeable to gases[46].

Although it may seem hard to believe, the potential of two-dimensional materials goes far beyond graphene. One of the fields that has most affected the researchers is that of surfaces. The idea of create a coating to protect or functionalize surfaces has pushed research to develop two-dimensional layers always with greater precisions Y he results of these efforts was the discovery of monolayers. Self-assembly is a powerful strategy to form ordered two-dimensional monolayers chemisorption of appropriately functionalised molecules onto substrate surfaces. Monolayers are typically formed by amphiphiles comprising long alkyl chains in conjunction with a polar head group, or long-chain molecules bearing a functional group at one end capable of surface binding[2]. Self-assembled monolayers are commonly prepared by immersing a clean substrate with a reactive surface in a solution of the coating molecules. At the beginning, chemisorbed coating molecules will exist on the surface in a disordered fashion. But slowly

intermolecular interactions will drive molecules in stable, ordered, close-packed monolayer. Thiol self-assembled monolayers are the most common and extensively studied monolayers. They exploit the strong and selective sulphur-gold bond. A gold surface is immersed into a solution of thiol that rapidly attach to the substrate. The stating random configuration evolves in an ordered monolayer according to self-assembly principles.

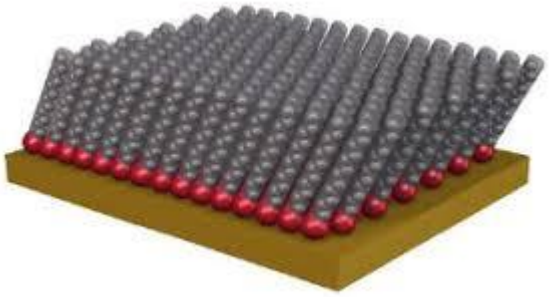

Fig.1.10 Schematic showing an ordered self-assembled monolayer of densely packed alkane thiols[47].

Moreover, it is possible functionalize monolayer once it has formed. Many functional groups can be appended at the end of the thiol, which leads to the use of thiol self-assembled monolayers in molecular recognition[48], bio sensing[49] and devices[50]. A similar technique is used to prepare thiol-coated nanoparticles. In chapter x we report an original work where gold nanoparticles are decorated with a thiol-monolayer for active pharmaceutical ingredient sensing. The strong point of this technique is its simplicity, the weak point is that the choice of materials is limited by the mutual affinity of the substrate and the coating.

Langmuir–Blodgett technique to overcome these limitations, by arranging molecules in organised assemblies. Highly structured, controlled multi-layered thin films are prepared by the repetitive dipping of a solid substrate through a mechanically compressed monolayer spread, usually, at the air–water interface[2]. Monolayer at the air–water interface is built exploiting intrinsic properties of molecules called surfactant. They have an amphiphilic nature and decrease the surface tension of water but are insoluble in it[51]. As the process proceeds the solid material is assembled onto the surface and this leads to a material that has a uniform thickness and laminar structure.

Many surprises also derive from single-dimensional materials. This class includes whiskers, fibers or fibrils, nanowires and nanotubes. The latter exist as single-walled carbon nanotubes and multi-walled carbon nanotubes. The first structure can be described as an enrolled graphene sheet the second one is like as graphite fibres. They stand out among the one-dimensional materials thanks to their electronic and mechanical properties. Nanotubes present high electrical conductivity, that depends on diameter and can modulated to pass from a

semiconductor to metallic behaviour[52] The large surface area can be used in catalytic[53] or adsorption processes. They have been proposed in energy storage, particularly hydrogen storage[54]. Nanotubes curvature possess specific features. Indeed, here there is a π–orbital mismatch which makes them selectively reactive points[55]. They can be exploited for specific endcap modifications[56] or nanotubes purifications[57]. Also, mechanical properties of the nanotubes are remarkable. Indeed, nanotube are characterized by high tensile strength and stiffness, thanks to the strength of the C-C bond[58]. Then they could be excellent instruments because they would be able to withstand the impact with the surface and could lead to improved resolution and robustness in comparison to conventional materials, such as silicon and metal tips[59]. Moreover, elasticity of nanotubes in axial direction has been evaluated and resulted in a large Young's modulus[60]. They, also, present high flexibility that suits for composite materials which need anisotropic properties[61]. In the end there are the materials of zero order, that is those materials with all three dimensions in the nanometric range. These are commonly referred to as nanoparticles and represent one of the most extensive and varied classes of nanomaterials. In fact, the enormous potentialities contained in these nanostructures have pushed the researchers to study them for decades producing an extremely wide range. The work in question focuses on nanoparticles versatility, the variety of their nature and their potential in many areas.

1.3 Nanoparticles

There are different ways to catalog nanoparticles, based on their synthesis, function, shape and composition. Here it was chosen to use the latter and nanoparticles can be organized into four material-based categories: i) Carbon-based nanoparticles; (ii) inorganic-based nanoparticles; (iii) organic-based nanoparticles.

One of the most important proponents of this category are the fullerenes. The fullerenes are closed carbon-cage molecules containing only pentagonal and rings. Icosahedral C_{60} molecule is a celebre example. Kroto and all synthetized C_{60} unintentionally for the first time during their graphite laser vaporisation experiments[62]. The fullerene family includes larger molecular weight fullerenes C_n (n>60), as C_{70}, that has a rugby ball-shaped symmetry C_{76}, C_{78}, C_{80}. However, C_{60} besides being the founder of the family, it is also the most studied. The 60 carbon atoms in C_{60} are located at the vertices of a regular truncated

icosahedron with a diameter of 7.10 Å[63]. The molecule is composed by 20 hexagonal faces and 12 additional pentagonal faces. Each carbon atom has four valence electrons for the formation of three chemical bonds, and there will be two single bonds and one double bond. The

hexagonal faces consist of alternating single and double bonds, whereas the pentagonal faces are defined by single bonds[64]. C60 possess 120 symmetrical operations and it is the most symmetrical molecule[65] The first intentional fullerenes was reported by Kratschmer that used an arc discharge between graphite electrodes[66]. The formation of fullerenes is a remarkable example of thermodynamic self-assembly, since under these high-energy conditions even C–C bond formation becomes somewhat reversible and closed-shell species with no dangling bonds are the most stable forms of carbon under these conditions[2]. Fullerene chemistry has been a very active research field, because of the uniqueness of the C_{60} molecule and its ability to have a variety of chemical reaction. The C=C bonds of C_{60} react like those of very electron-deficient arenes and alkenes. Therefore C_{60} behaves as an electron-deficient `superalkene' rather than as a `superaromatic'[67]. The most well-known derivatives of C_{60} are those with alkali metals, which become superconducting with high transition temperatures[68]. In general, fullerenes have found applications in many relevant sectors thanks to their intrinsic properties and thanks to possibility of large functionalization to achieve desired characteristic. For example C_{80} fullerenes incarcerating rare-earth metals have been used for photovoltaic devices with excellent results[69]. One of the biggest fullerene limitations is water insolubility and aggregation in aqueous media. To overcome this limit many different fullerene derivatives have been functionalised and, today, the medical applications of fullerenes include antiviral activity, antioxidant activity and their use in drug delivery[70].

A new class of carbon-based nanoparticles is represented by carbon nanodots, nanoparticles with a size below 10 nm typically composed by carbon, oxygen, nitrogen and hydrogen[71]. They were observed for the first time during purification of single-walled carbon nanotubes through preparative electrophoresis in 2004[72]. Carbon nanodots are ease of synthesis and of functionalization, water-soluble, biocompatible and non-toxicity[71]. Their most important properties is a bright fluorescence, tunable across the visible range[73]. Moreover, carbon nanodots were shown to possess excellent up-converted fluorescence. Interestingly, the carbon nanodots photoluminescence from can be quenched efficiently by either electron acceptor or electron donor molecules in solution, indicating that photoexcited carbon nanodots are excellent electron donors and electron acceptors[71]. Surprising photophysical properties of carbon nanodots and their interesting photoinduced electron transfer properties have stimulated interest in their application in fields such as energy and catalysis[74]. When exited with near-infrared emission carbon nanodots exhibit fluorescence in the ‘‘water window’’ a spectral region important for the transparency of body. This, combined with the high

biocompatibility of the material, opens the door to applications in biological labeling[75], bioimaging[76] and drug delivery[77].

Among inorganic based nanoparticles, a special place is reserved to metal nanoparticles.

The most ancient metal nanoparticles, and probably the most ancient nanomaterial, are gold nanoparticles. Their appearance dates back around the 5th or 4th century B.C. in Egypt and China as colloidal gold used to make ruby glass[78]. Perhaps the most famous example of gold colloids is the Lycurgus Cup. Transmitted light gives it a red color and reflected light green color[79]. In 1857, Faraday observed that reduction of an aqueous solution of chloroaurate ($AuCl^{4-}$) with phosphorus in CS_2 led to the formation of deep red solutions of colloidal gold[80]. During the twentieth century, the synthesis of gold nanoparticles was refined to reach citrate reduction of $HAuCl_4$ in water, which was introduced by Turkevitch in 1951[81]. Subsequently Brust and Schiffrin set up a method to synthetize thermally and air stable gold nanoparticles of reduced dispersity and controlled size for the first time. Gold nanoparticles have been stabilized by anionic mercaptoligand and they can be repeatedly isolated and redissolved in common organic solvents without irreversible aggregation or decomposition[82]. Later on, new synthetic strategies were developed that involve microemulsions[83], copolymer micelles[84], reversed and micelles[85]. The surfactant is solubilized in an organic solvent and here it self-assembles forming a microemulsions or a reversed micelle. $HAuCl_4$ is added and ions concentrate in the favorable microenvironment of surfactant. Then, a reducing agent starts the growth of the nanoparticles inside polar pools of surfactant allowing shape and size control[86]. The great interest in gold nanoparticles stems from their surprising properties. First, they are distinguished by their optical properties. Indeed, their broad absorption band in the visible region around 520 nm occurs only when gold is in this state of matter and is caused by the surface plasmon band Cit. When metal nanoparticles are hit by a radiation, the electron gas at the surface of nanoparticles begins to oscillate with the same frequency of the electromagnetic field[80]. To note that these arguments are not valid for particles with core sizes less than 2 nm in diameter due to the onset of quantum size effects[87]. Researchers focused their efforts in trying to exploit gold nanoparticles properties mainly for imaging[88]. Moreover, gold nanoparticles have been shown to be applied in many fields due to their reduced toxicity and to the fact that they can act as a functionalized scaffold to be functionalized. So recently, gold nanoparticles have found applications in biomedical fields as biosensors[89], immunoassays[90], genomics[91], photothermolysis of cancer cell[92] and targeted drug delivery[93]. Indeed, gold nanoparticles can be engineered to work as applicable nano-platforms for controlled drug delivery and as bioimaging probes at the same time[94]. The surface can be decorated with biological, biophysical,

and biomedical carriers[95]. Another advantage in nanoparticle-based drug transport is that they can be functionalized to selectively recognize only target tissue or cells[96]. Controlled release of drug can happen with two processes: internal stimuli operated system, which could occur in a biologically controlled manner, or external stimuli, operated by the support of stimuli-generated processes. Engineered gold nanoparticles can exploit both, enhancing the targeted drug delivery, especially in cancer therapies[97]. Silver nanoparticles have inimitable properties making them interesting for commercial and scientific appliance as antimicrobial[98], food storage[99], health industry, disinfectant[100] and chemotherapeutic agents[101]. Silver nanoparticles appear as a potential medication negotiator because of their massive surface-to-volume ratios and crystallographic surface structure[98]. Indeed, antimicrobial activity of silver nanoparticles is closely associated with their size. Smaller nanoparticles possess superior antibacterial activity. For this reason, specific synthetic strategies and stabilizers can be used to overcome the irregular size distribution. Most common chemical approaches are based on reduction, using a variety of inorganic and organic reducing agents[102], physicochemical reduction, electrochemical techniques[103], and radiolysis[104]. Lately, green chemistry approaches with proven validity are emerging. Here we mention polyoxometalates[105], Tollens[106], Polysaccharides[107], irradiation[108] and biological method[108]. Silver nanoparticles have been permitted as active ingredient by many agencies, including the US FDA, US EPA, SIAA of Japan, Korea's Testing and Research Institute for Chemical Industry and FITI Testing and Research Institute[98]. Silver nanoparticles are becoming a substitute of antibacterial agents, thanks to their effectiveness against a broad spectrum of gram-negative and gram-positive bacteria[109].
and their ability to overcome the bacterial resistance against antibiotics[110]. They have good results also in fighting fungal infections[111]. Moreover, silver nanoparticles are biocompatible and low-toxic, suitable for immunodeficient patients. Because least amount of silver nanoparticles is safe for human antifungicidal and anti-bactericidal activities of has been exploited for sanitization of food and water and in daily product as soaps[112], plastics[113] and textiles[114].

There are inorganic based nanoparticles made by semiconductors, called quantum dots. What distinguishes quantum dots from other inorganic nanoparticles are their optical properties. Indeed, they have dimensions and numbers of atoms between the atomic-molecular level and bulk material. The quantum confinement causes the electronic energy levels are not continuous as in the bulk, but are discrete (finite density of states), because of the confinement of the electronic wavefunction to the physical dimensions of the particles. This means that quantum confinement results in a widening of the band-gap with a decrease in the size of the quantum

dots. The band-gap in a material is the energy required to create an electron and a hole at rest (i.e., with zero kinetic energy) at a distance far enough apart that their Coulombic attraction is negligible. When the energy spacing between the electronic levels exceeds the thermal energy (kT) substantial variation of fundamental electrical and optical properties with reduced size will be observed This is why quantum dots exhibit different color of emission with change in size. As consequence, use of these quantum dots properties requires enough control during their synthesis, because their intrinsic properties are determined by different factors, such as size, shape, defect, impurities and crystallinity. The unique optical properties of quantum dots can find applications for devices, such as light emitting devices and solar cells. Indeed, the absorption of quantum dots can be tuned from UV through the visible into the near-infrared and the width of emission peak from quantum dots is almost half of organic dyes. Then, surface passivation can enhance photostability of quantum dots. Moreover, inorganic materials usually present increased thermostability than organic materials. So, they represent a better choice, in operating conditions they are subjected at great thermal stress.

Currently, a significant amount of research is aimed at using the unique optical properties of quantum dots in biological imaging. Quantum dots are very promising, respect common organic dyes thanks their higher extinction coefficients and emission quantum yield. Quantum dots undergo less photobleaching and multiple quantum dots can be used in the same assay with minimal interference with each other and they may be functionalized with different bio-active agents[115].

In recent years a new class of nanomaterials has begun to be developed, based on organic molecules. The intrinsic characteristics of these materials have delayed their study and research. Indeed, in comparison with inorganic materials, organic materials present lesser thermal stability and lower mechanical properties. These disadvantages were thought to limit synthesis and applications. Besides, it was believed no size effect is manifested in organic nanomaterials. This last statement was soon denied. Indeed, the size effects were discovered in studying the spectral properties of particles with the sizes from several tens to several hundreds of nanometers[116]. Organic nanoparticles include interesting materials as conjugated polymers, polydopamine, dendrimers, but the most versatile are the nanoparticles of organic molecules. The hallmark of molecular materials is the ability to tailor their assembly, structure and function, realized through the fine-tuning of the relatively weak intermolecular interactions. Effective utilization of this unique attribute of molecular materials is bound to be reflected in the emerging field of molecular nanomaterials[117]. When choosing to work with these fascinating and innovative materials, one must keep in mind that their electronic and

optical properties are fundamentally different from those of inorganic metals and semiconductors, due to weak intermolecular interaction forces of the van der Waals type. To understand how these properties, develop as a function of size is of fundamental and technological interest[116]. Indeed, the electronic properties of the obtained nanoparticles are very difficult to be predicted from the molecular structure. Now, weak intermolecular interactions, such as hydrogen bonds, π−π stacking, and Van der Waals contacts are responsible for the optical and electronic properties of organic nanostructures.

One of the first and simplest strategies exploited for synthesis of molecular nanoparticles was controlled solvent evaporation. Preparation of an aqueous colloidal solution of b-carotene and poly(vinylpyrrolidone) was described for the first time in 1965[118].They were dissolved in chloroform, that was evaporated. The solid mixture was redispersed in water forming an aqueous colloidal solution, called `hydrosol'. Commonly used techniques are drop casting, spin coating and zone casting. Best results can be achieved by optimizing polarity and volatility of the solvent, concentration of the solution and chain-length of any amphiphilic molecules present. Subsequently, by Nakanishi and coworkers reported reprecipitation method. It is based on quick exchange of the solvent environment that leads to limited crystal growth. Microliter quantities of a solution of the compound of interest in a good solvent are injected rapidly into excess of a second liquid which while being miscible with the first liquid, acts as a nonsolvent or poor solvent for the compound of interest. This addition is commonly carried out under vigorous stirring or ultrasonication. Molecules in the poor solvents start to aggregate in nanostructures dispersed homogeneously in the bulk medium[119]. The reprecipitation method was widely used to synthetize different molecular nanoparticles[120] because is relatively simple, accessible and occurs under mild conditions, which allows fabrication of nanoparticles of thermally unstable compounds. Another strategy is ion association. No organic solvents are employed, but the driving force of aggregation is the presence of suitable ions that are complexed of molecules, bringing to formation of nanostructures in solution. The particle size can be controlled by varying the cation-to-anion molar ratio[121]. As mentioned before, optical and electronic properties of molecular nanoparticles are ruled by weak intermolecular interactions at the base of their architecture. Indeed, electronic structure of molecules is perturbed by the interaction with neighboring molecules leading to significant changes in many cases, in optical responses such as absorption and emission. The exciton coupling model provides a framework to understand such effects which have important consequences for photo and electroluminescence applications[117]. Among the advantages in moving from simple organic molecules to molecular nanoparticles is that the properties of the latter can be

modulated with size and above all they can often be dispersed in water. Indeed, they demonstrate a great application potential in `green' chemistry and chemical biology. Researchers are beginning to work on applying molecular nanoparticles in different sectors. For example, thanks to their photophysical properties[122] were used, as the organic light-emitting diodes (OLED). Usually, solid state materials have reduced or absent fluorescence quantum yield. But in some fluorophore aggregation enhanced fluorescence, by reducing competitive non-radiative mechanism.

Production of drug nanoparticles is one of the main directions in the preparation of new highly efficient formulations. Indeed, often drugs are not water soluble and this reduces their efficacy, but and nanoforms of drugs exhibit unique properties solubilities that open new promising approaches to the treatment of different diseases[123].

1.4 Bioimaging and optical imaging

The introduction of biomedical imaging has revolutionized the healthcare for diagnosis and treatment of human diseases. Thanks to it the diagnosis and treatment of diseases has become increasingly specific, early and non-invasive for the patient. Over the years, bioimaging has developed starting from when Wilhelm Roentgen captured the first X-ray image of his wife's hand in 1896[124]. Today there are different techniques such as computer-assisted tomography (CAT scan), ultrasound imaging, and magnetic resonance imaging (MRI). However, these techniques investigate mainly anatomical state at the tissue or organ levels[125]. The currently biomedical imaging techniques used have of limitations. For example, x-ray imaging and CAT scan utilize ionizing radiations, ultrasound cannot provide resolution smaller than millimeters as well as to distinguish between a benign and a malignant tumor. Among the various investigative techniques, optical imaging is emerging more and more. Optical imaging is based on interaction between light and matter. The light, in particular the one of near-infrared region, is able to penetrate deep into the tissues and it can be reflected, scattered, absorbed and emitted. Each of these portions of the radiation is at the base of various techniques. However, almost all use the laser as a light source to generate an optical response, highly sensitive charged-coupled device (CCD) technology and powerful mathematical modeling of light propagation through the biological systems[126]. Optical imaging has several advantages including not being harmful, size scale investigation range from macroscopic object to 100 nm[127]. It can be applied for in vitro [128], in vivo[129], and ex vivo specimens[130]. Moreover, it is possible combine optical imaging techniques in multidimensional imaging, or with other imaging techniques such as ultrasound (photoacoustic imaging)[131].

The next step is to extend imaging at the cellular level. Indeed, information on the biological and molecular composition of tissues at the cellular level is necessary for early detection, screening and diagnosis. For example, detection of early molecular changes can anticipate cancer diagnosis.

A major step forward in optical imaging was made with the introduction of contrast agents. They allow to enhance the optical contrast by virtue of their contrast enhancing properties, for example reducing the background signal and improving the image resolution. The first contrast agents were organic fluorescent compounds, that possess strong signal capable to overcome tissue autofluorescence. A good contrast agent should be non-toxic, or low-toxic and they should be photostable and do not produce toxic products upon light excitation, so that they can be administered safely[131]. Then, they should have a high extinction coefficient for effective absorption and a high quantum yield for obtaining strong fluorescence signal, i.e. it should have high brightness. Brightness is defined as

$$B = \varepsilon \cdot \Phi$$

Where ε is molar extinction coefficient and Φ is fluorescence quantum yield.

Organic fluorescent contrast agents work very well at different level of investigation. Indeed, they have been used to study cells compositions, tissue damage and cancer propagations. But they have many limitations. First, organic molecules are not robust, but rapidly undergo photobleaching, when excited by light source. They can also undergo photoreactions with toxic sub product[132]. Then organic molecules are usually hydrophobic and this limit preparation of their aqueous-based formulation. Moreover, it is important that fluorescent compounds are delivered selectively to the target tissue to improve image contrast.

Introduction of nanoparticles as contrast agents for optical imaging present many advantages. Usually, nanoparticles have improved photophysical properties, as brightness, compared to single molecules. Then, they are objects more resistant undergo photobleaching more difficult. As consequence, their photophysical signals are stable over time[132]. This improves sensitivity of imaging techniques and it has tremendous potential for real-time monitoring, for example of cancer progression. Nanoparticles can be engineered to work as contrast agent for multiple techniques at the same time[133]. For example, a multifunctional nanoparticle can be suitable for optical imaging, MRI and CAT. In that way, complementary techniques can provide a complete picture of patient clinical situation. Moreover, it is possible add water soluble external shells and prepare non-toxic aqueous solutions. Then, nanoparticles permit to target desired tissue. There two strategies active and passive targeting. In the first case surface nanoparticle can be decorated with biological molecules as proteins, antibodies and enzymes. In this way they can

be programmed to recognize selectively a tissue target and accumulate here. The passive targeting is used mainly for tumor targeting. It is called enhanced permeation and retention and exploits vessel damages that are commonly in cancer presence[134]. Nanoparticles with diameter lower that 100 nm can be delivered to the injury tissue by systemic circulation.

Quantum dots have been largely studied for bioimaging purpose. They have a broad absorption spectrum with high molar extinction coefficient, that makes them bright probes in aqueous solutions and under photon-limited in vivo conditions.

Emission band is narrow and intense, with large fluorescence quantum yield. This allows to increase the signal/noise ratio. Moreover, the emission spectra can be tuned across a wide range by changing the size and composition of the quantum dots. In particular, they show strong emission in near infrared range where there is biological window, and light penetration is deeper. Moreover, quantum dots have long fluorescence lifetimes on the order of 20–50 ns, which allows them to be distinguished from background and other fluorophores for increased sensitivity of detection[135]. Quantum dots can undergo photobleaching upon excitation. It happens when the absorbed radiation causes irreversible alterations in the fluorophore that cannot emit anymore light. In is found that surrounding the core with a large band-gap semiconductor shell increase photostability of quantum dots. Another problem, it that they, often, undergo photoreactions, as photooxidation in biological environment. To overcome this limit, they can be capped with a protective shell. The shell in theory should not alter quantum dot photophysical properties[136]. That means that it should be transparent at excitation wavelength and not fluorescent. Moreover, quantum dots usually are not water soluble, but they can be dispersed in aqueous media by surface functionalization mercaptoacetic acid, silica over coat or amine-modified poly(acrylic acid)[137]. The only major concern about the biomedical use of quantum dots is their possible toxicity. In this regard, researchers are working to make these materials increasingly safe.

Silica nanoparticles offer a different approach to improve optical imaging with nanotechnology. They are made by amorphous silica dioxide, a transparent material, that do not possess own photophysical properties. But it is possible incorporate molecular fluorophore inside silica matrix. Encapsulation of dye do not alter its intrinsic photophysical properties and protect dye by chemical degradation in biological environment. For example, oxygen molecule penetration could quench the dye. Inside the silica the photostability of dye molecules increases substantially compared with bare dyes in solution. Silica nanoparticles are water soluble and can be used as medium to prepare stable water solution of organic hydrophobic dyes[132]. Moreover, dye doped silica nanoparticles are non-toxic and biocompatible. Their surface can

be derivatized with a peptides, antibodies or oligonucleotides to increase selectivity to the target. The advantage of this strategy is the great versatility. Indeed, almost any dye can be encapsulated, so it is possible select the fluorescent probe with the best properties for any purpose. Due to these novel features, functionalized silica nanoparticles have found widespread applications in bioanalysis and bioimaging applications[134].

Lately, molecular nanoparticles are attracting interest of researchers thanks to their specific characteristics. Their properties meet many needs of optical imaging. Novel strategies allow to synthetize nanomaterials where fluorophores are encapsulated inside nanostructures that can make them soluble in water and reduce their toxicity. In comparison with inorganic nanomaterials molecular nanoparticles have advantages such as biocompatibility and structural versatility[138]. Optical properties of molecular nanoparticles are mainly determined by the organic dye encapsulated inside nanoparticles. It is possible choose the specific chromophore to meet the requirements for any imaging task. Moreover, it provide the feasibility to develop nanoparticles with the same size but different signal outputs, enabling multiplexed imaging at different wavelengths without variations in pharmacokinetic properties[139].

Molecular nanoparticles can exploit biocompatible polymers to functionalize surface to reach desired biodistribution. It is important that nanoparticles can recognize the target and accumulate in specific area, to give best signals.

A common example of the proven efficacy of molecular nanoparticles is indocyanine green. It has been approved by FDA despite drawbacks such as poor photostability, extensive protein binding and degradation in water severely impede the biomedical application of free cyanine dye molecules[140]. The possibility to synthetize organic polymer core–shell nanoparticles permit to protect it by biodegradation and increase its photostability[141]. Another example are porphyrin chromophores. They possess strong absorption in Soret and Q bands and have been exploited as sensitizers for dye-sensitized solar cells[142]. Their use in the biomedical field was limited by their water insolubility. Porphyrin have been conjugated with phospholipid into nanovesicles via supramolecular self-assembly, which introduced a new kind of photonic nanomaterials[143].

Perylene tetracarboxylic diimide is a fluorophore with intense photoluminescence and photochemical stability used as industrial pigment[144]. The first perylene tetracarboxylic diimide based nanoparticles used in for bioimaging consisted of perylene tetracarboxylic diimide encapsulated in the amphiphilic polymers to obtain water-soluble nanoparticles[144a].

1.5 Fluorescent nanoparticles for sensing

A chemical sensor is a tool able to transform chemical information, such as analyte concentration or the complete composition of a sample, into a decodable analytical signal[145]. Classical analysis methods often require sample pretreatment and transport, the large data collection and often expensive instruments. Chemical sensors allow to overcome these limits, offering an economic and easy alternative. In its simplest design, a fluorescent chemosensor is composed of a fluorescent dye and a receptor, with a built-in transduction mechanism that converts recognition events into variations of the emission properties of the fluorescent dye. Such systems in solution can also behave as probes for the desired species, allowing them to monitor their variation in concentration over time and space[146]. Luminescent chemosensors have different advantages. Indeed, fluorescence measurements are sensitive, economical, easy to perform and can provide a very high spatial and temporal resolution[147]. For best results, luminescent moiety in chemosensors must have a high molar coefficient and a high quantum luminescence yield. Furthermore, a luminescent chemosensor must have different requirements. In particular the material should be photochemically stable, should be compatible with the medium of interest and should have photophysical properties that do not depend on the environment or the specific analyte[148].

The main interferences are scattering light and autofluorescence, especially in biological systems. Systems with absorption and emission bands between 600-1100 nm are advantaged. Indeed, in this range scattering and natural fluorescence of biomolecules are reduced[149]. Unfortunately, fluorescence efficiency tends to decrease as the energy of the excited state decreases. Another strategy exploits luminescent units characterized by a particularly long life time[150]. The light derived from other phenomena is excluded using time-resolved spectroscopy since scattering light and the autofluorescence decay much faster than that coming from the chemosensor. Finally, systems with high Stokes-shifts permit to reduce interference due to the Rayleigh and Raman band. Usually these systems are characterized by charge-transfer excited states or use a combination of two different fluorophores between which energy transfer occurs efficiently[151].

A huge number of organic dyes, fluorescent proteins and luminescent metal complexes have been used for this purpose over the years. Even the most efficient among conventional fluorophores, however, suffer from some inherent limitations. Photobleaching, limited brightness and short lifetimes are serious drawbacks in many applications[152]. Fluorescent nanoparticles have emerged as a new class of fluorophores with the potential to overcome

these limitations. At the beginning, nanoparticles were considered as better-performing substitutes of traditional dyes in chemosensing applications. It was early clear that the potential of nanoparticles went much further. The high amount of reactive sites found on their surface make them ideal multivalent scaffolds for the realization of supramolecular assemblies, while their high surface to volume ratio allows for distinct spatial domains (bulk, external surface, pores and shells) to be functionalized to a comparable extent with different organic species. Over the last few years, nanoparticles proved to be versatile synthetic platforms for the implementation of new chemosensing schemes[153]. Indeed, one of the main goals in chemosensors design is signal amplification that allows to lower the detection limit. A strategy is designing a chemosensor where coordination of a single analyte is able to change properties of a large number of active units. This approach is particularly favoured in luminescent chemosensors since even very weak electronic interactions may be sufficient to induce variations on a relatively large scale. In this way, each receptor is electronically bound to many chromophores simultaneously, so that luminescent properties of all of them can be modified by the state of a single receptor[149].

Typically, for chemosensors design with signal amplification are used as scaffolds polymers[154], which do not guarantee control over the distribution of receptors and chromophores, or dendrimers[155], obtainable exclusively through a very complex synthetic pathway. Nanoparticles offer an interesting alternative. Indeed, their surface can be functionalized with different fluorescent units in an ordered frame.

In particular, luminescent silica nanoparticles are interesting. Silica nanoparticles appear to have no intrinsic toxicity and are transparent to visible light. Photophysical properties derive from the dye with which they are doped or from the capping agents. The silica matrix also has the function of protect the active material located inside the nanoparticle from the external chemical environment. The external species are unable to reach the fluorophore in the heart of silica reducing the possibility that undesired photodegradation processes take place, and maintaining the fluorophore in a chemically constant environment [148]. Luminescent chemosensors that exploit silica nanoparticles can be used for the detection in biological environments of analytes such as cations, oxygen, ROS etc… both because they have a very low cytotoxicity and because they allow to considerably increase the signal by increasing the brightness and reducing background noise thanks to signal amplification.

Quantum dots are nanoparticles of semiconductor materials and their properties depend by their size. They show a broad absorption and narrow emission spectrum. Emission is originating from the recombination of photogenerated electron-hole pairs, that happens on the

surface of nanoparticle. When surface is functionalized with charged molecules, emission could be affected. Chemosensor building cannot been achieved only by simply grafting ligands to the particles. More sophisticated strategies are needed. For example Sensitivity towards organic molecules was obtained by decorating the quantum dots surface with calixarenes[156] or cyclodextrins[157].

Several other strategies based on energy transfer have been designed. The general idea is to use the analyte recognition to modulate the energy transfer process between the quantum dot and a dye appended to its surface. For example, if the photophysical properties of the fluorophore and of the quantum dot are modulated appropriately it is possible induce an electron transfer from the coating molecules to the valence band of an excited quantum dot results in emission quenching. If the electron donor is bound to a substrate, this process may be interrupted by analyte presence and the emission restored.[153]

Since their introduction in biological applications nanoparticles have quickly evolved from a generic "passive" fluorescent labels to "smart" nanoprobes that carry additional functions. Nanoparticles have made great impact on modern molecular biology by providing innovative tools to explore new biological events. Nanosensors based on energy transfer have been integrated into a great number of homogeneous molecular assays to detect specific targets and monitor reactions. Nanoparticles have also proven to be excellent systems in an assembly due to their extreme sensitivity[158].

1.6 Bibliography

1. Lehn, J.-M., Supramolecular chemistry. *Science* **1993,** *260* (5115), 1762-1764.
2. Steed, J. W.; Turner, D. R.; Wallace, K., *Core concepts in supramolecular chemistry and nanochemistry*. John Wiley & Sons: 2007.
3. Cram, D. J.; Cram, J. M., Host-guest chemistry. *Science* **1974,** *183* (4127), 803-809.
4. Koshland Jr, D. E., The key–lock theory and the induced fit theory. *Angewandte Chemie International Edition in English* **1995,** *33* (23-24), 2375-2378.
5. Dietrich, B.; Viout, P.; Lehn, J.-M., Macrocyclic chemistry: aspects of organic and inorganic supramolecular chemistry. *Acta Cryst* **1993,** *49*, 1074.
6. Thordarson, P., Determining association constants from titration experiments in supramolecular chemistry. *Chem. Soc. Rev.* **2011,** *40* (3), 1305-1323.
7. Han, Y.; Meng, Z.; Chen, C.-F., Acid/base controllable complexation of a triptycene-derived macrotricyclic host and protonated 4, 4′-bipyridinium/pyridinium salts. *Chem. Commun.* **2016,** *52* (3), 590-593.
8. Velazquez-Campoy, A.; Freire, E., Isothermal titration calorimetry to determine association constants for high-affinity ligands. *Nature protocols* **2006,** *1* (1), 186.
9. Eftink, M. R., [11] Fluorescence methods for studying equilibrium macromolecule-ligand interactions. In *Methods Enzymol.*, Elsevier: 1997; Vol. 278, pp 221-257.

10. Formica, M.; Fusi, V.; Giorgi, L.; Piersanti, G.; Retini, M.; Zappia, G., Neutral urea-based receptors for phosphates: synthesis and spectrophotometric studies. *Tetrahedron* **2016,** *72* (44), 7039-7049.
11. Whitesides, G. M.; Grzybowski, B., Self-assembly at all scales. *Science* **2002,** *295* (5564), 2418-2421.
12. Fujita, M.; Tominaga, M.; Hori, A.; Therrien, B., Coordination assemblies from a Pd (II)-cornered square complex. *Acc. Chem. Res.* **2005,** *38* (4), 369-378.
13. Swiegers, G. F.; Malefetse, T. J., Multiple-interaction self-assembly in coordination chemistry. *Journal of inclusion phenomena and macrocyclic chemistry* **2001,** *40* (4), 253-264.
14. Goujon, A.; Du, G.; Moulin, E.; Fuks, G.; Maaloum, M.; Buhler, E.; Giuseppone, N., Hierarchical Self-Assembly of Supramolecular Muscle-Like Fibers. *Angew. Chem. Int. Ed.* **2016,** *55* (2), 703-707.
15. Lührs, T.; Ritter, C.; Adrian, M.; Riek-Loher, D.; Bohrmann, B.; Döbeli, H.; Schubert, D.; Riek, R., 3D structure of Alzheimer's amyloid-β (1–42) fibrils. *Proceedings of the National Academy of Sciences* **2005,** *102* (48), 17342-17347.
16. Enciso, M., Hydrogen bond models for the simulation of protein folding and aggregation. *arXiv preprint arXiv:1208.2177* **2012**.
17. Zhang, H.; Lee, J.; Lammer, A. D.; Chi, X.; Brewster, J. T.; Lynch, V. M.; Li, H.; Zhang, Z.; Sessler, J. L., Self-assembled pyridine-dipyrrolate cages. *J. Am. Chem. Soc.* **2016,** *138* (13), 4573-4579.
18. Li, J.-R.; Zhou, H.-C., Bridging-ligand-substitution strategy for the preparation of metal–organic polyhedra. *Nat. Chem.* **2010,** *2* (10), 893.
19. Wang, M.-S.; Guo, G.-C.; Fu, M.-L.; Xu, L.; Cai, L.-Z.; Huang, J.-S., Self-assembly of copper (II) complexes with ladder, bi-rack, rack–ladder–rack and layer structures by the directional-bonding approach using a T-shaped ligand. *Dalton Transactions* **2005,** (17), 2899-2907.
20. Lehn, J.; Sauvage, J.; Simon, J.-F.; Ziessel, R.; Piccinnileopardi, C.; Germain, G.; Declercq, J.-P.; Vanmeerssche, M., Synthesis and Metal-complexes of a Conformationally Restricted Quaterpyridine-Crystal-structure of its Dimeric Dinuclear Cu (i) Complex,[cu2 (pqp) 2] 2+. *Nouveau Journal de Chimie* **1983,** *7* (7), 413.
21. Cesario, M.; Dietrich-Buchecker, C.; Guilhem, J.; Pascard, C.; Sauvage, J., Molecular structure of a catenand and its copper (I) catenate: complete rearrangement of the interlocked macrocyclic ligands by complexation. *J. Chem. Soc., Chem. Commun.* **1985,** (5), 244-247.
22. Cantrill, S. J.; Chichak, K. S.; Peters, A. J.; Stoddart, J. F., Nanoscale borromean rings. *Acc. Chem. Res.* **2005,** *38* (1), 1-9.
23. Bruns, C. J.; Stoddart, J. F., Rotaxane-based molecular muscles. *Acc. Chem. Res.* **2014,** *47* (7), 2186-2199.
24. Iqbal, P.; Preece, J. A.; Mendes, P. M., Nanotechnology: The "Top-Down" and "Bottom-Up" Approaches. *Supramolecular chemistry: from molecules to nanomaterials* **2012**.
25. Drexler, K. E., Machine-phase nanotechnology. *Sci. Am.* **2001,** *285* (3), 66-7.
26. Bueno, O., The Drexler-Smalley Debate on Nanotechnology. *HYLE–International Journal for Philosophy of Chemistry* **2004,** *10* (2), 83-98.
27. XIE, X. N.; CHUNG, H. J.; WEE, A. T. S., Scanning probe microscopy based nanoscale patterning and fabrication. *COSMOS* **2007,** *3* (01), 1-21.
28. Eigler, D. M.; Schweizer, E. K., Positioning single atoms with a scanning tunnelling microscope. *Nature* **1990,** *344* (6266), 524.
29. Whitesides, G. M.; Mathias, J. P.; Seto, C. T., Molecular self-assembly and nanochemistry: a chemical strategy for the synthesis of nanostructures. *Science* **1991,** *254* (5036), 1312-1319.
30. Boverhof, D. R.; Bramante, C. M.; Butala, J. H.; Clancy, S. F.; Lafranconi, M.; West, J.; Gordon, S. C., Comparative assessment of nanomaterial definitions and safety evaluation considerations. *Regul. Toxicol. Pharm.* **2015,** *73* (1), 137-150.

31. United Nations. Questions about nanotechnology. 2012; https://www.epa.gov/chemical-research/research-nanomaterials (accessed 11–9–2018).
.
32. Considering Whether an FDA-Regulated Product Involves the Application of Nanotechnology. Federal Drug Administration: USA, 2011; https://www.fda.gov/RegulatoryInformation/Guidances/ucm257698.htm (accessed Jan 25, 2016).
33. ISO/TS 80004-1:2010, Nanotechnology – Vocabulary – Part 1: Core Terms. International Organization for Standardization: Geneva, Switzerland, 2010; https://www.iso.org/standard/51240.html (accessed July 17, 2017).
34. Potocnik, J. Off. J. Eur. Communities: Legis. 2011, L275, 38–40. doi:10.3000/19770677.L_2011.275.eng.
35. Archer, S.; Weinstein, J. A., Charge-separated excited states in platinum (II) chromophores: Photophysics, formation, stabilization and utilization in solar energy conversion. *Coord. Chem. Rev.* **2012,** *256* (21-22), 2530-2561.
36. Kuciauskas, D.; Liddell, P. A.; Lin, S.; Johnson, T. E.; Weghorn, S. J.; Lindsey, J. S.; Moore, A. L.; Moore, T. A.; Gust, D., An artificial photosynthetic antenna-reaction center complex. *J. Am. Chem. Soc.* **1999,** *121* (37), 8604-8614.
37. Stadler, A.-M.; Kyritsakas, N.; Lehn, J.-M., Reversible folding/unfolding of linear molecular strands into helical channel-like complexes upon proton-modulated binding and release of metal ions. *Chem. Commun.* **2004,** (18), 2024-2025.
38. https://phys.org/news/2019-07-quantum-phenomenon-fundamental-limits-graphene.html.
39. Allen, M. J.; Tung, V. C.; Kaner, R. B., Honeycomb carbon: a review of graphene. *Chem. Rev.* **2009,** *110* (1), 132-145.
40. Abbott's, I. E., Graphene: exploring carbon flatland. *Phys. Today* **2007,** *60* (8), 35.
41. Lee, C.; Wei, X.; Kysar, J. W.; Hone, J., Measurement of the elastic properties and intrinsic strength of monolayer graphene. *Science* **2008,** *321* (5887), 385-388.
42. Morozov, S.; Novoselov, K.; Katsnelson, M.; Schedin, F.; Elias, D.; Jaszczak, J. A.; Geim, A., Giant intrinsic carrier mobilities in graphene and its bilayer. *Phys. Rev. Lett.* **2008,** *100* (1), 016602.
43. Bostwick, A.; Ohta, T.; Seyller, T.; Horn, K.; Rotenberg, E., Quasiparticle dynamics in graphene. *Nature physics* **2007,** *3* (1), 36.
44. Geim, A. K., Graphene: status and prospects. *Science* **2009,** *324* (5934), 1530-1534.
45. Balandin, A. A.; Ghosh, S.; Bao, W.; Calizo, I.; Teweldebrhan, D.; Miao, F.; Lau, C. N., Superior thermal conductivity of single-layer graphene. *Nano Lett.* **2008,** *8* (3), 902-907.
46. Bunch, J. S.; Verbridge, S. S.; Alden, J. S.; Van Der Zande, A. M.; Parpia, J. M.; Craighead, H. G.; McEuen, P. L., Impermeable atomic membranes from graphene sheets. *Nano Lett.* **2008,** *8* (8), 2458-2462.
47. https://www.sigmaaldrich.com/technical-documents/protocols/materials-science/preparing-self-assembled.html.
48. Spinke, J.; Liley, M.; Guder, H.; Angermaier, L.; Knoll, W., Molecular recognition at self-assembled monolayers: the construction of multicomponent multilayers. *Langmuir* **1993,** *9* (7), 1821-1825.
49. Wink, T.; Van Zuilen, S.; Bult, A.; Van Bennekom, W., Self-assembled monolayers for biosensors. *Analyst* **1997,** *122* (4), 43R-50R.
50. Schmaltz, T.; Sforazzini, G.; Reichert, T.; Frauenrath, H., Self-Assembled Monolayers as Patterning Tool for Organic Electronic Devices. *Adv. Mater.* **2017,** *29* (18), 1605286.

51. Schmittel, M.; Lal, M.; Graf, K.; Jeschke, G.; Suske, I.; Salbeck, J., N, N′-Dimethyl-2, 3-dialkylpyrazinium salts as redox-switchable surfactants? Redox, spectral, EPR and surfactant properties. *Chem. Commun.* **2005,** (45), 5650-5652.
52. Ebbesen, T.; Lezec, H.; Hiura, H.; Bennett, J.; Ghaemi, H.; Thio, T., Electrical conductivity of individual carbon nanotubes. *Nature* **1996,** *382* (6586), 54.
53. Che, G.; Lakshmi, B. B.; Martin, C. R.; Fisher, E. R., Metal-nanocluster-filled carbon nanotubes: catalytic properties and possible applications in electrochemical energy storage and production. *Langmuir* **1999,** *15* (3), 750-758.
54. Rajaura, R. S.; Srivastava, S.; Sharma, P. K.; Mathur, S.; Shrivastava, R.; Sharma, S.; Vijay, Y., Structural and surface modification of carbon nanotubes for enhanced hydrogen storage density. *Nano-Structures & Nano-Objects* **2018,** *14*, 57-65.
55. Deb, J.; Paul, D.; Sarkar, U.; Ayers, P. W., Characterizing the sensitivity of bonds to the curvature of carbon nanotubes. *J. Mol. Model.* **2018,** *24* (9), 249.
56. Karousis, N.; Tagmatarchis, N.; Tasis, D., Current progress on the chemical modification of carbon nanotubes. *Chem. Rev.* **2010,** *110* (9), 5366-5397.
57. Hou, P.-X.; Liu, C.; Cheng, H.-M., Purification of carbon nanotubes. *carbon* **2008,** *46* (15), 2003-2025.
58. Liew, K.; Lei, Z.; Zhang, L., Mechanical analysis of functionally graded carbon nanotube reinforced composites: a review. *Compos. Struct.* **2015,** *120*, 90-97.
59. Choi, J.; Park, B. C.; Ahn, S. J.; Kim, D.-H.; Lyou, J.; Dixson, R. G.; Orji, N. G.; Fu, J.; Vorburger, T. V., Evaluation of carbon nanotube probes in critical dimension atomic force microscopes. *Journal of Micro/Nanolithography, MEMS, and MOEMS* **2016,** *15* (3), 034005.
60. Lu, J. P., Elastic properties of carbon nanotubes and nanoropes. *Phys. Rev. Lett.* **1997,** *79* (7), 1297.
61. Wen, L.; Li, F.; Cheng, H. M., Carbon nanotubes and graphene for flexible electrochemical energy storage: from materials to devices. *Adv. Mater.* **2016,** *28* (22), 4306-4337.
62. Kroto, H. W.; Heath, J. R.; O'Brien, S. C.; Curl, R. F.; Smalley, R. E., C60: Buckminsterfullerene. *Nature* **1985,** *318* (6042), 162.
63. Kroto, H. W.; Fischer, J. E.; Cox, D., *The fullerenes*. Newnes: 2012.
64. Guozhong, C., *Nanostructures and nanomaterials: synthesis, properties and applications*. World scientific: 2004.
65. Ala'a, K., Isolation, separation and characterisation of the fullerenes C 60 and C 70: the third form of carbon. *J. Chem. Soc., Chem. Commun.* **1990,** (20), 1423-1425.
66. Krätschmer, W., LD lamb, K. Fostiropoulos, DR Hufman. *Nature* **1990,** *347*, 354.
67. Guldi, D.; Martin, N., 1.07 Functionalized Fullerenes: Synthesis and Functions. *Comprehensive Nanoscience and Nanotechnology* **2019**, 187.
68. Ramirez, A. P., Superconductivity in alkali-doped C60. *Physica C: Superconductivity and its Applications* **2015,** *514*, 166-172.
69. Jin, P.; Li, Y.; Magagula, S.; Chen, Z., Exohedral functionalization of endohedral metallofullerenes: Interplay between inside and outside. *Coord. Chem. Rev.* **2019,** *388*, 406-439.
70. Rašović, I., Water-soluble fullerenes for medical applications. *Mater. Sci. Technol.* **2017,** *33* (7), 777-794.
71. Li, H.; Kang, Z.; Liu, Y.; Lee, S.-T., Carbon nanodots: synthesis, properties and applications. *J. Mater. Chem.* **2012,** *22* (46), 24230-24253.
72. Xu, X.; Ray, R.; Gu, Y.; Ploehn, H. J.; Gearheart, L.; Raker, K.; Scrivens, W. A., Electrophoretic analysis and purification of fluorescent single-walled carbon nanotube fragments. *J. Am. Chem. Soc.* **2004,** *126* (40), 12736-12737.
73. Sciortino, A.; Cannizzo, A.; Messina, F., Carbon Nanodots: A Review—From the Current Understanding of the Fundamental Photophysics to the Full Control of the Optical Response. *C* **2018,** *4* (4), 67.

74. (a) Wang, X.; Cao, L.; Lu, F.; Meziani, M.; Li, H., G, Qi, B. Zhou, BA Harruff, F. Kermarrec and YP. Sun. *Chem. Comm* **2009,** *3774*; (b) Shen, J.; Zhu, Y.; Yang, X.; Li, C., Graphene quantum dots: emergent nanolights for bioimaging, sensors, catalysis and photovoltaic devices. *Chem. Commun.* **2012,** *48* (31), 3686-3699.
75. Wang, D.; Wang, Z.; Zhan, Q.; Pu, Y.; Wang, J.-X.; Foster, N. R.; Dai, L., Facile and scalable preparation of fluorescent carbon dots for multifunctional applications. *Engineering* **2017,** *3* (3), 402-408.
76. Peng, Z.; Han, X.; Li, S.; Al-Youbi, A. O.; Bashammakh, A. S.; El-Shahawi, M. S.; Leblanc, R. M., Carbon dots: biomacromolecule interaction, bioimaging and nanomedicine. *Coord. Chem. Rev.* **2017,** *343*, 256-277.
77. Cao, X.; Wang, J.; Deng, W.; Chen, J.; Wang, Y.; Zhou, J.; Du, P.; Xu, W.; Wang, Q.; Wang, Q., Photoluminescent cationic carbon dots as efficient non-viral delivery of plasmid SOX9 and chondrogenesis of fibroblasts. *Scientific reports* **2018,** *8* (1), 7057.
78. Patkar, N.; Sharan, M.; Twain, M., Did Nanotechnology Flourish During the Roman Empire and Medieval Periods? *History of Nanotechnology: From Pre-Historic to Modern Times* **2019**, 113-140.
79. Schaming, D.; Remita, H., Nanotechnology: from the ancient time to nowadays. *Foundations of Chemistry* **2015,** *17* (3), 187-205.
80. Das, M.; Shim, K. H.; An, S. S. A.; Yi, D. K., Review on gold nanoparticles and their applications. *Toxicology and Environmental Health Sciences* **2011,** *3* (4), 193-205.
81. Turkevich, J.; Stevenson, P.; Hiller, J., Synthesis of gold nanoparticles Turkevich method. *Discuss. Faraday Soc* **1951,** *11*, 55-75.
82. Brust, M.; Walker, M.; Bethell, D.; Schiffrin, D. J.; Whyman, R., Synthesis of thiol-derivatised gold nanoparticles in a two-phase liquid–liquid system. *J. Chem. Soc., Chem. Commun.* **1994,** (7), 801-802.
83. Tianimoghadam, S.; Salabat, A., A microemulsion method for preparation of thiol-functionalized gold nanoparticles. *Particuology* **2018,** *37*, 33-36.
84. Li, X.; Iocozzia, J.; Chen, Y.; Zhao, S.; Cui, X.; Wang, W.; Yu, H.; Lin, S.; Lin, Z., From precision synthesis of block copolymers to properties and applications of nanoparticles. *Angew. Chem. Int. Ed.* **2018,** *57* (8), 2046-2070.
85. Monti, G. A.; Fernández, G. A.; Correa, N. M.; Falcone, R. D.; Moyano, F.; Silbestri, G. F., Gold nanoparticles stabilized with sulphonated imidazolium salts in water and reverse micelles. *Royal Society open science* **2017,** *4* (7), 170481.
86. Longo, A.; Banerjee, D.; Hermida-Merino, D.; Portale, G.; Calandra, P.; Turco Liveri, V., Induced Chirality in Confined Space on Halogen Gold Complexes. *The Journal of Physical Chemistry C* **2015,** *119* (32), 18798-18807.
87. Daniel, M.-C.; Astruc, D., Gold nanoparticles: assembly, supramolecular chemistry, quantum-size-related properties, and applications toward biology, catalysis, and nanotechnology. *Chem. Rev.* **2004,** *104* (1), 293-346.
88. Liu, M.; Li, Q.; Liang, L.; Li, J.; Wang, K.; Li, J.; Lv, M.; Chen, N.; Song, H.; Lee, J., Real-time visualization of clustering and intracellular transport of gold nanoparticles by correlative imaging. *Nat. Commun.* **2017,** *8*, 15646.
89. Vicentini, F. C.; Garcia, L. L.; Figueiredo-Filho, L. C.; Janegitz, B. C.; Fatibello-Filho, O., A biosensor based on gold nanoparticles, dihexadecylphosphate, and tyrosinase for the determination of catechol in natural water. *Enzyme Microb. Technol.* **2016,** *84*, 17-23.
90. Daraee, H.; Eatemadi, A.; Abbasi, E.; Fekri Aval, S.; Kouhi, M.; Akbarzadeh, A., Application of gold nanoparticles in biomedical and drug delivery. *Artificial cells, nanomedicine, and biotechnology* **2016,** *44* (1), 410-422.

91. Blumenfeld, C. M.; Schulz, M. D.; Aboian, M. S.; Wilson, M. W.; Moore, T.; Hetts, S. W.; Grubbs, R. H., Drug capture materials based on genomic DNA-functionalized magnetic nanoparticles. *Nat. Commun.* **2018,** *9* (1), 2870.
92. Chauhan, D. S.; Reddy, B. P. K.; Mishra, S. K.; Prasad, R.; Dhanka, M.; Vats, M.; Ravichandran, G.; Poojari, D.; Mhatre, O.; De, A., A Comprehensive Evaluation of Degradable and Cost Effective Plasmonic Nanoshells for Localized Photothermolysis of Cancer Cells. *Langmuir* **2019**.
93. Kong, F.-Y.; Zhang, J.-W.; Li, R.-F.; Wang, Z.-X.; Wang, W.-J.; Wang, W., Unique roles of gold nanoparticles in drug delivery, targeting and imaging applications. *Molecules* **2017,** *22* (9), 1445.
94. Yang, Y.; Mu, J.; Xing, B., Photoactivated drug delivery and bioimaging. *Wiley Interdisciplinary Reviews: Nanomedicine and Nanobiotechnology* **2017,** *9* (2), e1408.
95. Elahi, N.; Kamali, M.; Baghersad, M. H., Recent biomedical applications of gold nanoparticles: A review. *Talanta* **2018,** *184*, 537-556.
96. Velasco-Aguirre, C.; Morales, F.; Gallardo-Toledo, E.; Guerrero, S.; Giralt, E.; Araya, E.; Kogan, M. J., Peptides and proteins used to enhance gold nanoparticle delivery to the brain: preclinical approaches. *International journal of nanomedicine* **2015,** *10*, 4919.
97. Bazak, R.; Houri, M.; El Achy, S.; Kamel, S.; Refaat, T., Cancer active targeting by nanoparticles: a comprehensive review of literature. *J. Cancer Res. Clin. Oncol.* **2015,** *141* (5), 769-784.
98. Rai, M.; Yadav, A.; Gade, A., Silver nanoparticles as a new generation of antimicrobials. *Biotechnol. Adv.* **2009,** *27* (1), 76-83.
99. Carbone, M.; Donia, D. T.; Sabbatella, G.; Antiochia, R., Silver nanoparticles in polymeric matrices for fresh food packaging. *Journal of King Saud University-Science* **2016,** *28* (4), 273-279.
100. Deshmukh, S.; Patil, S.; Mullani, S.; Delekar, S., Silver nanoparticles as an effective disinfectant: A review. *Materials Science and Engineering: C* **2018**.
101. De Matteis, V.; Cascione, M.; Toma, C.; Leporatti, S., Silver nanoparticles: Synthetic routes, in vitro toxicity and theranostic applications for cancer disease. *Nanomaterials* **2018,** *8* (5), 319.
102. Guzmán, M. G.; Dille, J.; Godet, S., Synthesis of silver nanoparticles by chemical reduction method and their antibacterial activity. *Int J Chem Biomol Eng* **2009,** *2* (3), 104-111.
103. Rodriguez-Sanchez, L.; Blanco, M.; Lopez-Quintela, M., Electrochemical synthesis of silver nanoparticles. *The Journal of Physical Chemistry B* **2000,** *104* (41), 9683-9688.
104. Ramnani, S.; Biswal, J.; Sabharwal, S., Synthesis of silver nanoparticles supported on silica aerogel using gamma radiolysis. *Radiat. Phys. Chem.* **2007,** *76* (8-9), 1290-1294.
105. Dhayagude, A. C.; Newase, S. K.; Joshi, S. S.; Kapadnis, B. P.; Kapoor, S., Preparation of silver nanoparticles in the presence of polyoxometalates. *Materials Science and Engineering: C* **2019,** *94*, 437-444.
106. AbuDalo, M. A.; Al-Mheidat, I. R.; Al-Shurafat, A. W.; Grinham, C.; Oyanedel-Craver, V., Synthesis of silver nanoparticles using a modified Tollens' method in conjunction with phytochemicals and assessment of their antimicrobial activity. *PeerJ* **2019,** *7*, e6413.
107. Petrović, P.; Kostić, D.; Klaus, A.; Vunduk, J.; Nikšić, M.; Veljović, Đ.; van Griensven, L., Characterisation and antimicrobial activity of silver nanoparticles derived from Vascellum pratense polysaccharide extract and sodium citrate. *Journal of Engineering & Processing Management* **2018,** *10* (1), 1-8.
108. Bogle, K.; Dhole, S.; Bhoraskar, V., Silver nanoparticles: synthesis and size control by electron irradiation. *Nanotechnology* **2006,** *17* (13), 3204.
109. Fayaz, A. M.; Balaji, K.; Girilal, M.; Yadav, R.; Kalaichelvan, P. T.; Venketesan, R., Biogenic synthesis of silver nanoparticles and their synergistic effect with antibiotics: a study against

gram-positive and gram-negative bacteria. *Nanomed. Nanotechnol. Biol. Med.* **2010,** *6* (1), 103-109.
110. Lara, H. H.; Ayala-Núñez, N. V.; Turrent, L. d. C. I.; Padilla, C. R., Bactericidal effect of silver nanoparticles against multidrug-resistant bacteria. *World J. Microbiol. Biotechnol.* **2010,** *26* (4), 615-621.
111. Kim, K.-J.; Sung, W. S.; Moon, S.-K.; Choi, J.-S.; Kim, J. G.; Lee, D. G., Antifungal effect of silver nanoparticles on dermatophytes. *J Microbiol Biotechnol* **2008,** *18* (8), 1482-1484.
112. Gajbhiye, S.; Sakharwade, S., Silver nanoparticles in cosmetics. *Journal of Cosmetics, Dermatological Sciences and Applications* **2016,** *6* (01), 48.
113. Roe, D.; Karandikar, B.; Bonn-Savage, N.; Gibbins, B.; Roullet, J.-B., Antimicrobial surface functionalization of plastic catheters by silver nanoparticles. *J. Antimicrob. Chemother.* **2008,** *61* (4), 869-876.
114. Dubas, S. T.; Kumlangdudsana, P.; Potiyaraj, P., Layer-by-layer deposition of antimicrobial silver nanoparticles on textile fibers. *Colloids Surf. Physicochem. Eng. Aspects* **2006,** *289* (1-3), 105-109.
115. (a) Bera, D.; Qian, L.; Tseng, T.-K.; Holloway, P. H., Quantum dots and their multimodal applications: a review. *Materials* **2010,** *3* (4), 2260-2345; (b) Burda, C.; Chen, X.; Narayanan, R.; El-Sayed, M. A., Chemistry and properties of nanocrystals of different shapes. *Chem. Rev.* **2005,** *105* (4), 1025-1102; (c) El-Sayed, M. A., Small is different: shape-, size-, and composition-dependent properties of some colloidal semiconductor nanocrystals. *Acc. Chem. Res.* **2004,** *37* (5), 326-333.
116. Fu, H.-B.; Yao, J.-N., Size effects on the optical properties of organic nanoparticles. *J. Am. Chem. Soc.* **2001,** *123* (7), 1434-1439.
117. Patra, A.; Chandaluri, C. G.; Radhakrishnan, T., Optical materials based on molecular nanoparticles. *Nanoscale* **2012,** *4* (2), 343-359.
118. Tachibana, T.; Nakamura, A., A methode for preparing an aqueous colloidal dispersion of organic materials by using water-soluble polymers: Dispersion ofB-carotene by polyvinylpyrrolidone. *Kolloid-Zeitschrift und Zeitschrift für Polymere* **1965,** *203* (2), 130-133.
119. Kasai, H.; Nalwa, H. S.; Oikawa, H.; Okada, S.; Matsuda, H.; Minami, N.; Kakuta, A.; Ono, K.; Mukoh, A.; Nakanishi, H., A novel preparation method of organic microcrystals. *Japanese Journal of Applied Physics* **1992,** *31* (8A), L1132.
120. Schwarz, K. N.; Farley, S. B.; Smith, T. A.; Ghiggino, K. P., Charge generation and morphology in P3HT: PCBM nanoparticles prepared by mini-emulsion and reprecipitation methods. *Nanoscale* **2015,** *7* (47), 19899-19904.
121. Utekhina, A. Y.; Sergeev, G. B., Organic nanoparticles. *Russian Chemical Reviews* **2011,** *80* (3), 219.
122. An, B. K.; Kwon, S. K.; Park, S. Y., Photopatterned arrays of fluorescent organic nanoparticles. *Angew. Chem. Int. Ed.* **2007,** *46* (12), 1978-1982.
123. Wais, U.; Jackson, A. W.; He, T.; Zhang, H., Nanoformulation and encapsulation approaches for poorly water-soluble drug nanoparticles. *Nanoscale* **2016,** *8* (4), 1746-1769.
124. Berger, M.; Yang, Q.; Maier, A., X-ray Imaging. In *Medical Imaging Systems*, Springer: 2018; pp 119-145.
125. Vadivambal, R.; Jayas, D. S., *Bio-imaging: principles, techniques, and applications*. CRC Press: 2015.
126. Santra, S.; Dutta, D., Nanoparticles for optical imaging of Cancer. *Nanotechnologies for the Life Sciences: Online* **2007**.
127. Culley, S.; Albrecht, D.; Jacobs, C.; Pereira, P. M.; Leterrier, C.; Mercer, J.; Henriques, R., Quantitative mapping and minimization of super-resolution optical imaging artifacts. *Nat. Methods* **2018,** *15* (4), 263.

128. Aiyer, S.; Prasad, R.; Kumar, M.; Nirvikar, K.; Jain, B.; Kushwaha, O. S., Fluorescent carbon nanodots for targeted in vitro cancer cell imaging. *Applied Materials Today* **2016,** *4*, 71-77.
129. Bruns, O. T.; Bischof, T. S.; Harris, D. K.; Franke, D.; Shi, Y.; Riedemann, L.; Bartelt, A.; Jaworski, F. B.; Carr, J. A.; Rowlands, C. J., Next-generation in vivo optical imaging with short-wave infrared quantum dots. *Nature biomedical engineering* **2017,** *1* (4), 0056.
130. Wells, W. A.; Thrall, M.; Sorokina, A.; Fine, J.; Krishnamurthy, S.; Haroon, A.; Rao, B.; Shevchuk, M. M.; Wolfsen, H. C.; Tearney, G. J., In Vivo and Ex Vivo Microscopy: Moving Toward the Integration of Optical Imaging Technologies Into Pathology Practice. *Arch. Pathol. Lab. Med.* **2018,** *143* (3), 288-298.
131. Jovin, T. M., Introduction to Biophotonics By Paras N. Prasad (SUNY-Buffalo). J. Wiley & Sons, Inc.: Hoboken, NJ. 2003. xviii+ 594 pp. $99.95. ISBN: 0-471-28770-9. ACS Publications: 2004.
132. Wolfbeis, O. S., An overview of nanoparticles commonly used in fluorescent bioimaging. *Chem. Soc. Rev.* **2015,** *44* (14), 4743-4768.
133. Reguera, J.; de Aberasturi, D. J.; Henriksen-Lacey, M.; Langer, J.; Espinosa, A.; Szczupak, B.; Wilhelm, C.; Liz-Marzán, L. M., Janus plasmonic–magnetic gold–iron oxide nanoparticles as contrast agents for multimodal imaging. *Nanoscale* **2017,** *9* (27), 9467-9480.
134. Santra, S.; Dutta, D.; Walter, G. A.; Moudgil, B. M., Fluorescent nanoparticle probes for cancer imaging. *Technology in cancer research & treatment* **2005,** *4* (6), 593-602.
135. Sharma, P.; Brown, S.; Walter, G.; Santra, S.; Moudgil, B., Nanoparticles for bioimaging. *Adv. Colloid Interface Sci.* **2006,** *123*, 471-485.
136. Chen, M.; Yin, M., Design and development of fluorescent nanostructures for bioimaging. *Prog. Polym. Sci.* **2014,** *39* (2), 365-395.
137. Banerjee, A.; Pons, T.; Lequeux, N.; Dubertret, B., Quantum dots–DNA bioconjugates: synthesis to applications. *Interface Focus* **2016,** *6* (6), 20160064.
138. Yin, C.; Zhen, X.; Fan, Q.; Huang, W.; Pu, K., Degradable semiconducting oligomer amphiphile for ratiometric photoacoustic imaging of hypochlorite. *ACS nano* **2017,** *11* (4), 4174-4182.
139. Jiang, Y.; Pu, K., Advanced photoacoustic imaging applications of near-infrared absorbing organic nanoparticles. *Small* **2017,** *13* (30), 1700710.
140. An, H.-W.; Qiao, S.-L.; Hou, C.-Y.; Lin, Y.-X.; Li, L.-L.; Xie, H.-Y.; Wang, Y.; Wang, L.; Wang, H., Self-assembled NIR nanovesicles for long-term photoacoustic imaging in vivo. *Chem. Commun.* **2015,** *51* (70), 13488-13491.
141. Gong, H.; Dong, Z.; Liu, Y.; Yin, S.; Cheng, L.; Xi, W.; Xiang, J.; Liu, K.; Li, Y.; Liu, Z., Engineering of multifunctional nano-micelles for combined photothermal and photodynamic therapy under the guidance of multimodal imaging. *Adv. Funct. Mater.* **2014,** *24* (41), 6492-6502.
142. Mathew, S.; Yella, A.; Gao, P.; Humphry-Baker, R.; Curchod, B. F.; Ashari-Astani, N.; Tavernelli, I.; Rothlisberger, U.; Nazeeruddin, M. K.; Grätzel, M., Dye-sensitized solar cells with 13% efficiency achieved through the molecular engineering of porphyrin sensitizers. *Nat. Chem.* **2014,** *6* (3), 242.
143. Huynh, E.; Leung, B. Y.; Helfield, B. L.; Shakiba, M.; Gandier, J.-A.; Jin, C. S.; Master, E. R.; Wilson, B. C.; Goertz, D. E.; Zheng, G., In situ conversion of porphyrin microbubbles to nanoparticles for multimodality imaging. *Nature nanotechnology* **2015,** *10* (4), 325.
144. (a) Fan, Q.; Cheng, K.; Yang, Z.; Zhang, R.; Yang, M.; Hu, X.; Ma, X.; Bu, L.; Lu, X.; Xiong, X., Perylene-diimide-based nanoparticles as highly efficient photoacoustic agents for deep brain tumor imaging in living mice. *Adv. Mater.* **2015,** *27* (5), 843-847; (b) Huynh, E.; Lovell, J. F.; Helfield, B. L.; Jeon, M.; Kim, C.; Goertz, D. E.; Wilson, B. C.; Zheng, G., Porphyrin shell microbubbles with intrinsic ultrasound and photoacoustic properties. *J. Am. Chem. Soc.* **2012,** *134* (40), 16464-16467.

145. Hulanicki, A.; Glab, S.; Ingman, F., Chemical sensors: definitions and classification. *Pure Appl. Chem.* **1991,** *63* (9), 1247-1250.
146. Spichiger-Keller, U. E., *Chemical sensors and biosensors for medical and biological applications*. John Wiley & Sons: 2008.
147. Prodi, L.; Bolletta, F.; Montalti, M.; Zaccheroni, N., Luminescent chemosensors for transition metal ions. *Coord. Chem. Rev.* **2000,** *205* (1), 59-83.
148. Bonacchi, S.; Genovese, D.; Juris, R.; Montalti, M.; Prodi, L.; Rampazzo, E.; Sgarzi, M.; Zaccheroni, N., Luminescent chemosensors based on silica nanoparticles. In *Luminescence Applied in Sensor Science*, Springer: 2010; pp 93-138.
149. Prodi, L., Luminescent chemosensors: from molecules to nanoparticles. *New J. Chem.* **2005,** *29* (1), 20-31.
150. Zhao, Q.; Li, F.; Huang, C., Phosphorescent chemosensors based on heavy-metal complexes. *Chem. Soc. Rev.* **2010,** *39* (8), 3007-3030.
151. Ji, S.; Guo, H.; Yuan, X.; Li, X.; Ding, H.; Gao, P.; Zhao, C.; Wu, W.; Wu, W.; Zhao, J., A highly selective OFF-ON red-emitting phosphorescent thiol probe with large stokes shift and long luminescent lifetime. *Org. Lett.* **2010,** *12* (12), 2876-2879.
152. Somers, R. C.; Bawendi, M. G.; Nocera, D. G., CdSe nanocrystal based chem-/bio-sensors. *Chem. Soc. Rev.* **2007,** *36* (4), 579-591.
153. Baù, L.; Tecilla, P.; Mancin, F., Sensing with fluorescent nanoparticles. *Nanoscale* **2011,** *3* (1), 121-133.
154. Dabrowski, M.; Lach, P.; Cieplak, M.; Kutner, W., Nanostructured molecularly imprinted polymers for protein chemosensing. *Biosens. Bioelectron.* **2018,** *102*, 17-26.
155. An, Z.; Chen, S.; Tong, X.; He, H.; Han, J.; Ma, M.; Shi, Y.; Wang, X., Widely Applicable AIE Chemosensor for On-Site Fast Detection of Drugs Based on the POSS-Core Dendrimer with the Controlled Self-Assembly Mechanism. *Langmuir* **2019,** *35* (7), 2649-2654.
156. Jin, T.; Fujii, F.; Sakata, H.; Tamura, M.; Kinjo, M., Amphiphilic p-sulfonatocalix [4] arene-coated CdSe/ZnS quantum dots for the optical detection of the neurotransmitter acetylcholine. *Chem. Commun.* **2005,** (34), 4300-4302.
157. Han, C.; Li, H., Chiral recognition of amino acids based on cyclodextrin-capped quantum dots. *Small* **2008,** *4* (9), 1344-1350.
158. Ng, S. M.; Koneswaran, M.; Narayanaswamy, R., A review on fluorescent inorganic nanoparticles for optical sensing applications. *RSC Advances* **2016,** *6* (26), 21624-21661.

Chapter 2: Aim of the work

Nanotechnology is a new emerging field that involves many disciplines, including chemistry, materials science, medicine, electronics, environmental protection etc... Nanotechnology aims at the design, synthesis, characterization and application of materials and devices on the nanoscale. Nanoparticles are defined as materials with the three dimensions in the space less than 100 nm. They possess chemical, biological, mechanical, electronic and magnetic properties hugely different from the corresponding macroscopic materials. Their peculiarities depend on the reduced size, shape, composition and interface, all aspects that can be controlled during the synthesis. Moreover, nanoparticles can act as platforms for assemble well-defined multifunctional structures able to perform varied tasks such as drug delivery, sensors and contrast agent for bioimaging. Nanoparticles can be made by inorganic materials, as in the case of transition metals or silica, and by soft materials as molecular dye or organic polymers.

In the currently work a wide range of nanoparticles have been designed, synthesized and characterized for various purposes. In chapter 4 we propose simple and cheap strategy to develop multi-stimuli sensitive perylene diimide (PDI) molecules to create new smart materials by self-assembly. PBI has been chosen as a platform because it is a well-known fluorophore, stable and with a high emission quantum yield that decreases considerably when the fluorophore aggregates. Best results have been obtained for N,N'-bis[2-(1-piperazino)ethyl]-3,4,9,10-perylenetetracarboxylic diimide (PIPER3). PIPER3 was prepared by microwave assisted reaction of PDA with aminoethylpiperazine (Fig.2.1). Presence of amine groups allow to control aggregation by pH thanks to protonable groups and made PIPER3 water soluble.

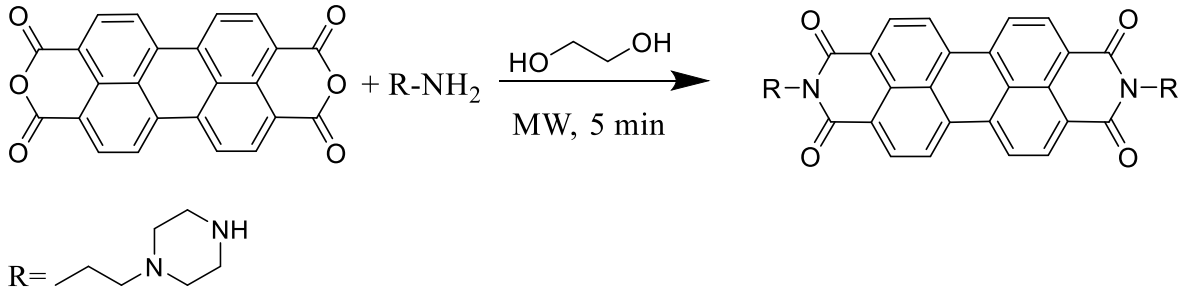

Fig.2.1 Schematic synthesis of PIPER3

PIPER3 emission quantum yield trend as a function of concentration increases and different pH is reported in Fig.2.2. As concentration increases, quantum yield decreases drastically. Indeed, in water π–π stacking interactions between perylene core promote dye aggregation in small nanoparticles, quenching fluorescence. Effect of pH was studied keeping constant PIPER3 concentration (Fig.2.2).

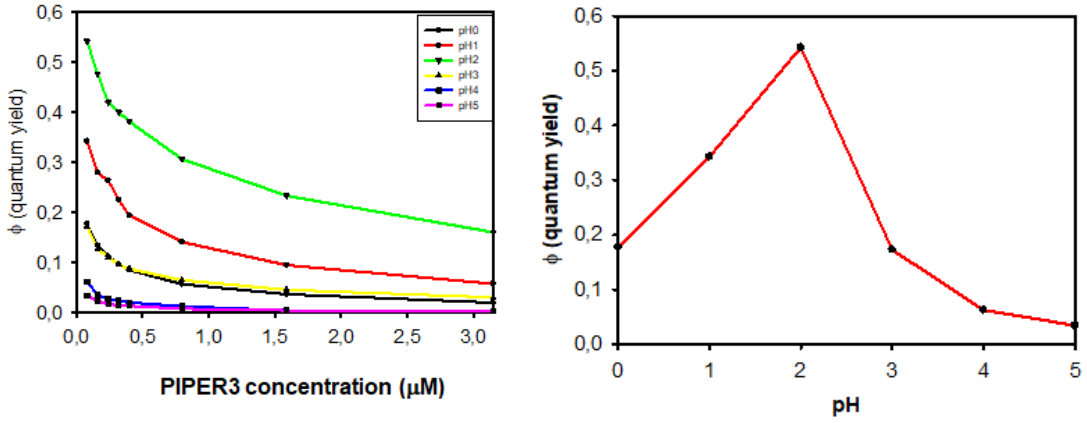

Fig.2.2 On the left: PIPER3 fluorescence quantum yield as concentration increases; on the right: PIPER3 fluorescence quantum yield at different pH

From pH 5 to 2 quantum yield increases as the pH decreases, revealing increase of the fraction of free molecule in solution, i.e. system disaggregates because of amino groups protonation causes repulsion between molecular units. On the other hand, going from pH 2 to 0 there is a sharp quantum yield fall. This reveals that a new stimulus encouraged dye aggregation. It is likely that high ion chloride concentration in low pH solutions (derived by HCl) begin to intervene in PIPER3 aggregation. To demonstrate this hypothesis, salts with different anions were added to a controlled pH PIPER3 solution. Emission quantum yield trend as ionic strength increases is reported (Fig.2.3).

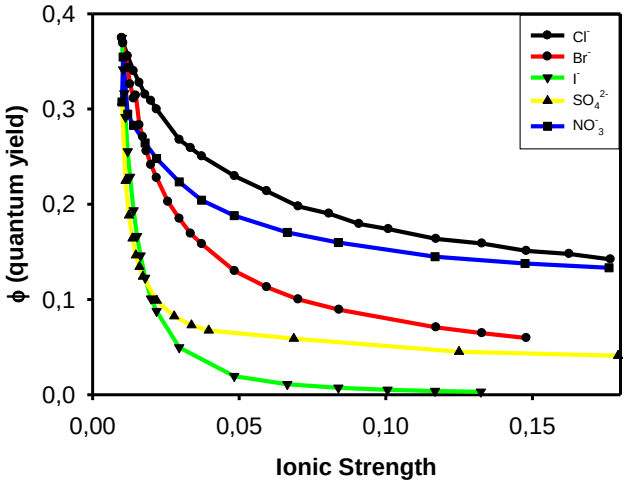

Fig.2.3 PIPER3 fluorescence quantum yield as anion concentration increases

Quantum yield decreases when the concentration of anion is increased suggesting that anions themselves participate in aggregation by shielding the repulsion of the protonated amine groups. In conclusion, new nanoparticles which disaggregate because of the effect of pH has been created. The free molecule fraction can be monitored by fluorescence detection.

Therefore, system respond to anions that play an important role in the aggregation state. This system is potentially suitable for pH and anion sensor**.**

Fluorescence is a powerful tool for mapping biological events in real-time with high special resolution. To achieve high sensitivity ultra-bright probes are needed as a huge number of fluorophores assembled in a single nanoparticle. Unfortunately, as just discussed for PBI, assembly results in fluorescence quenching because of short-range intermolecular interaction. In chapter 5 we report synthesis of designed molecule that self-assemble in nanoparticles in biocompatible environment without any dramatic decrease of fluorescence brightness (Fig.2.4). 4-Chloro-7-nitrobenzo-2-oxa-1,3-diazole (Cl-NBD) was the starting point to synthetize a stable and fluorescent trisphosphazene (NBD-PhM).

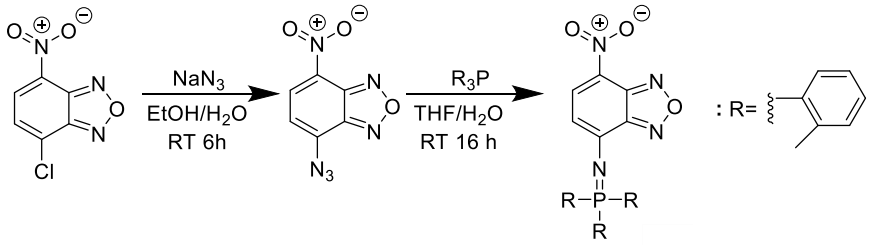

Fig.2.4 Reaction scheme of NBD-PhM

Nanoparticles (NBD-PhM_NPs) were prepared via nanoprecipitation in the presence of Pluronic F127 as a stabilizer in water. Nanoparticles presence was demonstrated by dynamic light scattering (DLS) and transmission electron microscopy (TEM) (Fig.2.5).

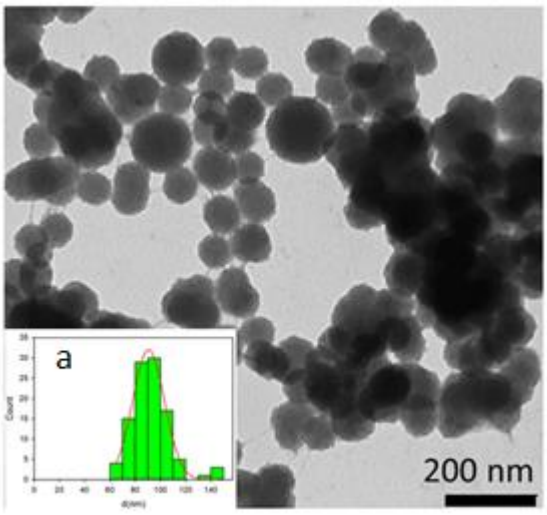

Fig.2.5 TEM images of NBD-PhM_NPs; a) Size distribution[1]

NBD-PhM and nanoparticles were characterized via UV-Vis absorption spectroscopy and steady-state and time resolved fluorescence spectroscopy. Result are in reported Table2.1.

Table2.1 Photophysical properties of NBD-PhM and nanoparticles

Compound	NBD-PhM in CH_2Cl_2	NP in H_2O
$\lambda_{max,abs}$	488 nm	480 nm
ε_{max}	32.600	29.300
$\lambda_{max,flu}$	526 nm	536 nm
QY	0.65	0.31
<n>	-	$1.1 \cdot 10^6$
B	$2.1 \cdot 10^5$	$1.0 \cdot 10^{10}$

Nanoparticles brightness results about six order of magnitude higher then molecular precursor one. This demonstrate that nanoparticles are suitable for bio-imaging, they were incubated with living HeLa cells and their ability to label the cells was demonstrated via confocal scanning fluorescence microscopy (Fig.2.6). Finally, toxicity assays demonstrated the high biocompatibility of the NPs (Fig.2.6).

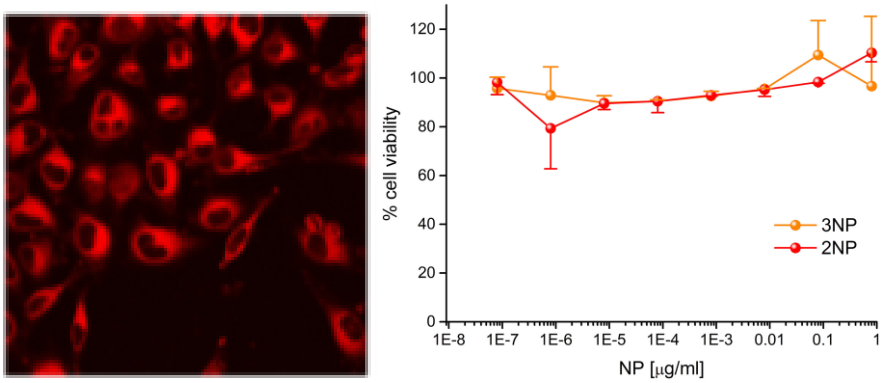

Fig.2.6 On the left: Fluorescence signal of NBD-PhM nanoparticles in cells. On the right: Cytotoxicity of NBD-PhM nanoparticles

In conclusion we believe that these highly bright, nanoparticles represent a promising platform for designing new versatile multifunctional nanoprobes.

In chapter 6 a similar work has been repeated with commercial fluorophores. The most interesting results have been obtained for diphenylanthracene (DPA) and N,N′-Bis(2,5-di-tert-butylphenyl)-3,4,9,10-perylenedicarboximide (P) showed in Fig.2.7.

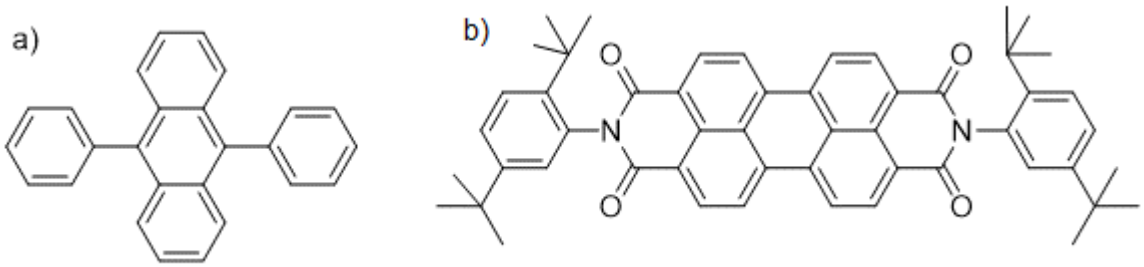

Fig.2.7 10-Diphenylanthracene (DPA) a); N,N′-Bis(2,5-di-tert-butylphenyl)-3,4,9,10-perylenedicarboximide (P) b).

In the first section of chapter 6, nanoparticles containing only one type of fluorophore have been studied. The photophysical properties of nanoparticles have been compared with those of the fluorophore in THF. The purpose of this first section of the work was to characterize a set of nanoparticles with high brightness that can cover the entire spectral zone from UV to NIR. As mentioned, the most interesting results have been obtained for diphenylanthracene (DPA) and N,N′-Bis(2,5-di- tert-butylphenyl)-3,4,9,10-perylenedicarboximide(P). In Fig.2.8 are reported absorption and emission spectra of DPA and P and respective nanoparticles (DPA-NP and P-NP).

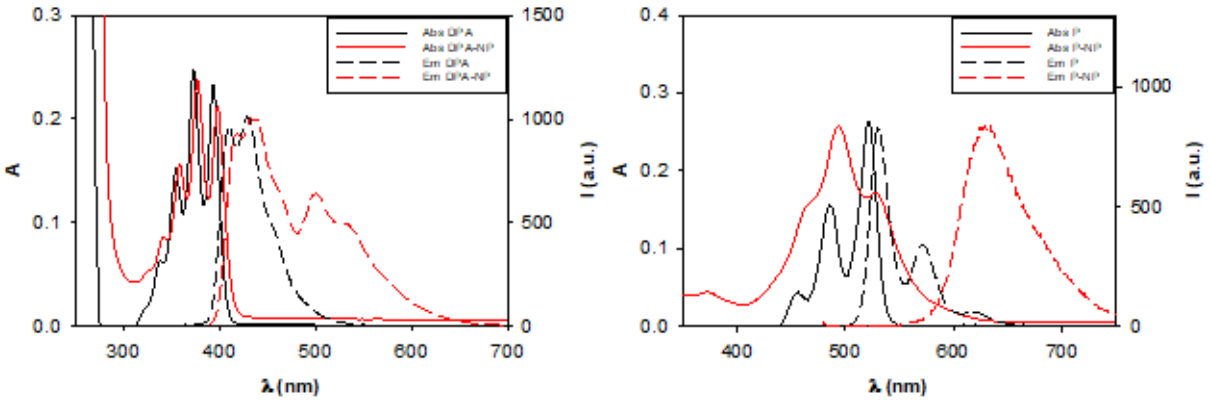

Fig.2.8 On the left: continuous lines are absorption specta of DPA (black line) and of DPA-NP (red line); dashed lines are emission spectra of DPA (black line) and of DPA-NP (red line); On the right: continuous lines are absorption spectra of P (black line) and of P-NP (red line); dashed lines are emission spectra of P (black line) and of P-NP (red line);

In the second section of the work nanoparticles containing two fluorophores a donor D and an acceptor A, with a ratio 10 to 1 have been characterized. The two kind of fluorophore when incorporated in the nanoparticles, can give rise to energy transfer processes. In this way it was possible to modulate both the excitation and emission wavelengths and increase the brightness of the NPs. The main purpose of the second part of the second section was indeed to study the interaction between D and A in the nanoparticles obtained by co-precipitation, to verify presence of energy transfer processes. In Fig.2.9 (left) absorption spectra of DPA, P and nanoparticles with DPA and P (DPA_P-NP) are reported together with the emission spectra of DPA and DPA_P-NP (right): it can clearly be observed that in presence of P the DPA emission is quenched. This demonstrate that there is interaction between fluorophores inside nanoparticles.

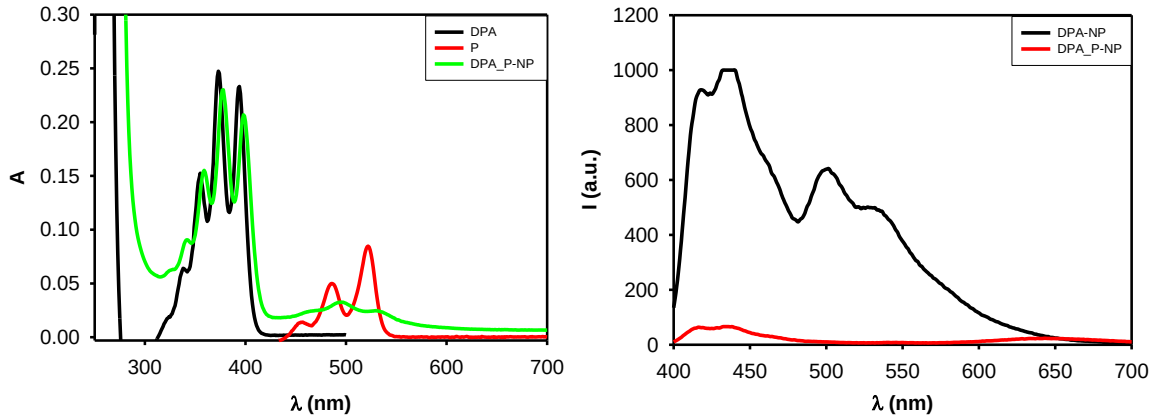

Fig.2.9 On the left: absorption spectra of DPA (black line), of P (red line) and of DPA_P-NP (green line). On the right: emission spectra of DPA-NP (black line) and of (DPA_P-NP (red line)

In the third section of chapter 6, it has been studied the result of mixing two aqueous solutions containing nanoparticles of different molecules. The goal was to verify the possible exchange of molecules between the different particles. For this reason mixture of nanoparticles were prepared having exactly the same total concetration of fluorophore used in the second part of the work, With the difference that in this case, the two fluorophores D and A were nanoprecipitated separately and then mixed (DPA_Pm_NP). The absorption spectra of DPA_P-NP and of DPA_Pm_NP are reported in Fig.2.10 (left) while the emission spectra of DPA_Pm_NP has been compared with emission spectra of DPA-NP in Fig.2.10 (right). It can be observed that in DPA_Pm_NP a strong emission of PDA is present, demonstrating that P is not quenching DPA, i.e. they are not incorporated in the same nanoparticles. We can conclude that, surprisingly, there is not molecular exchange between nanoparticles, even if they are not covalently bonded. This is very important since it demonstrated the high stability of these self-assembed nanoparticles in view of their application for bioimaging.

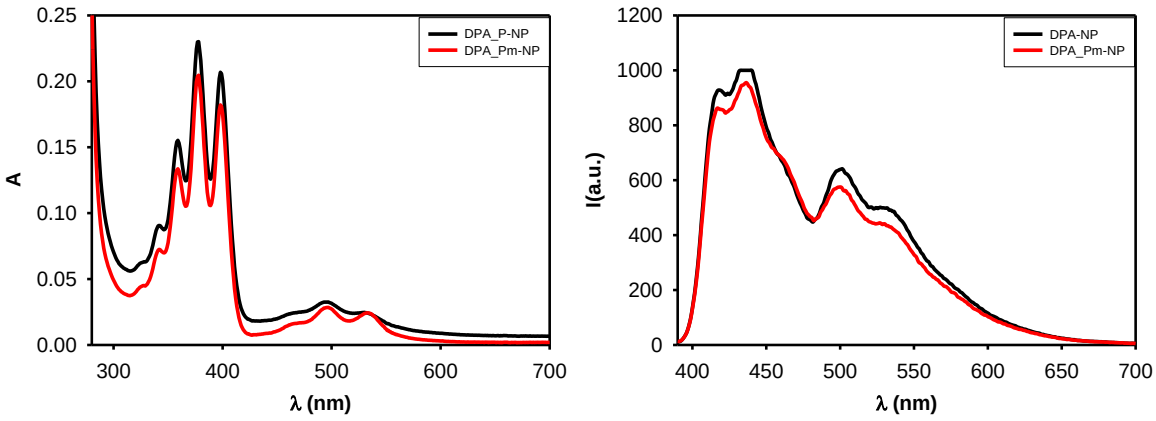

Fig.2.10 On the left: absorption spectra of DPA_P-NP (black line) and of DPA_Pm-NP (red line. On the right: emission spectra of DPA_NP (black line) and of DPA_Pm-NP (red line)

Detection of chemical and biological agents plays a fundamental role in environmental and biomedical sciences. Among the various investigation techniques, luminescence-based ones are between the most sensitive and selective. For investigation of biological systems luminescent sensors working in correspondence of the biologically transparent optical window in NIR region are particularly advantageous. Gold nanocluster offer a suitable platform for multi-functionalization with a wide range of organic or biological ligands suitable for the selective binding and detection of small molecules and biological targets. Gold nanocluster with diameter lower than 2 nm show detectable photoluminescence in NIR region. In chapter 7 small gold nanoclusters functionalised with seven different kinds of thiol have been studied in order to investigate their ability to recognize and signal the presence of some important active pharmaceutical ingredients (API). Best results have been obtained with thiols 1 and 3 showed in Fig.2.11. These gold nanoclusters have been respectively called AuNCs-1 and AuNCs-3.

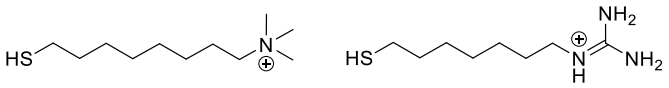

Fig.2.11 structure of thiols1(left) and 3(right) for coating gold nanoclusters

Gold nanocluster were characterized via UV-Vis absorption photoluminescence spectroscopy. They absorb in all UV-visible region and show emission in NIR region (Fig.2.12).

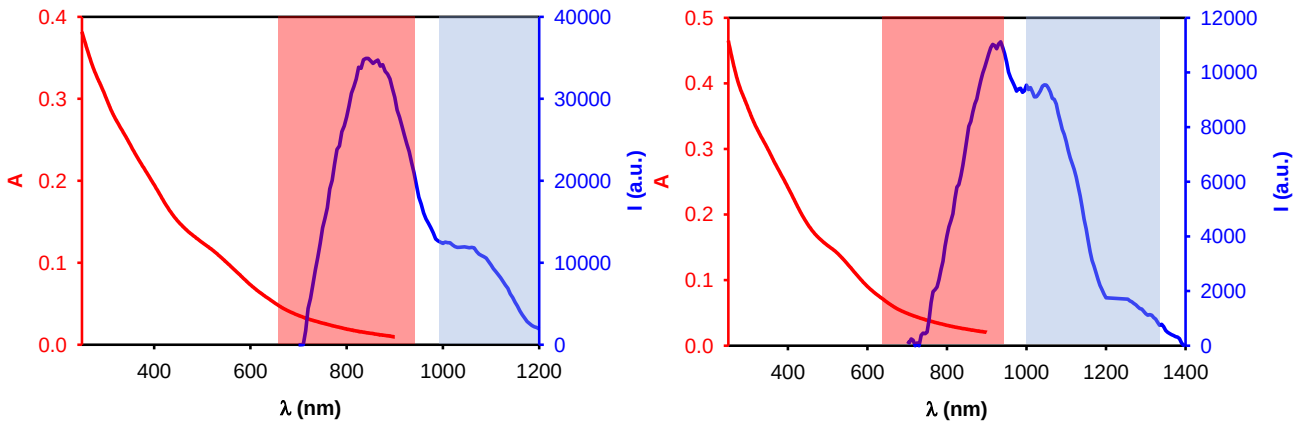

Fig.2.12 Photophysical properties of AuNCs-1 (left) and AuNCs-3 (right)

Gold nanocluster have been tested with API reported in Fig.2.13, that are some of most common commercial anti-inflammatory molecules.

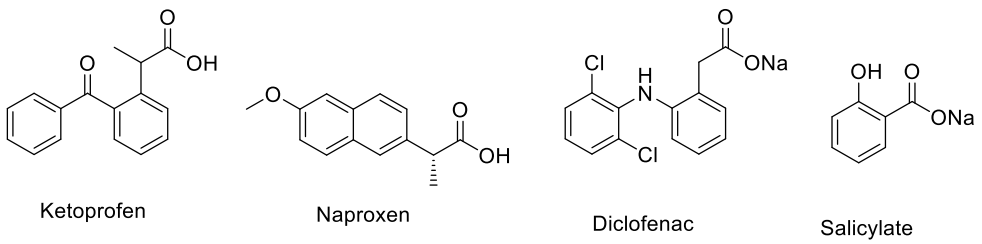

Fig.2.13 API structures

Experiments have been conducted in biological conditions at pH 7 (HEPES buffer in water) where ligands have a terminal quaternary nitrogen positively charged and API are dissociated and have a negative charge. The driving force of gold nanoclusters and amphiphilic organic anions interaction is a combination of hydrophobic effects due to the presence of an apolar portion of the substrate which can accommodate in the apolar monolayer alkyl layer of the nanoclusters, and the simultaneous ion-pairing interaction which involves the charged head groups. This combination of effects provides selectivity and high affinity. A simple model to understand why the just described recognition process is expected to modify photophysical properties of gold nanoclusters takes into account two different mechanisms. The first mechanism considers the direct excitation energy and electron transfer processes involving API and gold nanoclusters upon binding. The second mechanism take into consideration the presence of positively charged API on gold nanoclusters surface that changes gold nanoclusters global charge distribution and hence influences their photophysical properties. We would like to stress that while the first mechanism is expected to affect the photoluminescence of both the API molecules and the gold NPs, the second one only modifies the gold emission. In Fig.2.14 are reported API photophysical properties. All of the molecules have an absorption band in the UV region and an emission in visible region. In order to discriminate which mechanisms of interaction between gold nanoclusters and API were involved, all the hybrid systems were exited at two different wavelengths: at 300 nm where API absorb, and both mechanisms can occur, and at 500 nm where API do not absorb and only the second mechanism can occur.

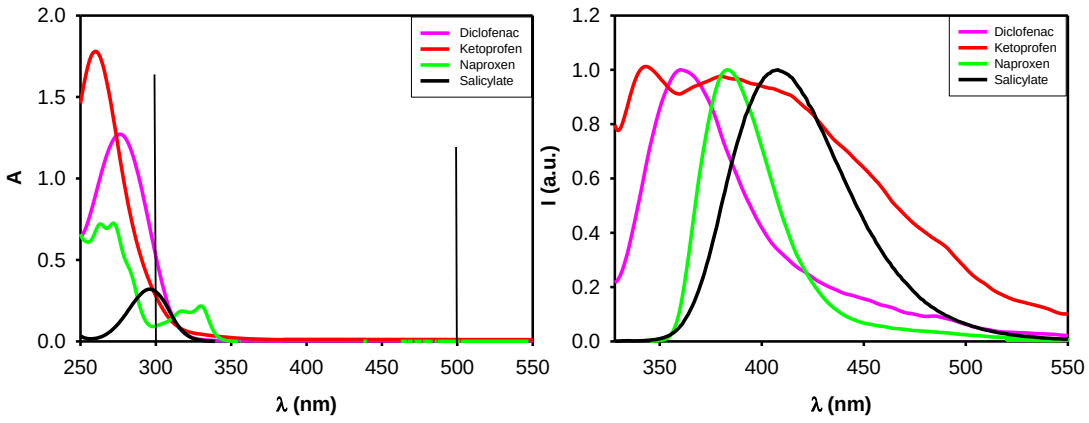

Fig.2.14 On the left: API absorption spectra. On the right: API emission spectra

In Fig.2.15 percentage variation of AuNCs-1NIR emission exited at 300 nm and at 500 nm as API concentration is increased are reported.

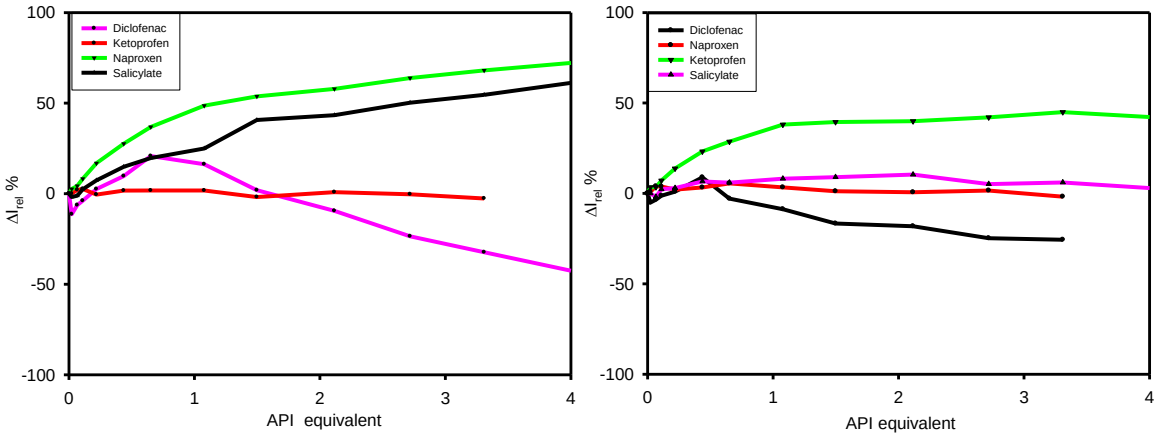

Fig.2.15 On the left: percentual variation of AuNCs-1 NIR emission exited at 300 nm; on the right:) percentual variation of AuNCs-1 NIR emission exited at 300 nm

Considering only most interesting trends, we can observe that in presence of Naproxen there is a considerable emission increase, almost 100%. Then, by comparing the response of the system excited at 300 nm and at 500 nm, we can deduce that both mechanisms discussed above contribute concurrently with the same importance.

Similarly, with salicylate it is possible observe an emission increase of about 100%. But in this case direct energy transfer from the drug molecules to gold nanoclusters is the only contribution. In fact, when the system is excited at 500 nm there are no significative AuNCs-1 emission changes.

In Fig.2.16 the percentual variation of AuNCs-3 NIR emission exited at 300 nm and at 500 nm (Fig.2.16) as API concentration is increased are reported.

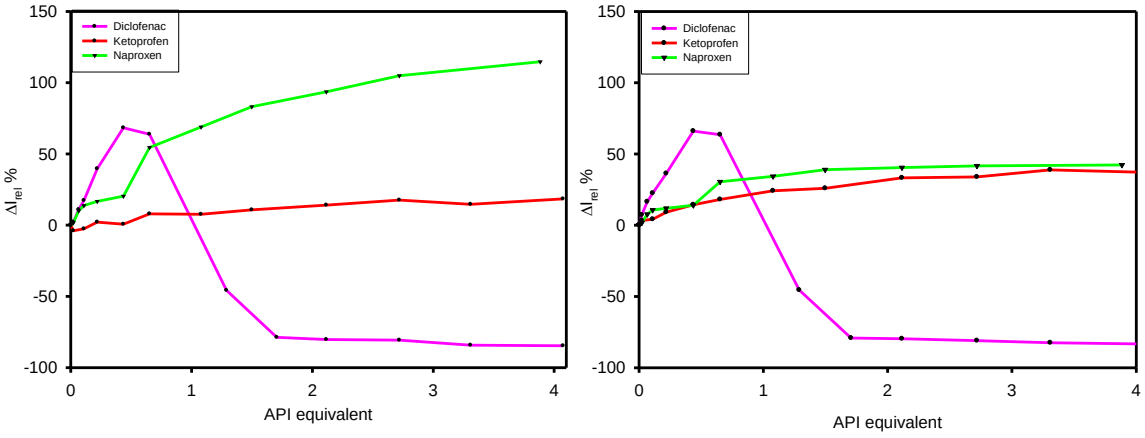

Fig.2.16 On the left: percentual variation of AuNCs-3 NIR emission exited at 300 nm; on the right:) percentual variation of AuNCs-3 NIR emission exited at 300 nm

In presence of Naproxen a huge enhancement of emission is observed, more than 100%. Then, by comparing the system response upon excitation at 300 nm and at 500 nm, we can say that both mechanisms occur concurrently giving similar contributions.

As shown in Fig.2.16, in presence of Diclofenac at the beginning AuNCs-3 emission increases but beyond a concentration threshold emission is totally quenched. This result suggests that a high concentration of Diclofenac on the surface of gold the formation of organic dimer or aggregates quenches any emission. In conclusion in this work have been developed a new class of photophysical API-sensors operating in biological conditions and active in the NIR spectral region where biological samples and tissues are more transparent and that is attracting a lot of attentions for bioimaging and sensing. Gold nanoclusters based sensors have showed a good selectivity towards specific drugs, demonstrating that these systems are potentially suitable as drug sensors.

In the final part of this thesis I worked on another interesting material: melanin. Melanin is an abundant and heterogeneous bio-pigment found ubiquitously in many livings being. In particular melanin plays an exemplary role as a radioprotector, thanks to its broad band absorption spectrum, its ability to convert 90% of absorbed light into heat and to behave as free radical scavenger. There are many sources in nature from which it is possible to extract melanin. Nevertheless, this operation has drawbacks. In fact, to date no extraction technique has been found that guarantees not to affect the properties of melanin in its natural environment. Therefore, researchers have sought alternative ways to obtain synthetic materials that reproduce the most interesting characteristics of melanin.

Currently the best candidate is polydopamine (PDA), a black insoluble material produced by oxidative polymerization of dopamine under alkaline conditions. PDA shares chemical functionalities (i.e., catechol and nitrogen-containing groups) with natural eumelanin and present similar features as broad band absorption spectrum, it is insoluble in almost all solvents, ability in metal chelation, free radical stable and semiconducting activity. The unique characteristics of melanin, conferring antioxidant and radio- and photo-protective properties, are mostly due to the presence of unpaired electrons in the structure that results in a stable free radical property. We can suppose that increasing stable free radicals on melanin corresponds in increase the intrinsic free radical scavenging ability and consequently radioprotective effects. The presence of heavy transition metal, as Fe(III) and Mn(III) can contribute to increase the intrinsic melanin free radical scavenging ability, at the basis of radiation protection activity. Indeed, when Fe(III) and Mn(III) meets a free electron it can catch them reducing respectively at Fe(II)and Mn(II). In chapter eight we try to increase melanin radiation protection activity both increasing number of stable free radicals and introducing oxidative ion transition metal. We chose Fe(III) and Mn(III) to increase oxidative ability and

Zn(II), that do not possess oxidative ability as reference. We used 4-amino-TEMPO to increase number of stable free radicals.

Synthesis of PDA with 4-amino-TEMPO and Fe(III) is reported in Fig.2.17.

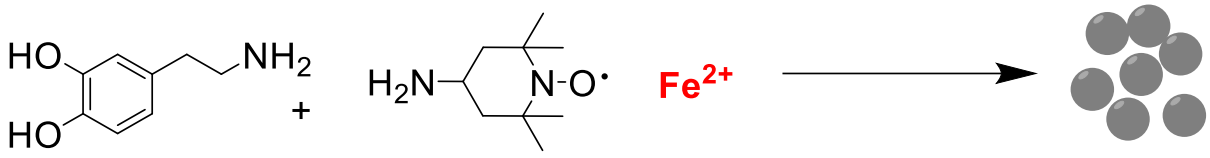

Fig.2.17 Synthesis of PDA nanoparticles with Fe and 4-amino- TEMPO

Reagents are presents with the sequent ratio: dopamine 3, Fe(III) 1, 4-amino-TEMPO 1.

Since scalability is a major issue in melanin preparation synthesis has been carried out first in small scale (Fe_T_PDAss) and then in a large scale (Fe_T_PDAls). Then we tried to increase iron concentration. We repeated reaction with the sequent ratio of reagents: dopamine 3, Fe(III) 2, 4-amino-TEMPO 1. Also, in this case synthesis has been carried out in small scale (Fe2_T_PDAss) and then in a large scale (Fe2_T_PDAls).

Then we used Mn(III). Synthesis of PDA with 4-amino-TEMPO and Mn(III) is reported in Fig.2.18.

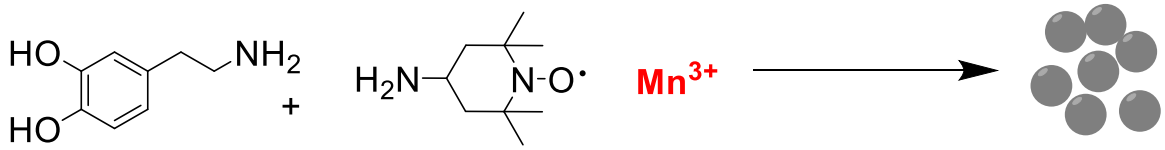

Fig.2.18 Synthesis of PDA nanoparticles with Mn and 4-amino- TEMPO

Reagents are presents with the sequent ratio: dopamine 2, Mn(III) 1, 4-amino-TEMPO 1.

For starting, synthesis has been carried out in small scale (Mn_T_PDAss) and then in a large scale (Mn_T_PDAls).

Then we used Zn(II). Synthesis of PDA with 4-amino-TEMPO and Zn(II) is reported in Fig.2.19.

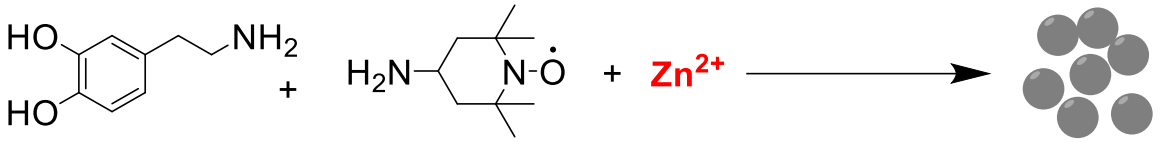

Fig.2.19 Synthesis of PDA nanoparticles with Zn and 4-amino- TEMPO

Reagents are presents with the sequent ratio: dopamine 3, Zn(II) 1.5, 4-amino-TEMPO 1.

For starting, synthesis has been carried out in small scale (Zn_T_PDAss). Unfortunately, it was not possible obtain this material in large scale. Then we tried to increase zinc concentration. We repeated reaction with the sequent ratio of reagents: dopamine 3, Zn(II) 3, 4-amino-TEMPO 1. Synthesis has been carried out in small scale (Zn2_T_PDAss) and then in a large scale (Zn2_T_PDAls).

All materials have been characterized by dynamic light scattering (DLS), transmission electron microscopy (TEM), energy dispersive spectroscopy (EDS), X-ray photoelectron spectroscopy (XPS), electron paramagnetic resonance (EPR) and inductively coupled plasma-atomic emission spectrometry (ICP- AES). In conclusion DPPH assay was used to test antioxidant activity of nanoparticles.

2.1 Conclusions

In this thesis nanoparticles have proven to be applicable in numerous high-profile fields as bioimaging, environmental and pharmaceutical sensors. We believe there is still much to be discovered about nanoparticles potential and applications. For this reason, we hope that in the coming years the study of these fascinating and surprising materials will continue.

2.2 Bibliography

1. Caponetti, V.; Trzcinski, J. W.; Cantelli, A.; Tavano, R.; Papini, E.; Mancin, F.; Montalti, M., Self-assembled biocompatible fluorescent nanoparticles for bioimaging. *Frontiers in chemistry* **2019,** *7*.

Chapter 3: Techniques

3.1. Electronic absorption spectra

The acquisition of electronic absorption spectra was carried out at room temperature on air-equilibrated solutions in quartz cuvettes.

The absorption spectra of each compound in the 900-190 nm range was performed with a UV/Vis Perkin Elmer LS55 double beam spectrophotometers. The precision on the wavelength values was ± 1 nm. Molar extinction coefficient values were determined using the Lambert-Beer law and the experimental error associated to each value is estimated to be ±5%. Titrations with spectrophotometric method were carried out by the addition of small volume (usually in the range 1-50 μL) of a mM concentrated solution of titrating species. Titrating species were added to the titrated species directly into the cuvette.

When the light passes through a sample or is reflected, the outgoing light have a lower intensity than the incident one. The transmittance (T) is defined by the ratio between the intensity of the transmitted radiation (I) and the intensity of the incident radiation (I_0):

$$T = \frac{I}{I_0}$$

The following equation defines the absorbance:

$$A = -\log_{10} T = \log_{10} \frac{I_o}{I}$$

The cell containing the sample in solution must be transparent to the incident radiation, even if is clean and completely transparent, it will never be possible to cancel the reflection phenomena that take place at the air / wall and wall / interface of the solution. To consider the instrumental error of this measurement, the intensity of the radiation transmitted by the solution is compared with the intensity of the beam transmitted by another cell containing only the solvent:

$$A = \log_{10} \frac{I_{solvent}}{I_{solution}} \approx \log_{10} \frac{I_o}{I}$$

Furthermore, before carrying out the measurement, it is also necessary to calibrate the instrument by adjusting 0% and 100% transmittance.

The empirical relationship that correlate the amount of light absorbed with the concentration of the sample is the Lambert-Beer law:

$$T = \frac{I}{I_0} = 10^{-\varepsilon bc}$$

$$A = -\log_{10} T = \log_{10} \frac{I_o}{I} = \varepsilon bc$$

Where ε is the molar absorption coefficient, characteristic of each substance under defined conditions of wavelength, solvent and temperature, b is the length of the optical path (in centimetres) and c is the concentration in molarity of the sample in solution. The Lambert-Beer law is a limit law, that is perfectly verified only in the case of infinite dilution; it is however reasonable to apply it in the case of diluted solutions, even if it is not possible to define a unique limit value for the applicability area (for absorbances above 2-2.5 the equation is no longer applicable).

The instrument that allows transmittance/absorbance measurements according to the wavelength is the spectrophotometer, a block diagram is shown below:

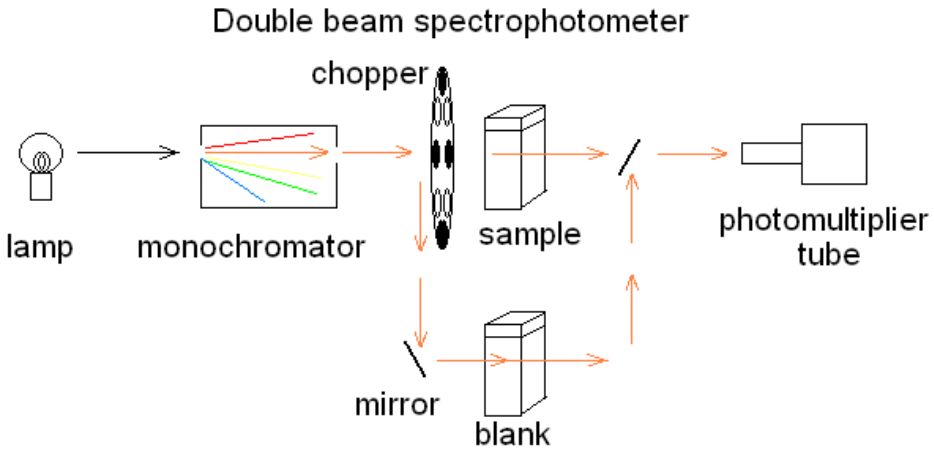

Fig.3.1 General scheme of a spectrophotometer

This instrument consists of a light source consisting of two lamps, one tungsten to cover the spectral range from 900 nm to 320 nm and one to the deuterium that radiates from 320 nm to 190 nm, from a monochromator able to select a particular length wave in the broadband of the radiations emitted from the source, from a special sample-holder and from a detector (photomultiplier) able to convert the transmitted light signal into an electrical signal[1].

3.2 Luminescence spectra

The emission spectra were recorded with a Perkin Elmer LS 50 spectrophotometer and a Varian Cary Eclipse spectrofluorometer.

The electronically excited state populated by absorption of light is metastable and will decay with different pathways. The deactivation of the excited state could occur by radiative pathway, by emission of a photon and this process is called fluorescence (for spin-allowed transition) or phosphorescence (spin-forbidden transition).

With a spectrofluorometer it is possible to record both emission and excitation spectra.

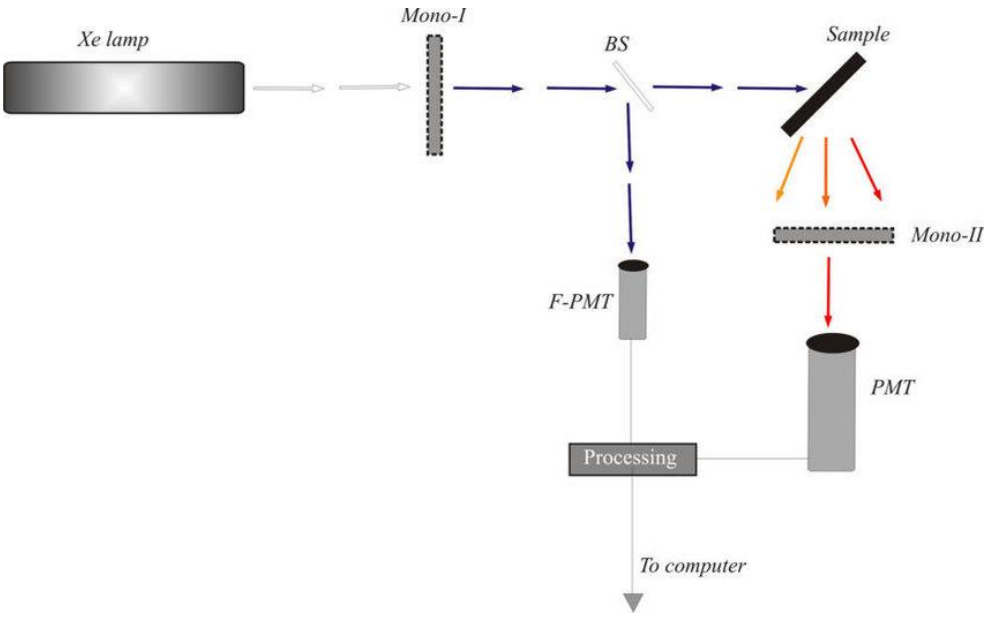

Fig.3.2 General scheme of a spectrofluorometer

The instrumentation is composed by a radiation source in the UV and visible spectrum (Xenon lamp), an emission and an excitation monochromator, a sample holder and a detection system that includes a reference photomultiplier used to correct the emission spectrum of the lamp and a photomultiplier used to detect the emission signal of the sample.

To record an emission spectrum, the sample by a certain wavelength and the intensity varies as the emission wavelength varies operationally, the excitation monochromator is positioned at a certain wavelength and a scan is performed with the emission monochromator. To record an excitation spectrum, the emission monochromator is maintained at a given wavelength and the spectral interval in which the sample absorbs with the excitation monochromator is explored: for this reason, the excitation spectrum is expected to be proportional to the absorption one (the two spectra have the same shape) [2].

3.3 Luminescence quantum yield

Luminescence quantum yield represents a ratio between the number of photons absorbed by a chromophore and the number of photon emitted. This parameter is useful because is possible to compare different chromophore and evaluate their emission. The most employed method for the assessment of the luminescence quantum yield in solution is based on the direct comparison with a reference standard, whose quantum yield (Φ_r) is known. The equation that allows its determination is given by

$$\Phi = \Phi_r \frac{S}{S_r} \frac{n^2}{n_r^2}$$

where *S* and *n* represent the area of the emission profile and the refractive index of the solvent used to prepare both the solution of the sample and there refence, respectively. This equation is valid only if the absorbance values referring to the excitation wavelength of both the reference and the sample are the same and are below 0.1.

The spectral region of its emission must be superimposable to the one of the samples, in order to obtain emission spectra using the same experimental conditions. The determination of the luminescence quantum yield was performed by following the experimental procedure proposed by Demas and Crosby[3] and the most suitable standard for the measurement was chosen depending on the spectral region related to the emission of the sample[1].

3.4 Luminescence lifetime determination

Fluorescence lifetime measurements were carried out at room temperature. Measurements were performed by using an Edinburgh Analytical Instruments time-correlated single photon counting (TCSPC) equipment, which allows the assessment of lifetimes in a time range between 0.5 ns and 30μs. Like other time-domain measurements, TCSPC technique measures sample luminescence as a function of time, in terms of a direct proportionality between the number of emitted photons and the concentration of excited states of samples.

The block diagram of TCSPC is depicted in Fig.3.3:

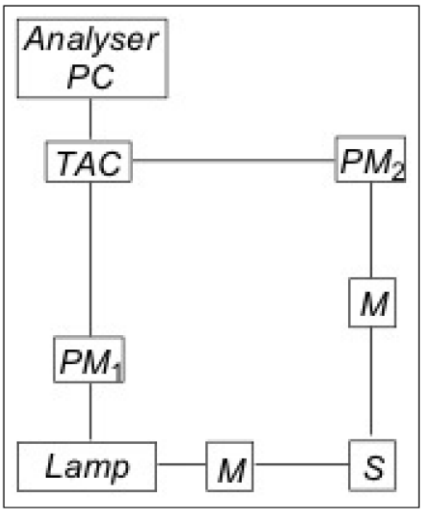

Fig.3.3 General scheme of a time-correlated single photon counting (TCSPC)

By observing the scheme, it is possible to distinguish the main components of the apparatus:

– sources(Lamp): they can be a pulsed diode laser or a low-pressure discharge lamp (nF900,filled with nitrogen or deuterium), which is able to deliver 0.5 ns pulses at a frequency in the range of 100KHz;

– two monochromators (M);

– two photomultipliers (PM1,PM2);

– sample (S);

– time-to-amplitude converter (TAC);

– computer(PC).

The measurement starts with the emission of a short laser pulse (1-5ns) and at the same time the start photomultiplier sends a signal to the TAC. The TAC run a linear voltage ramp until the first photon emitted by the sample is recorded and the stop photomultiplier and sends a stop signal to the TAC, thus blocking the voltage ramp. The TAC resembles a chronometer since it measures the time elapsed from the start and the stop signals and this time interval is sent to the multi-channel analyser (MCA) as an electrical signal. Repetition of many excitation emission cycles allows the MCA to accumulate and organize the obtained signals indifferent channels based on their delay form the excitation. For statistical reasons, the frequency of the registered events must be less than 2% of the working frequency of the lamp. In this way, it is possible to avoid detecting only the contribution of photons that are emitted immediately after the excitation: these photons have a high detection probability, and this results in a shift of the luminescence decay curve towards shorter times.

Fluorescence lifetimes were determined by applying mono and biexponential fitting were models and the factor χ^2 was employed as quality parameter of the fits[1].

3.4 Dynamic light scattering

The determination of the hydrodynamic diameter distribution of the NPs was carried out through Dynamic Light Scattering measurements employing a Malvern Nano ZS instrument equipped with a 633 nm laser diode. Samples were housed in disposable polystyrene cuvettes of 1 cm optical path length, using water as the solvent. PDl (Polydispersion Index) indicates the width of the DLS hydrodynamic diameter distribution. In case of a mono-modal distribution (Gaussian) calculated by means of cumulant analysis

$$\mathrm{PDI} = \left(\frac{\sigma}{Z_{avg}}\right)2$$

where σ is the width of the distribution and Z_{avg} is the average diameter of the particle population.

The main components of a DLS are:

- Laser: He-Ne laser;
- Attenuator: reduces the light intensity of the laser;

- Detector: records the light signal scattered from the sample and can be positioned at 173 ° or 90 ° with respect to the incident laser light.
- Correlator: compare the scattering intensity for different time intervals
- Software

The diagram of the instrument is shown in Fig.3.4.

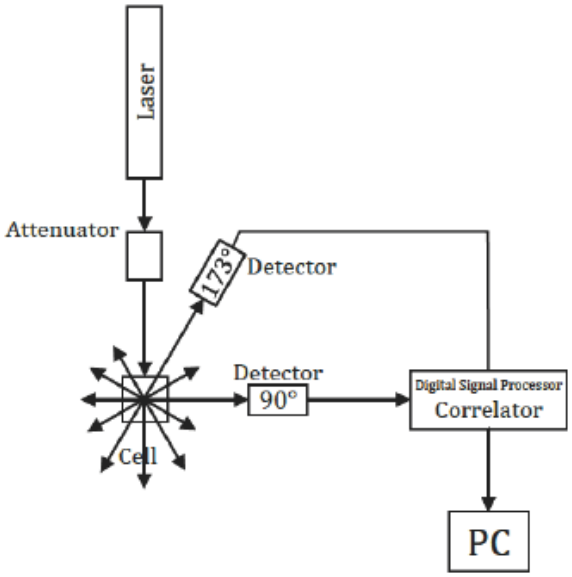

Fig.3.4 General scheme of a DLS instrument

The DLS is a useful technique for the determination of sub-micrometric particle size. This technique correlates Brownian motion and the size of particle, in terms of hydrodynamic diameter. Using the Stoke-Einstein equation and measuring the translational diffusion coefficient (D) it is possible to calculate the particle size.

$$d(H) = \frac{kT}{3\pi\eta D}$$

Where d (H) is the hydrodynamic diameter, k is the Boltzmann constant, T is the absolute temperature and η corresponds to the viscosity of the medium.

The hydrodynamic diameter is the sum of the particle size and the first shell of solvation around it. This value depends on the temperature and viscosity of the medium, but also on the surface structure of the particle and the ionic strength of the medium. Rayleigh's approximation describes the relationship between the intensity of the scattered light (I) and the particle size (d) and the wavelength of the laser (λ).

$$I \propto d^6 \qquad I \propto \lambda^4$$

A DLS measurement in addition to the value of the hydrodynamic diameter give also other important parameters:

- Correlation function: in order to have a good measure it must have a sigmoidal pattern and the intercept with the y axis must tend to 1. Furthermore, the time required for the decay from information on the particle size, for large particles there is a greater decay time. The angle of the decay from information about the particle distribution, the greater the most monodisperse slope is the sample, and the baseline can give information about the presence of large aggregates or dust.
- Polydispersion index (PDI): indicates the size distribution of the sample population. For a monodisperse sample the value tends to be close to PDI values between 0.05 and 0.2 indicate well monodisperse samples. Values above 0.2 indicate medium-to-monodisperse or polydisperse samples whereas values below 0.05 indicate very monodisperse samples and these values are mainly for standards.

3.5 Transmission electron microscopy

Transmission Electron Microscopy (TEM) was performed on a FEI Sphera microscope operating at 200 keV. TEM grids were prepared by depositing small (3.5 µL) aliquots of sample onto grids (~ 2 min, Formvar stabilized with carbon (5-10 nm) on 400 copper mesh (Ted Pella Inc.), that had previously been glow discharged using an Emitech K350 glow discharge unit and plasma-cleaned for 90 s in an E.A. Fischione1020 unit. Micrographs were recorded on a 2 KX2 KGatan CCD camera.

Transmission electron microscopy (TEM) is a technique where an electron beam goes through a thin layer of sample. The interaction of accelerated electrons and sample generates an image that is focused on a fluorescent screen or a CCD. The resolution of TEM images reaches the Angstrom scale by the very low wavelength of the electron beam.

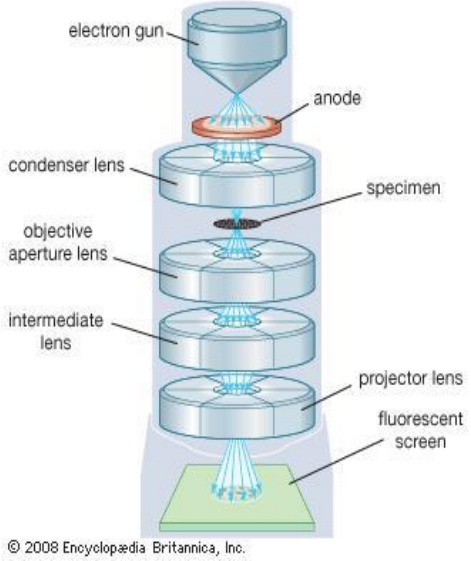

Fig.3.5 General scheme of a trasmission electron microscopy

The typical TEM instruments is composed by an electron gun, a sample holder, a set of lens and magnifiers and a detector. The electron gun is based on a thermoionic emission of a tungsten wire of LaB_6 that generates an electron beam that are accelerated by an electric field. The electron gun has also condenser lens that align the electron beam on a precise small region of the sample. The electron beam hit the sample and is diffracted by the crystal reticulum of the sample with the formation of the Bragg ray along specific direction. The wave function phi transmitted from the sample is composed by the sum of all the diffused wave. This wave function has all the structural information but is transmitted in a non-linear way by the optic system. The parallel transmitted waves generate the diffraction pattern. The waves with an angle higher than q have a change in the phases due to the defocus effect of the lens. These waves have a longer pathway that generate a shift in the phase, this is the reason why phi is non-linear.

The image on the retrofocale is unfocus and to obtain the right image a mathematical operation is required, the convolution of Fourier transform.

TEM image could be recorded with three different contrast. The first is the diffraction contrast, where the defects in the amplitude of the trasmitted waves. For nanocrystals most of the defects are not in the volume of the crystals but on the surface, this kind of contrast could be useful to highlight deformation in the nanocrystal structure.

A second type is the phase contrast, that is genarated by the modulation of the incident electronic waves when is trasmitted trough the crystal field. This type of contrast is sensitive to the atomic composition of the sample.

The last contrast is the atomic number contrast. The atoms with different atomic number have different scattering properties. If the image is recorded by acquiring electrons at high angles, the contrast pictures is sensitive to the mean atomic number along the beam direction. This type os contrast is the most common. A TEM investigation at high resolution is crucial to obtain several information on the structure and the caracterization of nanomaterials[4].

3.6 Energy Dispersive Spectroscopy

Energy dispersive spectroscopy (EDS) characterization was done using a Hitachi HD2300A microscope operating at 200 kV (beam current: 49 μA, extraction voltage: 2.4 kV), which is equipped with dual Thermo Fischer Scientific (Waltham, MA) EDS detectors (total X-ray collection angle ~0.7 steradian). Analysis and visualization of EDS data was done using Thermo Fischer Scientific NSS software. Grids were prepared by depositing small (3.5 μL) aliquots of sample onto grids (~ 2 min, Formvar stabilized with carbon (5-10 nm) on 400 copper mesh

(Ted Pella Inc.), that had previously been glow discharged using an Emitech K350 glow discharge unit and plasma-cleaned for 90 s in an E.A. Fischione1020 unit.

EDS is an analytical technique used to probe the composition of a solid materials. Several variants exist, but the all are based on exciting inner electrons, causing more distant electrons to drop energy levels to fill the resulting "holes." One of the most common and useful ways energy can be transferred into and out of an atom is by electromagnetic radiation. Core shell transitions correspond to radiation in the X-ray portion of the spectrum; however, because the core shells are normally full by definition, these transitions are not usually observed.

X-ray spectroscopy uses a beam of electrons to excite core electrons to high energy states, creating a low-energy vacancy in the atoms' electronic structures. This leads to a cascade of electrons from higher energy levels until the atom regains a minimum-energy state. Due to conservation of energy, the electrons emit X-rays as they transition to lower energy states. It is these X-rays that are being measured in X-ray spectroscopy. Since each element has a different nuclear charge, the energies of the core shells and, more importantly, the spacing between them vary from one element to the next. While not every peak in an element's spectrum is exclusive to that element, there are enough characteristic peaks to be able to determine composition of the sample, given sufficient resolving power[5].

3.7 Electron Paramagnetic Resonance

Electron Paramagnetic Resonance (EPR) is a magnetic spectroscopy used to study materials with unpaired electrons.

A charged spinning particle immersed in an external magnetic field B_0 possess a magnetic moment μ. EPR spectroscopy is based on the interaction between μ with the magnetic component B_1 of an incident electromagnetic radiation.

Classical physics describe the energy of a magnetic dipole as the scalar product between the external magnetic field B_0 and the intrinsic magnetic moment of the dipole, μ

$$E = -|\mu B_0|\cos(\mu, B_0)$$

where (μ, B_0) is the angle between the magnetic moment of the dipole and the direction of the external magnetic field. According this equation, for a given B_0, the minimum and the maximum energy levels occur when the dipole is oriented respectively in parallel and anti-parallel to the direction of B_0, but it is not able to explain EPR spectroscopy.

The mathematical models that describes the theory of this technique are the Zeeman effect and the hyperfine splitting The Zeeman effect describes the splitting of electronic energy levels of an atom, molecule or material immersed in an external magnetic field B_0.

It can be explained by the quantum mechanical physics, which reports that the quantization of the electron spin angular moment leads to the quantization of the energy levels of an electron immersed in a magnetic field. The energy levels can be described as follow:

$$E = g_e \beta_e B_0 Ms$$

where g_e is the Zeemann splitting constant for a free electron and the value is 2.0023, β_e is the Bohr magneton and the value is $9.274 \cdot 10^{-24}$ JT $^{-1}$, and $M_s = \pm 1/2$ is the z component of the spin

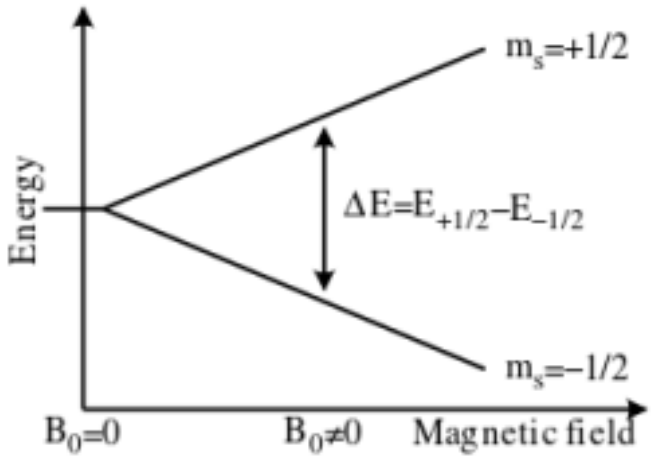

Fig.3.6 Scheme of the energy levels splitting for a single spin system with spin quantum number M_S = 1/2 and immersed in an external magnetic field B_0.

An EPR transition involves two electronic energy levels of a spin system separated by the energy, ΔE, and takes place when the spin system is irradiated by an electromagnetic radiation of frequency, ν, that meets the resonance condition:

$$\Delta E = g_e \beta_e B_0 \Delta Ms = h\nu$$

ΔE increases linearly with the intensity of B_0 applied. This description is valid only for free electrons immersed in a magnetic field.

For unpaired electrons of molecules in real sample the magnetic field is a linear combination of the external magnetic field B_0 and the local magnetic field B_{loc} generated by magnetically active nuclei eventually present in the molecule.

$$B_{act} = B_0 + B_{loc}$$

where the B_{loc} has typically two contributions: a local field induced and proportional to the external B_0 and a permanent local field that depends only on their mutual orientation with respect to B_0. The spin-orbit coupling, caused by the electron spin interacting with its own motion along its orbit, generates a local field of the first type, the impact on B_{act} can be described as:

$$B_{act} = (1\text{-}\sigma)B_0 = \left(\frac{g}{g_e}\right) B_0$$

where g is the effective Zeemann factor and σ, defined as a distance from the Zeemann splitting constant is the EPR analogous to the chemical shift in NMR.

With the resonant magnetic field is not possible individuate a specific a spin system, because the resonant condition depends on instrumental parameters. The g-factor, instead, can be defined to indicate the resonant conditions unambiguously:

$$g = \frac{h\nu}{\beta_e B_0}$$

The g-factor helps to distinguish and characterize paramagnetic species under investigation.

The spin-orbit coupling is usually weak for elements in the first row of the periodic table and strong for transition metals and heavier elements. The most important example of the second type of local field, is the permanent local field generated by the magnetic moment associated with the nuclear-spin angular moment. Magnetically active nuclei have non-zero nuclear-spin quantum number, I, which can assume values equal to 1/ 2, 1, 3/ 2, 2,⋯.I determines the number of nuclear spin states according to the 2I+1 and each nuclear spin state can assume values MI=±I. For hydrogen atoms I=1/2 and MI=±1/2. The resulting B_{act} is:

$$B_{act} = B_0\text{-a MI}$$

where a is the hyperfine constant, it has most commonly the unit of magnetic field and it can be determined experimentally, whereas

$$B_0 = \frac{h\nu}{g\beta_e}$$

is the resonant field resulting from the perturbation due to spin-orbit interactions[6].

3.9 X-ray photoelectron spectroscopy

X-ray photoelectron spectroscopy (XPS) analysis were conducted on Thermo Fisher Scientific ESCALab 250Xi spectrometer using Al K-alpha X-ray source (1486.6 eV). The XPS spectra were calibrated with adventitious carbon peak at 284.8 eV.

X-ray photoelectron spectroscopy (XPS) is based on irradiation of a solid sample with x-rays. It is an essential method to study the chemical composition of surfaces by qualitative and quantitative analysis. Most materials are not affected by x-rays and they may be examined with no change of the composition of their surfaces, as well as the conservation of the oxidation state of the specimen, if an appropriate sample preparation is performed. In addition, the chemical shift measured by XPS signal provides detailed information on the distribution of the chemical composition, including their oxidation state and the chemical binding of the species.

The absorption of a high-energy x-ray photon causes the ionization of the material, especially ejection of electrons from core levels (within the energy range of the x-ray beam). Typical X-ray sources are Al Kα and the Mg Kα radiations with energies hν = 1486.6 and 1253.6 eV and have a line width of 1.0 and 0.8 eV, respectively. This line width restricts in many cases the spectral resolution. It can be improved by an x-ray monochromator to 0.5 eV or less with a strong loss of the intensity of the exciting beam. This loss can be compensated for modern spectrometers by the use of magnetic lenses and more sensitive detectors.

After absorption of x-ray, the electron is ejected from its level to the vacuum with the kinetic energy E_K. This value depends material and x-ray energy with the equation

$$h\nu = E_k + E_e$$

where E_e is the energy that electron needs to be removed from the material.

This equation shows that knowing energy hν of the radiation source and measuring kinetic energy E_K, E_e may be calculated. The energy spectrum of the ejected electrons is characteristic for the element involved in the process[7].

3.10 DPPH assay

DPPH radical scavenging activity of PDA particles was measured according to the literature method. We freshly prepared 0.1 mM of DPPH solution in 95% ethanol before use. We mixed 1.4-3.6-6.8-10.4-13.5-17.1-20 μL of PDA nanoparticles dispersed-water solution with concentration 1mg/mL in 0.45 mL of DPPH solution. The scavenging activity was evaluated by monitoring the absorbance decrease at 516 nm after it remained in the dark for 20 min. DPPH radical scavenging activity was calculated as

$$I = \frac{\left[1-\left(A_i-A_j\right)\right]}{A_c} 100$$

where *Ac* is the absorbance of DPPH solution without DPA nanoparticle samples, *Ai* is the absorbance of the samples of DPA mixed with DPPH solution, and *Aj* is the of the samples of DPA nanoparticle themselves without DPPH solution[8].

3.11 Bibliography

1. Moggi, L.; Juris, A.; Gandolfi, M., Manuale del fotochimico. Bononia University Press, Bologna: 2006.
2. Montalti, M.; Credi, A.; Prodi, L.; Gandolfi, M. T., *Handbook of photochemistry*. CRC press: 2006.
3. Crosby, G. A.; Demas, J. N., Measurement of photoluminescence quantum yields. Review. *The Journal of Physical Chemistry* **1971,** *75* (8), 991-1024.
4. (a) Ma, H.; Shieh, K.-J.; Qiao, T. X.; Cherng, S., Transmission Electron Microscopy (TEM) and Scanning Electron Microscopy (SEM). *Nature and Science* **2006**, 14; (b) Wang, Z., Transmission electron microscopy of shape-controlled nanocrystals and their assemblies. ACS Publications: 2000.
5.https://chem.libretexts.org/Bookshelves/Analytical_Chemistry/Book%3A_Physical_Methods_in_Chemistry_and_Nano_Science_(Barron)/01%3A_Elemental_Analysis/1.12%3A_An_Introduction_to_Energy_Dispersive_X-ray_Spectroscopy.
6. Eaton, G. R.; Eaton, S. S.; Barr, D. P.; Weber, R. T., *Quantitative Epr*. Springer Science & Business Media: 2010.
7. Marcus, P.; Mansfeld, F. B., Analytical methods in corrosion science and engineering. CRC press: 2005.
8. Ju, K.-Y.; Lee, Y.; Lee, S.; Park, S. B.; Lee, J.-K., Bioinspired polymerization of dopamine to generate melanin-like nanoparticles having an excellent free-radical-scavenging property. *Biomacromolecules* **2011,** *12* (3), 625-632.

Chapter 4: Self-assembling supramolecular structures as stimuli-responsive systems for sensing pH and anions in water

4.1 Introduction

The class of pigments named perylene-3,4,9,10-tetracarboxylic acid diimide (PDI) has distinguished itself over the years in the last century thanks to the excellent chemical, thermal, and photostability[1]. They have a perylene core rigid, polycyclic and aromatic substituted with two dicarboxylic acid imide groups at the 3,4- and 9,10-peri-position, forming an acceptor-donor-acceptor scaffold between the electron-rich core and the strongly conjugated electron-withdrawing amino groups[2].

Most common synthetic approach consists of the condensation reaction of Perylene-3,4,9,10-tetracarboxylic dianhydride (PTCDA), with anilines and aliphatic primary amines to obtain symmetrically N,N'-substituted PDIs[3]. Because PTCDA is strongly insoluble in almost all the most common organic solvents, the reaction can be carried out in molten imidazole or quinoline at temperatures higher than 160°C and with zinc acetate anhydrous (typically 10-30 mol %) as a catalyst[1,4] or PTCDA can be treated with primary amines in hot alcohols (e.g. n-butanol), carboxylic acids (e.g. acetic and propionic acid), or alcohol/water mixtures (e.g. 1:1 n-butanol/water) (B, scheme 5.1)[4b].

In the work under examination are studied the properties of N,N'-bis(2-(1-piperazinyl)ethyl)-3,4,9,10-perylenetetracarboxylic acid diimide. In literature reported synthetic strategies are: i)1g PTCDA dissolved in 20 mL of 1-(2-aminoethyl) piperazine at 160°C and stirred for 22 h under nitrogen[5]; ii) PTCDA and 1-(2-aminoethyl) piperazine in a refluxing mixture of N,N-dimethylacetamide and 1,4-dioxane[6]. The reaction products were precipitated adding water and separated by filtration. The resulting products were purified dissolving in HCl solution and precipitating the respective hydrochlorides with acetone. Both strategies are energy and time requiring. Here we propose an innovative, green and cheap synthetic strategy based on microwave heating.

From a photophysical point of view PDI can be regarded as a closed system with an $S_0 \rightarrow S_1$ transition polarized along molecular axis and described as a HOMO-LUMO excitation[7]. Absorption spectrum has maxima that changes from 517 nm in aliphatic solvents to 530 nm in chloroform for alkyl substituted PDIs[8]. This effect can be attributed to the excited state polarization by the solvent molecules. Absorption band is characterized by defined vibrational

structure and peak absorption coefficients approaching 10^5 $M^{-1}cm^{-1}$. The fluorescence spectrum exhibits a small Stokes shift and mirrors the absorption spectrum. Fluorescent quantum yield is almost unitary because the triplet level is very low and the scaffold is rigid and planar. The symmetry of the orbitals implies that the nitrogen atoms are located on nodal planes of both HOMO and LUMO and, accordingly, the effects of imide substitution optical properties for absorption and emission maxima are very little.

Presence of imide substituents could affect fluorescence quantum yield. Simple phenyl group can induce the vibrionic motion ('loose bolt effect')[9] reducing the quantum yield of 30%[7b] while more electron-rich aromatic groups, such as alkylate and alkoxylate phenyl groups[10] can reduce the quantum yield to values < 5%[9, 11] in polar solvents, as a consequence of the photo-induced electron transfer that occurs from the substituent to the electron-poor perylene scaffold.

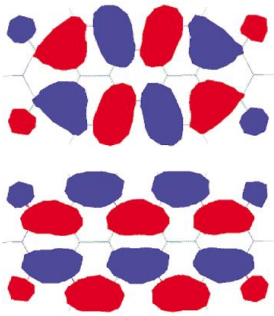

Fig.4.1 (top) HOMO and (bottom) LUMO of perylene diimides. Both the frontiers orbitals exhibit nodes at the imide nitrogens.[1]

When PDI forms self-assembled structure by π–π stacking interaction, the absorption spectrum can be bathochromically (longer wavelengths) shifted with band sharpening and increasing of absorption coefficient, or hypsochromically (shorter wavelengths) shifted with band broadening and intensity decreasing.

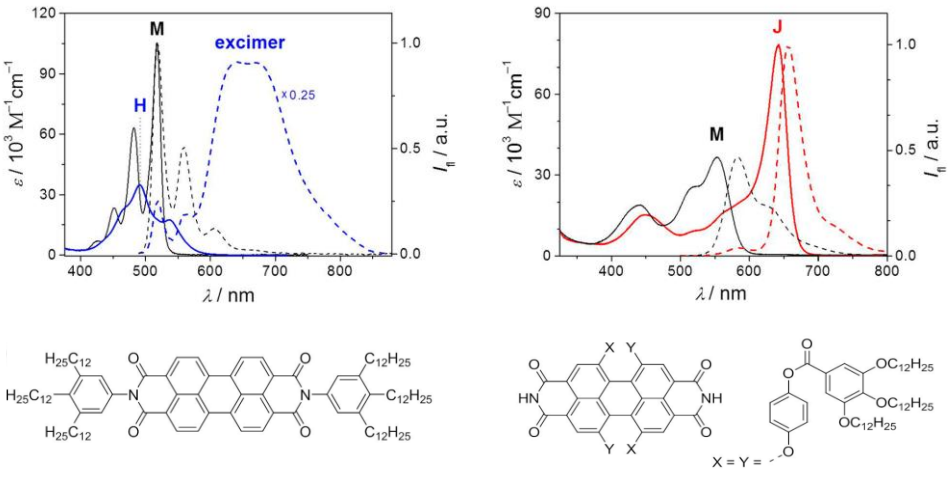

Fig.4.2 UV/Vis absorption (solid lines) and fluorescence spectra (dashed lines) of (left) an H-aggregating PDI and (right) a J-aggregating PDI in methylcyclohexane. (left) Monomer absorption (black, solid line; denoted with M) and emission spectra (black, dashed line) of the PDI at a low concentration of $2 \cdot 10^{-7}$ M and hypsochromically shifted absorption (blue, solid line; denoted with H) and bathochromically shifted, broad excimer emission spectra (blue, dashed line) upon aggregation at a higher concentration of $1 \cdot 10^{-3}$M at 25 °C. (right) Monomer absorption (black, solid line; at 90 °C; denoted with M) and emission spectra (black, dashed line; at 50 °C) of the PDI, and bathochromically shifted J-aggregate absorption (red, solid line; denoted as J) and

emission spectra (red, dashed line) at 15 °C. For the H-aggregating PDI the concentrations of the absorption measurements are $6 \cdot 10^{-7}$ M and of the fluorescence experiments $2 \cdot 10^{-7}$ M.[12]

The simplest model[1-2] considers dimer, where Van der Waals forces reduce both the energies of the ground state and of the excited state respect to that of the monomers. The effect is stronger for excited state, because here molecules are more polarizable and Van der Waals interactions are increased. The excited state of such dimer splits in two excitonic state because of excitonic coupling.

In the two borderline cases transition moments are in-line with a slip angle of θ = 0° and resulting absorption spectrum is hypsochromically shifted. They are called J-aggregate. On the other hand, when dyes are stacked on top of each other with a slip angle of θ = 90° absorption spectrum is bathochromically shifted and they are called H-aggregate.

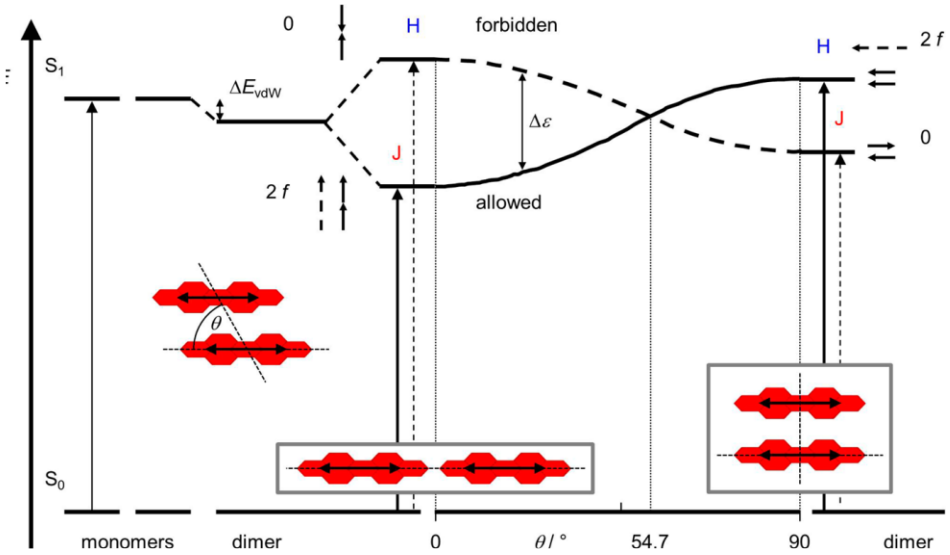

Fig.4.3 Schematic energy level diagram for the excitonic coupling of PDI dimers with coplanar transition dipole moments (μ_{eg}, depicted as double arrows) tilted toward the interconnecting axis by the slip angle θ. The two borderline cases, i.e., in-line (θ= 0°) and sandwich-like arrangement (θ= 90°), are shown in the gray boxes on the left and right side of the diagram. Additionally, for these two alignments, the resulting overall oscillator strengths (small dashed arrows) as well as the oscillator strengths (f, small solid arrows) of the two individual PDI units are indicated.[12]

In both dimers excitation of an individual chromophore can lead to new additional relaxation processes that could reduce fluorescence quantum yield. An example is formation of an excimer 1(PDI-PDI)*, with a red-shifted fluorescence, or a PDI-PDI dimer at the ground state could be directly excited at the first 1(PDI-PDI)* state and then undergoes ISC to the triplet state, forming the triplet-singlet state 3(PDI-PDI). This path is facilitated in dimer because it may occur through intermediate charge transfer (PDI^{+}-PDI^{-})[13] or excimer state. However, if charge separation take place (PDI^{+}-PDI^{-}), the radiationless charge recombination become strongly competitive[13-14].

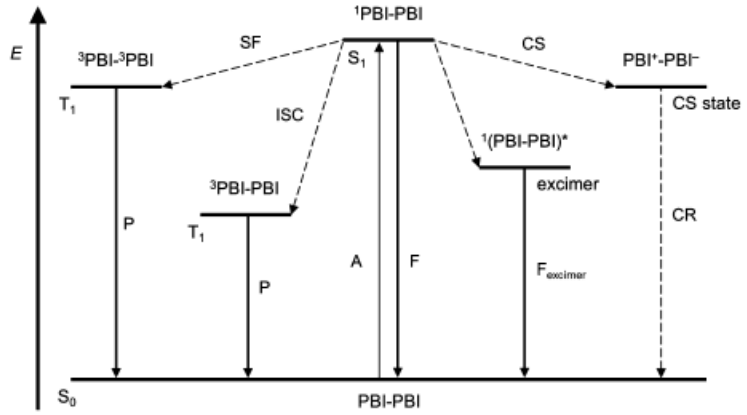

Fig.4.4 Simplified schematic energy level diagram for different excited states of a hypothetical PDI dimer (PDI–PDI) with possible radiative (solid arrows) or radiationless (dashed arrows) relaxation and excitation processes (A, absorption; F, fluorescence; SF, singlet fission; ISC, intersystem crossing; P, phosphorescence; CS, charge separation; CR, charge recombination). The respective higher vibrational levels of each state are not shown for clarity.12

When the aggregated species become larger than dimer, this simple model does not fit anymore and other mathematical models has to be used to describe the aggregation process of PDIs in solution[15], such as the isodesmic[16] and the modified isodesmic model[17]. In the isodesmic model the PDIs ensemble grows as a chain with a binding constant (K) equal for every monomer addition[16,18]. To describe the situation in a more realistic way, the constant of the initial binding step (nucleation) can be considered different from that of the rest of the chain elongation. In this way it is possible to differentiate two situations, the cooperative mechanism, where the nucleation is less favourable than the chain elongation step, and the anti-cooperative, when the opposite situation is verified[16]. These common mathematical models revealed to be useful to explore the mechanisms of self-assembly process. It allows to analyse the process by simple fitting of the UV/Vis spectroscopic changes upon aggregation or fluorescence quantum yield variations.

Formation of different kinds of aggregate structures and their sizes are dependent on many factors, such as temperature[19], concentration[20], solvent composition[21], molecular structure and form of building blocks[22], steric interactions between molecular units, presence of particular additives[23] and relative ratio of hydrophobic and hydrophilic units within the molecules[24].

Sensibility to different stimuli is increased in assemblies formed by amphiphilic building blocks in water, where the hydrophobic effect exerts a decisive influence.

These features, combined with the strong photostability, made PDIs attractive for sensing and stimuli-responsive engineered materials. Among the various types of materials stimuli-responsive materials are one of the most interesting. They can adapt to their environment and to respond to external stimuli and they are emerging as “smart materials”.

4.2 Summary

Here we propose a simple and cheap strategy to develop multi-stimuli sensitive PDI molecules that can be used to create new smart materials exploiting self-assembly.

PBI has been chosen as a platform because it is a well-known fluorophore, stable and with a high emission quantum yield that decreases considerably when the fluorophore aggregates. Best results have been obtained for N,N'-bis[2-(1-piperazino)ethyl]-3,4,9,10-perylenetetracarboxylic diimide (PIPER3). PIPER3 was prepared by microwave assisted reaction of PDA with aminoethylpiperazine (Fig.4.5). Presence of amine groups allow to control aggregation by pH thanks to protonable groups and made PIPER3 water soluble.

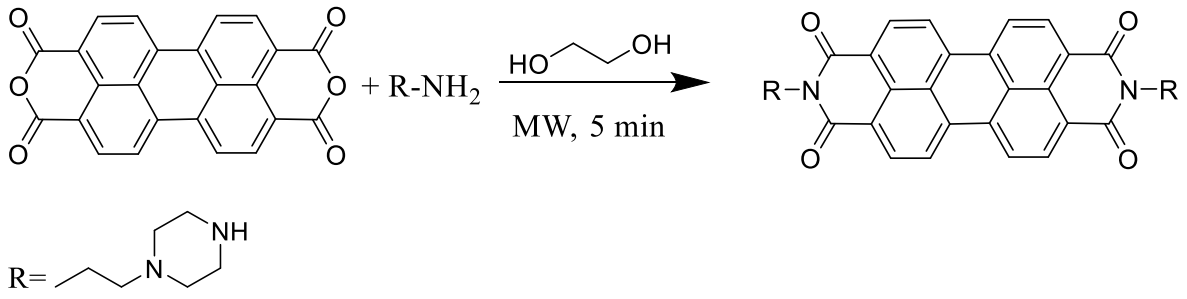

Fig.4.5 Schematic synthesis of PIPER3

PIPER3 emission quantum yield trend as a function of concentration increases and different pH is reported in Fig.4.6. As concentration increases, quantum yield decreases drastically. Indeed, in water π–π stacking interactions between perylene core promote dye aggregation in small nanoparticles, quenching fluorescence. Effect of pH was studied keeping constant PIPER3 concentration (Fig.4.6).

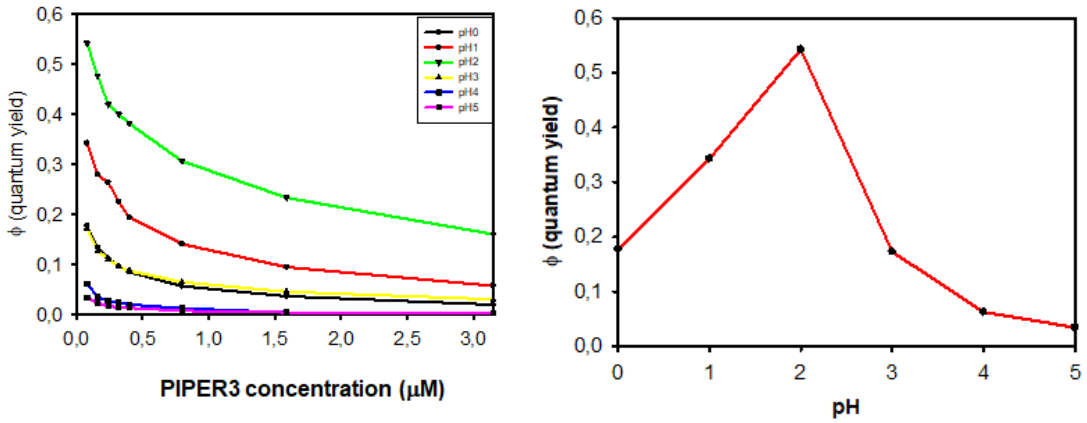

Fig.4.6 On the left: PIPER3 fluorescence quantum yield as concentration increases; on the right: PIPER3 fluorescence quantum yield at different pH

From pH 5 to 2 quantum yield increases as the pH decreases, revealing increase of the fraction of free molecule in solution, i.e. system disaggregates because of amino groups protonation causes repulsion between molecular units. On the other hand, going from pH 2 to 0 there is a

sharp quantum yield fall. This reveals that a new stimulus encouraged dye aggregation. It is likely that high ion chloride concentration in low pH solutions (derived by HCl) begin to intervene in PIPER3 aggregation. To demonstrate this hypothesis, salts with different anions were added to a controlled pH PIPER3 solution. Emission quantum yield trend as ionic strength increases is reported (Fig.4.7).

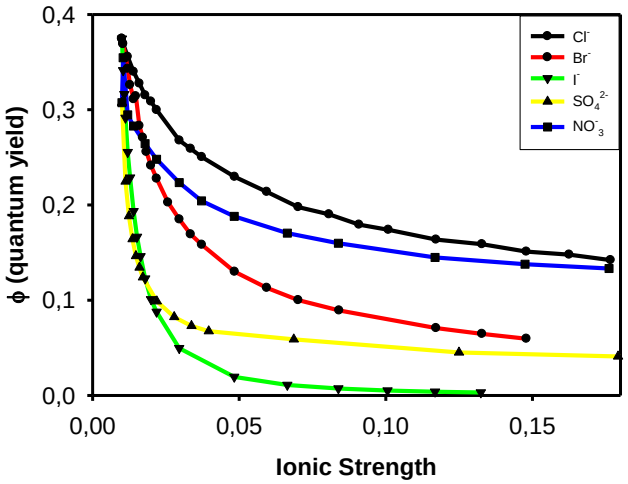

Fig.4.7 PIPER3 fluorescence quantum yield as anion concentration increases

Quantum yield decreases when the concentration of anion is increased suggesting that anions themselves participate in aggregation by shielding the repulsion of the protonated amine groups.

We demonstrate that aggregation of properly designed PDI amino derivate can be controlled by pH in water solution. As shown in Fig.4.8 the dye molecules aggregate in water because of π–π stacking interaction, causing fluorescence quenching. The system can be disaggregated and the fluorescence switched on by protonation exploiting the electrostatic repulsion between the positive cations.

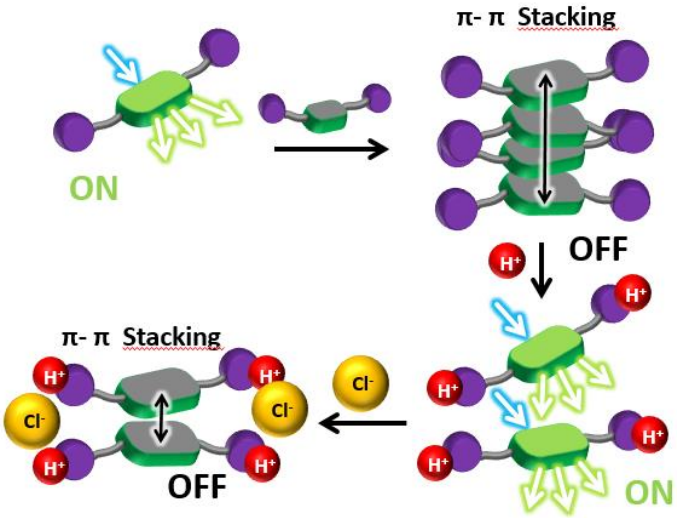

Fig.4.8 Schematic response of the system at different stimuli

Even more interestingly we observed that the protonated system can be re-assembled by increasing the concentration of anion that partially shield the positive charge of the ammonium substituents. Finally, our molecules show a unique response to protonation and anion concentration in water. These features make them very promising tools for ion sensing in view of biological and environmental applications.

In conclusion, new nanoparticles which disaggregate because of the effect of pH has been created. The free molecule fraction can be monitored by fluorescence detection. Therefore, system respond to anions that play an important role in the aggregation state. This system is potentially suitable for pH and anion sensor

4.3 Synthesis

For the synthesis of our molecules we propose an innovative and green method that involves microwave (MW) heating to achieve convenient and efficient conversion of PDA into PDI in a few minutes using glycols as solvents.

To functionalize the PDI we chosen ether and amine groups in the chain to control the aggregation by the presence of protonable groups. Amines have been chosen with a sufficiently low base dissociation constant so that protonation does not occur at too alkaline pH. In addition, the presence of these groups makes PDI derivative water soluble.

What we expect from this system is that the molecules aggregate as the concentration increases and that they disaggregate as the pH decreases.

In Fig.4.9 are reported the chains that we used to functionalize PDI derivative.

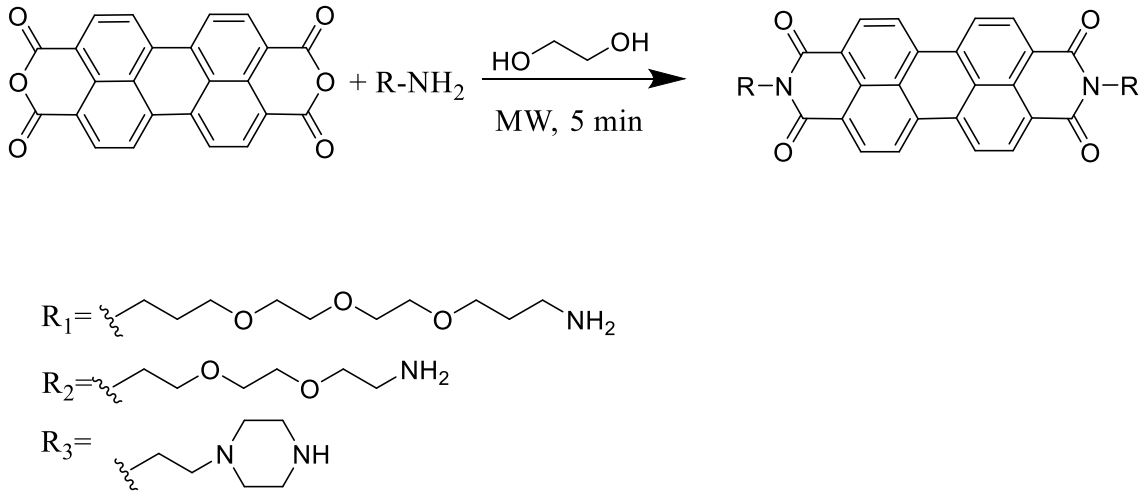

Fig.4.9 Reaction scheme of PDI derivatives

We used in all cases the same synthetic strategy: NH_2-R group (20 equivalents) has been solubilized in ethylene glycol. Subsequently perylene-3,4,9,10-tetracarboxylic dianhydride

(PTCDA) (1 equivalent) has been added. The reaction is carried out in a microwave oven at 900w for 5 minutes. At the end of the solution appears black with suspended granules. For the work out, the solution has been centrifugated for 10 minutes. The ethylene glycol is thrown and the solid is washed with water and centrifugated for 3 times. Then water is thrown the solid is washed with ethanol and centrifugated for 3 times. At the end the solid is filtered and dried under vacuum.

The product obtained by reaction with 4,7,10-Trioxa-1,13-tridecanediamine (chain R_1 in Fig.4.9) is N,N'-Bis[2-(2-(2-(3-aminopropoxy)ethoxy)ethyl]-3,4,9,10-perylenetetracarboxylic diimide (PIPER1). ESI-MS m/z calculated for $C_{44}H_{53}N_4O_{10}^+$797; obs.: 797

The product obtained by reaction with 2,2′-(Ethylenedioxy)bis(ethylamine) (chain R_2 in Fig.4.9) is N,N'-Bis[2-(2-(3-aminopropoxy)ethoxy)ethyl]-3,4,9,10-perylenetetracarboxylic diimide (PIPER2). ESI-MS m/z calculated for $C_{36}H_{37}N_4O_8^+$ 653; obs.: 653

The product obtained by reaction with 1-(2-Aminoethyl)piperazine (chain R_3 in Fig.4.9) is N,N'-bis[2-(1-piperazino)ethyl]-3,4,9,10-perylenetetracarboxylic diimide(PIPER3). ESI-MS m/z calculated for $C_{36}H_{35}N_6O_4^+$ 615; obs.: 615

4.4 PDI in water: concentration effect

Unique photophysical properties of PDI has been exploited to monitor system answer to different stimuli. Based on the above, aggregates of PDI often do not show any emission spectrum and the only signal that can be recorded is the emission of the free molecule. That is, it is possible to calculate the molar fraction of the free molecule from this equation:

where Φ is the quantum yield of the solution, Φ_m is the quantum yield of the monomer,

$$\Phi = \chi_m \Phi_m + \chi_a \Phi_a$$

Φ_a is the quantum yield of the aggregate, χ_m is the quantum yield of the monomer and χ_a is the quantum yield of the aggregate: By approximating that the free molecule has a quantum yield equal 1 and the one of aggregate equal to 0 the result is:

$$\Phi = \chi_m$$

The first stimuli that has been investigated was concentration. Indeed, as concentration increases p-p stacking interactions becomes more important and PIPER3 molecules starts to stack together in not fluorescent aggregates, as shown in Fig.4.10.

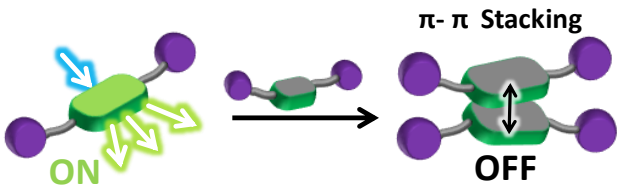

Fig.4.10 Schematic representation of concentration effect on PIPER3 aggregation

To study the behaviour in aqueous solution, stock solution of the three molecules were prepared with a concentration of $2 \cdot 10^{-4}$ M in water at pH 2 (HCl 0.01M). The first molecules that we investigated was PIPER1.

Increasing volumes (from 1μL to x μL) were taken from the stock solution and added to 2.5 mL of aqueous at pH 2 (HCl 0.01M).

In Fig.4.11 are reported absorption spectrum (on the left) and emission spectrum (on the right).

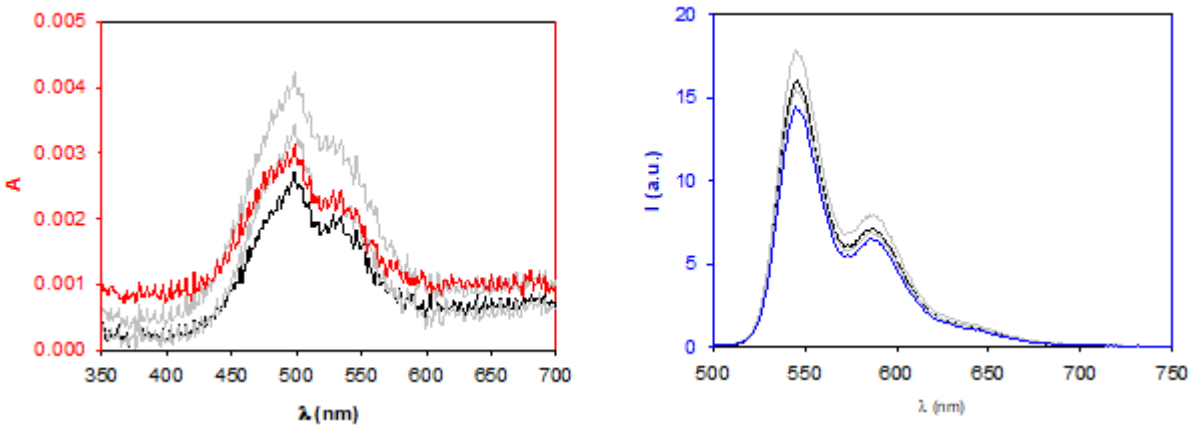

Fig.4.11 On the left: absorption spectrum of PIPER1 at pH 2. Black spectrum is the first addition, red spectrum is the last addiction. On the right: emission spectrum of PIPER1at pH 2. Black spectrum is the first addition, blue spectrum is the last addiction.

It is obvious that PIPER1 it is not soluble in these conditions. For this reason, we did not investigate it anymore.

Second molecule studied was PIPER2. Increasing volumes (from 1μL to 40 μL) were taken from the stock solution ($2 \cdot 10^{-4}$ M in water at pH 2 (HCl 0.01M)) and added to 2.5 mL of different water solutions with buffers at increasing pH (from 0 to 8).

In Fig.4.12 are reported absorption spectrum (on the left) and emission spectrum (on the right) at pH 4.

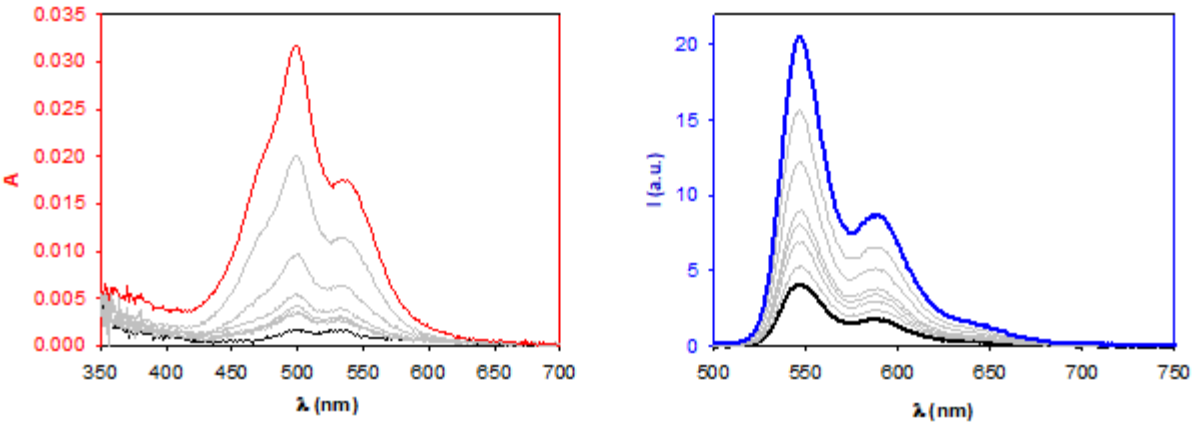

Fig.4.12 On the left: absorption spectrum of PIPER2 at pH 4. Black spectrum is the first addition, red spectrum is the last addiction. On the right: emission spectrum of PIPER2at pH 4. Black spectrum is the first addition, blue spectrum is the last addiction.

PIPER2 demonstrated to be slightly soluble in all the range of pH investigated. In Fig.4.13 is reported fluorescence quantum yields measured at increasing concentration of PIPER2 at different pH.

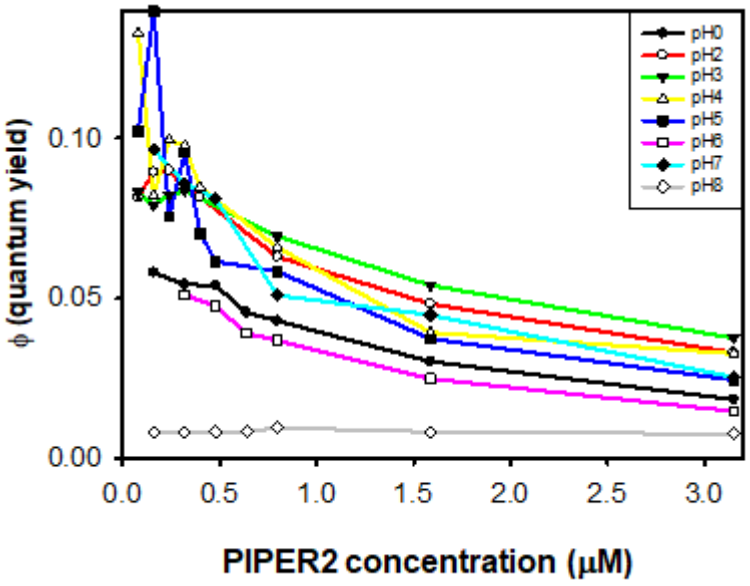

Fig.4.13 Fluorescence quantum yields measured at increasing concentration of PIPER2 at different pH.

It is observed that as concentration increases, quantum yield decreases drastically as expected. In fact, in a polar solvent such as water π–π stacking interactions between perylene core become very important and therefore the fraction of free molecules decreases more and more. Subsequently, the behaviour of PIPER3 was investigated. Increasing volumes (from 1μL to 40 μL) were taken from the stock solution ($2 \cdot 10^{-4}$ M in water at pH 2 (HCl 0.01M)) and added to 2.5 mL of different water solutions with buffers at increasing pH (from 0 to 9) In Fig.4.14 are reported absorption spectrum (on the left) and emission spectrum (on the right) at pH 3.

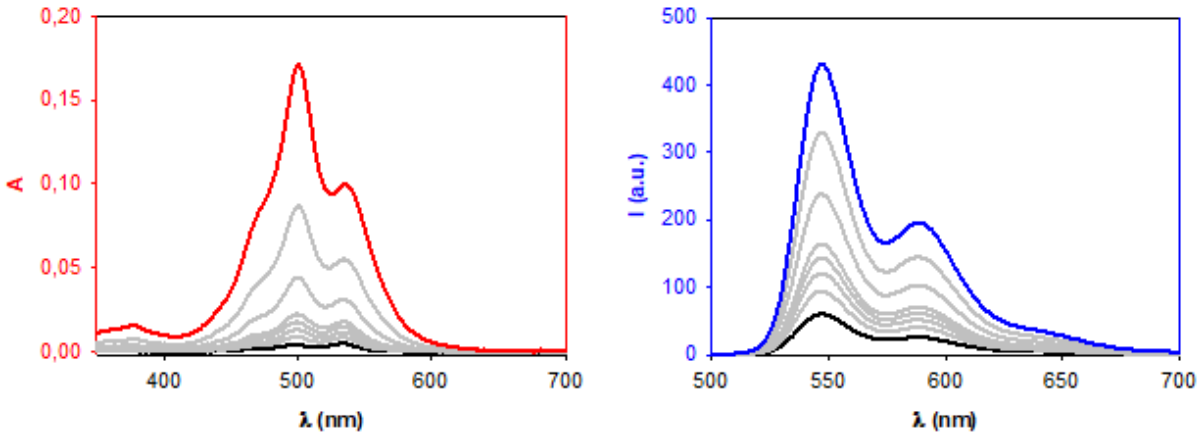

Fig.4.14 On the left: absorption spectrum of PIPER3 at pH 3. Black spectrum is the first addition, red spectrum is the last addiction. On the right: emission spectrum of PIPER3 at pH 3. Black spectrum is the first addition, blue spectrum is the last addiction.

PIPER3 demonstrated to be soluble in most the range of pH investigated. In Fig.4.15 is reported fluorescence quantum yields measured at increasing concentration of PIPER3 at different pH.

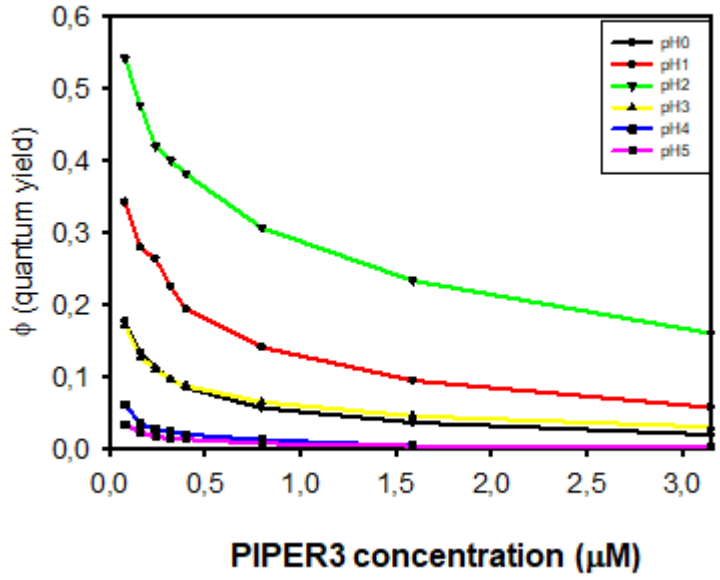

Fig.4.15 Fluorescence quantum yields measured at increasing concentration of PIPER3 at different pH.

It is observed that as concentration increases, quantum yield decreases drastically as expected. PIPER3 solubility is more pH dependent then PIPER2. Quantum yield value reaches 0.5 at pH 2 and collapses to 0.05 at pH 5. Over pH 5, quantum yield decreases so much that it is no longer possible measure quantum yield.

This behaviour is more interesting for our purpose. For this reason, our efforts focused on study PIPER3 behaviour.

4.5 PIPER3 in water: pH effect

Then, the effect of pH was studied keeping constant the concentration of PIPER3. We expected that when the pH decreases, the system disaggregates because of the protonation of the amino groups that causes electrostatic repulsion between PIPER3 molecules as shown in Fig.4.16. Consequently, decreasing pH fluorescence quantum yield should increase.

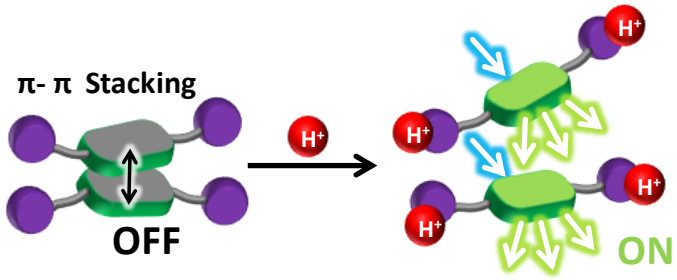

Fig.4.16 Schematic representation of pH effect on PIPER3 aggregation

PIPER3 presents four protonable nitrogen atoms, two in each chain. Because of perylene core presence between the two chains, it can be assumed that they do not influence each other. External nitrogen atom has a pKa≈5.5 and chain-connected nitrogen atom has a pKa≈11[25]. So that a small fraction of molecules will be singled charged in our experimental conditions, while most of molecules will be double charged. In Fig.4.17 is reported a logarithmic concentration diagram that shows concentration of all the species at different pH.

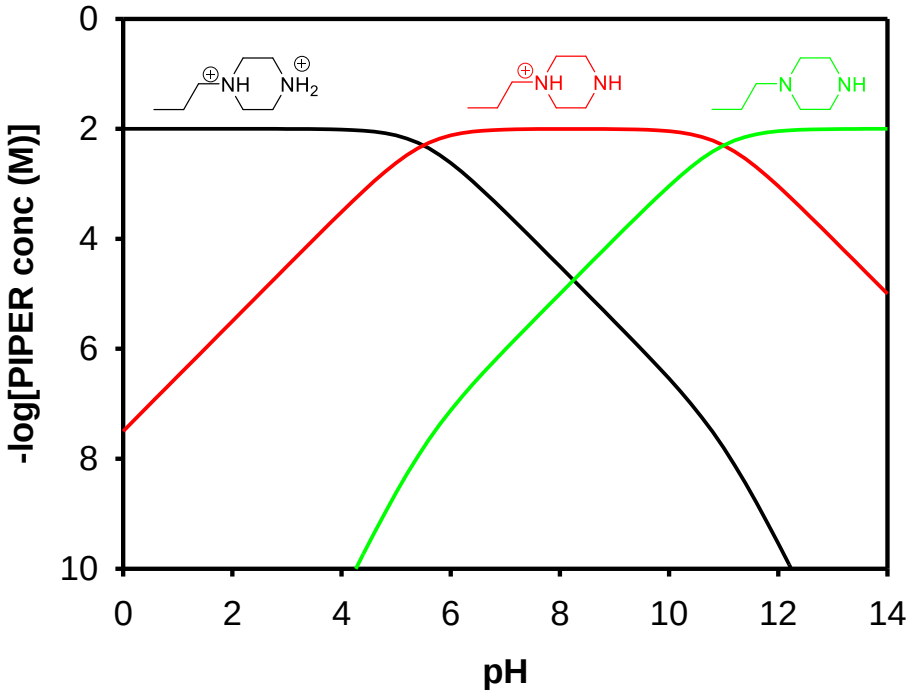

Fig.4.17 Concentration of protonated species of PIPER3 at different pH.

In Fig.4.18 is reported quantum yield of PIPER3 at $8 \cdot 10^{-8}$ M at different pH.

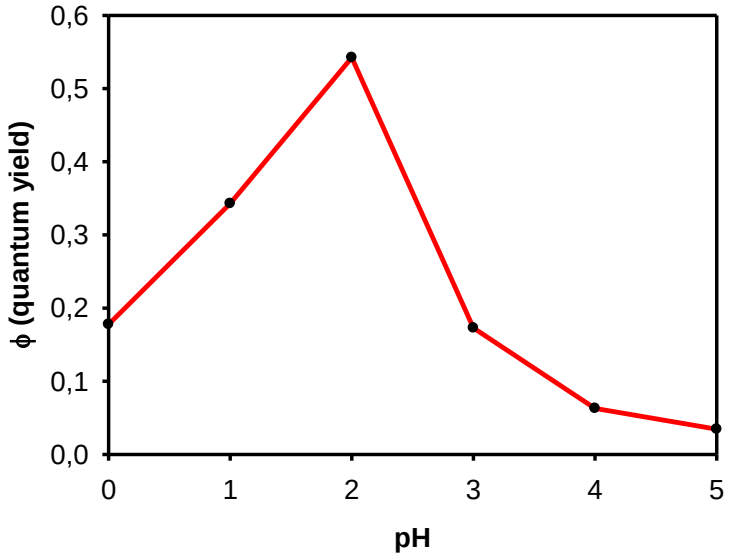

Fig.4.18 emission quantum yield of PIPER3 at different pH ($8 \cdot 10^{-8}$ M)

What is observed is that initially the quantum yield increases as the pH decreases, indicating an increase in the concentration of free molecules of PIPER3. But from pH 2 to pH 1 there is a sharp decrease in quantum yield. Then by decreasing the pH beyond a threshold, system aggregates again. This behavior can be observed at any concentration of PIPER3 and cannot be explained just considering role of pH.

In Fig.4.19 are reported molar extinction coefficient of PIPER3 at different pH. It is possible observe increasing of ratio of peak at 498 nm and at 535 nm as pH decrease, indicating aggregation of PBI molecules.

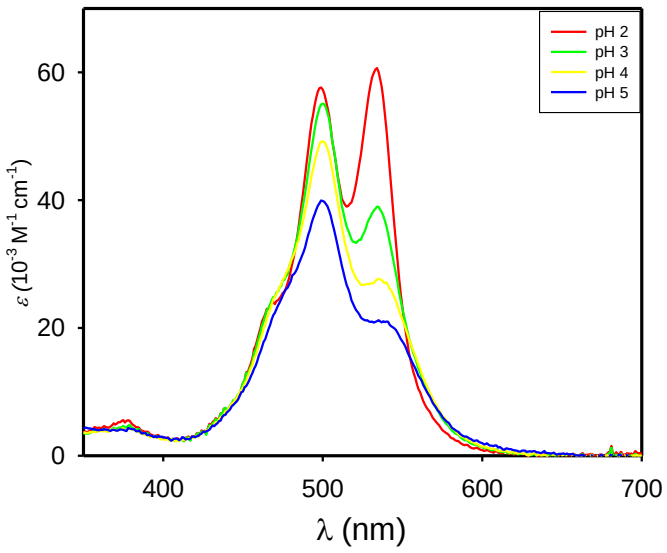

Fig.4.19 Molar extinction coefficient of PIPER3 at different pH

To understand what is happening we must take in account buffer preparation reported in Table 4.1.

Table 4.1 Buffer used for different pH

pH	Buffer
0	HCl 1M
1	HCl 0.1M
2	HCl 0.01M
3	HCl 10^{-3}M
4	Acetate buffer 0.1 M
5	Acetate buffer 0.1 M

For pH 4 and 5 common acetate buffer 0.1M have been chosen. Instead, for pH from 0 to 3 we used different concentration of HCl to regulate pH because volume of PIPER3 solution needed is so few that eventual pH change because of that can be neglected. But such high chloride ion concentration could interact with protonated amino chain of PIPER3 with electrostatic interaction. As consequence it could promote PIPER3 aggregation in water even at low pH To demonstrate this hypothesis, salts with different anions were added to a controlled pH PIPER3 solution.

4.6 PIPER3 in water: anions effect

To demonstrate influence of chloride ions on PIPER3 aggregations, salts with different anions were added to $8 \cdot 10^{-7}$ M PIPER3 solution at pH 2. In Fig.4.20 is reported fluorescence quantum yield as anion concentration is increased. To take in account the different contribution of different salts ionic strength has been chosen as parameter.

Ionic strength has been calculated with the formula:

$$I = \frac{1}{2}\sum_i m_i z_i^2$$

Where *I* is the ionic strength, m_i is concentration of ion and z_i is ionic charge. In the final count of ionic strength HCl contribution has been added.

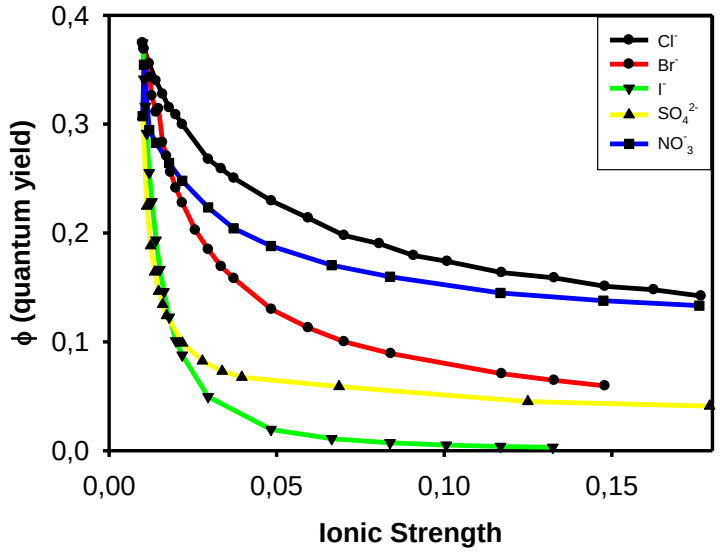

Fig.4.20 Fluorescence quantum yield of 8 ·10^{-7} M PIPER3 solution at pH 2 at different anions concentration

It is noted that in all cases the quantum yield decreases when the concentration of anion is increased. We have therefore deduced that anions participate in the aggregation. Indeed, they could interact with protonated amine groups of different chain and shield repulsion between them, as shown in Fig.4.21.

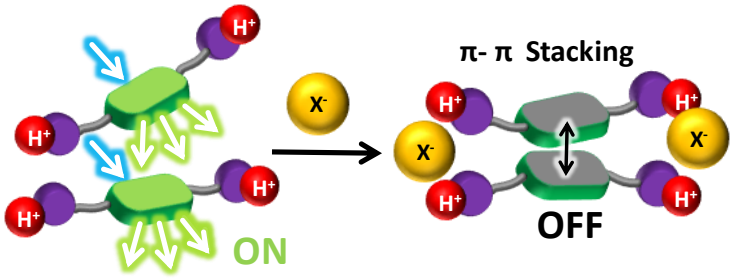

Fig.4.21 Schematic representation of anion effect on PIPER3 aggregation

4.7 Fluorescence quantum yield fitting

In the chapters above, we have synthetized water soluble PBI and studied its aggregation in water. Moreover, we have investigated how different stimuli, as concentration, pH and ionic strength, influence equilibrium between monomer species and aggregate species. Next step consist in determinate which kind of aggregation is happening. Given the fact that aggregation causes a hypsochromic shift of maximum of absorption spectrum, it is possible deduce that in water PIPER3 forms H aggregates with monodirectional sandwich-like arrangement. The two borderline cases for aggregation are the monomer-dimer model and the isodesmic model[18].

In the first one PBI molecules exist only as monomer or dimer, because after aggregation of two molecules Ka, aggregation constant value is zero. Therefore, in solution the only possible chemical equilibrium is:

$$M + M \leftrightarrow M_2$$

Where M is the monomer and M_2 is the dimer. The constant of equilibrium is

$$K_D = \frac{C_2}{C_1^2}$$

Where K_D is the equilibrium constant, C_1 is monomer concentration and C_2 is dimer concentration. Total concentration C_T of molecules is:

$$C_T = 2C_2 + C_1$$

By it, derives that:

$$C_2 = \frac{(C_T\text{-}C_1)}{2}$$

replacing this equation in the previous one it is possible to obtain the expression of C_1 as function only of C_T and K_D:

$$C_1 = \frac{\text{-}1 + \sqrt{1 + 8K_D C_T}}{4K_D}$$

The molar fraction of monomer species χ_1 can be given as:

$$\chi_1 = \frac{C_1}{C_T}$$

This equation combined with the previous one becomes:

$$\chi_1 = \frac{\text{-}1 + \sqrt{1 + 8K_D C_T}}{4K_D C_T}$$

In the isodesmic model the aggregation constant is equal for all binding event and different extended dye aggregates coexist in solution. Thus, aggregation isodesmic model can be represented as:

$$M + M \leftrightarrow M_2 \qquad C_2 = K_2 C_1^2$$

$$M_2 + M \leftrightarrow M_3 \qquad C_3 = K_3 C_2 C_1 = K_2 K_3 C_1^3$$

…

$$M_{n\text{-}1} + M \leftrightarrow M_n \qquad C_n = K_n C_{n\text{-}1} C_1 = K_2 K_3 \dots K_{n\text{-}1} K_n C_1^n$$

where C_1, C_2, C_3, . . ., C_n are the molar concentrations of monomer, dimer, trimer, and n-mer species, respectively, and K_2, K_3, K_n are the equilibrium constants for the addition of a monomer to another monomer, a dimer, and a (n-1)-mer, respectively. For the isodesmic model applies:

$$K = K_2 = K_3 = \cdots = K_n$$

Accordingly, the concentration of n-mer C_n and the total concentration of molecules C_T, respectively, can be given as:

$$C_n = K^{n\text{-}1} C_1^n$$

$$C_T = (C_1 + 2KC_1^2 + 3K^2C_1^3 + \cdots + nK^{n-1}C_1^n)$$

Considering the series expansion for 0<x<1:

$$1 + 2x + 3x^2 + \cdots + nx^{n-1} = \frac{1}{(1-x)^2}$$

The previous equation becomes:

$$C_T = \frac{C_1}{(1-KC_1)^2}$$

The solution of equation x is:

$$C_1 = \frac{2KC_T + 1 - \sqrt{4KC_T + 1}}{2K^2C_T}$$

Substituting C_1 with χ_1 (molar fraction):

$$\chi_1 = \frac{2KC_T + 1 - \sqrt{4KC_T + 1}}{2K^2C_T^2}$$

Now that we have expressed monomer molar fraction as function of total concentration and of aggregation constant it is possible fitting χ_1 trend as function of C_T and calculate K_D. Indeed, it is convenient to remember that fluorescence quantum yield can be approximated at monomer molar fraction.

Here we report PIPER3 fluorescence quantum yield as function of PIPER3 concentration at different pH. Every trend has been fitted with formula of the monomer-dimer model and the isodesmic model. In Fig.4.22 are shown different cases (blue line for monomer-dimer model and red line for isodesmic model).

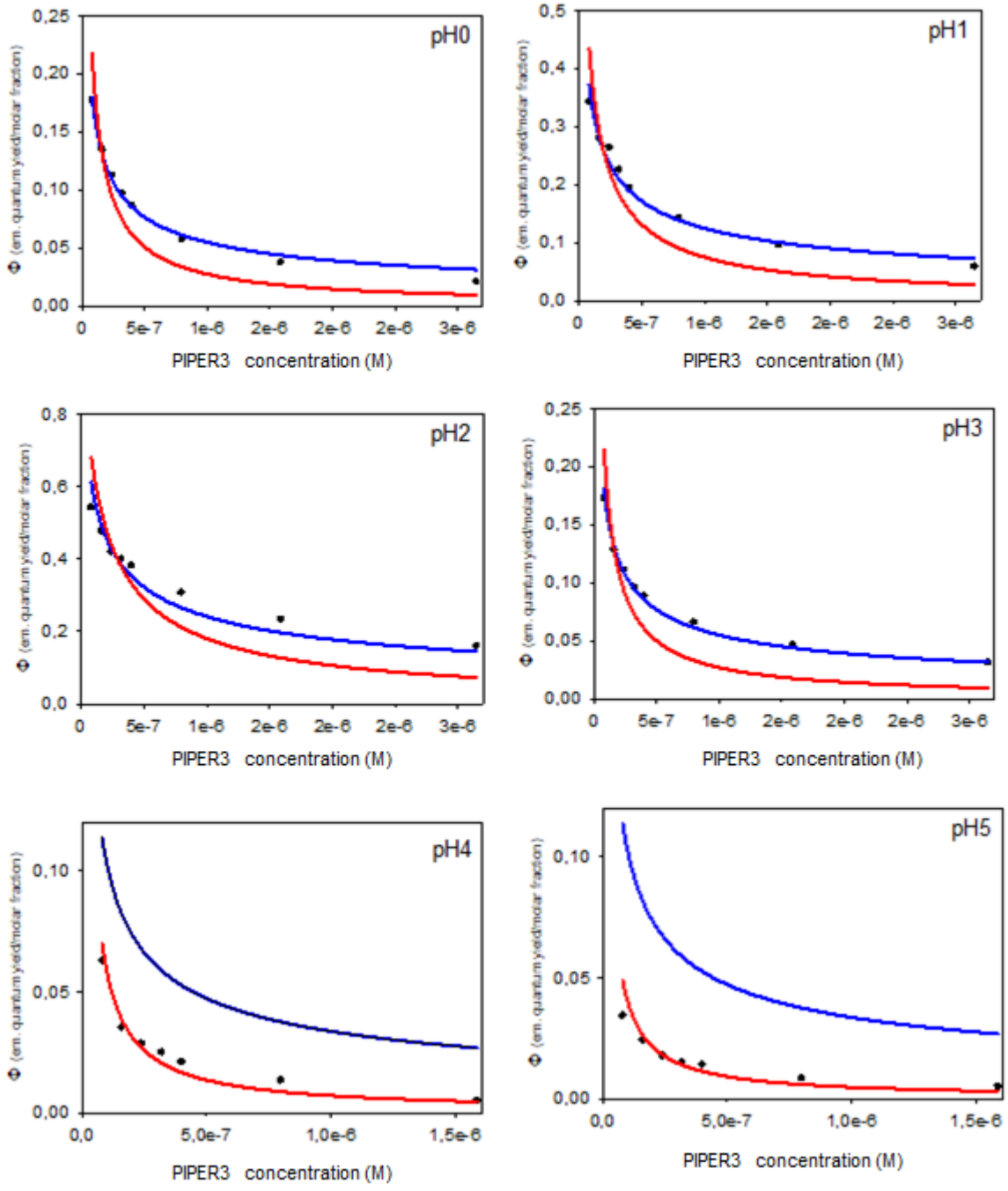

Fig.4.22 PIPER3 fluorescence quantum yield as function of concentration at different pH. Every trend has been fitted with formula of the monomer-dimer model (blue line) and the isodesmic model (red line).

It can be observed that for pH from 0 to 3 monomer-dimer model fit data indicating that equilibrium in solution is between monomer species and dimer species and that larger aggregates are not favourite. On the other hand, for pH 4 and 5 isodesmic model fit data very well. This means that aggregation is changed and that larger aggregates are favourites. Therefore, changing pH we can tune aggregation type spacing from lower pH that favours dimer, to higher pH where larger aggregates are preferred. It was also possible calculate equilibrium constant at every pH for both models. They are reported in Table 4.2

Table 4. 2 equilibrium constant calculated at every pH for both models

pH	K dimer	K isodesmic
0	$1.6 \cdot 10^8$	$3.1 \cdot 10^7$
1	$2.8 \cdot 10^7$	$9.8 \cdot 10^6$
2	$6.5 \cdot 10^6$	$3.2 \cdot 10^6$
3	$1.6 \cdot 10^8$	$3.1 \cdot 10^7$
4	$4.3 \cdot 10^8$	$1.3 \cdot 10^8$
5	$4.3 \cdot 10^8$	$2.0 \cdot 10^8$

4.8 Conclusions

In conclusion in this work we have found an innovative synthetic cheap, fast and green way for PBI amine derivates. PBI derivates have been functionalized with polar chain that makes them both water soluble and pH sensitive. They have been tested at different concentration and different pH. PIPER3 has given best results responding to concentration, PH and ionic strength. It was also possible discriminate two different aggregations with monomer-dimer model and isodesmic model. Low pH favour dimer formation, on the other hand at higher pH larger aggregates are preferred.

4.9 Bibliography

1. Würthner, F., Perylene bisimide dyes as versatile building blocks for functional supramolecular architectures. *Chem. Commun.* **2004,** (14), 1564-1579.

2. (a) Würthner, F.; Saha-Möller, C. R.; Fimmel, B.; Ogi, S.; Leowanawat, P.; Schmidt, D., Perylene bisimide dye assemblies as archetype functional supramolecular materials. *Chem. Rev.* **2015,** *116* (3), 962-1052; (b) Ford, W. E.; Kamat, P. V., Photochemistry of 3, 4, 9, 10-perylenetetracarboxylic dianhydride dyes. 3. Singlet and triplet excited-state properties of the bis (2, 5-di-tert-butylphenyl) imide derivative. *J. Phys. Chem.* **1987,** *91* (25), 6373-6380.

3. Herbst, W.; Hunger, K., Industrial organic pigments: Production, Properties. *Applications. Verlagsgesellschaft* **1997**, 201-205.

4. (a) Langhals, H., Cyclic carboxylic imide structures as structure elements of high stability. Novel developments in perylene dye chemistry. *Heterocycles* **1995,** *1* (40), 477-500; (b) Nagao, Y., Synthesis and properties of perylene pigments. *Prog. Org. Coat.* **1997,** *31* (1-2), 43-49.

5. Rossetti, L.; Franceschin, M.; Bianco, A.; Ortaggi, G.; Savino, M., Perylene diimides with different side chains are selective in inducing different G-quadruplex DNA structures and in inhibiting telomerase. *Bioorg. Med. Chem. Lett.* **2002,** *12* (18), 2527-2533.

6. Biver, T.; Criscitiello, F.; Di Francesco, F.; Minichino, M.; Swager, T.; Pucci, A., MWCNT/perylene bisimide water dispersions for miniaturized temperature sensors. *RSC Advances* **2015,** *5* (80), 65023-65029.

7. (a) Kazmaier, P. M.; Hoffmann, R., A theoretical study of crystallochromy. Quantum interference effects in the spectra of perylene pigments. *J. Am. Chem. Soc.* **1994,** *116* (21), 9684-9691; (b) Sadrai, M.; Hadel, L.; Sauers, R. R.; Husain, S.; Krogh-Jespersen, K.; Westbrook, J. D.; Bird, G. R., Lasing action in a family of perylene derivatives: singlet absorption and emission spectra, triplet absorption and oxygen quenching

constants, and molecular mechanics and semiempirical molecular orbital calculations. *The Journal of Physical Chemistry* **1992,** *96* (20), 7988-7996.
8. Chen, Z.; Fimmel, B.; Würthner, F., Solvent and substituent effects on aggregation constants of perylene bisimide π-stacks–a linear free energy relationship analysis. *Organic & biomolecular chemistry* **2012,** *10* (30), 5845-5855.
9. Rademacher, A.; Märkle, S.; Langhals, H., Lösliche Perylen-Fluoreszenzfarbstoffe mit hoher Photostabilität. *Chem. Ber.* **1982,** *115* (8), 2927-2934.
10. (a) Beckers, E. H.; Meskers, S. C.; Schenning, A. P.; Chen, Z.; Würthner, F.; Janssen, R. A., Charge separation and recombination in photoexcited oligo (p-phenylene vinylene): Perylene bisimide arrays close to the marcus inverted region. *The Journal of Physical Chemistry A* **2004,** *108* (34), 6933-6937; (b) Hippius, C.; van Stokkum, I. H.; Zangrando, E.; Williams, R. M.; Würthner, F., Excited State Interactions in Calix [4] arene− Perylene Bisimide Dye Conjugates: Global and Target Analysis of Supramolecular Building Blocks. *The Journal of Physical Chemistry C* **2007,** *111* (37), 13988-13996.
11. Würthner, F.; Thalacker, C.; Diele, S.; Tschierske, C., Fluorescent J-type aggregates and thermotropic columnar mesophases of perylene bisimide dyes. *Chemistry–A European Journal* **2001,** *7* (10), 2245-2253.
12. Würthner, F.; Saha-Möller, C. R.; Fimmel, B.; Ogi, S.; Leowanawat, P.; Schmidt, D., Perylene Bisimide Dye Assemblies as Archetype Functional Supramolecular Materials. *Chemical Reviews* **2015**.
13. Veldman, D.; Chopin, S. p. M.; Meskers, S. C.; Groeneveld, M. M.; Williams, R. M.; Janssen, R. A., Triplet formation involving a polar transition state in a well-defined intramolecular perylenediimide dimeric aggregate. *The Journal of Physical Chemistry A* **2008,** *112* (26), 5846-5857.
14. Giaimo, J. M.; Gusev, A. V.; Wasielewski, M. R., Excited-state symmetry breaking in cofacial and linear dimers of a green perylenediimide chlorophyll analogue leading to ultrafast charge separation. *J. Am. Chem. Soc.* **2002,** *124* (29), 8530-8531.
15. Martin, R. B., Comparisons of indefinite self-association models. *Chem. Rev.* **1996,** *96* (8), 3043-3064.
16. De Greef, T. F.; Smulders, M. M.; Wolffs, M.; Schenning, A. P.; Sijbesma, R. P.; Meijer, E., Supramolecular polymerization. *Chem. Rev.* **2009,** *109* (11), 5687-5754.
17. Zhao, D.; Moore, J. S., Nucleation–elongation: a mechanism for cooperative supramolecular polymerization. *Organic & biomolecular chemistry* **2003,** *1* (20), 3471-3491.
18. Chen, Z.; Lohr, A.; Saha-Möller, C. R.; Würthner, F., Self-assembled π-stacks of functional dyes in solution: structural and thermodynamic features. *Chem. Soc. Rev.* **2009,** *38* (2), 564-584.
19. Yin, H.; Zhou, Z.; Huang, J.; Zheng, R.; Zhang, Y., Temperature-induced micelle to vesicle transition in the sodium dodecylsulfate/dodecyltriethylammonium bromide system. *Angew. Chem. Int. Ed.* **2003,** *42* (19), 2188-2191.
20. Leng, J.; Egelhaaf, S. U.; Cates, M. E., Kinetics of the micelle-to-vesicle transition: aqueous lecithin-bile salt mixtures. *Biophys. J.* **2003,** *85* (3), 1624-1646.
21. Zhang, L.; Eisenberg, A., Multiple morphologies and characteristics of "crew-cut" micelle-like aggregates of polystyrene-b-poly (acrylic acid) diblock copolymers in aqueous solutions. *J. Am. Chem. Soc.* **1996,** *118* (13), 3168-3181.
22. Zhang, X.; Chen, Z.; Würthner, F., Morphology control of fluorescent nanoaggregates by co-self-assembly of wedge-and dumbbell-shaped amphiphilic perylene bisimides. *J. Am. Chem. Soc.* **2007,** *129* (16), 4886-4887.
23. Kim, H.-J.; Kim, T.; Lee, M., Responsive nanostructures from aqueous assembly of rigid− flexible block molecules. *Acc. Chem. Res.* **2010,** *44* (1), 72-82.
24. Shimizu, T.; Masuda, M.; Minamikawa, H., Supramolecular nanotube architectures based on amphiphilic molecules. *Chem. Rev.* **2005,** *105* (4), 1401-1444.
25. Rossetti, L.; Franceschin, M.; Schirripa, S.; Bianco, A.; Ortaggi, G.; Savino, M., Selective interactions of perylene derivatives having different side chains with inter-and intramolecular G-quadruplex DNA structures. A correlation with telomerase inhibition. *Bioorg. Med. Chem. Lett.* **2005,** *15* (2), 413-420.

Chapter 5: Self-assembled biocompatible fluorescent nanoparticles for bioimaging

5.1 Introduction

Fluorescence imaging is a not invasive, highly sensitive, technique that allows biological organisms investigation with high three-dimensional resolution in real time, by making use of suitable fluorescent contrast agents[1]. Tailored fluorescent nanoparticles[2], promise to surpass conventional molecular probes as fluorescent markers especially as far as sensitivity is concerned. Indeed, nanoparticles potentially emit a much brighter signal with respect to molecules, in the same excitation conditions.

Most of nanoparticles proposed and applied for bio-imaging, result from the assembly of molecular fluorophores in an organized nanostructure. These assemblies may be stabilized: (i) via covalent bonds, hence by modifying the molecular fluorophores chemical structure with reactive terminal groups [e.g., alkoxysilanes[3], acrylates[4], or thiolates[5]] to form polymer/copolymer or by (ii) non-covalent interactions, involving either molecular fluorophores or additional groups specifically introduced in the structure to achieve supramolecular polymerization[6].

Size control is a critical issue in nanoparticles design. It can be achieved by exploiting surfactants or stabilizers as templates, that physically or chemically incorporate molecules, typically giving a compartmentalized nanostructure (e.g., core-shell).

Nevertheless, achieving an enhanced brightness is still a challenge[7].

Brightness is the parameter used to compare emission intensity. It is defined as:

$$B = \varepsilon \cdot \Phi$$

where ε is the molar absorption coefficient (and is a measure of the ability of nanoparticles to absorb the excitation light) and Φ is the quantum fluorescence yield (i.e. efficiency with which the molecules that have absorbed light emit photons). The brightness therefore represents a mixed parameter that considers both the absorption and the emission of light capacity of the chromophore. So, it can be used to evaluate intensity of fluorescence signal. Nanoparticles advantage lies in high number of molecular fluorophores in each one, that drastically increases nanoparticles molar extinction coefficient. Indeed, it is calculated as:

$$\varepsilon_{NP} = < n > \varepsilon_{MF}$$

Where ε_{NP} is molar extinction coefficient of nanoparticles, $<n>$ is the average number of molecular fluorophores in nanoparticles and ε_{MF} is molar extinction coefficient of molecular

fluorophores inside nanoparticles. But without a rational design, molecular fluorophores normally aggregate in highly densely packed nanoparticles, undergoing strong fluorescence quenching, a process which reduces drastically their emission quantum yield This phenomenon known as aggregation caused quenching[8], typically occurs in self-assembled multi-fluorophoric systems and it is the result of short-range interactions between molecular fluorophores. It can be prevented, at least in part, by spacing the molecular fluorophores[9] by incorporating them in an inactive matrix (e.g., silica) as in typical dye-doped nanoparticles. A major drawback of this strategy is the drastic reduction of emitting molecules density in nanoparticles and consequently, of the molar extinction coefficient of dye doped nanoparticles with respect to the matrix-free ones. The challenge is to devise new synthetic strategies allowing the highest possible number of fluorophores to be packaged, without this resulting in a drastic drop in photophysical properties.

5.2 Summary

Here we describe the synthesis and the properties of a new family of molecular fluorophores, which are water insoluble and do not suffer from aggregation caused quenching. Moreover, we demonstrate that a rational design of the molecular structure allows us to achieve a molecular unit that self-organizes in highly bright, and fluorescent nanoparticles which are very stable in PBS (phosphate buffered saline) solution.

In designing the new molecular fluorophores, our attention was attracted by the N-(7-Nitrobenz-2-oxa-1,3-diazol-4-yl) (NBD) dye derivatives[10]. This family of dyes has interesting properties for imaging applications.

In particular the synthetic precursor NBD chloride is cheap, and it is easily conjugated with amine derivatives, yielding fluorescent dyes featuring absorption and emission in the visible range, large Stokes shift and good quantum yields.

Unfortunately, emission of NBD derivative in the aggregated form is often low and it is almost completely quenched in aqueous environment[10a]. We reasoned that such limitation could be overcome by the introduction of a triphenylphosphazene group in the NBD structure. This group has been reported to result into(i) a red shift of both the absorption and luminescence maxima,(ii) an increase of the Stokes-shift and (iii) an increase of the luminescence intensity[11]. Three different NBD-triarylphosphazene derivatives were prepared in high yields with straightforward procedures. Here we report synthesis of the most interesting NBD-triarylphosphazene. 4-Chloro-7-nitrobenzo-2-oxa-1,3-diazole (Cl-NBD) was the starting point to synthetize a stable and fluorescent trisphosphazene (NBD-PhM) (Fig.5.1).

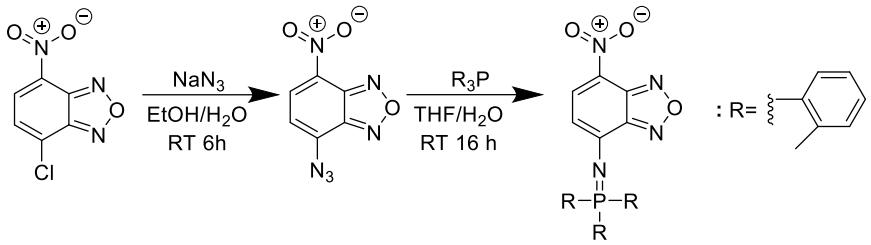

Fig.5.1 Reaction scheme of NBD-PhM

Nanoparticles (NBD-PhM_NPs) were prepared via nanoprecipitation in the presence of Pluronic F127 as a stabilizer in water. Nanoparticles presence was demonstrated by dynamic light scattering (DLS) and transmission electron microscopy (TEM) (Fig.5.2).

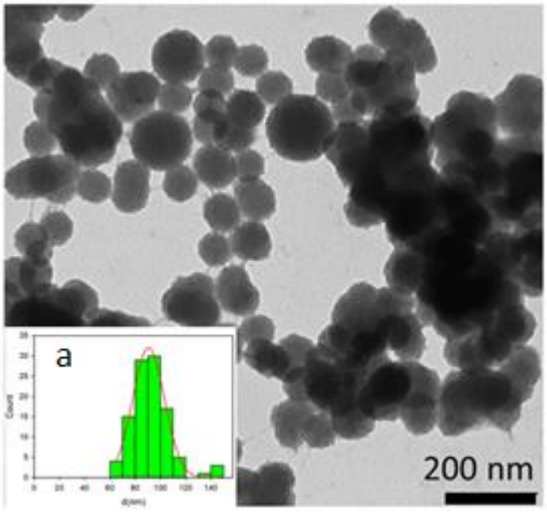

Fig.5.2 TEM images of NBD-PhM_NPs; a) Size distribution[1]

NBD-PhM and nanoparticles were characterized via UV-Vis absorption spectroscopy and steady-state and time resolved fluorescence spectroscopy. Result are in reported Table5.1.

Table5.2 Photophysical properties of NBD-PhM and nanoparticles

Compound	NBD-PhM in CH_2Cl_2	NP in H_2O
$\lambda_{max,abs}$	488 nm	480 nm
ε_{max}	32.600	29.300
$\lambda_{max,flu}$	526 nm	536 nm
QY	0.65	0.31
<n>	-	$1.1 \cdot 10^6$
B	$2.1 \cdot 10^5$	$1.0 \cdot 10^{10}$

Nanoparticles brightness results about six order of magnitude higher then molecular precursor one. This demonstrate that nanoparticles are suitable for bio-imaging, they were incubated with living HeLa cells and their ability to label the cells was demonstrated via confocal scanning fluorescence microscopy (Fig.5.3). Finally, toxicity assays demonstrated the high biocompatibility of the NPs (Fig.5.3).

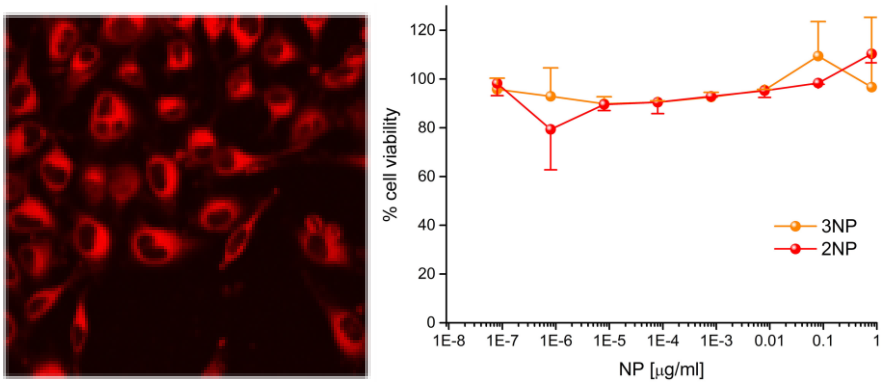

Fig.5.3 On the left: Fluorescence signal of NBD-PhM nanoparticles in cells. On the right: Cytotoxicity of NBD-PhM nanoparticles

In conclusion we believe that these highly bright, nanoparticles represent a promising platform for designing new versatile multifunctional nanoprobes.

5.3 Synthesis

For molecular fluorophores synthesis NBD chloride (NBD-Cl) has been chosen as precursor because is quite inexpensive and it is easily conjugated with amine derivatives, yielding fluorescent dyes featuring absorption and emission in the visible range, large Stokes shift and good quantum yields.

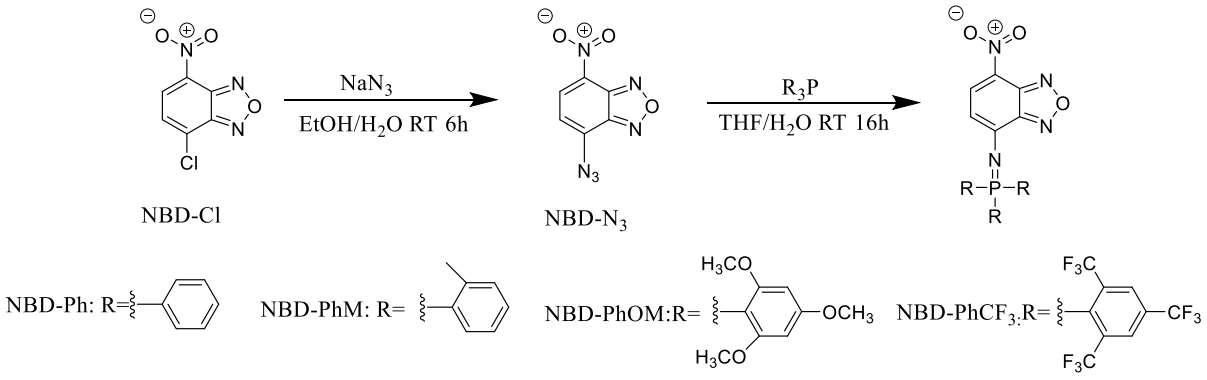

Fig. 5.4 Reaction scheme of NBD derivatives

Synthetic pathway for molecular fluorophores has been reported in Fig.5.4. For the first step into a flask, covered with an aluminium foil and containing NaN_3 (0.350 g, 5.39 mM) dissolved in a EtOH/H_2O mixture (1:1 v/v, 20 mL), a solution of NBD-Cl (0.5 g, 2.505 mM) in EtOH (40 mL) was added dropwise within a 1 h period. The reaction was left stirring for 6 h at room temperature. Subsequently, the solvent was removed under reduced pressure and crude was

purified via column chromatography on silica gel using petroleum ether/AcOEt 4:6 as eluent. The product NBD-N_3 was obtained as an orange solid in 90% yield. Subsequently into a flask, covered with aluminum foil and containing 1 (0.1 g, 0.485 mM) and the desired phosphine (3 eq.) dissolved in THF (8 mL), H_2O (2.6 mL, 145.553 mM) was added at once and left to react overnight under stirring. The formed solid was filtered-off, washed with cold THF and dried giving the final product as an orange solid with quantitative yield.

Synthesis has been carried out by Professor Mancin at University of Padova, Department of Chemistry.

Phosphazene has been decorated with three phenyl rings (NBD-Ph) in order to prevent aggregation caused quenching of nitrobenzene-2-oxa-1,3-diazole moiety. Then, phenyl substituent has been chosen to tailor photophysical properties. Indeed, methoxy, in NBD-PhMO, is a strong electron donating group, methyl, in NBD-PhM slightly an electron donating group and 3-fluoromethyl in NBD-PhCF_3 is a strong electron withdrawing group. The first two create a “pull-push” system with nitro group. “Pull-push” systems can stabilize charge-separated excited states and emission is red-shifted as consequence. On the other hand, 3-fluoromethil groups have the reverse effect, so emission in blue-shift.

5.4 Photophysical properties of the molecules in DCM

NBD derivatives were characterized via UV-Vis absorption spectroscopy and steady-state and time resolved fluorescence spectroscopy in dichloromethane. UV-Vis absorption spectra and normalized fluorescence are shown in Fig.5.5. Photophysical properties are summarized in Table 5.2.

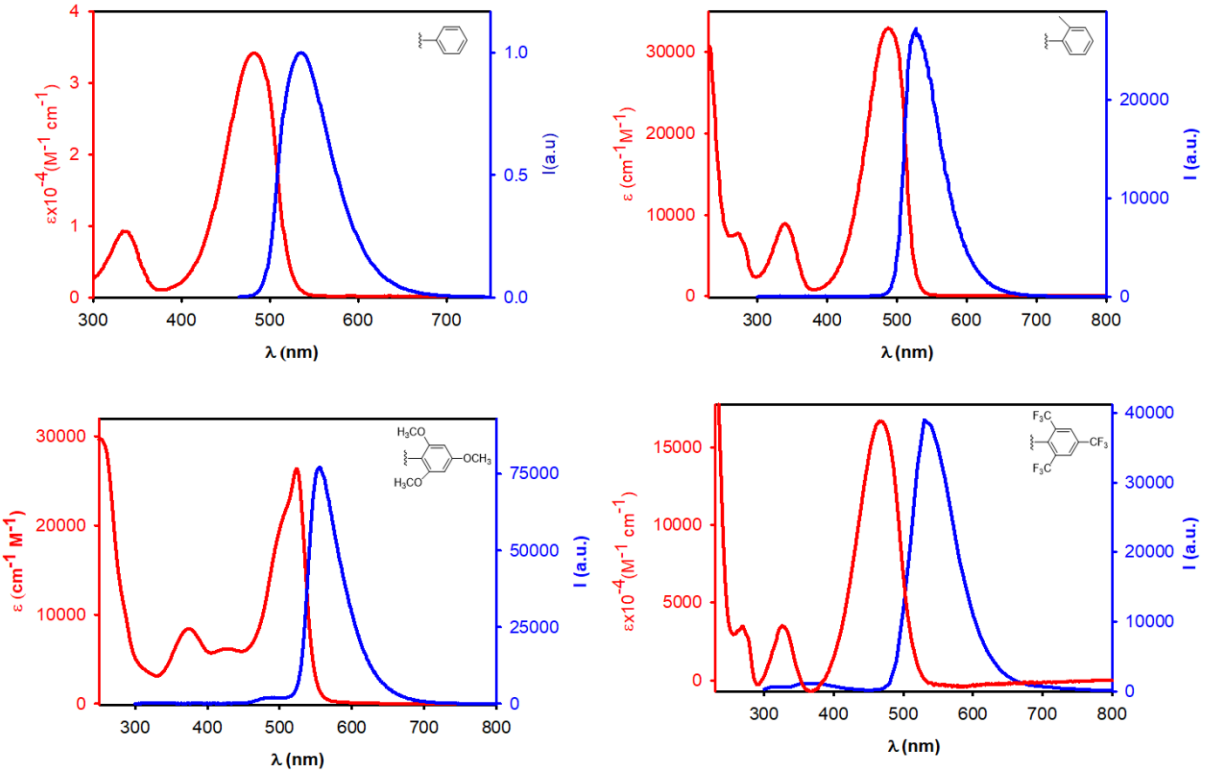

Fig.5.5 Absorption (red line) and fluorescent (blue line) spectra of a) NBD-Ph; b) NBD-PhM; c) NBD-PhOM; d) NBD-PhCF₃.

Table 5.2 Photophysical properties of molecular dyes in DCM.

Name	Substituent	$\lambda_{max,abs}$ (nm)	ε_{max} ($M^{-1}cm^{-1}$)	$\lambda_{max,em}$ (nm)	QY	τ (ns)	Exited state energy (eV)	Stokes-shift (eV)
NBD-Ph	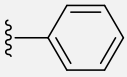	482	34,300	536	0.50	5.7	0.26	2.44
NBD-PhM	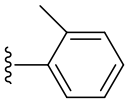	488	32,600	526	0.65	7.7	0.18	2.45
NBD-PhOM	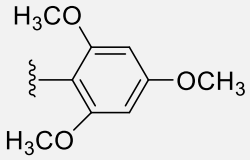	524	26,200	555	0.09	4.2	0.13	2.30
NBD-PhCF₃	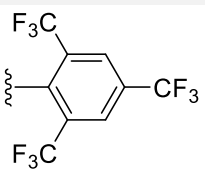	467	16,600	533	0.72	7.7	0.32	2.49

The absorption spectrum of NBD-Ph shows a maximum at λ = 482 nm (ε = 34,300 $M^{-1}cm^{-1}$) while the fluorescence band presents a peak at 536 nm. Fluorescence quantum yield results 0.50 and the excited state lifetime is 5.7 ns.

These bands are attributed to an electronic transition with charge transfer character, then they are affected by the polarity of substituents. Introduction of methyl group on phenyl substituent, in NBD-PhM, produces a shift of the absorption maximum to 488 nm and of the fluorescence to 526 nm. It is interesting to observe that going from NBD-Ph to NBD-PhM, the energy of the lowest singlet excited state changes from 2.44 eV for NBD-Ph to 2.45 eV for NBD-PhM. This means that there is a little increase, even if electronic effect of methyl group, a weak electron donor, should promote singlet excited state stabilization. On the other hand, a relevant decrease of the Stokes shift from 0.26 to 0.18 eV occurs. This indicates that the effect of the methylation is to increase the hindrance of the bulky triphenylphosphazene substituents on the phosphorous atom. It reduces reorganization conformational degree of the excited states and this causes the Stokes shift decrease and lowest singlet excited state energy increase. The rigidification effect due to the bulkier substituents also affects the fluorescence quantum yield and the excited state lifetime that rise, with respect to NBD-Ph, to QY = 0.65 and τ = 7.7 ns in NBD-PhM. Instead, the substitution of each of the three phenyl rings with three strong electron donor methoxy groups to give NBD-PhOM produces a large red-shift both of the absorption band, λ = 524 nm (ε = 26,200 $M^{-1}cm^{-1}$) and of the fluorescence maximum λ= 555 nm, corresponding to an energy decrease of the transition to 2.30 eV. The further increase of the hindrance of the phosphazene substituents in NBD-PhOM with respect to NBD-PhM leads to a decrease of the Stokes-shift to 0.13 eV. On the other hand, the presence of the electron rich trimethoxy phenyl group causes a decrease of the fluorescence QY to 0.09 and of the excited state lifetime to τ = 4.2 ns.

In the end, the substitution of each of the three phenyl rings with three strong electron withdrawing 3-fluoromethyl groups to give NBD-PhCF_3 produces a blue-shift of absorption band, λ = 467 nm (ε = 16,600 $M^{-1}cm^{-1}$) of the fluorescence maximum λ = 533 nm corresponding to an energy increase of the transition to 2.49 eV. Then, excited state has access to energy surplus that allows him to reach a new reorganization conformational, as demonstrated by the considerable increase of the SS to 0.32 eV. Presence of 3-fluoromethyl groups increase fluorescence QY to 0.72 and of the excited state lifetime to τ = 7.7 ns.

5.5 Preparation and characterization of nanoparticles

Dye molecules NBD-Ph, NBD-PhM, NBD-PhOM and NBD-PhCF$_3$ are water insoluble and nanoparticles were prepared by nanoprecipitation[6c]. A small volume (10 μL) of a THF solution of NBD-Ph, NBD-PhM, NBD-PhOM and NBD-PhCF$_3$ (2 mg/ml) and the surfactant Pluronic F127 (20 mg/mL) was rapidly injected into 2.5mL of Millipore water under vigorous stirring. The reaction vial was kept open to atmospheric air to allow complete organic solvent evaporation. After 2 h of stirring, a precipitate was formed in the case of compound NBD-Ph and NBD-PhCF$_3$, while transparent, coloured suspensions were obtained for samples containing NBD-PhM and NBD-PhOM. The formation of nanoparticles constituted by NBD-PhM and NBD-PhOM was demonstrated by dynamic light scattering (DLS), transmission electron microscopy (TEM) and fluorescence microscopy (FM). Photophysical and chemical-physical properties have been reported in Table 5.3.

Table 5.3 Photophysical and chemical-physical properties of NBD-PhM and NBD-PhOM nanoparticles

Name	$\lambda_{max,abs}$ (nm)	ε_{max} ($M^{-1}cm^{-1}$)	$\lambda_{max,em}$ (nm)	QY	τ (ns)	$\langle n \rangle$	B ($M^{-1}cm^{-1}$)	d DLS (nm)	d TEM (nm)
NBD-PhM NPs	480	29,300	536	0.31	1.01	$1.1 \cdot 10^6$	$1 \cdot 10^{10}$	128	91±13
NBD-PhOM NPs	520	17,800	556	0.01	0.77	$1.6 \cdot 10^5$	$2.8 \cdot 10^7$	140	54 ± 9

DLS measurements are showed in Fig.5.6 and it is possible observe the presence of a quite monodisperse single population of both nanoparticles. DLS of NBD-PhM nanoparticles shows a single population with a diameter of 128 nm and PdI = 0.11. For NBD-PhOM nanoparticles DLS reports a single population with a diameter of 140 nm and PdI = 0.06. The size distribution of the two samples is shown in Fig. 5.6. DLS measurements were performed after dilution of the nanoparticles suspension in phosphate-buffered saline (PBS) solution (1:50, v/v). After such a dilution, surfactant Pluronic F127 concentration resulted 0.13μM, more than three order of magnitude below the critical micelles concentration (cmc = 0.3mM at r.t.) (Rampazzo et al., 2011). In order to exclude the formation of nanoparticles constituted by the surfactant (micelles that, on the other hand, have been reported to show size of tens of nm), a blank sample was prepared following the same procedure used for NBD-PhM and -PhOM nanoparticles. No relevant scattering signal was detected in the case of the blank samples, confirming the absence of NPs.

The size distribution of NBD-PhM and -PhOM nanoparticles was also investigated by TEM: representative images of the two samples are shown in Fig.5.6 with the histogram obtained by

measuring the size of the nanoparticles in the images with the software Image J. NBD-PhM nanoparticles size obtained by fitting data with a Gaussian model results 91 ± 13 nm. Using the same procedure NBD-PhOM nanoparticles, the size results 54 ± 9 nm. Diameter of NBD-PhM nanoparticles measured by TEM is consistent with the hydrodynamic diameter measured by DLS. Instead, a significant difference was observed in the case of NBD-PhOM nanoparticles. The larger hydrodynamic diameter measured by DLS for this latter sample revealed a partial aggregation of NBD-PhOM nanoparticles in water.

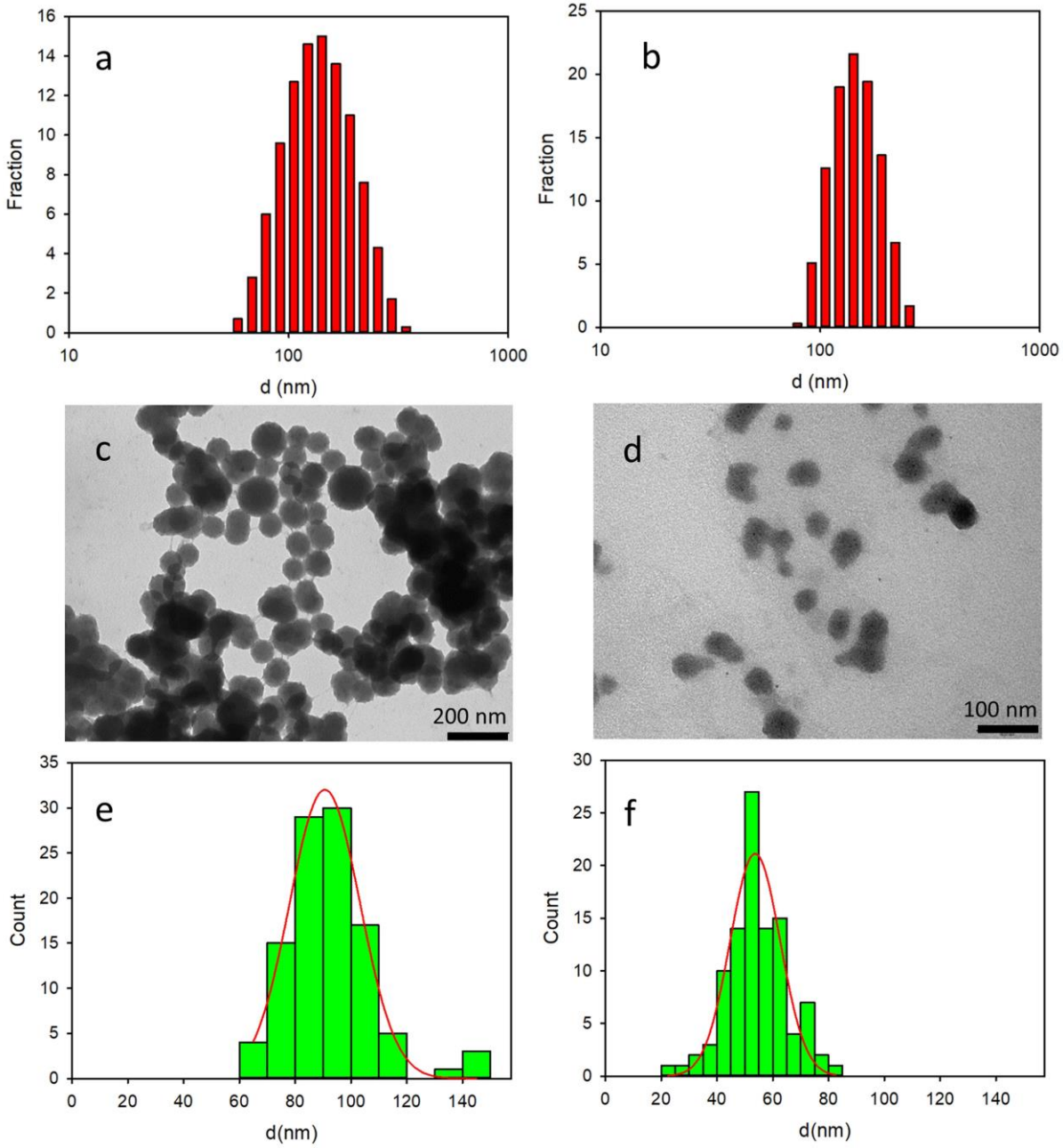

Fig.5.6 Top: size distribution obtained by DLS analysis of NBD-PhM nanoparticles (a) and NBD-PhOM nanoparticles (b). Center: representative TEM images of NBD-PhM (c) and NBD-PhOM (d). Bottom: size distribution resulting from the analysis of the TEM images of NBD-PhM nanoparticles (e) and NBD-PhOM nanoparticles (f).

The photophysical characterization of NBD-PhM and NBD-PhOM nanoparticles was performed in PBS and results are summarized in Table 5.3.

Photophysical properties of NBD-PhM and NBD-PhOM nanoparticles are shown in Fig.5.7 together with Photophysical properties of molecular dye. The molar extinction coefficient was calculated for the molecules NBD-PhM and NBD-PhOM in nanoparticles considering their average concentration.

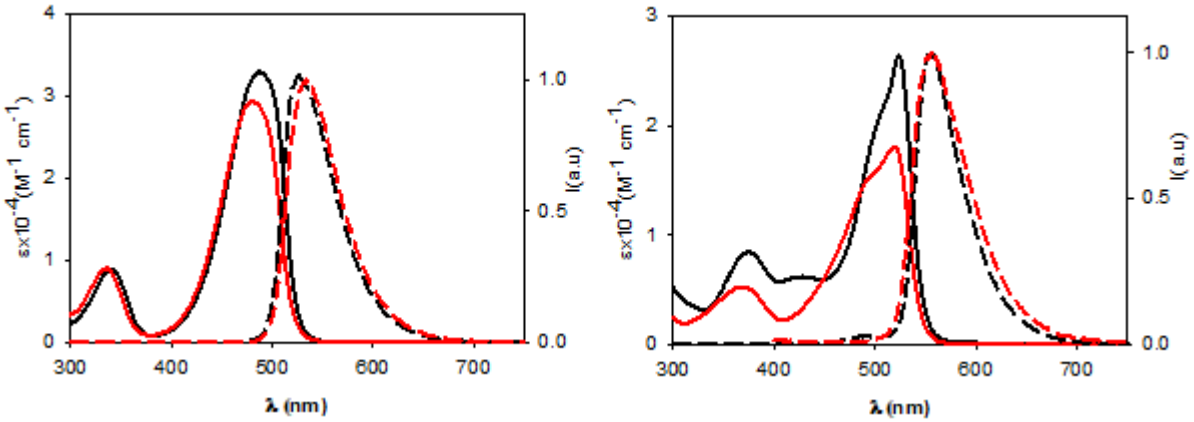

Fig.5.7 On the right: Absorption spectra (continuous line) and fluorescent spectra (dash line) of NBD-PhM (black line) and NBD-PhM nanoparticles. On the left: Absorption spectra (continuous line) and fluorescent spectra (dash line) of NBD-PhOM (black line) and NBD-PhOM nanoparticles.

The absorption spectrum of NBD-PhM nanoparticles shows a maximum at λ = 480 nm and ε = 29,300 $M^{-1}cm^{-1}$. If we compare these data with molecular dye photophysical properties (λ = 482 nm and ε = 34,300 $M^{-1}cm^{-1}$) it results clear that aggregation in nanoparticles has only a minor effect on the absorption properties of the dye molecules that undergo only a modest hypsochromic shift and a moderate decrease of ε.

The absorption band of NBD-PhOM nanoparticles has a maximum at λ = 520 nm and ε = 17,800 $M^{-1}cm^{-1}$. Also, in this case, photophysical properties of molecular dye aggregated in nanoparticles do not change significatively compared to molecular dye in solution (λ = 524 nm and ε = 26,200 $M^{-1}cm^{-1}$).

The fluorescence band of NBD-PhM nanoparticles presents a peak at 536 nm, as the corresponding molecular dye. The fluorescence band of NBD-PhOM nanoparticles has at maximum at λ = 556 nm, close to molecular dye value (555 nm).

On the contrary, nanoparticles formation had strong effect on the fluorescence quantum yield of NBD-PhM and NBD-PhOM.

NBD-PhM maintains in the nanoparticles an acceptable quantum yield (QY = 0.31) while NBD-PhOM undergoes strong aggregation induced quenching (QY = 0.01). This observation suggests that the introduction of methyl on the bulky tri(phenyl)phosphazene group is suitable to decrease the intermolecular electronic interactions in the nanoparticles by reducing the overlap of the molecular orbitals of the fluorescent NBD units. Nevertheless, the presence of

electron donating tri-methoxyphenyl groups is known to cause fluorescence quenching because of the formation of charge-transfer nonfluorescent excited states[13]. Fluorescence anisotropy measurements demonstrated that the quenching effect is enhanced by excitation energy migration inside the nanoparticles[14]. Indeed, NBD-PhM and NBD-PhOM molecular dyes showed in a high viscosity medium like propylene glycol, quite a high value of fluorescence anisotropy r. For NBD-PhM is 0.21 and for NBD-PhOM is 0.23 at r.t.). On the contrary, the two fluorophores immobilized in the nanostructure showed a fluorescence anisotropy which is zero both for NBD-PhM and NBD-PhOM nanoparticles. The complete depolarization observed in nanoparticles is in contrast with the lack of rotational freedom of the fluorophores in the nanostructures and can be explained only by considering a fast depolarization involving the homo-energy transfer processes[8]. Time resolved fluorescence measurements (time correlated single photon counting, TCSPC) showed that the spectral changes observed upon nanoparticles formation were due to the presence, in the nanoparticles, of populations of fluorophores experiencing different environments.

If the sample possess more than one lifetime multi-exponential decay are observed and the amplitude-weighted lifetime of the fluorophore is then given by

$$< \tau > = \frac{\sum B_i \tau_i}{\sum B_i}$$

where B_i is the pre-exponential factor and can be used to represent the fraction of fluorophores with lifetime τ_i.

Triple-exponential decays were observed both in the case of NBD-PhM and NBD-PhOM nanoparticles. Data collected for NBD-PhM nanoparticles are τ_1 = 0.62 ns, B_1 = 4,132, τ_2 = 2.44, B_2 = 372, τ_3 = 7.81, B_3 = 156 and average excited lifetime was calculated to be <τ> = 1.01 ns. For NBD-PhOM resulted were τ_1= 0.46 ns, B_1 = 3,196, τ_2 = 1.45, B_2 = 1,085, τ_3 = 6.16, B_3 = 44 and average excited lifetime < τ > = 0.77 ns. This result agrees with the low fluorescence QY measured for NBD-PhOM nanoparticles.

Dye molecules number per particles was calculated as

$$n_{dye} = \frac{V_{mol\ NP}}{V_{mol\ dye}}$$

Where n_{dye} is number of dyes in nanoparticles, V_{molNP} is nanoparticles molar volume and V_{moldye} dye molar volume.

Sphere equation and Avogadro number have calculated nanoparticles molar volume, as shown:

$$V_{mol\ NP} = \frac{\pi}{6} d^3 N$$

where *d* is TEM diameter in dm and *N* is Avogadro number.

Dye molar volume has been calculated as:

$$V_{\text{mol dye}} = V_{\text{molec dye}} N$$

where $V_{molecdye}$ is dye molecular volume that has been calculated with an online Molecular Volume Calculator. Molecular volume of NBD-PhM results 380.9 $Å^3$ and for NBD-PhOM is 533.6 $Å^3$. Adopting previous equations, it is obtained that molar volume for NBD-PhM and NBD-PhOM are 0.23and 0.32 L mol^{-1}, respectively. Instead, molar volume for NBD-PhM and NBD-PhOM nanoparticles result were $2.4 \cdot 10^5$ and $5.0 \cdot 10^4$ L mol^{-1}. Hence NBD-PhM and NBD-PhOM nanoparticles contain about $1.1 \cdot 10^6$ and $1.6 \cdot 10^5$ dye molecules, respectively.

Now, considering these values and the previous equation it is possible evaluate the order of magnitude of the fluorescence brightness of nanoparticles. The brightness of NBD-PhM nanoparticles results to be $1 \cdot 10^{10}$ $M^{-1}cm^{-1}$ while NBD-PhM molecular dye is about $2.1 \cdot 10^4$ $M^{-1}cm^{-1}$. Then, nanoprecipitation has increased brightness of six order of magnitude. For NBD-PhOM nanoparticles brightness is about $2.8 \cdot 10^7$ $M^{-1}cm^{-1}$ while for NBD-PhOM molecular dye is $2.6 \cdot 10^3$ $M^{-1}cm^{-1}$. Then, even if nanoprecipitation has caused a strong quenching of molecular dye, brightness results increased of four order of magnitude.

5.6 Size Characterization by fluorescence optical tracking

Thanks to their outstanding brightness, NBD-PhM nanoparticles could be detected, in suspension, as single bright spots in a conventional fluorescence microscope. Using an acquisition time as short as 10 ms, the nanoparticles appeared motionless as shown in Fig.5.8 (inset). Thermal motions of nanoparticles were clearly observed by time lapsed acquisition (4,000 frames). The resulting movies were analysed to measure the linear displacements of the NPs using the plugin MOSAIC for Image J[15]. The displacements were then plotted in a histogram as shown in Fig.5.8.

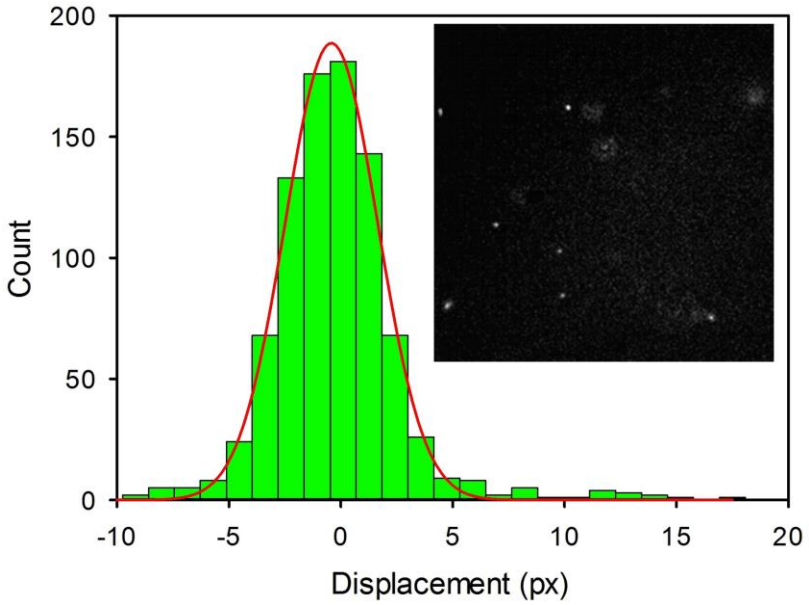

Fig.5.8 Histogram of the linear displacements measured for NBD-PhM nanoparticles in PBS by fluorescence microscopy for a time interval δt = 10ms. Images were acquired in time-lapse mode (4,000 frames) with an EMCCD Camera and processed with Image J (Plug-in MOSAIC). Each pixel corresponds to 0.16μm. A representative image of the NP (bright white spots) is shown in the inset.

We would like to stress that an analogous experiment was performed for a NBD-PhOM sample and no emissive spots attributable to nanoparticles diffusion could be observed. This demonstrated that these nanoparticles were not bright enough to be detectable as individual objects by fluorescence microscopy. Moreover, by comparing two samples of NBD-PhM and NBD-PhOM with the same concentration (8μg/ml), the average intensity measured within a frame in the case of NBD-PhM nanoparticles were more than 2 orders of magnitude higher than the one measured for NBD-PhOM nanoparticles.

The diffusion coefficient of NBD-PhM nanoparticles were calculated by tracking the fluorescent nanoparticles via fluorescence microscopy considering the following equations:

$$P(x,t) = \frac{1}{\sqrt{4\pi Dt}} \exp\left(-\frac{(x-x_0)^2}{4Dt}\right)$$

Where P is the probability of observing a displacement of an nanoparticle from the position x to the position x_0 after a time delay t and D is the diffusion coefficient of the nanoparticles that, in a spherical approximation, is dependent on the diameter d of the nanoparticles according to the Stokes-Einstein equation:

$$D = \frac{kT}{3\pi nd}$$

Where k is the Boltzmann constant, T the temperature and n is the viscosity of the medium. Image sequences were processed to acquire the positions of the nanoparticles in each frame and to identify individual nanoparticles movements. The trajectories of the nanoparticles were used to get the displacement (in pixels, where a pixel corresponds to 0.16μm) of the

nanoparticles in the frame acquisition time interval (t = $1.0 \cdot 10^{-2}$ s). Data represented in the histogram were fitted with a Gaussian model, as shown in Fig.5.8, to obtain the diffusion coefficient D = $2.65 \cdot 10^{-12}$ $m^2 s^{-1}$; a value that corresponds to nanoparticles with an average diameter of 160 nm in good agreement with the DLS analysis.

5.7 Biological experiments

To demonstrate their efficacy as a fluorescent probe, NBD-PhM nanoparticles and of NBD-PhOM nanoparticles were incubated with HeLa cells at the relatively low dose of 80 ng/ml at 37◦C. After confocal microscopy analysis of 20 h, cells (Fig.5.9) revealed an intense structured of NBD-PhM nanoparticles signal within the cell cytoplasm, suggesting endosomal nanoparticles internalization, although cytoplasmatic internalization cannot be completely ruled out. As expected, based on their weak intrinsic fluorescence, of NBD-PhOM nanoparticles cellular signal was much weaker.

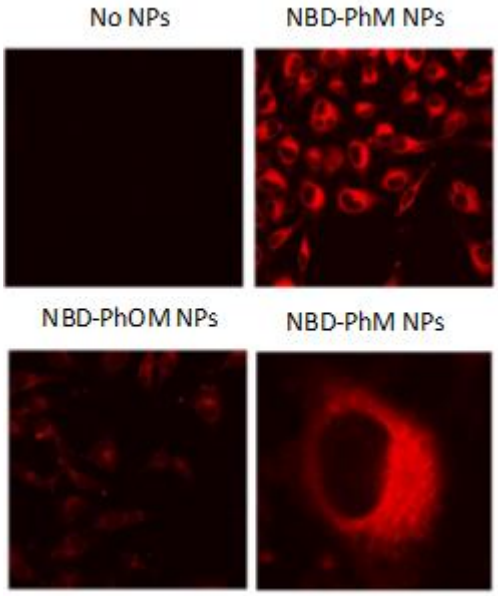

Fig.5.9 Fluorescence signal of NPs in cells. HeLa cells grown on glass cover slips were incubated for 20 h with no nanoparticles (medium alone), NBD-PhM or NBD-PhOM nanoparticles, as indicated and analysed by fluorescence confocal microscopy with the same instrumental.

MTS assays showed that both of NBD-PhM nanoparticles and of NBD-PhOM nanoparticles are devoid of the toxic effects on HeLa cells of up to 1μg/ml (Fig.5.10).

Biological experiments were performed by Prof. Papini at University of Padova, Department of Biomedical Science.

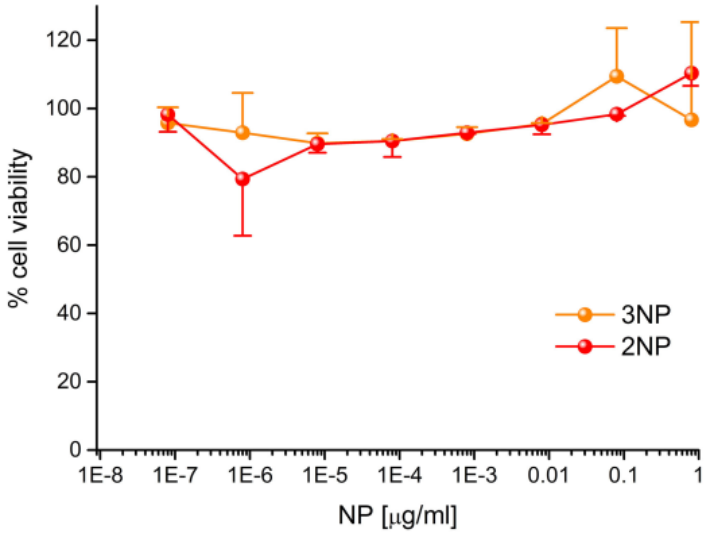

Fig.5.10 Cytotoxicity of NBD-PhM and NBD-PhOM nanoparticles. HeLa cells were incubated for 20 h with the indicated doses of NPs in DMEM at 37□C and subjected to MTS assay. Data, expressed as % of control (no nanoparticles) samples, are mean ± SE (N=3).

5.8 Conclusions

Summarizing the results so far discussed, we found that molecule NBD-Ph does not form stable nanoparticles upon nanoprecipitation in our experimental conditions. On the contrary, nanoprecipitation of molecules NBD-PhM and NBD-PhOM leads to nanoparticles formation. The quantum yield of molecule NBD-PhOM, which is already low in the non-aggregated form, further decreases upon assembly in the nanoparticles. As a result, the brightness of NBD-PhOM nanoparticles is about two orders of magnitude lower than the one of NBD-PhM nanoparticles. Such a difference is so relevant that while NBD-PhM nanoparticles can be clearly tracked at the single NP level in solution at very low concentration by fluorescence microscopy, NBD-PhOM nanoparticles cannot be observed with the same technique.

Most interestingly, the brightness of NBD-PhM nanoparticles could be estimated to be about six orders of magnitude higher than an NBD water soluble derivative used as reference. These results demonstrate that rational design of the molecular precursor is fundamental for producing stable and strongly bright nanoparticles by self-assembly.

Cellular experiments proved that NBD-PhM nanoparticles are suitable to be used as fluorescent contrast agents for bioimaging, also thanks to their good biocompatibility. We believe that our approach can be extended to other molecules and surfactants in order to tune the excitation/emission wavelength as well as the nanoparticles size.

5.9 Bibliography

1. (a) Rio-Echevarria, I. M.; Tavano, R.; Causin, V.; Papini, E.; Mancin, F.; Moretto, A., Water-soluble peptide-coated nanoparticles: control of the helix structure and enhanced differential binding to immune cells. *J. Am. Chem. Soc.* **2010,** *133* (1), 8-11; (b) Chen, K. H.; Boettiger, A. N.; Moffitt, J. R.; Wang, S.; Zhuang, X., Spatially resolved, highly multiplexed RNA profiling in single cells. *Science* **2015,** *348* (6233), aaa6090; (c) Grimm, J. B.; English, B. P.; Chen, J.; Slaughter, J. P.; Zhang, Z.; Revyakin, A.; Patel, R.; Macklin, J. J.; Normanno, D.; Singer, R. H., A general method to improve fluorophores for live-cell and single-molecule microscopy. *Nat. Methods* **2015,** *12* (3), 244; (d) Lee, M. H.; Kim, J. S.; Sessler, J. L., Small molecule-based ratiometric fluorescence probes for cations, anions, and biomolecules. *Chem. Soc. Rev.* **2015,** *44* (13), 4185-4191; (e) Mei, J.; Leung, N. L.; Kwok, R. T.; Lam, J. W.; Tang, B. Z., Aggregation-induced emission: together we shine, united we soar! *Chem. Rev.* **2015,** *115* (21), 11718-11940; (f) Tang, Y.; Lee, D.; Wang, J.; Li, G.; Yu, J.; Lin, W.; Yoon, J., Development of fluorescent probes based on protection–deprotection of the key functional groups for biological imaging. *Chem. Soc. Rev.* **2015,** *44* (15), 5003-5015; (g) Proetto, M. T.; Anderton, C. R.; Hu, D.; Szymanski, C. J.; Zhu, Z.; Patterson, J. P.; Kammeyer, J. K.; Nilewski, L. G.; Rush, A. M.; Bell, N. C., Cellular delivery of nanoparticles revealed with combined optical and isotopic nanoscopy. *ACS nano* **2016,** *10* (4), 4046-4054; (h) Xu, W.; Zeng, Z.; Jiang, J. H.; Chang, Y. T.; Yuan, L., Discerning the chemistry in individual organelles with small-molecule fluorescent probes. *Angew. Chem. Int. Ed.* **2016,** *55* (44), 13658-13699.

2. (a) Jiang, K.; Sun, S.; Zhang, L.; Lu, Y.; Wu, A.; Cai, C.; Lin, H., Red, green, and blue luminescence by carbon dots: full-color emission tuning and multicolor cellular imaging. *Angew. Chem. Int. Ed.* **2015,** *54* (18), 5360-5363; (b) Ma, K.; Mendoza, C.; Hanson, M.; Werner-Zwanziger, U.; Zwanziger, J.; Wiesner, U., Control of ultrasmall sub-10 nm ligand-functionalized fluorescent core–shell silica nanoparticle growth in water. *Chem. Mater.* **2015,** *27* (11), 4119-4133; (c) Pyo, K.; Thanthirige, V. D.; Kwak, K.; Pandurangan, P.; Ramakrishna, G.; Lee, D., Ultrabright luminescence from gold nanoclusters: rigidifying the Au (I)–thiolate shell. *J. Am. Chem. Soc.* **2015,** *137* (25), 8244-8250; (d) Wolfbeis, O. S., An overview of nanoparticles commonly used in fluorescent bioimaging. *Chem. Soc. Rev.* **2015,** *44* (14), 4743-4768; (e) Müller, B. J.; Zhdanov, A. V.; Borisov, S. M.; Foley, T.; Okkelman, I. A.; Tsytsarev, V.; Tang, Q.; Erzurumlu, R. S.; Chen, Y.; Zhang, H., Nanoparticle-Based Fluoroionophore for Analysis of Potassium Ion Dynamics in 3D Tissue Models and In Vivo. *Adv. Funct. Mater.* **2018,** *28* (9), 1704598.

3. (a) Rio-Echevarria, I. M.; Selvestrel, F.; Segat, D.; Guarino, G.; Tavano, R.; Causin, V.; Reddi, E.; Papini, E.; Mancin, F., Highly PEGylated silica nanoparticles:“ready to use” stealth functional nanocarriers. *J. Mater. Chem.* **2010,** *20* (14), 2780-2787; (b) Rampazzo, E.; Bonacchi, S.; Genovese, D.; Juris, R.; Sgarzi, M.; Montalti, M.; Prodi, L.; Zaccheroni, N.; Tomaselli, G.; Gentile, S., A versatile strategy for signal amplification based on core/shell silica nanoparticles. *Chemistry–A European Journal* **2011,** *17* (48), 13429-13432; (c) Selvestrel, F.; Moret, F.; Segat, D.; Woodhams, J. H.; Fracasso, G.; Echevarria, I. M. R.; Baù, L.; Rastrelli, F.; Compagnin, C.; Reddi, E., Targeted delivery of photosensitizers: efficacy and selectivity issues revealed by multifunctional ORMOSIL nanovectors in cellular systems. *Nanoscale* **2013,** *5* (13), 6106-6116.

4. Chen, J.; Zeng, F.; Wu, S.; Su, J.; Tong, Z., Photoreversible Fluorescent Modulation of Nanoparticles via One-Step Miniemulsion Polymerization. *Small* **2009,** *5* (8), 970-978.

5. (a) Battistini, G.; Cozzi, P. G.; Jalkanen, J.-P.; Montalti, M.; Prodi, L.; Zaccheroni, N.; Zerbetto, F., The erratic emission of pyrene on gold nanoparticles. *ACS nano* **2007,** *2* (1), 77-84; (b) Bonacchi, S.; Cantelli, A.; Battistelli, G.; Guidetti, G.; Calvaresi, M.; Manzi, J.; Gabrielli, L.; Ramadori, F.; Gambarin, A.; Mancin, F., Photoswitchable NIR-Emitting Gold Nanoparticles. *Angew. Chem. Int. Ed.* **2016,** *55* (37), 11064-11068.

6. (a) Génin, E.; Gao, Z.; Varela, J. A.; Daniel, J.; Bsaibess, T.; Gosse, I.; Groc, L.; Cognet, L.; Blanchard-Desce, M., "Hyper-bright" Near-Infrared Emitting Fluorescent Organic Nanoparticles for Single Particle Tracking. *Adv. Mater.* **2014,** *26* (14), 2258-2261; (b) Montalti, M.; Battistelli, G.; Cantelli, A.; Genovese, D., Photo-tunable multicolour fluorescence imaging based on self-assembled fluorogenic nanoparticles. *Chem. Commun.* **2014,** *50* (40), 5326-5329; (c) Reisch, A.; Klymchenko, A. S., Fluorescent polymer nanoparticles based on dyes: seeking brighter tools for bioimaging. *Small* **2016,** *12* (15), 1968-1992; (d) Faucon, A.; Benhelli-Mokrani, H.; Fleury, F.; Dutertre, S.; Tramier, M.; Boucard, J.; Lartigue, L.; Nedellec, S.; Hulin, P.; Ishow, E., Bioconjugated fluorescent organic nanoparticles targeting EGFR-overexpressing cancer cells. *Nanoscale* **2017,** *9* (45), 18094-18106; (e) Boucard, J.; Linot, C.; Blondy, T.; Nedellec, S.; Hulin, P.; Blanquart, C.; Lartigue, L.; Ishow, E., Small Molecule-Based Fluorescent Organic Nanoassemblies with Strong Hydrogen Bonding Networks for Fine Tuning and Monitoring Drug Delivery in Cancer Cells. *Small* **2018,** *14* (38), 1802307.

7. (a) Ow, H.; Larson, D. R.; Srivastava, M.; Baird, B. A.; Webb, W. W.; Wiesner, U., Bright and stable core− shell fluorescent silica nanoparticles. *Nano Lett.* **2005,** *5* (1), 113-117; (b) Wu, C.; Szymanski, C.; McNeill, J., Preparation and encapsulation of highly fluorescent conjugated polymer nanoparticles. *Langmuir* **2006,** *22* (7), 2956-2960; (c) Sun, G.; Berezin, M. Y.; Fan, J.; Lee, H.; Ma, J.; Zhang, K.; Wooley, K. L.; Achilefu, S., Bright fluorescent nanoparticles for developing potential optical imaging contrast agents. *Nanoscale* **2010,** *2* (4), 548-558; (d) Cho, E. B.; Volkov, D. O.; Sokolov, I., Ultrabright fluorescent silica mesoporous silica nanoparticles: control of particle size and dye loading. *Adv. Funct. Mater.* **2011,** *21* (16), 3129-3135; (e) Volkov, D. O.; Cho, E.-B.; Sokolov, I., Synthesis of ultrabright nanoporous fluorescent silica discoids using an inorganic silica precursor. *Nanoscale* **2011,** *3* (5), 2036-2043; (f) Trofymchuk, K.; Reisch, A.; Didier, P.; Fras, F.; Gilliot, P.; Mely, Y.; Klymchenko, A. S., Giant light-harvesting nanoantenna for single-molecule detection in ambient light. *Nature photonics* **2017,** *11* (10), 657; (g) Melnychuk, N.; Klymchenko, A. S., DNA-functionalized dye-loaded polymeric nanoparticles: ultrabright FRET platform for amplified detection of nucleic acids. *J. Am. Chem. Soc.* **2018,** *140* (34), 10856-10865.

8. Genovese, D.; Bonacchi, S.; Juris, R.; Montalti, M.; Prodi, L.; Rampazzo, E.; Zaccheroni, N., Prevention of self-quenching in fluorescent silica nanoparticles by efficient energy transfer. *Angew. Chem. Int. Ed.* **2013,** *52* (23), 5965-5968.

9. Mak, C. C.; Pomeranc, D.; Sanders, J. K.; Montalti, M.; Prodi, L., A versatile synthetic strategy for construction of large oligomers: binding and photophysical properties of a nine-porphyrin array. *Chem. Commun.* **1999,** (12), 1083-1084.

10. (a) Fery-Forgues, S.; Fayet, J.-P.; Lopez, A., Drastic changes in the fluorescence properties of NBD probes with the polarity of the medium: involvement of a TICT state? *J. Photochem. Photobiol. A: Chem.* **1993,** *70* (3), 229-243; (b) Mukherjee, S.; Chattopadhyay, A.; Samanta, A.; Soujanya, T., Dipole moment change of NBD group upon excitation studied using solvatochromic and quantum chemical approaches: implications in membrane research. *The Journal of Physical Chemistry* **1994,** *98* (11), 2809-2812.

11. (a) Bodige, S. G.; Méndez-Rojas, M. A.; Watson, W. H., Structure and properties of N-phenylmaleimide derivatives. *J. Chem. Crystallogr.* **1999,** *29* (1), 57-66; (b) Nifant'ev, E.; Belov, S.; Komlev, I.; Petukhov, V.; Semenov, M.; Mezentseva, G.; Tavrizova, M.; Ponomareva, O., Synthesis and investigation of new organophosphorus dyes of green and red luminescence. *Russ. J. Gen. Chem.* **2008,** *78* (3), 383; (c) Joshi, S.; Kumari, S.; Bhattacharjee, R.; Sakhuja, R.; Pant, D. D., Estimation of ground and excited state dipole moments of synthesized coumarin derivative [N-(2-oxo-2H-chromen-4-yl) imino] triphenyl-phosphorane. *J. Mol. Liq.* **2014,** *200*, 115-119; (d) De Xu, S.; Fang, C. H.; Tian, G. X.; Chen, Y.; Dou, Y. H.; Kou, J. F.; Wu, X. H., Reduction of 4-azidonaphthalimide with different phosphine ligands and exploration of their spectroscopic properties. *J. Mol. Struct.* **2015,** *1102*, 197-202; (e) Ragab, S. S.; Thapaliya, E. R.; Zhang, Y.; Tang, S.; McMahan, J. B.; Syed, S.; Captain, B.; Raymo, F. M., Synthesis in living cells with the assistance of supramolecular nanocarriers. *RSC Advances* **2016,** *6* (39), 32441-32445.

12. Pitto-Barry, A.; Barry, N. P., Pluronic® block-copolymers in medicine: from chemical and biological versatility to rationalisation and clinical advances. *Polymer Chemistry* **2014,** *5* (10), 3291-3297.

13. Shukla, D.; Wan, P., Product studies of electron transfer from dimethoxybenzene and trimethoxybenzene to photoexcited xanthenium cations in S1 in aqueous acid solution. *J. Photochem. Photobiol. A: Chem.* **1993,** *76* (1-2), 47-53.

14. (a) Bonacchi, S.; Rampazzo, E.; Montalti, M.; Prodi, L.; Zaccheroni, N.; Mancin, F.; Teolato, P., Amplified fluorescence response of chemosensors grafted onto silica nanoparticles. *Langmuir* **2008,** *24* (15), 8387-8392; (b) Jiang, Y.; McNeill, J., Light-harvesting and amplified energy transfer in conjugated polymer nanoparticles. *Chem. Rev.* **2016,** *117* (2), 838-859.
15. Sbalzarini, I. F.; Koumoutsakos, P., Feature point tracking and trajectory analysis for video imaging in cell biology. *J. Struct. Biol.* **2005,** *151* (2), 182-195.

Chapter 6: Design and synthesis of molecular dye self-assembled nanoparticles

6.1 Introduction

In the last years interest in molecular nanoparticles is growing. This new approach stands out for its versatility. Indeed, it is potentially possible to create new nanoparticles from any organic molecule, paving the way for new materials. Possibility of encapsulating organic molecules in nanostructures has attracted interest in particular for organic dye[1]. Today, interaction of light and matter has been exploited for different applications, as photovoltaic devices, solar cells and biomedical imaging. Organic molecules have been surpassed by inorganic material because are more photostable and water soluble. But, molecular nanoparticles can overcome these limits. When one decides to work with molecular nanoparticles, it is important consider that interactions of dyes inside nanoparticles can lead to significative variations of photophysical properties.

Generally, as already mentioned in the previous chapter, brightness is defined as

$$B = \varepsilon \cdot \Phi$$

where ε is the molar absorption coefficient (and is a measure of the ability of nanoparticles to absorb the excitation light) and Φ is the quantum fluorescence yield (i.e. efficiency with which the molecules that have absorbed light emit photons). The brightness therefore represents a mixed parameter that considers both the absorption and the emission of light capacity of the chromophore. So, it can be used to evaluate intensity of fluorescence signal.

Weak electronic interaction represents ideal conditions, where the molar absorption coefficient of a nanoparticle is the sum of coefficients of molecules that compose it.

Molecular nanoparticles therefore have a high brightness value, since they contain a high number of chromophores within them. So, the above equation becomes:

$$B_{NP} = n_{mol} \cdot \varepsilon_{mol} \cdot \Phi$$

where n_{mol} is the number of dyes in a nanoparticle.

Actually, when the chromophore is inside the molecular nanoparticles the molar absorption coefficient and the emission quantum yield, as a result of quenching processes between the same chromophores due to their proximity.

Despite the reduction of photophysical properties of individual chromophores, a molecular nanoparticle is an entity with a much higher *brightness* than the starting fluorophore.

A common fluorophore has a molar absorption coefficient of 10^5 $cm^{-1}M^{-1}$ and emission quantum yield of 1^2. The *brightness* results 10^5 $cm^{-1}M^{-1}$. Usually in a molecular nanoparticle there are 10^6 dyes. If molar absorption coefficient of the fluorophore inside the nanoparticle is reduced by 70%, becoming $3 \cdot 10^4$ $cm^{-1}M^{-1}$, and emission quantum yield is reduced to 0.01, the *brightness* results $3 \cdot 10^4$ $cm^{-1}M^{-1}$, one thousand times higher than the single fluorophore.

This simple calculation demonstrates that, although in real systems *brightness* of nanoparticles does not grow linearly with the number of components, however it is possible to obtain nanoparticles with an extremely intense fluorescence.

Several methods have been developed for molecular nanoparticles preparation, such as self-assembly, macro / micro / nanoemulsion and nanoprecipitation. All of them exploit surfactant molecules. Surfactants are amphiphilic molecules; they have a hydrophobic and a hydrophilic portion. In a diluted aqueous solution, they are in monomeric form and behave like strong electrolytes, completely dissociated. By increasing the concentration of monomers until exceeding a concentration limit value, called critical micellar concentration, the amphiphilic nature of the species leads to the formation of supramolecular systems. Most common are spherical micelles, ellipsoidal micelles, cylindrical micelles and liquid-crystalline structures deriving from cylindrical micelles arranged neatly within a crystal lattice. The micelles are defined as stable and dynamic aggregates of amphiphilic molecules in water, whose constituents are subjected to rapid dynamic equilibrium regulated by diffusion. This balance is the result of two parallel processes: the first is faster and consists of the association and dissociation of a monomer from the aggregate, while the second, slower, consists in the formation and disintegration of the entire structure. An important requirement for micelle formation is that the alkyl chain has at least 8-10 methyl groups, so to reduce water solubility and a sufficiently active polar group to allow the solubility of the molecule itself. Micelles formation also depends on the balance between the tendency of the hydrocarbon chains to cling together, through hydrophobic interactions, to minimize the contact between the alkyl chains and the water molecules and the electrostatic repulsions of the polar heads that tend to remove the chains; this destabilizing effect is partly attenuated by the association of counterions on the micellar surface.

The self-assembly method uses surfactant that tend to self-assemble into nano-aggregates in aqueous solution. When a non-solvent is added to the mixture of surfactant and organic molecules dissolved in a "good" solvent, the hydrophobic surfactant segments tend to aggregate and encapsulate the organic matrix within a polar pool while the hydrophilic head tend to form

a shell that stabilizes the obtained nanoparticles. The organic species can also be directly linked to the hydrophobic end chains of surfactant or to the side chains[3].

The emulsification process is based on the formation of an emulsion. The term emulsion means a mixture of two or more liquids, completely or partially immiscible, obtained in the presence or absence of an active surfactant. Based on the size of the drops the emulsion can be classified as macro, micro or nanoemulsion. The last two are used for the preparation of molecular nanoparticles with size below 500 nm. In a typical emulsion process the emitting species and the surfactant are dissolved together in a solvent, which is immiscible with water. Then the solvent is added to the aqueous solution containing an emulsifier. Subsequently it can be sonicated or mixed vigorously to form organic drops which are stabilized by the emulsifier[4].

Finally, the nanoprecipitation method is very efficient and with low energy expenditure for molecular nanoparticles production. The main difference between this method and emulsification is the organic solvent used to solubilize the dye. Indeed, for the nanoprecipitation the solvent must be miscible in water and easily removable by evaporation. The solvents most often used are ethanol, acetone, hexane, THF etc.

In a typical nanoprecipitation process the solution of the organic species and the surfactant is rapidly added to water that is present in excess. The sudden increase in solvent polarity leads to the aggregation of organic species and hydrophobic segments of the surfactant, with formation of molecular nanoparticles. This method permits to obtain molecular nanoparticles with a narrow size distribution. The formation of nanoparticles is influenced by many factors such as: the rate of organic phase addition, the mixing during the addition and miscibility of organic solvent and water. This method is widely used for the precipitation of molecular nanoparticles, thanks to its simplicity, rapidity and reproducibility[5].

For these reasons, in the present thesis work, nanoprecipitation method was used for nanoparticles preparation. The surfactant chosen to stabilize molecular nanoparticles is Pluronic F127. It is a three-block non-ionic copolymer, polyoxyethylene-polyoxypropylene-polyoxiethylene (PEO-PPO-PEO), with a molecular weight of 12600 g / mol (Fig.6.1.)

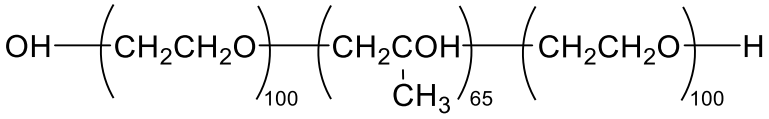

Fig.6.1 Pluronic structure

Copolymer aggregation behaviour is complicated and it is not possible to define a single critical micellar concentration, since it depends on various factors. In fact it has been noted that aggregation occurs in a concentration range, rather than at a single critical micellar

concentration value. Several researchers have hypothesized the presence of two or more types of micelles due to changes in shape, size and polarity. These observations have been attributed to the intrinsic polydispersity of the copolymer. However, critical micellar concentration at 20°C has been estimated 3.174 mM. Pluronic forms micelles with a core mainly constituted by the PPO block, the hydrophobic moiety, and the shell is constituted by the PEO block, the hydrophilic moiety of the copolymer and therefore is in contact with the aqueous environment. Pluronic F127 is very suitable for solubilize hydrophobic molecular compounds that would otherwise be insoluble in water. As in our case, in which the surfactant surrounds the fluorescent organic nanoparticles, making them soluble in an aqueous environment and suitable for our purposes.

Five fluorophores were used, selected for their structural and electronic properties. In particular, organic dyes have been chosen with a planar geometry and an extensive π system. These characteristics favour the emergence of intermolecular interactions, for example π–π stacking interactions, which can be exploited for the formation of organic nanoparticles in polar solvents.

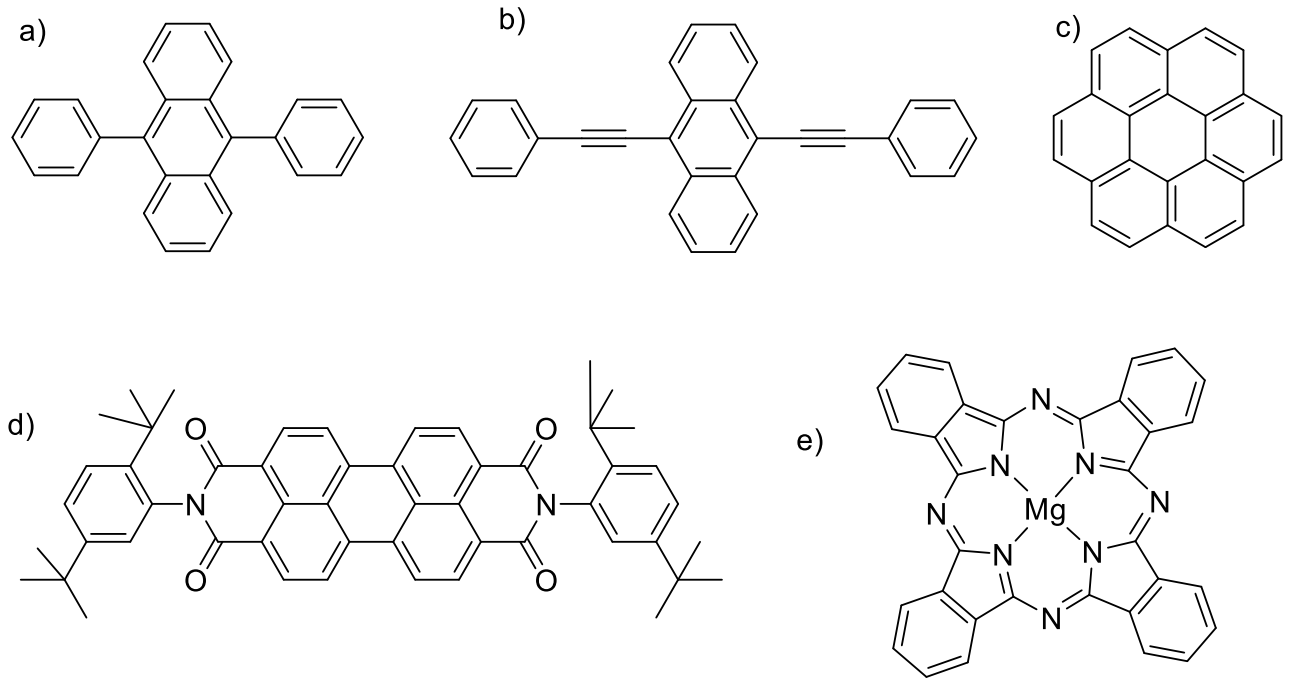

Fig.6.2 Commercial dyes used; ,10-Diphenylanthracene (DPA) a); 9,10-Bis(phenylethynyl)anthracene (DPEA) b); Coronene (C) c); N,N′-Bis(2,5-di-tert-butylphenyl)-3,4,9,10-perylenedicarboximide (P) d); Magnesium phthalocyanine (Mg) e).

The first dye that has been studied is 9,10-Diphenylanthracene (DPA). The second dye is 9,10-Bis(phenylethynyl)anthracene (DPEA). The third is Coronene (C), then there is N,N′-Bis(2,5-di-tert-butylphenyl)-3,4,9,10-perylenedicarboximide (P) and at the end Magnesium phthalocyanine (Mg).

This chapter will be developed in three sections with different objectives.

- **Section 1: Nanoparticles with a single dye**

In Section 1, nanoparticles containing only one type of fluorophore have been studied. The photophysical properties of nanoparticles have been compared with those of the fluorophore in THF. The purpose in Section 1 of the work is to characterize a set of nanoparticles with high brightness that can cover the entire spectral zone from UV to NIR. The work consists in:

1) Verify nanoparticles formation. Dynamic Light Scattering have been performed.

2) Study the effect fluorophores aggregation on photophysical properties by comparing the properties of nanoparticles with those of molecules in tetrahydrofuran (THF).

3) Study the stability of nanoparticles over time. UV-vis, fluorescence and DLS measurements have been performed after the nanoprecipitation and in the following days.

To prepare molecular nanoparticles studied Section 1, 2 mg of dye (DPA, DPEA, C, P) have been solubilized in 1 ml of THF containing 20 mg of Pluronic F127.

1 mg of Mg was dissolved in 1 mL of THF containing 20 mg of Pluronic F127. Then from the starting solutions 10µl were taken and added in 2.5 ml of water (Fig 6.3).

Nanoparticles samples have been indicated as F-NP where F is the symbol of the fluorophore.

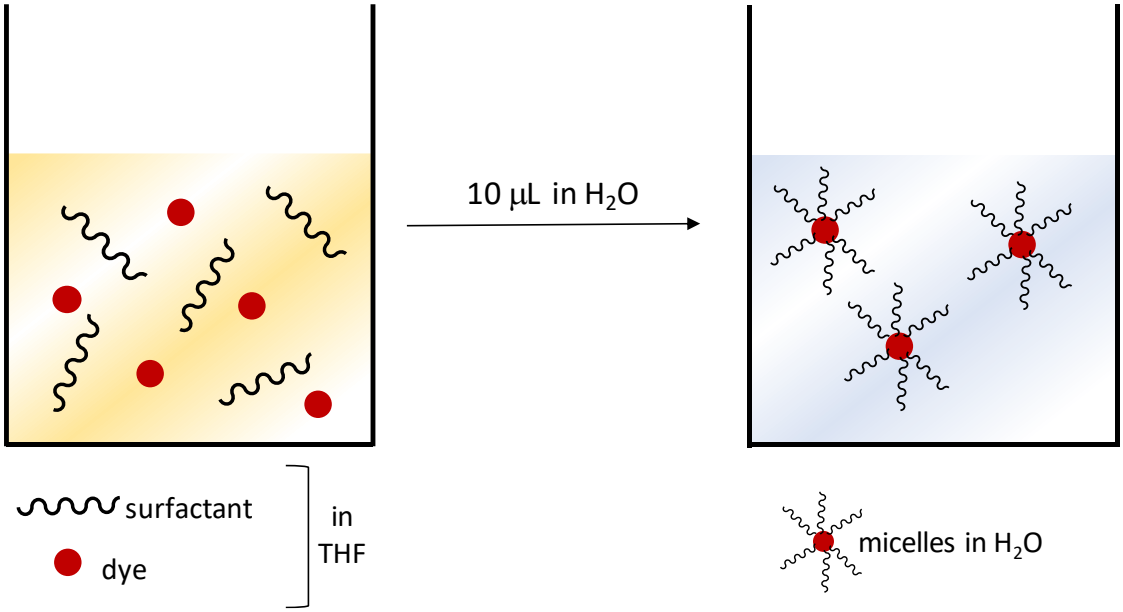

Fig.6.3 Schematic process of nanoprecipitation of a single dye.

- **Section 2: Nanoparticles of two dye, by coprecipitation**

In Section 2 have been characterized nanoparticles containing two fluorophores an excitation energy donor D and an excitation energy acceptor A, with a ratio 10 to 1, that incorporated in the nanoparticles, can give rise to energy transfer processes. In this way it is possible to modulate both the excitation and emission wavelengths and increase the brightness. The main purpose in Section 2 is study interaction between D and A in the nanoparticles obtained by co-precipitation, to verify presence of energy transfer processes.

The systems studied are:

1) DPA, as donor, and P, as acceptor
2) DPEA, as donor, and P, as acceptor
3) C, as donor, and P, as acceptor
4) P, as donor, and Mg, as acceptor

To prepare molecular nanoparticles studied in this Section 2 mg of dye (DPA, DPEA, C, P) have been solubilized in 1 ml of THF containing 20 mg of Pluronic F127. 1 mg of Mg was dissolved in 1 mL of THF containing 20 mg of Pluronic F127. Then, 200 µl of the donor and 20 µl of the acceptor have been mixed. From this solution 10µl have been taken and added in 2.5 ml of H_2O. (Fig.6.3). Nanoparticles samples have been indicated as D_A-NP where D is the symbol of the donor, A is the symbol of acceptor.

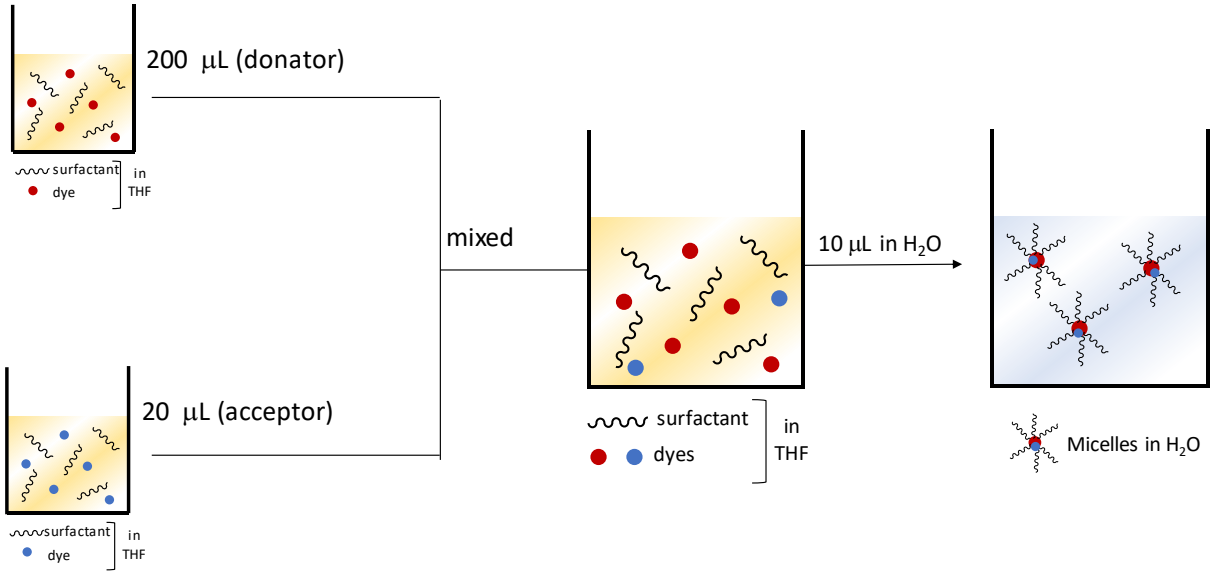

Fig.6.4 Schematic process of nanoprecipitation of two dyes

- **Section 3: Nanoparticles of two dye, by mixing**

In Section 3 we have studied the result of mixing two aqueous solutions containing nanoparticles of different molecules. The goal is to verify the possible exchange of molecules between the different particles. Systems will then be prepared with the same composition as the second part. In this case, however, the two fluorophores D and A will be nanoprecipitated separately and then mixed. Results obtained in the second part have been used as a reference. The work consists in:

1) Investigate presence of dye exchange between nanoparticles
2) Study the effect on photophysical properties of dyes. Analysis by UV-Vis and steady-state fluorescence spectroscopy and resolved over time have been performed.

To prepare molecular nanoparticles studied in this Section 2 mg of dye (DPA, DPEA, C, P) have been solubilized in 1 ml of THF containing 20 mg of Pluronic F127.

1 mg of Mg was dissolved in 1 mL of THF containing 20 mg of Pluronic F127. Then, from the starting solutions were taken 10µl and added in 2.5 ml of water (Fig.6.3). Subsequently, 250 µl of water solution of acceptor were added to water solution of donator (Fig.6.5). Nanoparticles samples have been indicated as D_Am-NP where D is the symbol of the donor, A is the symbol of acceptor and m means *mixed*, in contrast with nanoparticles prepared in Section 2.

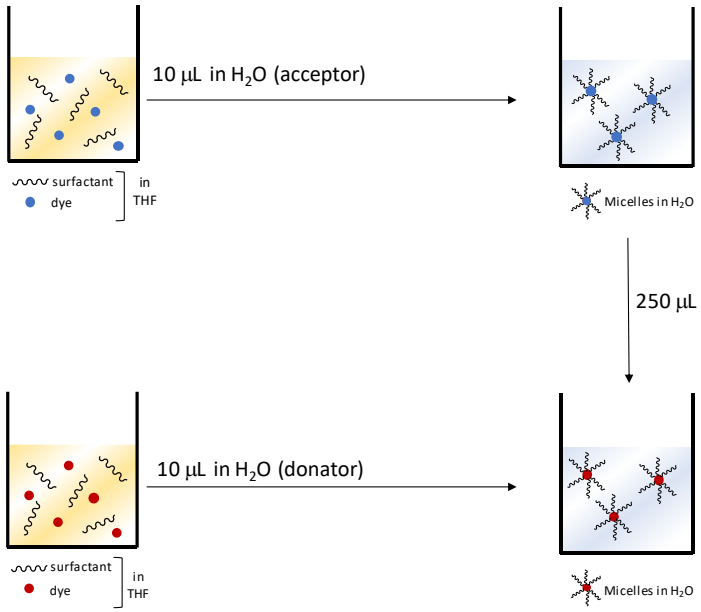

Fig.6.5 Schematic process of nanoprecipitation of a single dye and successive nanoparticles mixing

6.2 Summary

The most interesting results have been obtained for diphenylanthracene (DPA) and N,N′-Bis(2,5-di-tert-butylphenyl)-3,4,9,10-perylenedicarboximide (P) showed in Fig.6.6.

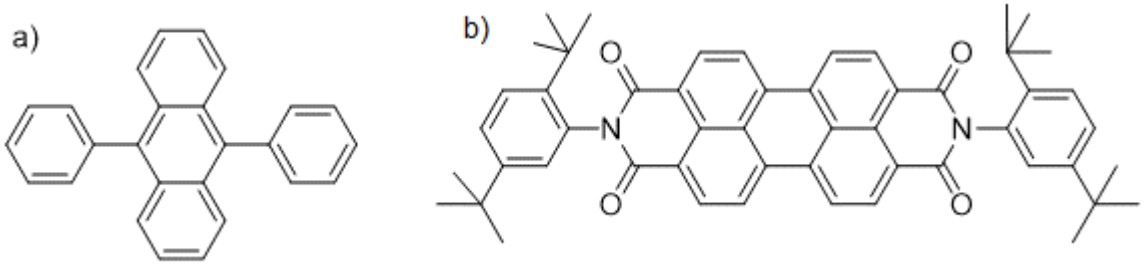

Fig.6.6 10-Diphenylanthracene (DPA) a); N,N′-Bis(2,5-di-tert-butylphenyl)-3,4,9,10-perylenedicarboximide (P) b).

In Section 1, nanoparticles containing only one type of fluorophore have been studied. The photophysical properties of nanoparticles have been compared with those of the fluorophore in THF. The purpose of Section 1 of the work was to characterize a set of nanoparticles with

high brightness that can cover the entire spectral zone from UV to NIR. As mentioned, the most interesting results have been obtained for diphenylanthracene (DPA) and N,N′-Bis(2,5-di- tert-butylphenyl)-3,4,9,10-perylenedicarboximide(P). In Fig.6.7 are reported absorption and emission spectra of DPA and P and respective nanoparticles (DPA-NP and P-NP).

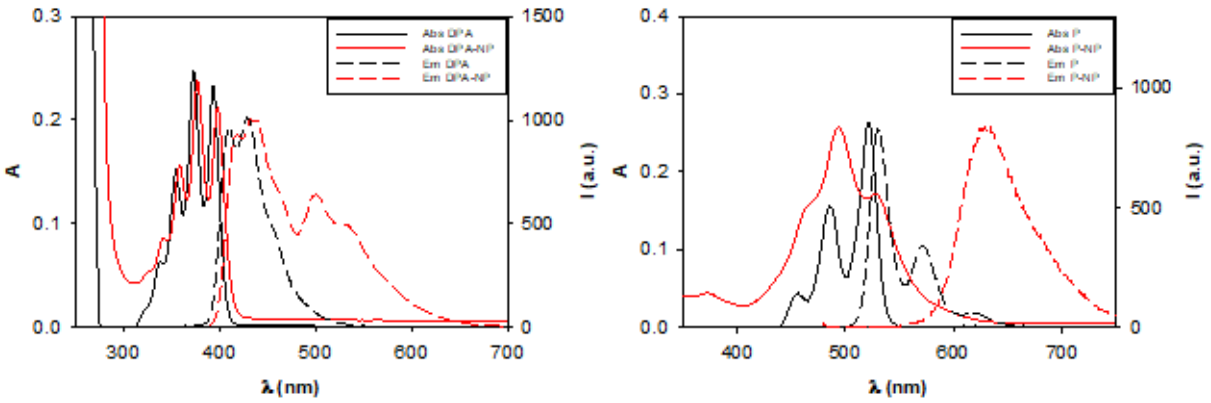

Fig.6.7 On the left: continuous lines are absorption specta of DPA (black line) and of DPA-NP (red line); dashed lines are emission spectra of DPA (black line) and of DPA-NP (red line); On the right: continuous lines are absorption spectra of P (black line) and of P-NP (red line); dashed lines are emission spectra of P (black line) and of P-NP (red line);

In Section 2, nanoparticles containing two fluorophores a donor D and an acceptor A, with a ratio 10 to 1 have been characterized. The two kind of fluorophore when incorporated in the nanoparticles, can give rise to energy transfer processes. In this way it was possible to modulate both the excitation and emission wavelengths and increase the brightness of the NPs. The main purpose of the second part of Section 2 was indeed to study the interaction between D and A in the nanoparticles obtained by co-precipitation, to verify presence of energy transfer processes. In Fig.6.8 (left) absorption spectra of DPA, P and nanoparticles with DPA and P (DPA_P-NP) are reported together with the emission spectra of DPA and DPA_P-NP (right): it can clearly be observed that in presence of P the DPA emission is quenched. This demonstrate that there is interaction between fluorophores inside nanoparticles.

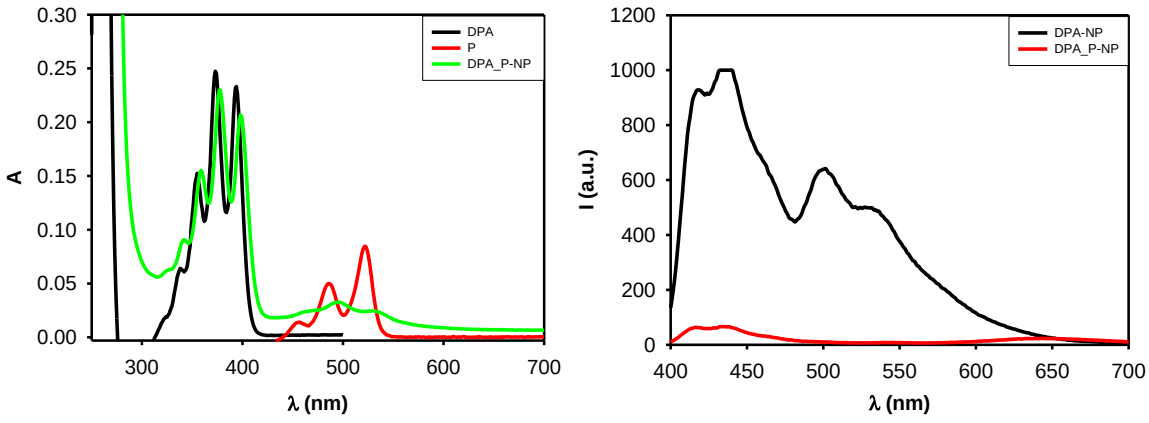

Fig.6.8 On the left: absorption spectra of DPA (black line), of P (red line) and of DPA_P-NP (green line). On the right: emission spectra of DPA-NP (black line) and of (DPA_P-NP (red line)

In Section 3, it has been studied the result of mixing two aqueous solutions containing nanoparticles of different molecules. The goal was to verify the possible exchange of molecules between the different particles. For this reason mixture of nanoparticles were prepared having exactly the same total concetration of fluorophore used in the second part of the work, With the difference that in this case, the two fluorophores D and A were nanoprecipitated separately and then mixed (DPA_Pm_NP). The absorption spectra of DPA_P-NP and of DPA_Pm_NP are reported in Fig.6.9 (left) while the emission spectra of DPA_Pm_NP has been compared with emission spectra of DPA-NP in Fig.6.9 (right). It can be observed that in DPA_Pm_NP a strong emission of PDA is present, demonstrating that P is not quenching DPA, i.e. they are not incorporated in the same nanoparticles. We can conclude that, surprisingly, there is not molecular exchange between nanoparticles, even if they are not covalently bonded. This is very important since it demonstrated the high stability of these self-assembed nanoparticles in view of their application for bioimaging.

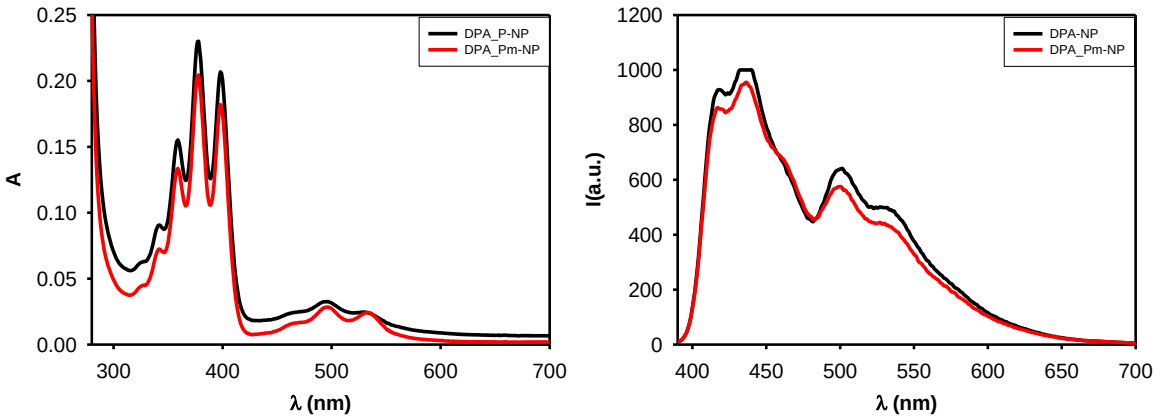

Fig.6.9 On the left: absorption spectra of DPA_P-NP (black line) and of DPA_Pm-NP (red line. On the right: emission spectra of DPA_NP (black line) and of DPA_Pm-NP (red line)

6.3 Section 1: Nanoparticles with a single dye

6.3.1 Characterization of DPA-NP

Molecular nanoparticles with DPA have been prepared following procedure reported Fig.6.3. Photophysical properties of DPA in THF solution have been compared with DPA-NP.

Absorption spectrum of DPA in THF presents a band between 320 and 410 nm with a defined vibrational structure characterized by three peaks at 340 nm, 370 nm and 400 nm. Absorption spectrum of DPA-NP samples have been registered after 30 minutes of THF solution injection in water. Presence of well-defined absorption bands demonstrates that the nanoprecipitation process has allowed the dispersion of DPA in water. It can also be observed that the shape of

the absorption spectrum of DPA nanoparticles is the same of the monomer and is red-shifted of about 10 nm compared to that of DPA in THF (Fig.6.10)

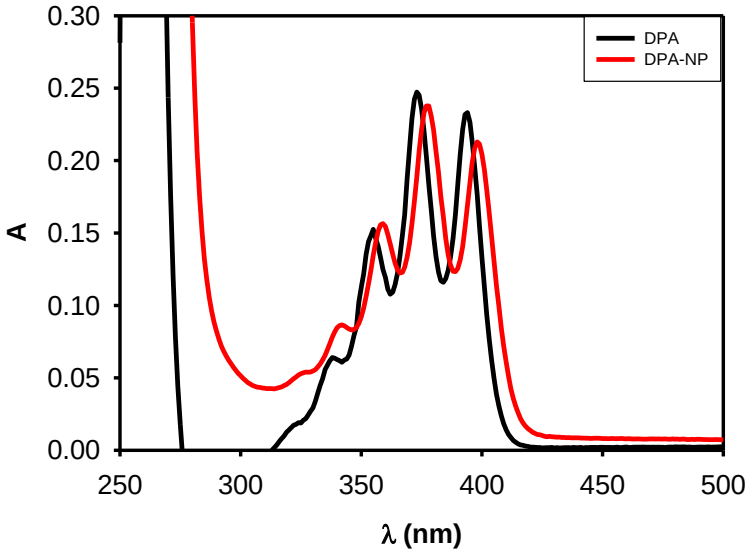

Fig.6.10 Absorption spectra od DPA (black line) and DPA-NP (red line)

Fluorescence spectrum of DPA in THF have been obtained by exciting samples at 380 nm, after 30 minutes of THF solution injection in water. It presents a band between 420 nm and 520 nm with two peaks at at 405nm and 430nm. Absorption spectrum of DPA-NP samples have been registered by exciting samples at 380 nm. Fluorescence band results red-shifted of 10 nm and are lower in intensity compared with the monomer one in THF. Vibrational bands are less defined. Moreover, at about 500nm and 540nm appear two bands with lower intensity. The differences observed in the absorption and fluorescence spectra of the DPA-NP aqueous dispersions compared to those of the THF molecule are compatible with the formation of nanoaggregates (Fig.6.11).

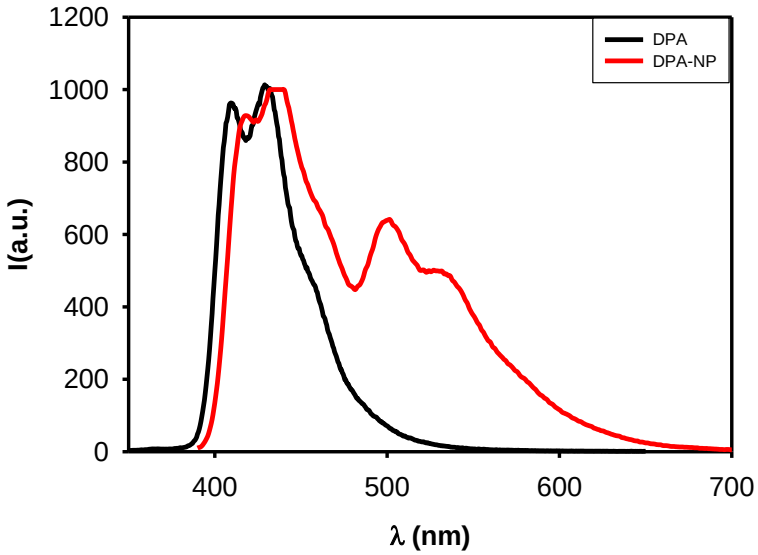

Fig.6.11 Emission spectra of DPA (black line) and DPA-NP (red line)

Nanoparticles presence in the DPA-NP was confirmed by the DLS measurements. In DPA-NP nanoparticles with a diameter of about 120 nm are presents with a PDI of 0.42. It is important to note that sample with only F127 at the same concentration of DPA-NP have been analysed with DLS and it does not form stable micelles, because under the critical micellar concentration. The absorption spectrum recorded for DPA-NP have been compared with the one registered 24 hours after injection. They are shown in Fig.6.12. Absorption spectrum registered after 24 hours is different from the initial one. In particular it can be clearly observed a scattering signal due to the partial formation of precipitate. This shows that this system is partially unstable over time.

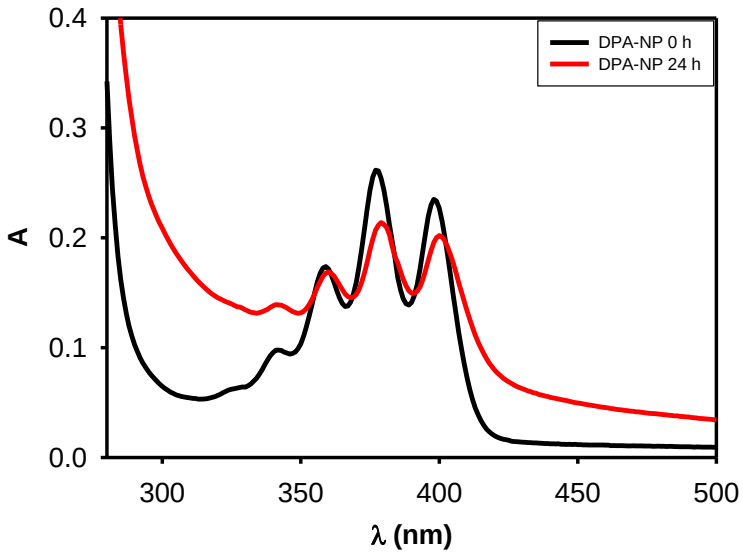

Fig.6.12 Absorption spectra of DPA-NP 30 minute (black line) and after 24 hours (red line) after injection

Emission spectrum recorded for DPA-NP have been compared with the one registered 24 hours after injection. They are shown in Fig.6.13. In emission spectrum registered after 24 hours there is a decrease in intensity, probably due to a reorganization of the system over time, i.e. the passage from one aggregate to another, confirming instability of the system.

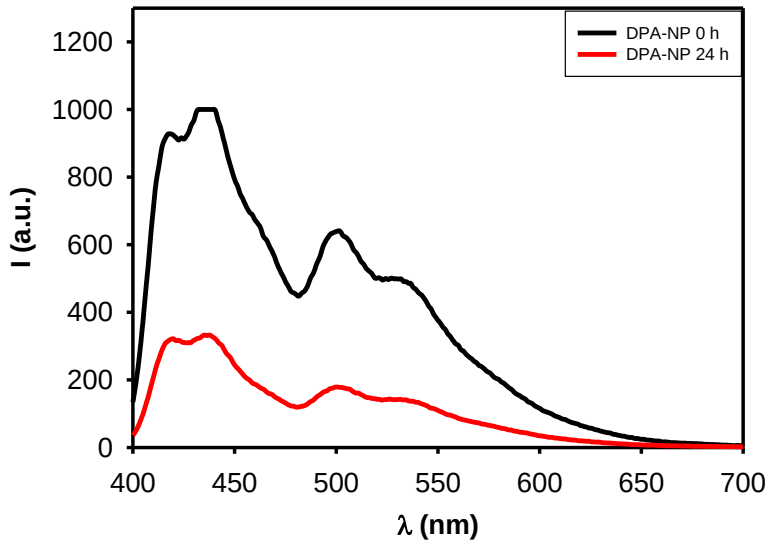

Fig.6.13 Emission spectra of DPA-NP 30 minute (black line) and after 24 hours (red line) after injection

6.3.2 Characterization of DPEA-NP

Molecular nanoparticles with DPEA have been prepared following procedure reported in Fig.6.3. Photophysical properties of DPEA in THF solution have been compared with nanoparticles DPEA-NP.

Absorption spectrum of DPEA in THF presents a band with two peaks at 450 and 475 nm. Absorption spectrum of DPEA-NP has been registered after 30 minutes of THF solution injection in water. Nanoparticles in water have a wide absorption band ranging from 350 nm to 520 nm. This demonstrates shows that nanoprecipitation allowed DPEA dispersion in water and that aggregation changes photophysical properties broadening absorption band (Fig.6.14).

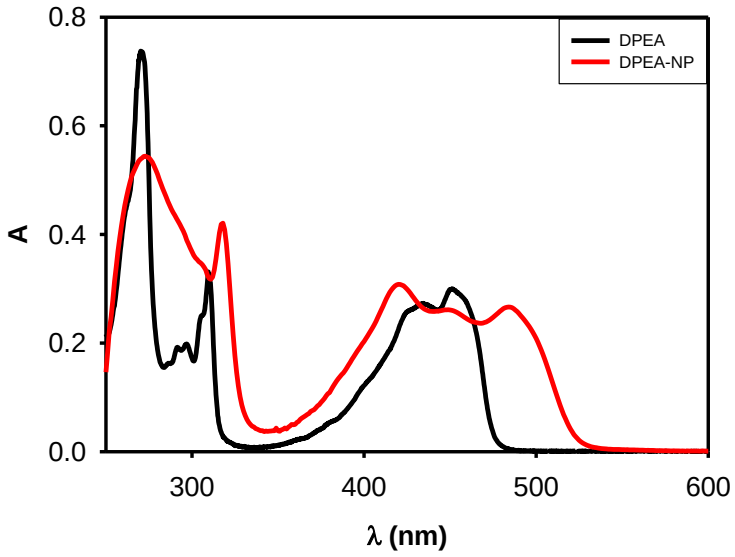

Fig.6.14 Absorption spectrum of DPEA (black line) and of DPEA-NP (red line)

Fluorescence spectrum of DPEA in THF has been obtained by exciting samples at 400 nm, after 30 minutes of THF solution injection in water. It presents a band with maximum at 470 and a shoulder at 520 nm. Emission band of nanoparticles in water is red-shifted by about 50 nm and vibrational bands are less defined than the one of monomer in THF. These observable differences in the absorption and fluorescence spectra of the DPEA-NP aqueous dispersions compared to those of molecule in THF are compatible with the formation of nanoaggregates (Fig.6.15).

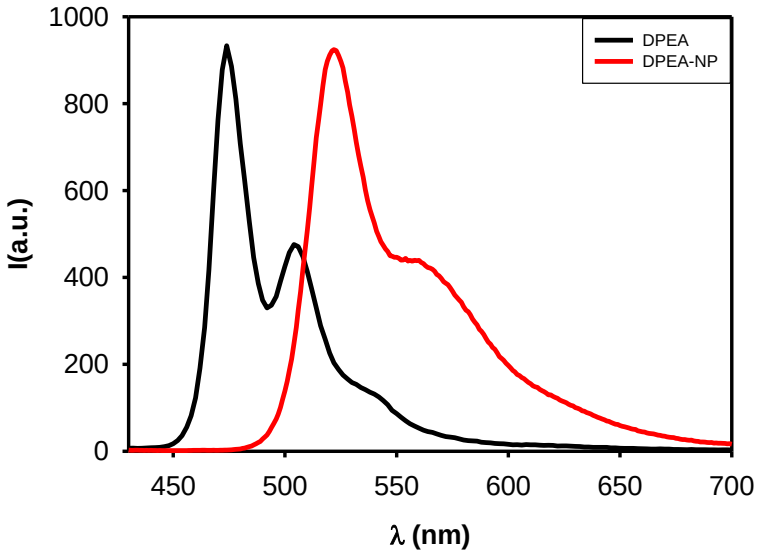

Fig.6.15 Emission spectrum of DPEA (black line) and of DPEA-NP (red line)

Nanoparticles presence in DPEA-NP was confirmed by the DLS measurements. In DPEA-NP nanoparticles with a diameter of about 120 nm are presents with a PDI 0.63. DLS measurement

of nanoparticles have been repeated after 24 hours. Results show that nanoparticles are still in solution with the same diameter of 120 nm and PDI of 0.50.

The absorption spectrum recorded for DPEA-NP has been compared with the one registered 24 hours after injection. They are shown in Fig.6.16. Absorption spectrum is not different from the initial one. This shows that this system is stable over time.

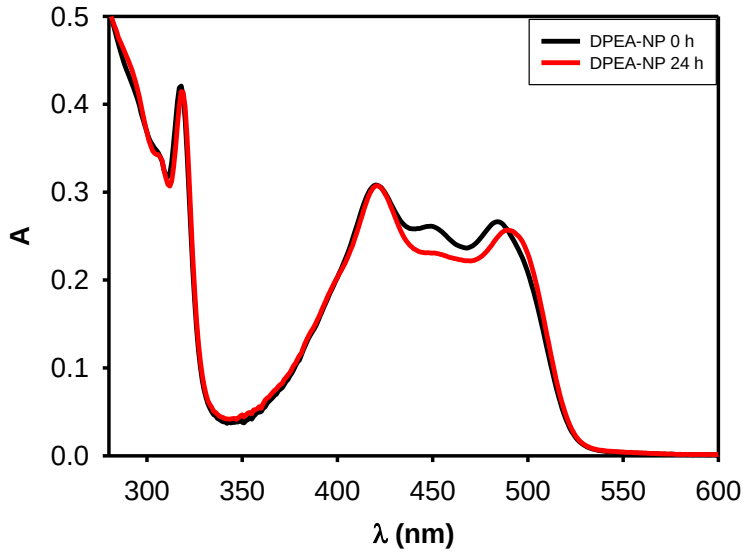

Fig.6.16 Absorption spectrum of DPEA-NP 30 minutes (black line) and 24 hours (red line) after injection

Emission spectrum recorded for DPEA-NP has been compared with the one registered 24 hours after injection. They are shown in Fig.6.17. In emission spectrum registered after 24 hours there is a decrease in intensity probably due to a change in the conformation of the aggregate of the system over time. Furthermore, the shoulder at 570 nm becomes more relevant with respect to the peak at 520 nm.

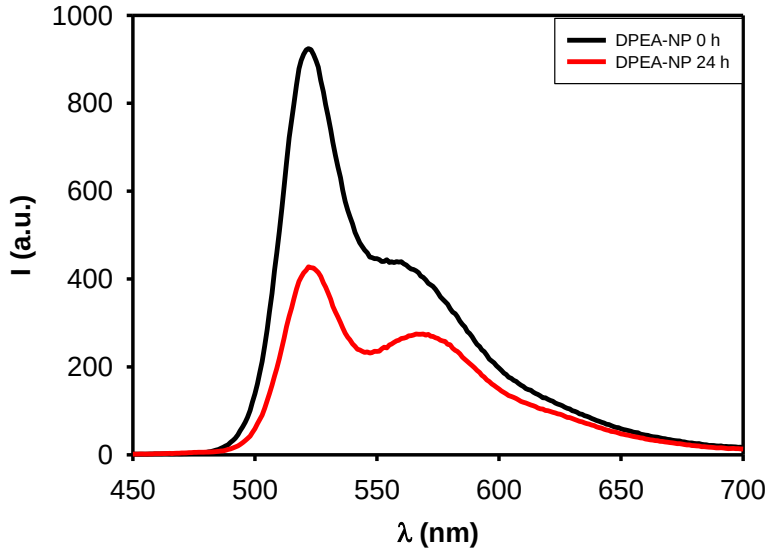

Fig.6.17 Emission spectrum of DPEA-NP 30 minutes (black line) and 24 hours (red line) after injection

6.3.3 Characterization of C-NP

Molecular nanoparticles with C have been prepared following procedure reported in Fig.6.3. Photophysical properties of C in THF solution have been compared with nanoparticles C-NP. Absorption spectrum of C in THF presents a band ranging from 280 nm to 350 nm with a defined vibrational structure. Absorption spectrum of C-NP has been registered after 30 minutes of THF solution injection in water. Absorption band of nanoparticles solution in water ranges from 280 nm to 500 nm with a maximum at 300 nm. It is broaden and poorly defined in comparison with the one of monomer in THF solution. This demonstrate that nanoprecipitation allowed the dispersion of C in water and that aggregation changes photophysical properties broadening absorption band (Fig.6.18).

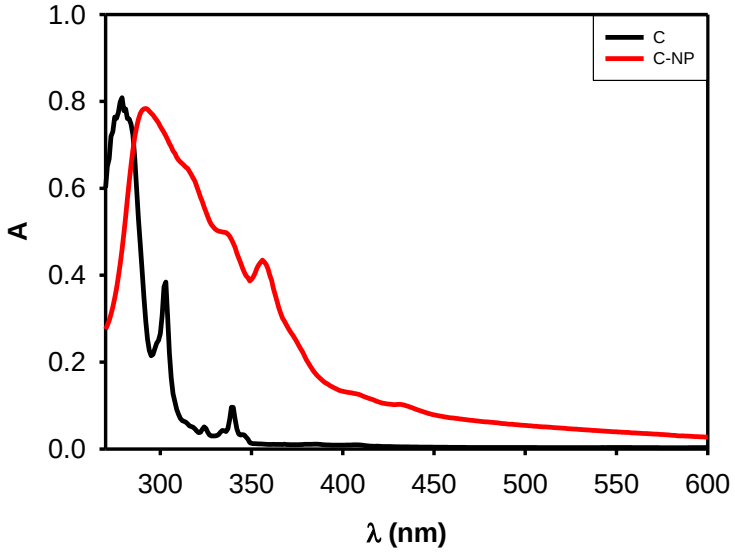

Fig.6.18 Absorption spectrum of C (black line) and od C-NP (red line)

Fluorescence spectrum of C in THF have been obtained by exciting samples at 370 nm, after 30 minutes of THF solution injection in water (Fig.6.19). It ranges from 400 nm to 550 nm with a maximum at 450 nm. It is characterized by a well-defined vibrational structure. Fluorescence spectrum of nanoparticles solution presents a new band with a maximum at 500 nm. Vibrational structure is absent. These observable differences in the absorption and fluorescence spectra of the C aqueous dispersions compared to those of the THF molecule are compatible with the formation of nanoaggregates.

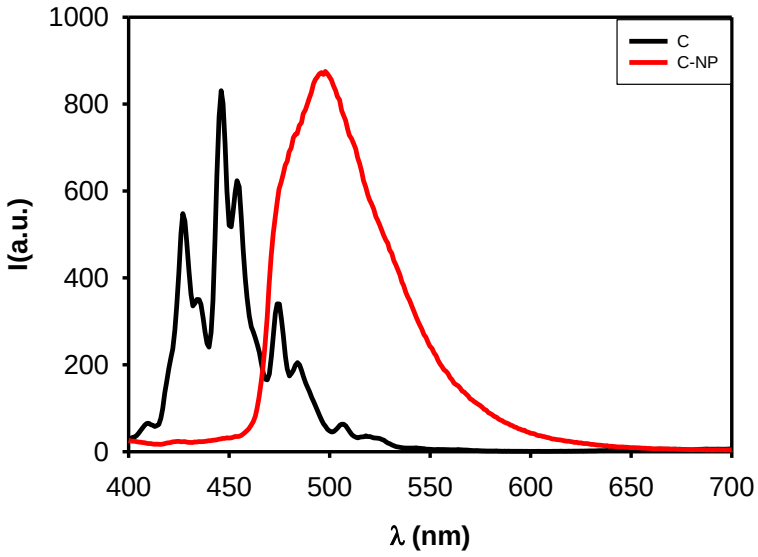

Fig.6.19 Emission spectrum of C (black line and of C-NP (red line)

Nanoparticles presence in the C-NP was confirmed by the DLS measurements. In C-NP nanoparticles with a diameter of about 140 nm are presents with a PDI of 0.27. DLS measurement of nanoparticles have been repeated after 24 hours. Results show that nanoparticles are still in solution, but diameter increase of 40 nm corresponding at 180 nm with PDI 0.29.

The absorption spectrum recorded for C-NP have been compared with the one registered 24 hours after injection. They are shown in Fig 6.20. Absorption spectrum is not different from the initial one. This shows that this system is stable over time.

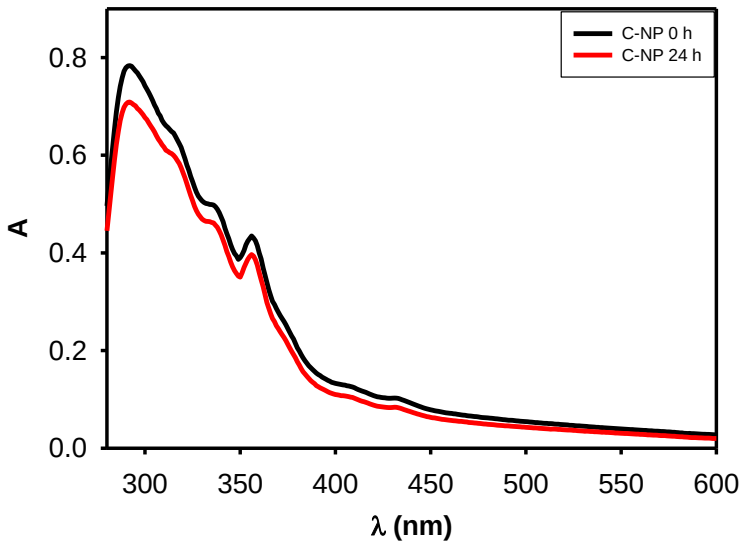

Fig.6.20 Absorption spectrum of C-NP 30 minutes (black line) and 24 hours (red line) after injection

Emission spectrum recorded for C-NP has been compared with the one registered 24 hours after injection. They are shown in Fig.6.21. In emission spectrum registered after 24 hours there

is a decrease in intensity probably due to a change in the conformation of the aggregate of the system over time.

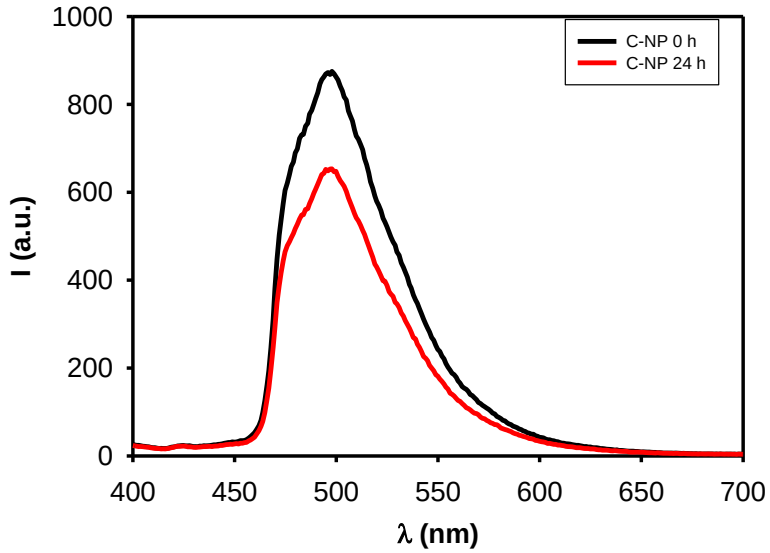

Fig.6.21 Emission spectrum of C-NP 30 minutes (black line) and 24 hours (red line) after injection

6.3.4 Characterization of P-NP

Molecular nanoparticles with P have been prepared following procedure reported in Fig.6.3. Photophysical properties of P in THF solution have been compared with nanoparticles P-NP.

Absorption spectrum of P in THF presents a band from 450 nm to 550 nm with two peak at 470 and 520 nm and a defined vibrational structure. Absorption spectrum of P-NP has been registered after 30 minutes of THF solution injection in water.

Nanoparticles in water have a wide absorption band ranging from 400 nm to 600 nm. Intensity of peaks is inverted in comparison with emission band of monomer in THF. Indeed, in nanoparticles emission band the maximum is at 470 nm and the shoulder at 510 nm. This demonstrates shows that nanoprecipitation allowed P dispersion in water and that aggregation changes photophysical properties broadening absorption band (Fig.6.22).

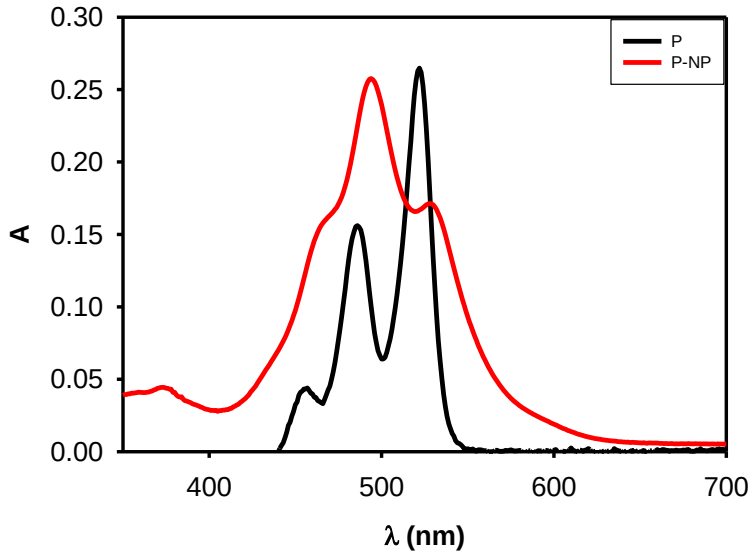

Fig.6.22 Absorption spectrum of P (black line) and of P-NP (red line)

Fluorescence spectrum of P in THF has been obtained by exciting samples at 470 nm, after 30 minutes of THF solution injection in water (Fig.6.23). It presents a band with maximum at 520 and a shoulder at 570 nm. Emission spectrum of nanoparticles in water presents a new broad band in the red and NIR region.

These observable differences in the absorption and fluorescence spectrum of P-NP aqueous dispersions compared to those of the THF molecule are compatible with the formation of nanoaggregates.

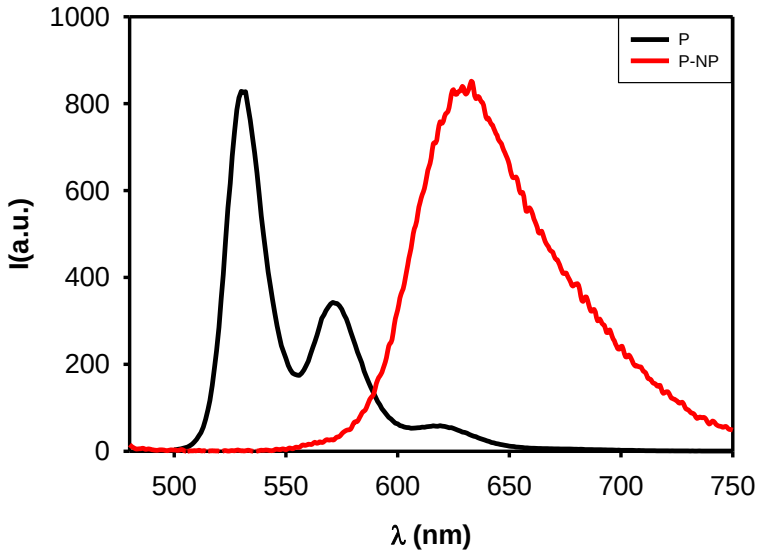

Fig.6.23 Emission spectrum of P (black line) and of P-NP (red line)

Nanoparticles presence in P-NP was confirmed by the DLS measurements. In P-NP nanoparticles with a diameter of 102 nm are presents with a PDI 0.35. DLS measurement of nanoparticles have been repeated after 24 hours and diameter is 104 nm with PDI 0.28. After

48 hours diameter is 102 nm and PDI 0.35. Results show that nanoparticles are still in solution and there is a slight increase in diameter over the time.

The absorption spectrum recorded P-NP has been compared with the ones registered one day (24h), two days (48 h) and 7 days (168 h) after injection. They are shown in Fig.6.24. Absorption spectra do not change over the time. This shows that this system is stable over time.

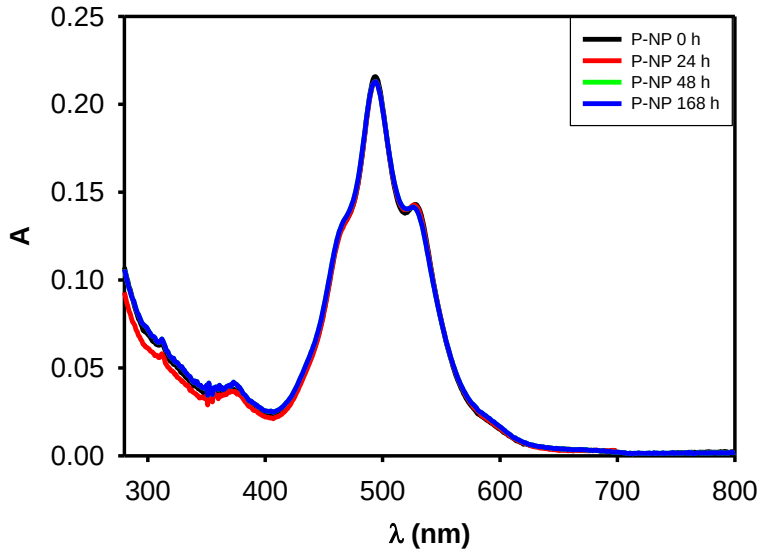

Fig.6.24 Absorption spectrum of P-NP 30 minutes (black line), 24 hours (red line), 48 hours (green line) and 168 hours (blue line) after injection

Emission spectrum recorded for P-NP has been compared with the ones registered one day (24h), two days(48 h) and 7 days (168 h) after injection. They are shown in Fig.6.25. It is observed that after 24 hours intensity of emission increases. Probably there is a reorganization in the most thermodynamically stable form, where non radiative process are reduced. Emission is still present after 7 days from and this is prove the system is stable for long time.

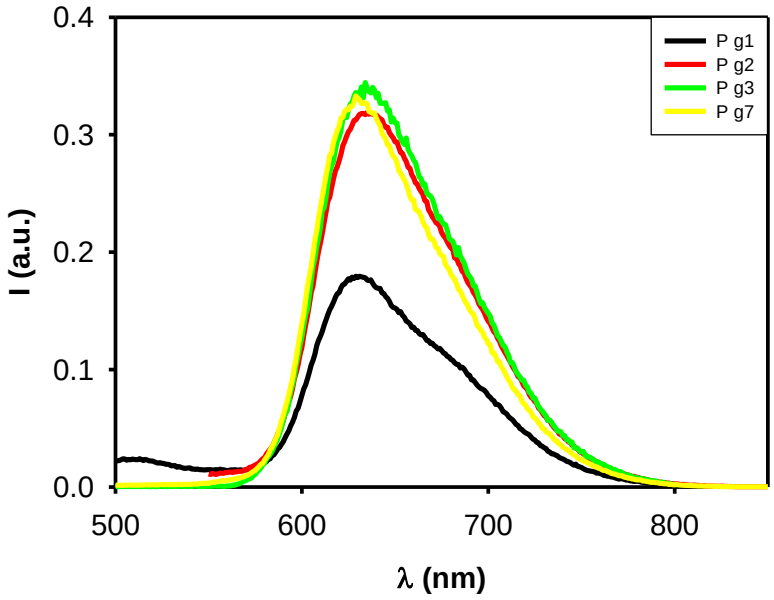

Fig.6.25 Emission spectrum of P-NP 30 minutes (black line), 24 hours (red line), 48 hours (green line) and 168 hours (jellow line) after injection

Time resolved fluorescence measurements (time correlated single photon counting, TCSPC) showed that the spectral changes observed upon nanoparticles formation were due to the presence, in the nanoparticles, of populations of fluorophores experiencing different environments. If the sample possess more than one lifetime multi-exponential decay are observed and the amplitude-weighted lifetime of the fluorophore is then given by

$$< \tau > = \frac{\sum B_i \tau_i}{\sum B_i}$$

where B_i is the pre-exponential factor and can be used to represent the fraction of fluorophores with lifetime τ_i. Triple-exponential decays were observed P-NP. Data collected for P-NP are τ_1 = 1.8 ns, B_1 = 2694, τ_2 = 6.7 ns, B_2 = 1207, τ_3 = 29.9 ns, B_3 = 190 and average excited lifetime was calculated to be $< \tau >$ = 4.52 ns.

6.3.5 Characterization of Mg-NP

Molecular nanoparticles with Mg have been prepared following procedure reported in Fig.6.3. Photophysical properties of Mg in THF solution have been compared with nanoparticles Mg-NP. Absorption spectrum of Mg in THF presents a sharp peak with a maximum at 680 nm. Absorption spectra of Mg-NP have been registered after 30 minutes of THF solution injection in water. Nanoparticles in water have a wide absorption band ranging from 500 nm to 900 nm. This demonstrates shows that nanoprecipitation allowed DPEA dispersion in water and that aggregation changes photophysical properties broadening absorption band.

It is extremely interesting that absorption spectrum of Mg-NP presents the same NIR band of Mg in solid state in the X-phase[6] (Fig.6.26).

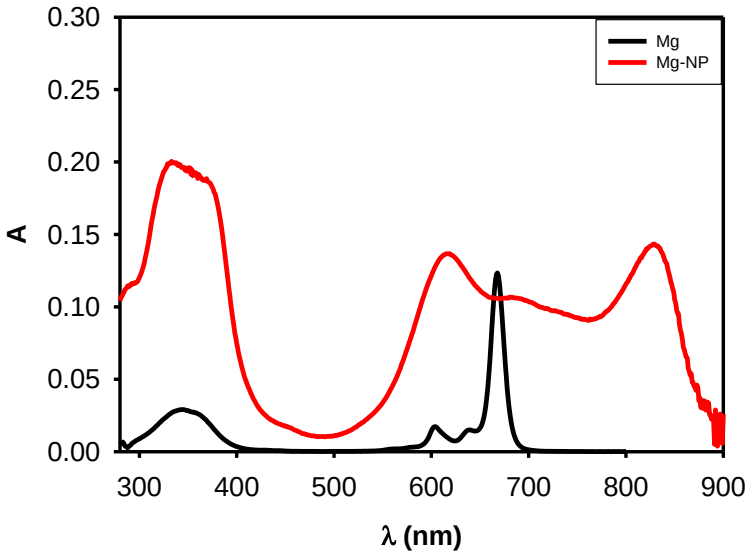

Fig.6.26 Absorption spectrum of Mg (black line) and Mg-NP (red line)

Fluorescence spectrum of Mg in THF have been obtained by exciting samples at 675 nm, after 30 minutes of THF solution injection in water (Fig.6.27). It presents a sharp peak with a maximum at 680 nm and a small shoulder at 0 m. In fluorescence spectrum of nanoparticles there is a new band in the NIR region with a maximum at 850 nm. These observable differences in the absorption and fluorescence spectra of the Mg aqueous dispersions compared to those of the THF molecule are compatible with the formation of nanoaggregates.

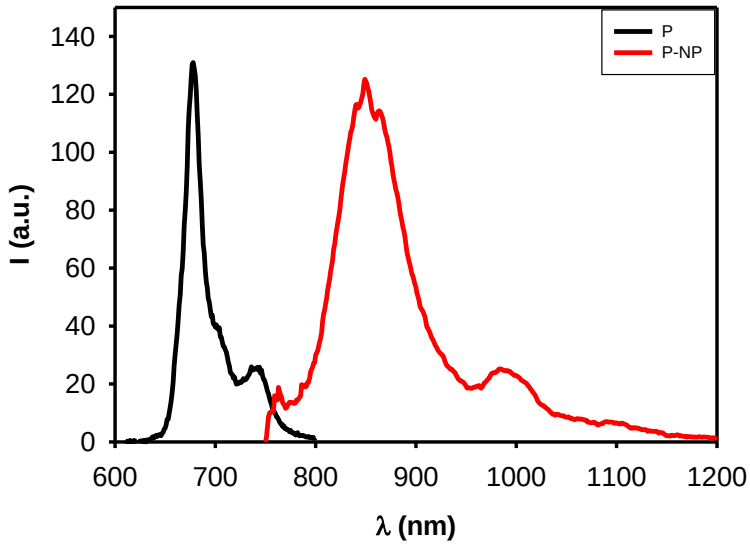

Fig.27 Emission spectrum of Mg (black line) and Mg-NP (red line)

The absorption spectrum recorded Mg-NP has been compared with the ones registered one day (24h), two days (48 h) and 7 days (168 h) after injection. They are shown in Fig.6.28. Absorption spectra do not change over the time. This shows that this system is stable over time.

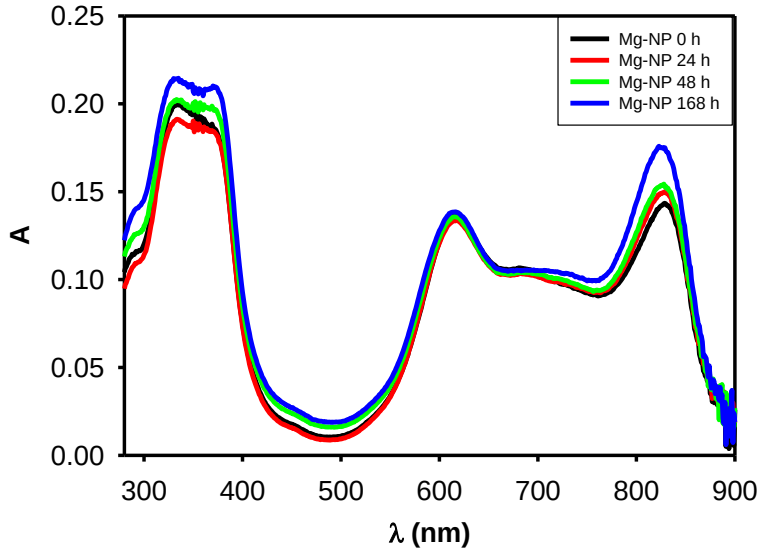

Fig.6.28 Absorption spectrum of Mg-NP 30 minutes (black line), 24 hours (red line), 48 hours (green line) and 168 hours (blue line) after injection

Emission spectrum recorded for Mg-NP has been compared with the ones registered one day (24h), two days (48 h) and 7 days (168 h) after injection. They are shown in Fig.6.29. It is observed that emission is still present after 7 days from and this prove the system is stable for long time. It is not possible compare emission variation over the time, because it was not possible register emission quantum yield for instrumental limits. Only consideration about shape can be made.

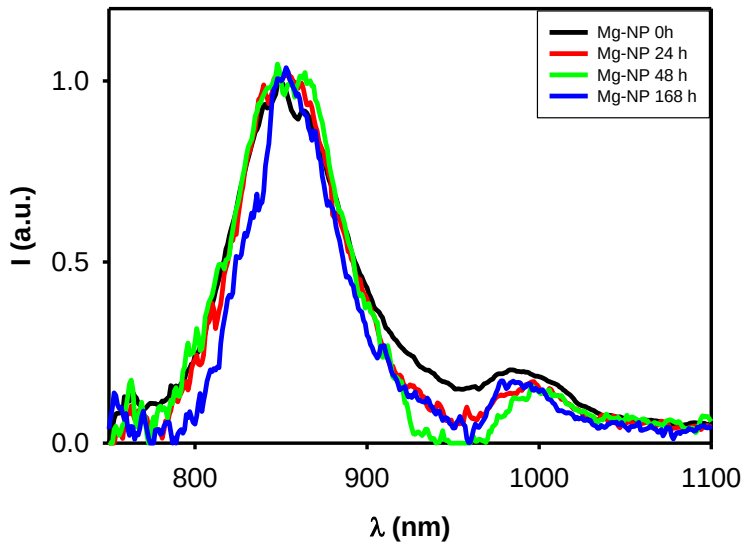

Fig.6.29 Emission spectrum of Mg-NP 30 minutes (black line), 24 hours (red line), 48 hours (green line) and 168 hours (blue line) after injection

6.4 Section 2: Nanoparticles of two dye, by coprecipitation

6.4.1 Characterization of DPA_P-NP

Molecular nanoparticles with DPA and P have been prepared following procedure reported in Fig.6.4. Photophysical properties of DPA and P in THF solution have been compared with nanoparticles DPA_P-NP. Absorption spectrum of DPA_P-NP samples have been registered after 30 minutes of THF solution injection in water (Fig.6.30).

The presence of well-defined absorption bands shows the nanoprecipitation process has allowed the dispersion of the DPA_P-NP in water, It can also be observed that the shape of the absorption spectrum of DPA_P-NP is the sum of the absorption spectra of the individual components in proportion to the quantities present in solution. The 500nm band differs from that of P in THF, as for P-NP in water.

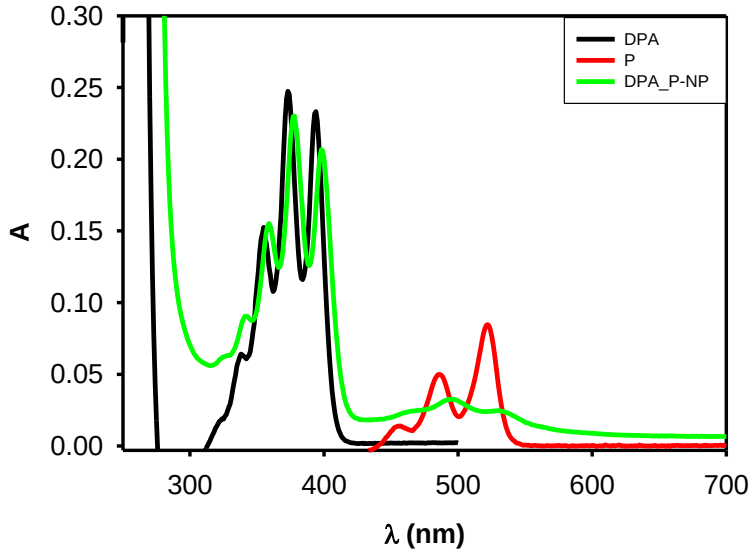

Fig.6.30 Absorption spectrum of DPA (black line), of P (red line) and of DPA_P-NP (green line)

Fluorescence spectrum of DPA_P-NP has been obtained by exciting at 380 nm, 30 min after injection in water (Fig.6.31). It can be observed that there are two emissions: a band relative to the donor, similar to that of DPA-NP at 420 nm and the other band, due to the sensitized emission of the acceptor, characteristic of P-NP at 640nm. Both bands deviate from the behaviour of the individual monomers. These observable differences in the absorption and fluorescence spectra of the DPA_P-NP aqueous dispersions compared to those of the THF molecule are compatible with the formation of nanoaggregates.

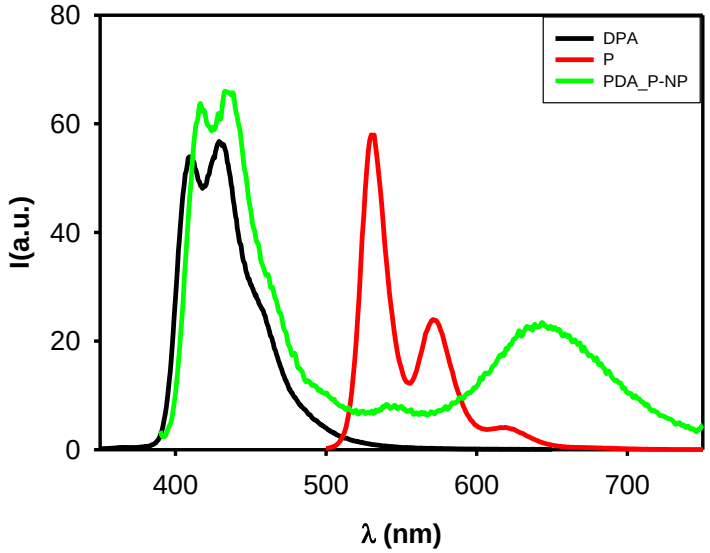

Fig.6.31 Emission spectrum of DPA (black line), P (red line) and of DPA_P-NP (green line)

In emission spectrum of DPA_P-NP there is a noticeable drop in intensity (around 90%) of the band at 420 nm, in comparison with emission spectrum of DPA-NP. This is due to the proximity of P which quenches DPA by an energy transfer process Fig.6.32.

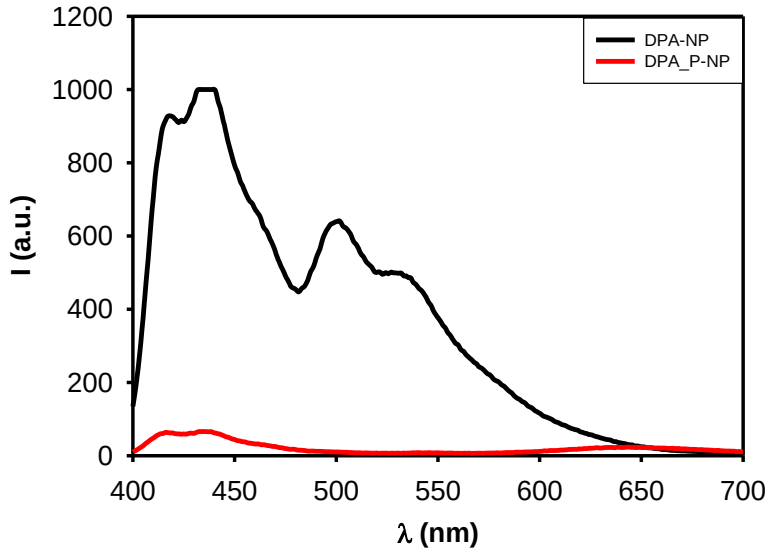

Fig.6.32 Emission spectrum of DPA-NP (black line) and of DPA_P-NP (red line)

Nanoparticles presence in DPA_P-NP was confirmed by the DLS measurements. In DPA_P-NP nanoparticles with a diameter of 127 nm are presents with a PDI 0.42. DLS measurement of nanoparticles have been repeated after 24 hours and diameter is 120 nm with PDI 0.08. The relevant decrease of PDI after 24 hours indicates that the system needs this time to rearrange in the most thermodynamically stable state.

The absorption spectrum recorded for DPA_P-NP has been compared with the one registered 24 hours after injection. They are shown in Fig.6.33. Absorption spectrum registered after 24

hours is different from the initial one. In particular it can be clearly observed a scattering signal due to the partial formation of precipitate. This shows that this system is partially unstable over time.

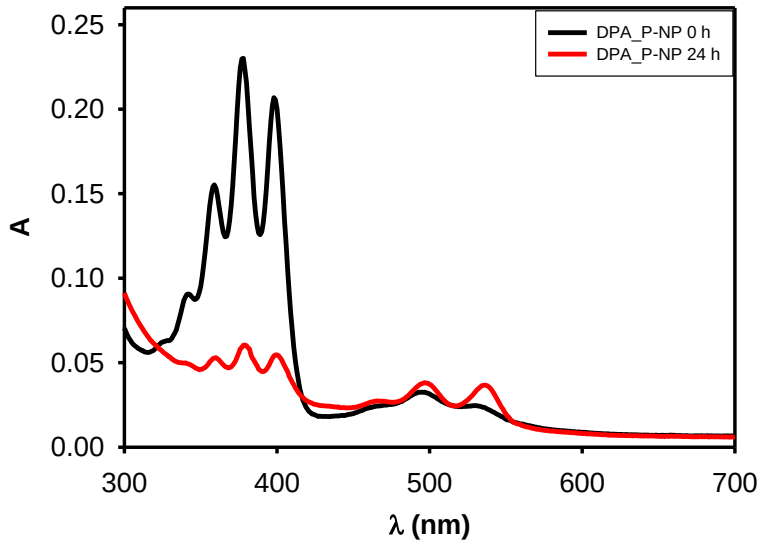

Fig.6.33 Absorption spectrum of P-NP 30 minutes (black line) and 24 hours (red line) after injection

Emission spectrum recorded for DPA_P-NP has been compared with the one registered 24 hours after injection. They are shown in Fig.6.34. Emission spectrum registered after 24 hours differ from the initial one. In particular it is observed that the characteristic band of the DPA with the maximum at 418nm, is always less intense while the fluorescence band of the P moves at 550 nm assuming characteristics more similar to those of the monomer. These changes observed over time clearly demonstrate that there is a reorganization of the structure that leads to an increase in the efficiency of the donor quenching process.

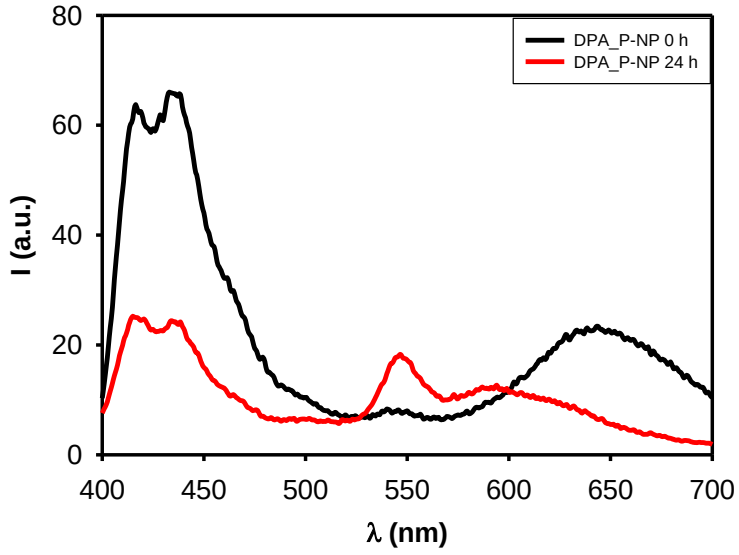

Fig.6.34 Emission spectrum of P-NP 30 minutes (black line) and 24 hours (red line) after injection

6.4.2 Characterization of DPEA_P-NP

Molecular nanoparticles with DPEA and P have been prepared following procedure reported in Fig.6.4. Photophysical properties of DPEA and P in THF solution have been compared with nanoparticles DPEA_P-NP.

Absorption spectrum of DPEA-NP samples have been registered after 30 minutes of THF solution injection in water (Fig.6.35). The presence of well-defined absorption bands shows the nanoprecipitation process has allowed the dispersion of the DPEA_P-NP in water.

It can also be observed that the shape of the absorption spectrum DPEA-NP seems similar to that of the DPEA-NP, with a wide band ranging from 350nm to 550nm. This band falls in the same spectral region of the absorption band of P and cover the signal of P, that is present in smaller quantities. It does not allow to understand if P has a behaviour that is closer to that of the monomer or to the aggregate system.

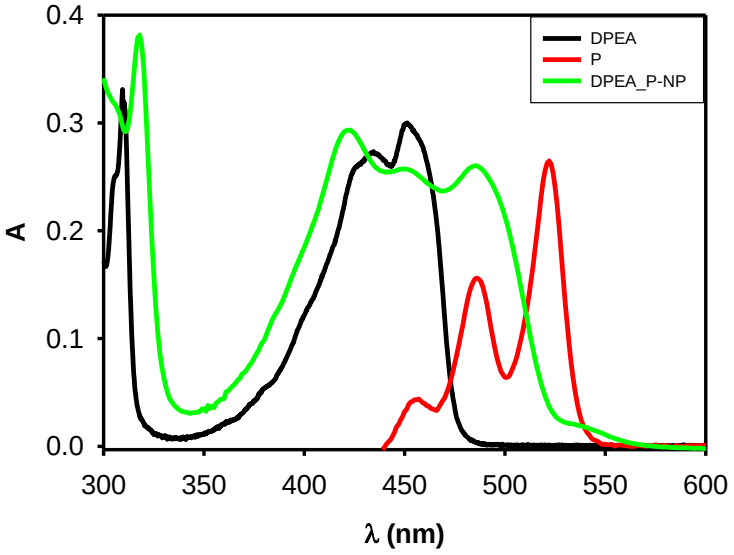

Fig.6.35 spectrum of DPEA (black line), P (red line) and of DPEA_P-NP (green line)

Fluorescence spectrum of DPEA_P-NP has been obtained by exciting at 400 nm, 30 min after injection in water (Fig.6.36). It can be observed that DPEA emission band is red-shifted of 50 nm-as for DPEA-NP. It is not observed the emission band of P. These observable differences in the absorption and fluorescence spectra of the DPEA_P-NP aqueous dispersions compared to those of the THF molecule are compatible with the formation of nanoaggregates.

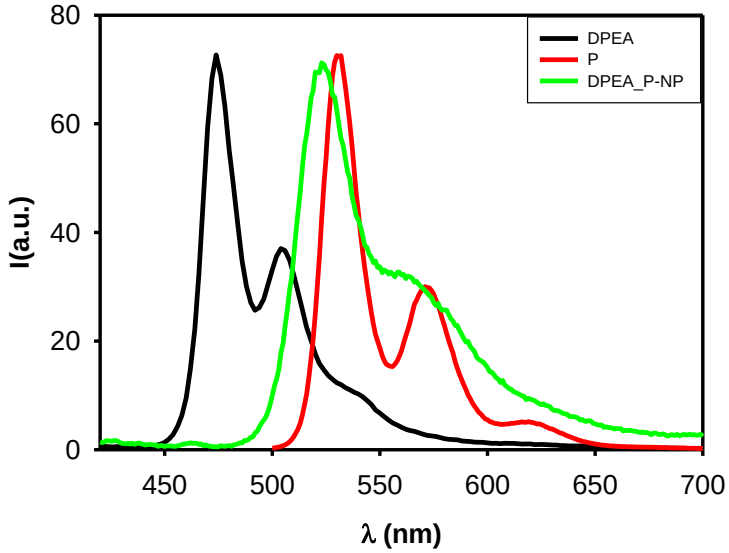

Fig.6.36 Emission spectra of DPEA (black line), P (red line) and of DPEA_P-NP (green line)

In emission spectrum of DPEA_P-NP there is a noticeable drop in intensity (around 90%) of the band at 520 nm, in comparison with emission spectrum of DPEA-NP (Fig.6.37). This is due to the proximity of P which quenches DPEA. However, no sensitized emission of P is observed. This result demonstrates that in this system an electron transfer process occurs which produces a non-luminescent excited state which is deactivated by non-radiative process.

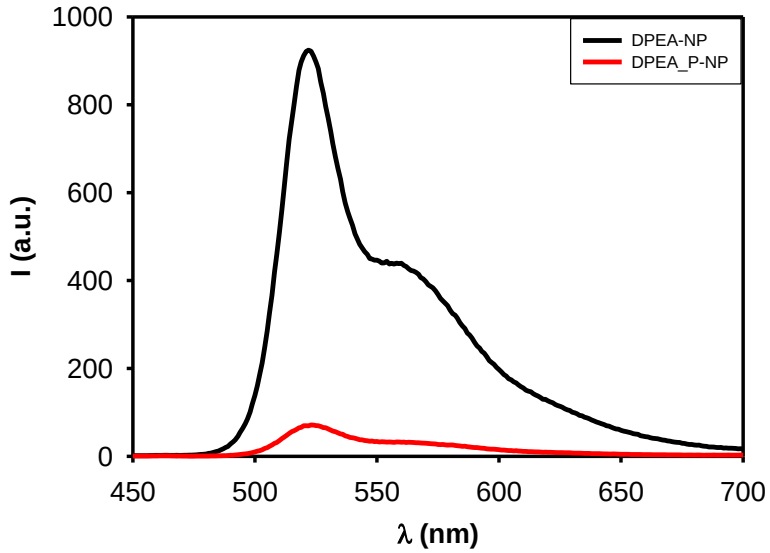

Fig.6.37 Emission spectrum of DPEA-NP (black line) and of DPEA_P-NP (red line)

Nanoparticles presence in DPEA_P-NP was confirmed by the DLS measurements. In DPEA_P-NP, nanoparticles with a diameter of 120 nm are presents with a PDI 0.63. DLS measurement of nanoparticles have been repeated after 24 hours and diameter is 120 nm with PDI 0.50. The decrease of PDI after 24 hours indicates that the system needs this time to rearrange in the most thermodynamically stable state.

The absorption spectrum recorded for DPEA_P-NP has been compared with the one registered 24 hours after injection. They are shown in Fig.6.38. Absorption spectrum registered after 24 hours is not different from the initial one. This shows that this system is stable over time.

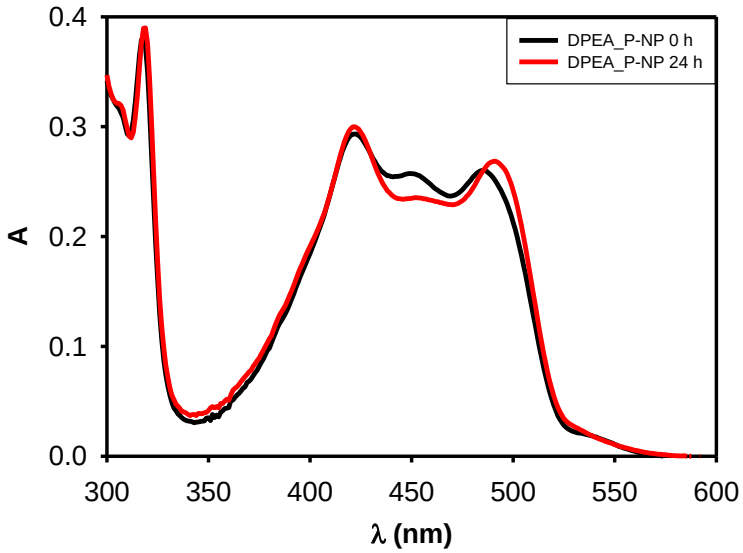

Fig.6.38 Absorption spectrum of DPEA_P-NP 30 minute (black line) and 24 hours (red line) after injection

Emission spectrum recorded for DPEA_P-NP has been compared with the one registered 24 hours after injection. They are shown in Fig.6.39. Emission spectrum registered after 24 hours differ from the initial one differs from the initial one, in particular it is observed that the characteristic band of the DPEA with the maximum at 522nm, is always less intense. This is probably due to a change in the conformation of the aggregate over time.

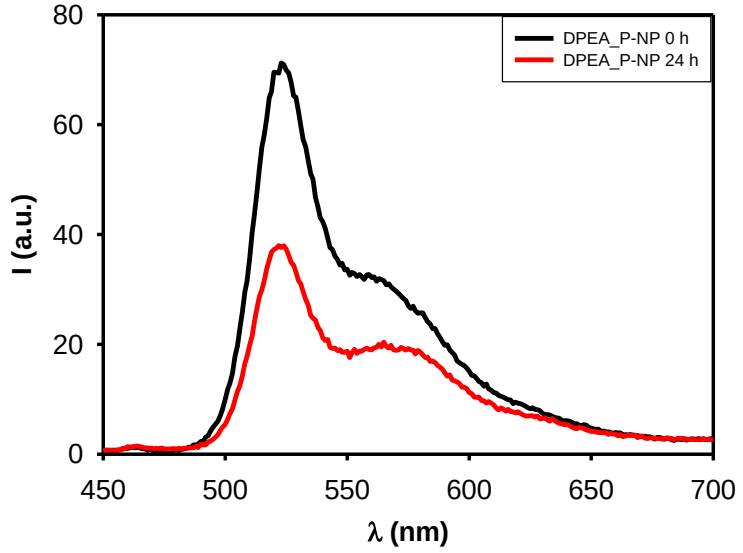

Fig.6.39 Emission spectrum of DPEA_P-NP 30 minutes (black line) and 24 hours (red line) after injection

6.4.3 Characterization of C_P-NP

Molecular nanoparticles with C and P have been prepared following procedure reported in Fig.6.4. Photophysical properties of C and P in THF solution have been compared with nanoparticles C_P-NP.

Absorption spectrum of C_P-NP samples have been registered after 30 minutes of THF solution injection in water (Fig.6.40). The presence of well-defined absorption bands shows the nanoprecipitation process has allowed the dispersion of the C_P-NP in water. It can also be observed that the shape of the absorption spectrum C-NP seems similar to that of the C-NP, with a wide band ranging from 280 nm to 400 nm. This band cover the signal of P, that is present in smaller quantities. It does not allow to understand if P has a behaviour that is closer to that of the monomer or to the aggregate system.

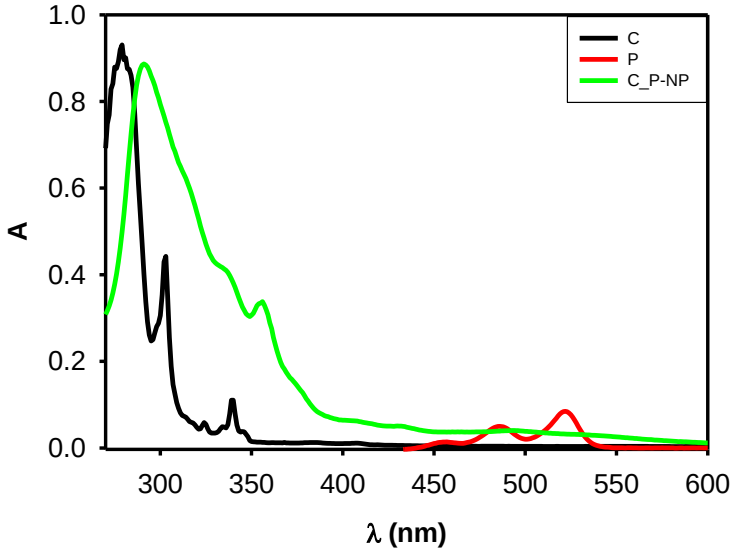

Fig.6.40 Absorption spectrum of C (black line), P (red line) an of C_P-NP (green line)

Fluorescence spectrum of C_P-NP has been obtained by exciting at 380 nm, 30 min after injection in water (Fig.6.41). It can be observed that C emission band is red-shifted of 35 nm-as for C-NP. It is not observed the emission band of P. These observable differences in the absorption and fluorescence spectra of the C_P-NP aqueous dispersions compared to those of the THF molecule are compatible with the formation of nanoaggregates.

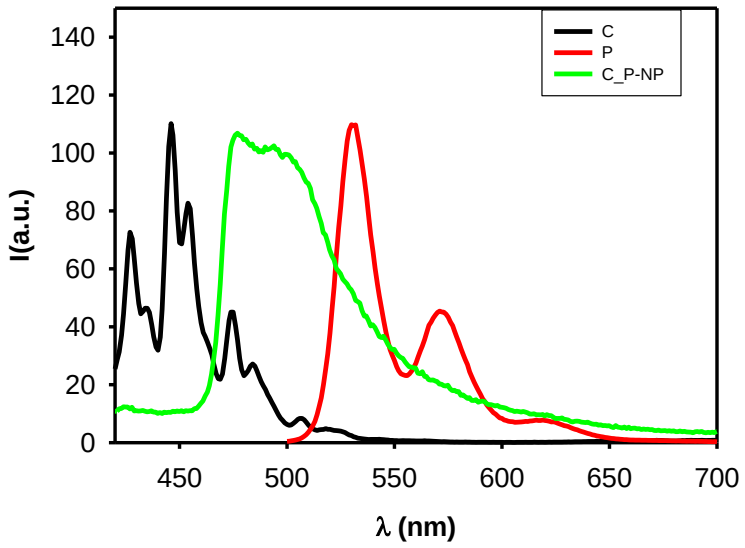

Fig.6.41 Emission spectrum of C (black line), P (red line and of C_P-NP (green line)

In emission spectrum of C_P-NP there is a noticeable drop in intensity (around 90%) of the band at 520 nm, in comparison with emission spectrum of C-NP. This is due to the proximity of P which quenches C. However, no sensitized emission of P is observed. This result demonstrates that in this system an electron transfer process occurs which produces a non-luminescent excited state which is deactivated by non-radiative process (Fig.6.42).

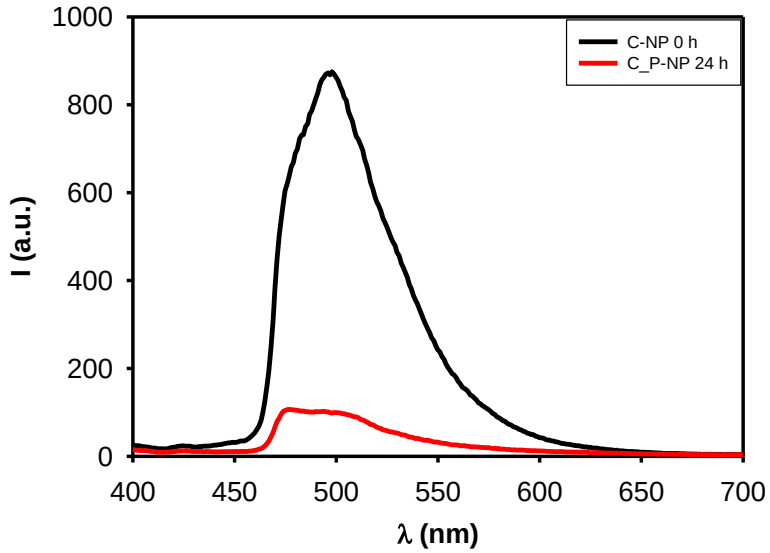

Fig.6.42 Emission spectrum of C-NP 30 minutes (black line) and 24 hours (red line) after injection

Nanoparticles presence in C_P-NP was confirmed by the DLS measurements. In C_P-NP nanoparticles with a diameter of 131 nm are presents with a PDI 0.27. DLS measurement of nanoparticles have been repeated after 24 hours and diameter is 147 nm with PDI 0.26.

The absorption spectrum recorded for C_P-NP has been compared with the one registered 24 hours after injection. They are shown in Fig.6.43. Absorption spectrum registered after 24 hours is not different from the initial one. This shows that this system is stable over time.

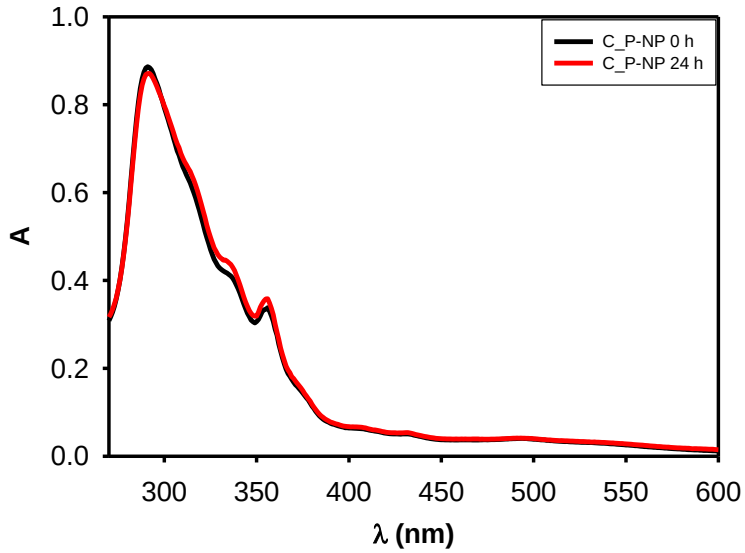

Fig.6.43 Absorption line of C_P-NP 30 minutes (black line) and 24 hours (red line) after injection

Emission spectrum recorded for C_P-NP has been compared with the one registered 24 hours after injection. They are shown in Fig.6.44 Emission spectrum is few different from the initial one. In particular we observe that the characteristic band of C is a little less intense. Results show that, in this case, system reorganization over time is limited.

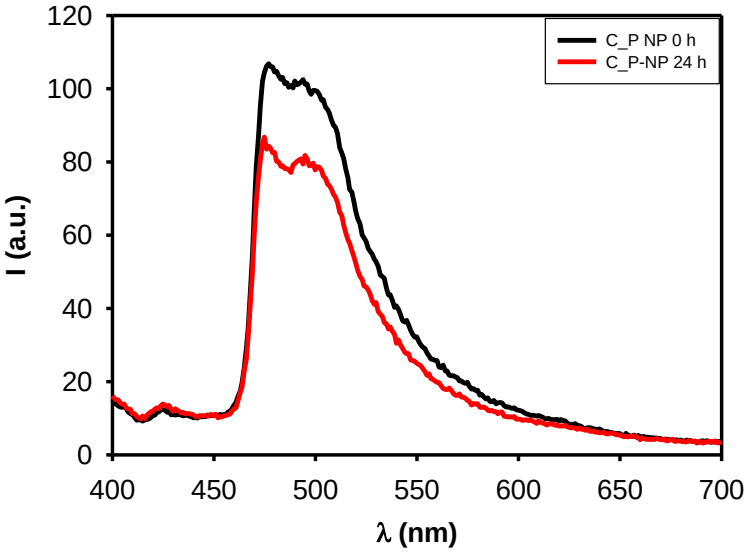

Fig.6.44 Emission spectrum of C_P-NP 30 minutes (black line) and 24 hours (red line) after injection

6.4.4 Characterization of P_Mg-NP

Molecular nanoparticles with P and Mg have been prepared following procedure reported in Fig.6.4. Photophysical properties of P and Mg in THF solution have been compared with nanoparticles P_Mg-NP. Absorption spectrum of P_Mg-NP samples have been registered after 30 minutes of THF solution injection in water (Fig.6.45). The presence of well-defined absorption bands shows the nanoprecipitation process has allowed the dispersion of the P_Mg-NP in water. The shape of P_Mg-NP absorption spectrum of is similar to that of P-NP, with a band ranging from 400nm to 600nm. The characteristic broad band of Mg-NP is not present, but there is a peak at 675nm, like that of Mg in the monomeric form in THF.

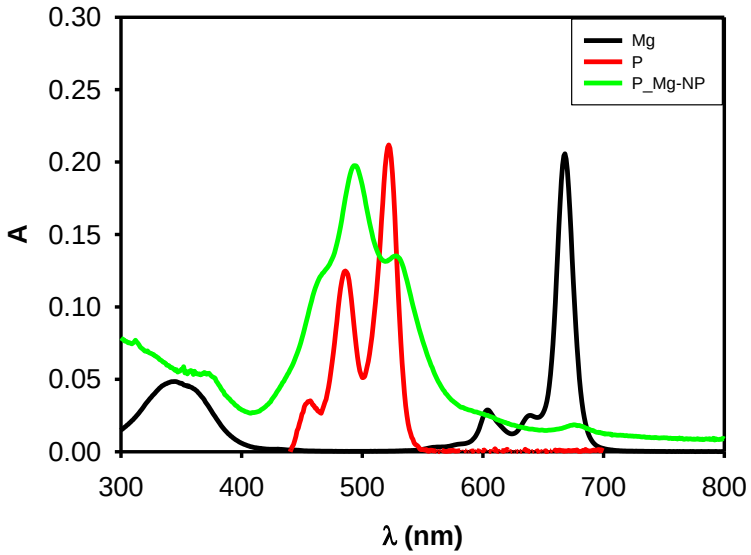

Fig.6.45 Absorption spectrum of Mg (black line), P (red line) and of P_Mg-NP (green line)

Fluorescence spectrum of P_Mg-NP has been obtained by exciting at 470 nm, 30 min after injection in water (Fig.6.46). It can be observed that emission band at 650 nm is similar at the emission band of P-NP. There is not emission of Mg, even exiting at 675 nm. These observable differences in the absorption and fluorescence spectra of the P_Mg-NP aqueous dispersions compared to those of the THF molecule are compatible with the formation of nanoaggregates.

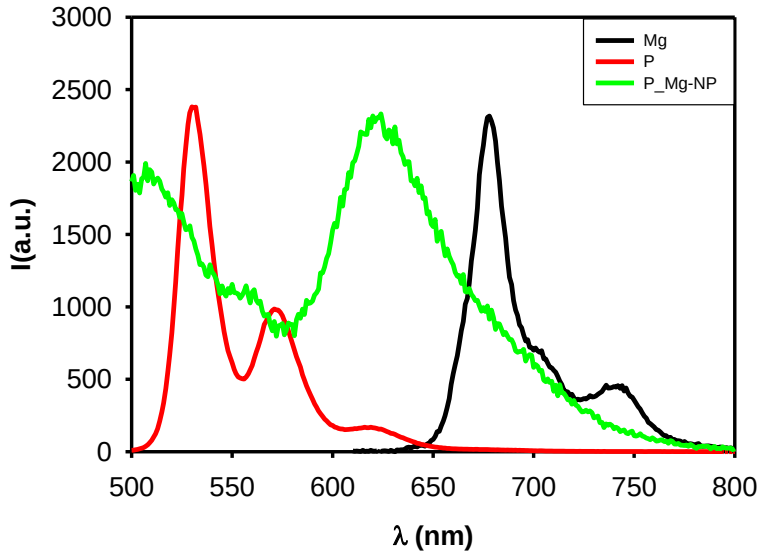

Fig.6.46 Emission spectrum of Mg (black line), P (red line) and Mg_P-NP (green line)

In emission spectrum of P_Mg-NP there is a noticeable drop in intensity (around 85%) of the band at 650 nm, in comparison with emission spectrum of P-NP. This is due to the proximity of Mg which quenches P. However, no sensitized emission of Mg is observed. This result demonstrates that in this system an electron transfer process occurs which produces a non-luminescent excited state which is deactivated by non-radiative process (Fig.6.47).

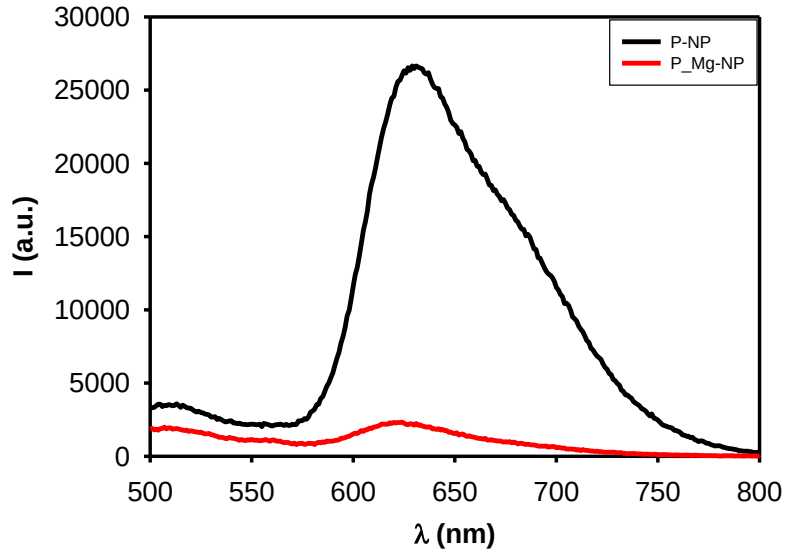

Fig.6.47 Emission spectrum of P-NP (black line) and of P_Mg-NP (red line)

Nanoparticles presence in P_Mg-NP was confirmed by the DLS measurements. In P_Mg-NP nanoparticles with a diameter of 95 nm are presents with a PDI 0.24. DLS measurement of nanoparticles have been repeated after 24 hours and diameter is 91 nm with PDI 0.25. After 48 hours diameter is 92 nm and PDI 0.25. The measurement have been repeated after 168 hours

(7 days) and diameter is 110 nm with PDI 0.19. Results show that nanoparticles are still in solution and there is a slight increase in diameter and PDI reduction over the time.

The absorption spectrum recorded P_Mg-NP has been compared with the ones registered one day (24h), two days (48 h) and 7 days (168 h) after injection. They are shown in Fig.6.48. Absorption spectra do not change over the time. This shows that this system is stable over time.

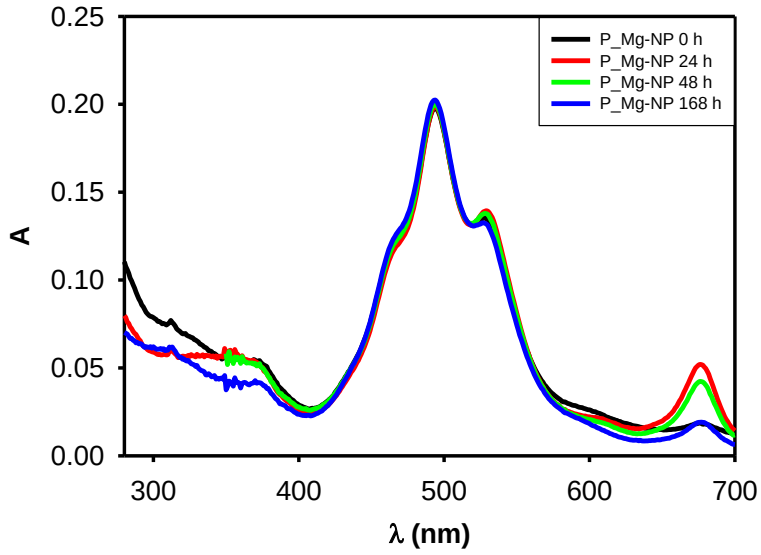

Fig.6.48 Absorption spectrum of P_Mg-NP 30 minutes (black line), 24 hours (red line), 48 hours (green line) and 168 hours (blue line) after injection

Emission spectrum recorded for P_Mg-NP has been compared with the ones registered one day (24h), two days (48 h) and 7 days (168 h) after injection. They are shown in Fig.6.49. It is observed that after 24 hours intensity of emission increases. Probably there is a reorganization in the most thermodynamically stable form, where non radiative process is reduced. Emission is still present after 7 days from and this prove the system is stable for long time.

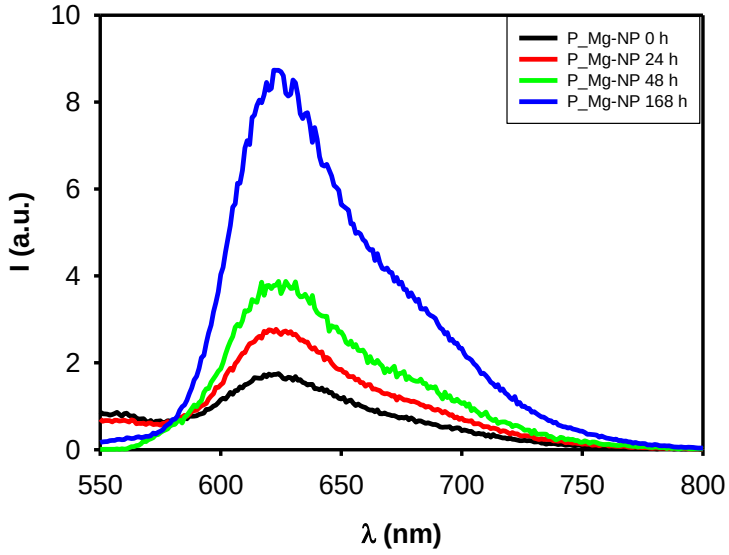

Fig.6.49 Emission spectrum of P_Mg-NP 30 minutes (black line), 24 hours (red line), 48 hours (green line) and 168 hours (blue line) after injection

TCSPC measurements showed that the spectral changes observed upon nanoparticles formation were due to the presence, in the nanoparticles, of populations of fluorophores experiencing different environments. Triple-exponential decays were observed P-NP. Data collected for P-NP are τ_1 = 0.76 ns, B_1 = 2901, τ_2 = 8.84 ns, B_2 = 1196, τ_3 = 21.4 ns, B_3 = 110 and average excited lifetime was calculated to be $< \tau >$ = 2.17 ns.

6.5 Section 3: Nanoparticles of two dye, by mixing

6.5.1 Characterization of DPA_Pm-NP

Molecular nanoparticles with DPA and P have been prepared following procedure reported in Fig.6.5. Absorption spectrum of DPA_Pm-NP samples have been registered after 30 minutes of THF solution injection in water. The presence of well-defined absorption bands shows that the nanoprecipitation process allowed the formation of nanoparticles in water. It has been compared with absorption spectrum of DPA_P-NP. No significant difference in spectrum shape are observed, showing that changing nanoprecipitation method does not affect the absorption properties of the nanoparticles (Fig.6.50).

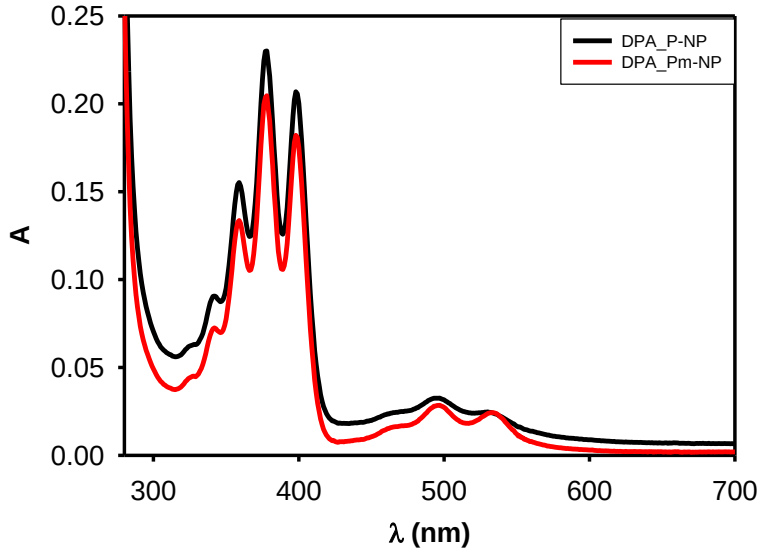

Fig.6.50 Absorption spectrum of DPA_P-NP (black line) and of DPA_Pm-NP (red line)

Fluorescence spectrum of DPA_Pm-NP has been obtained by exciting at 380 nm, 30 min after injection in water. It has been compared with emission spectrum of DPA_P-NP.

In the spectrum there is the broad band of the donor from 400nm to 600nm, much more intense than DPA_P-NP. The emission band of the acceptor is not observed. These results demonstrate that the particles of DPA and P, prepared separately and mixed, do not change their composition in the short term, i.e. there is no exchange of molecules between particles (Fig.6.51).

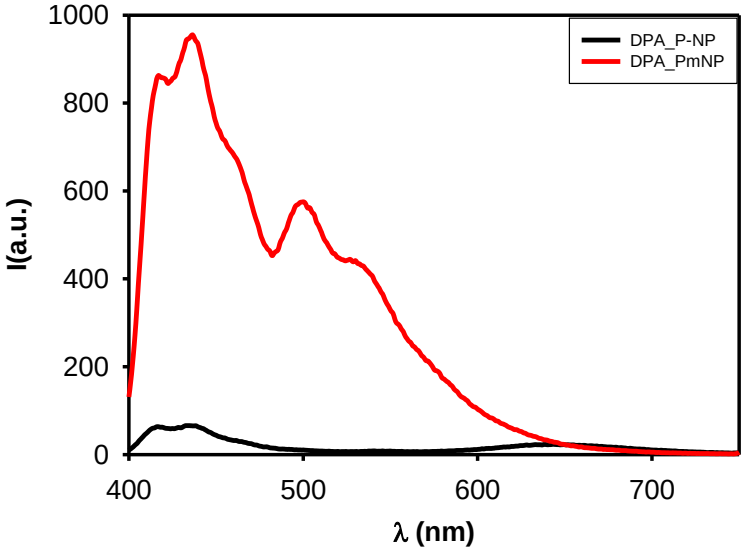

Fig.6.51 Emission spectrum of DPA_P-NP (black line) and of DPA_Pm-NP (red line)

As confirmation, emission of DPA-NP and DPA_Pm-NP is compared. A negligible variation of the donor emission is observed, showing that the DPA-NPs are not quenched by P-NP (Fig.6.52)

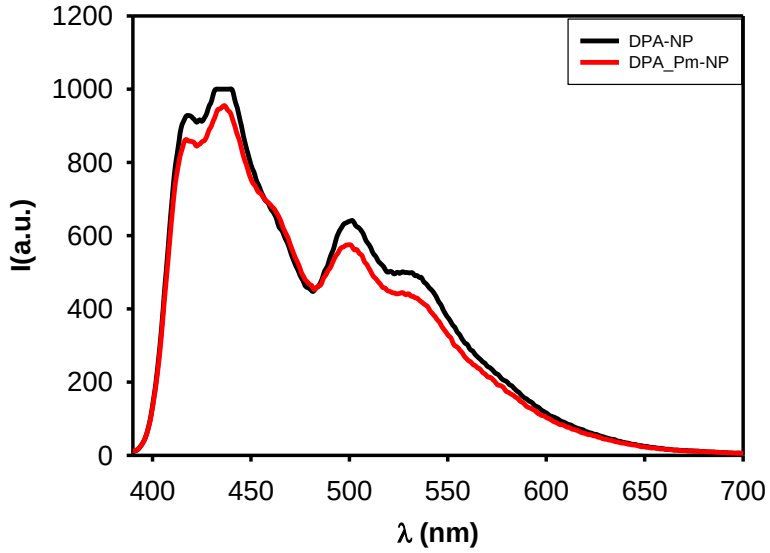

Fig.6.52 Emission spectrum of DPA-NP and of DPA_Pm-NP

The absorption spectrum recorded for DPA_Pm-NP has been compared with the one registered 24 hours after injection. They are shown in Fig.6.53. Absorption spectrum registered after 24 hours is not different from the initial one. This shows that this system is stable over time. It is interesting to note DPA-NP mixed with P-NP are more stable than DPA_P-NP.

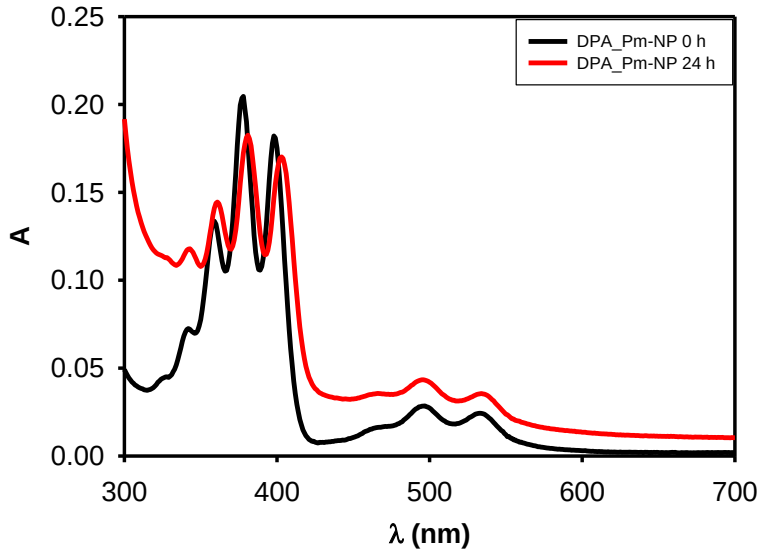

Fig.6.53 Absorption spectrum of DPA_Pm-NP 30 minutes (black line) and 24 hours (red line)

Emission spectrum recorded for DPA_Pm-NP has been compared with the one registered 24 hours after injection. It is observed a decrease of donor emission band and to the appearance of the acceptor emission band. These results show that after a day there is a partial exchange of molecules that leads to the formation of mixed nanoparticles where energy transfer process happens (Fig.6.54).

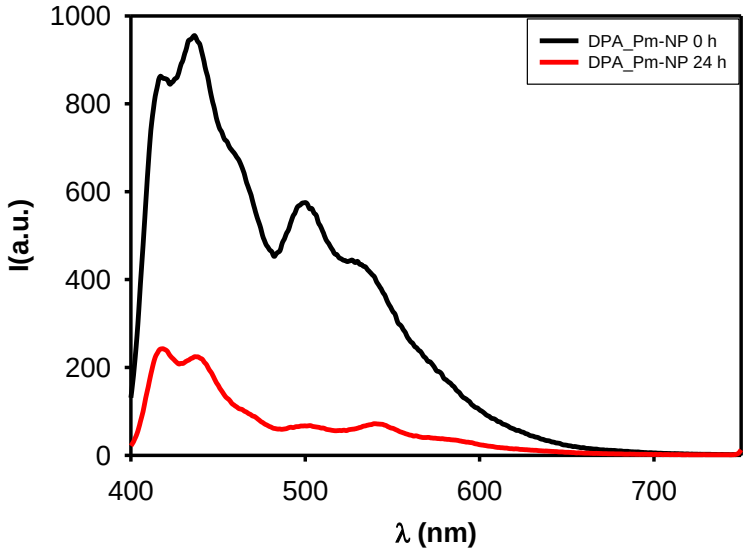

Fig.6.54 Emission spectrum of DPA_Pm-NP 30 minutes (black line) and 24 hours after injection

6.5.2 Characterization of DPEA_Pm-NP

Molecular nanoparticles with DPEA and P have been prepared following procedure reported in Fig.6.5. Absorption spectrum of DPEA_Pm-NP samples have been registered after 30 minutes of THF solution injection in water. The presence of well-defined absorption bands shows that the nanoprecipitation process allowed the formation of nanoparticles in water. It has been compared with absorption spectrum of DPEA_P-NP. No significant difference in spectrum shape are observed, showing that changing nanoprecipitation method does not affect the absorption properties of the nanoparticles (Fig.55).

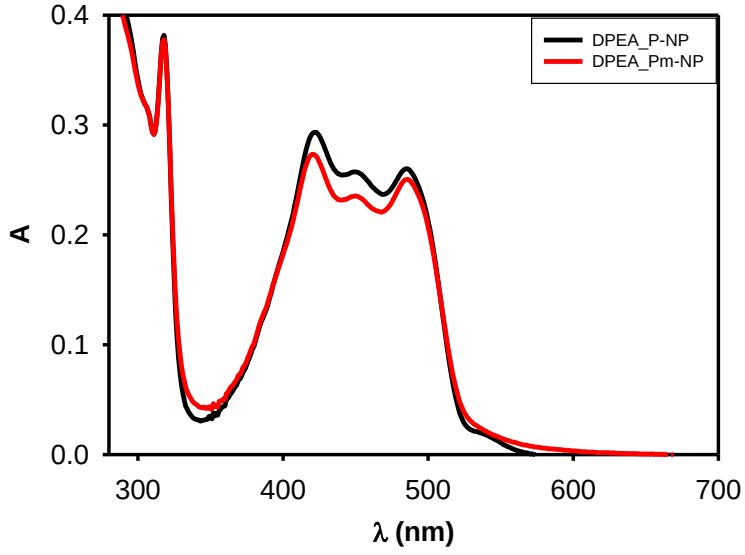

Fig.6.55 Absorption spectrum of DPEA_P-NP (black line) and of DPEA_Pm_NP (red line)

Fluorescence spectrum of DPEA_Pm-NP has been obtained by exciting at 400 nm, 30 minutes after injection in water. It has been compared with emission spectrum of DPEA_P-NP. In the spectrum there is the broad band of the donor with a maximum at 550 nm, much more intense than DPEA_P-NP. The emission band of the acceptor is not observed (Fig.56).

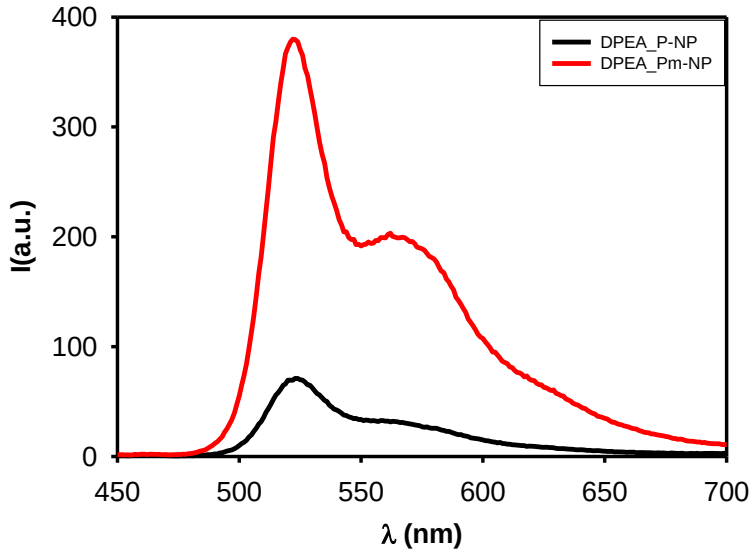

Fig.6.56 Emission spectrum of DPEA_P-NP (black line) and of DPEA_Pm-NP (red line)

However, by comparing the DPEA and DPEA_mP emission spectra, shown in Fig.6.57, it can be observed that there is donor emission is quenched of about 60%. These results demonstrate that the particles of DPEA and P, prepared separately and mixed, change their composition in the short term, i.e. there is exchange of molecules between particles.

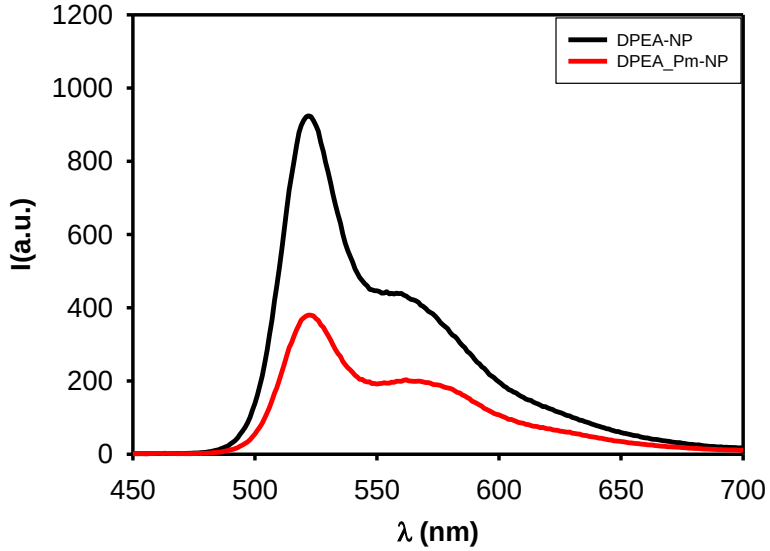

Fig.6.57 Emission spectrum of DPEA-NP (black line) and of DPEA_Pm-NP (red line)

The absorption spectrum recorded for DPEA_Pm-NP has been compared with the one registered 24 hours after injection. They are shown in Fig.6.58. Absorption spectrum registered

after 24 hours is not different from the initial one. This shows that this system is stable over time.

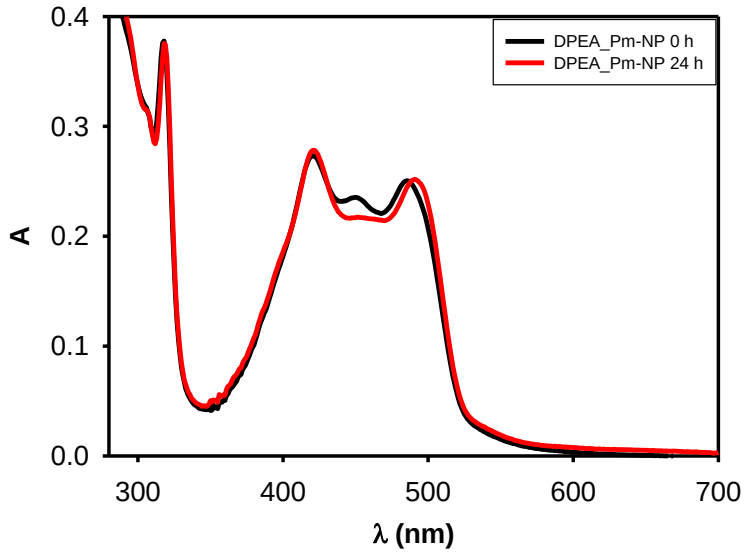

Fig.6.58 Absorption spectrum of DPEA_Pm-NP registered 30 minutes (black line) and 24 hours after injection

Emission spectrum recorded for DPEA_Pm-NP has been compared with the one registered 24 hours after injection. It is observed a huge decrease of donor emission band. This confirms that the process of exchange of molecules between different nanoparticles continues over time (Fig.6.59).

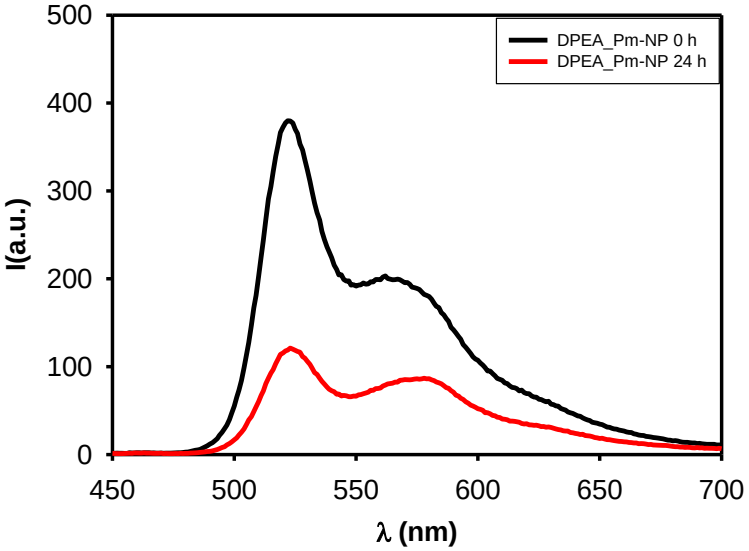

Fig.6.59 Emission spectrum of DPEA_Pm-NP registered 30 minutes (black line) and 24 hours (red line after injection

6.5.3 Characterization of C_Pm-NP

Molecular nanoparticles with C and P have been prepared following procedure reported in Fig.6.5. Absorption spectrum of C_Pm-NP (Fig.6.60) samples have been registered after 30

minutes of THF solution injection in water. The presence of well-defined absorption bands shows that the nanoprecipitation process allowed the formation of nanoparticles in water. It has been compared with absorption spectrum of C_P-NP. No significant difference in spectrum shape are observed, showing that changing nanoprecipitation method does not affect the absorption properties of the nanoparticles.

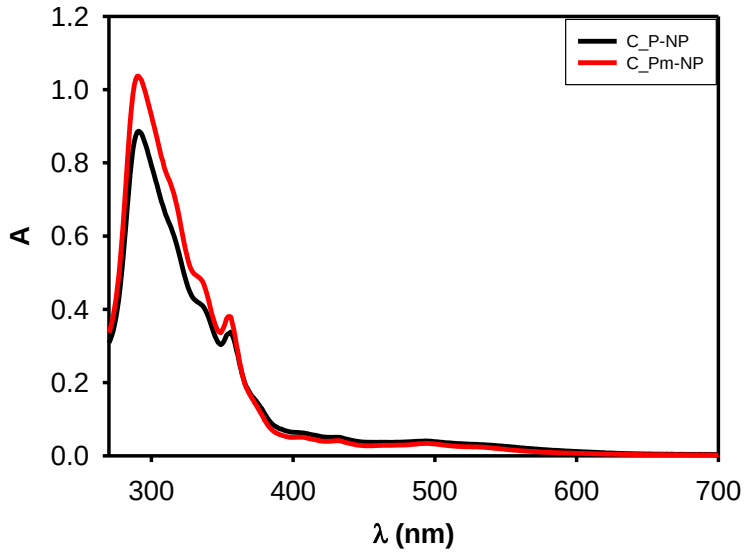

Fig.6.60 Absorption spectrum of C_P-NP (black line) and of C_Pm-NP (red line)

Fluorescence spectrum of C_Pm-NP has been obtained by exciting at 370 nm, 30 min after injection in water. It has been compared with emission spectrum of C_P-NP. In the spectrum there is the broad band of the donor with maximum at 500 nm, much more intense than C_P-NP. The emission band of the acceptor is not observed (Fig.6.61).

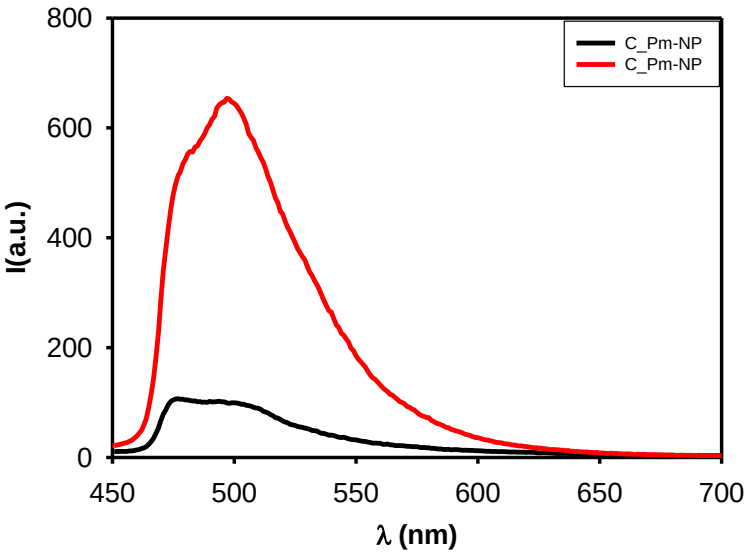

Fig.6.61 Emission spectrum of C-P-NP (black line) and of C_Pm-NP (red line)

However, by comparing the C and C_mP-NP emission spectra, shown in Fig.6.62, it can be observed that donor emission is quenched of about 60%. These results demonstrate that the nanoparticles of C and P, prepared separately and mixed, change a little bit their composition in the short term, i.e. there is exchange of molecules between particles.

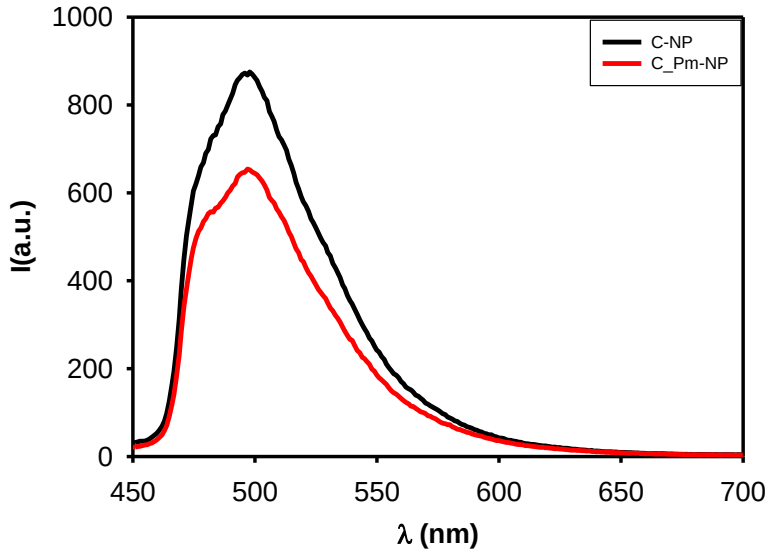

Fig.6.62 Emission spectrum of C-NP (black line) and of C_Pm-NP (red line)

The absorption spectrum recorded for C_Pm-NP has been compared with the one registered 24 hours after injection. They are shown in Fig.6.63. Absorption spectrum registered after 24 hours is not significatively different from the initial one.

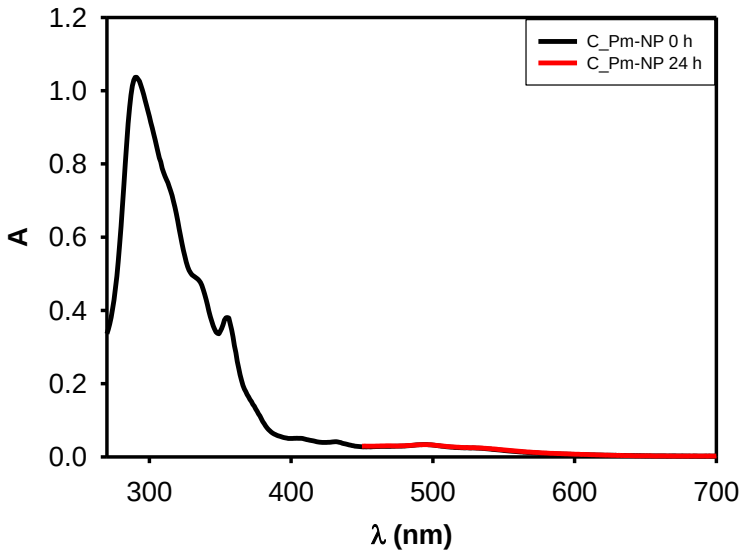

Fig.6.63 Absorption spectrum of C_Pm-NP registered 30 minutes (black line) and 24 hours (red line) after water injection

Emission spectrum recorded of C_Pm-NP has been compared with the one registered 24 hours after injection. It is observed a decrease of donor emission band. These results show that after

a day there is a partial exchange of molecules that leads to the formation of mixed nanoparticles where energy transfer process happens (Fig.6.64).

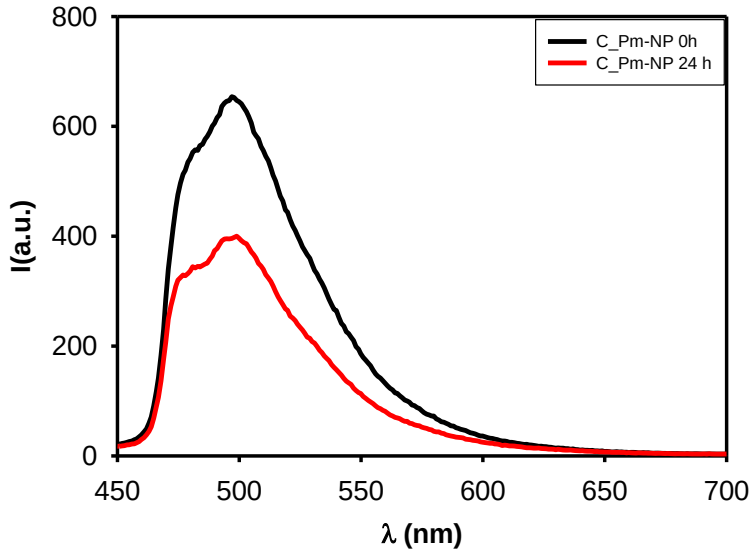

Fig.6.64 Emission spectrum of C_Pm-NP 30 minutes (black line) and 24 hours (red line) after injection

6.5.4 Characterization of Mg_Pm-NP

Molecular nanoparticles with P and Mg have been prepared following procedure reported in Fig.6.5. Absorption spectrum of P_Mgm-NP (Fig.6.65) samples have been registered after 30 minutes of THF solution injection in water. The presence of well-defined absorption bands shows that the nanoprecipitation process allowed the formation of nanoparticles in water. It has been compared with absorption spectrum of P_Mg-NP. It is observed that the peak at 675 nm of Mg is much more evident

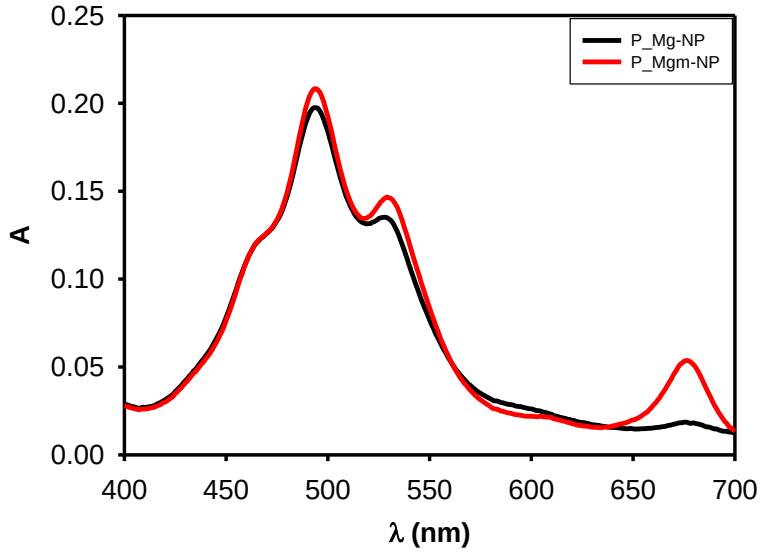

Fig.6.65 Absorption spectrum of P_Mg-NP (black line) and of P_Mgm-NP (red line)

Fluorescence spectrum of P_Mgm-NP has been obtained by exciting at 470 nm, 30 minutes after injection in water. It has been compared with emission spectrum of P_Mg-NP.
In the spectrum there is the broad band of the donor from 600nm to 800nm, much more intense than P_Mg-NP. The emission band of the acceptor is not observed (Fig.6.66).

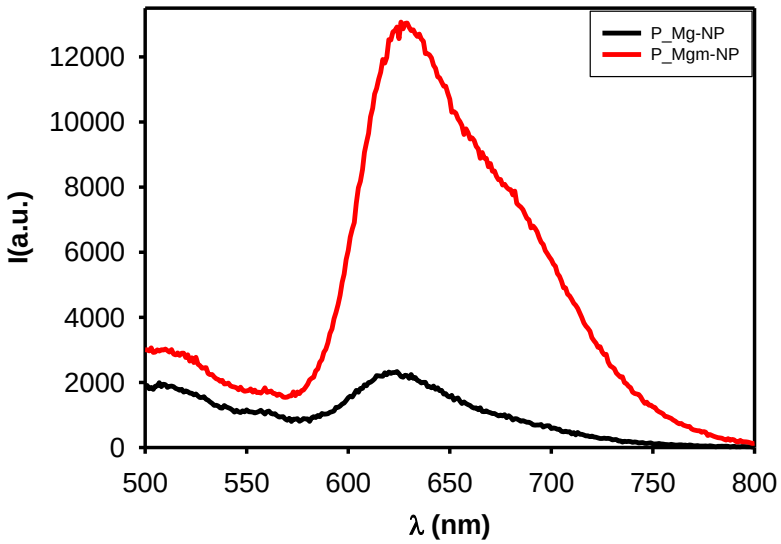

Fig.6.66 Emission spectrum of P_Mg-NP (black line) and of P_Mgm-NP (red line)

However, by comparing the P-NP and P_Mgm-NP emission spectra, shown in Fig.6.67, it can be observed that donor emission is quenched of about 50%. These results demonstrate that the nanoparticles of P and Mg, prepared separately and mixed, change a little bit their composition in the short term, i.e. there is exchange of molecules between particles.

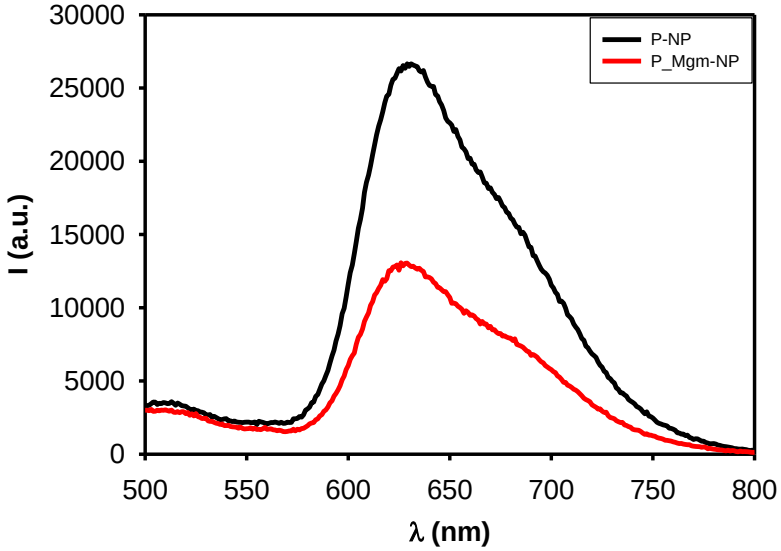

Fig.6.67 Emission spectrum of P-NP (black line) and of P-Mgm-NP (red line)

The absorption spectrum recorded P_Mgm-NP has been compared with the ones registered one day (24h), two days (48 h) and 7 days (168 h) after injection. They are shown in Fig.6.68. Peak at 675 nm disappear over the time, probably because of Mg degradation.

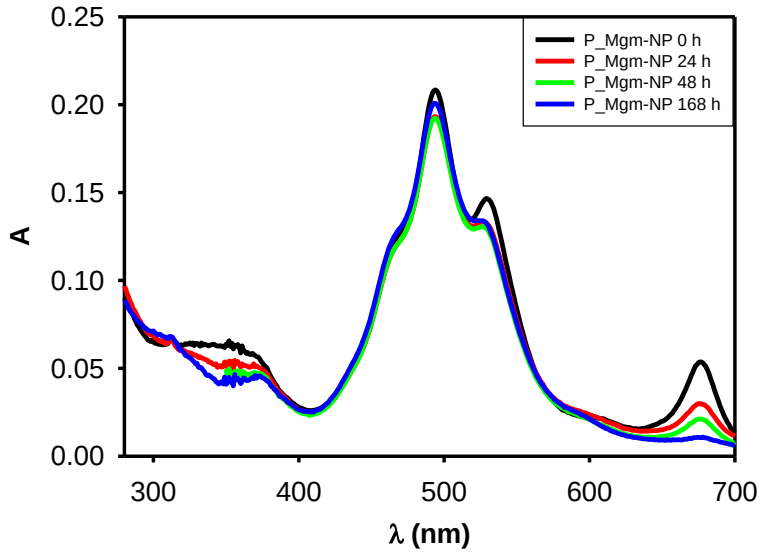

Fig.6.68 Absorption spectrum of P_Mgm-NP registered 30 minutes (black line), 24 hours (red line), 48 hours (green line) and 168 hours (blue line) after injection

Emission spectrum recorded for P_Mgm-NP has been compared with the ones registered one day (24h), two days (48 h) and 7 days (168 h) after injection. They are shown in Fig.6.69 It is observed that after 7 days intensity of emission increases, showing that the degradation of the acceptor leads to the recovery of the donor emission.

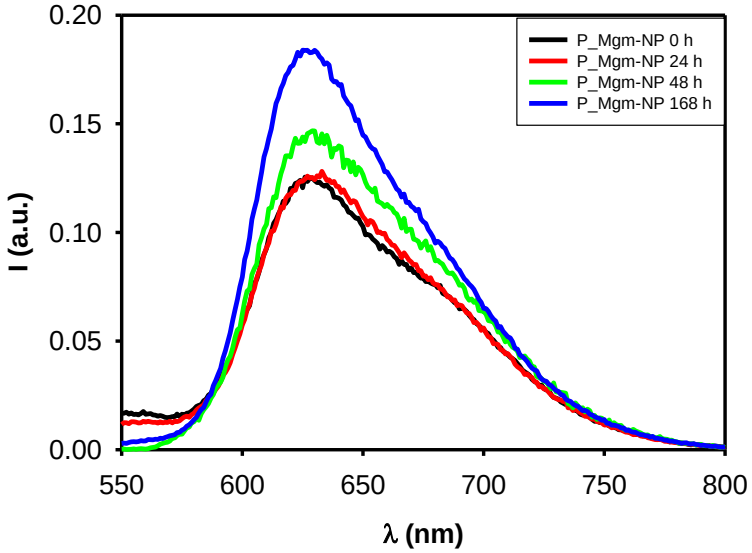

Fig.6.69 Emission spectrum of P_Mgm-NP registered 30 minutes (black line), 24 hours (red line), 48 hours (green line) and 168 hours after injection

TCSPC measurements showed that the spectral changes observed upon nanoparticles formation were due to the presence, in the nanoparticles, of populations of fluorophores experiencing different environments. Triple-exponential decays were observed P_Mgm-NP. Data collected are τ_1 = 0.44 ns, B_1 = 654, τ_2 = 2.36 ns, B_2 = 275, τ_3 = 9.9 ns, B_3 = 46 and average excited lifetime was calculated to be $< \tau >$ = 1.42 ns.

6.6 Conclusions

The aim of the present work was synthesis and characterization of new molecular nanoparticles potentially useful in the diagnostic and therapeutic field (optical imaging, photoacoustic imaging and photoacoustic therapy, photothermal therapy and photodynamic).
Molecular nanoparticles were synthesized using different chromophores (DPA, DPEA, C, P, MgPh) with similar chemical-physical characteristics to allow aggregation in aqueous solution.
Molecular nanoparticle were synthesized by the nanoprecipitation method (Section 1, 2, and 3) to obtain nanoparticles containing a single chromophore (Section 1), nanoparticles containing two chromophores, acceptor and a donor (Section 2) and systems consisting of two types of nanoparticles containing one the donor and the other the acceptor (Section 3).
In Section 1 the properties of molecular nanoparticles obtained from DPA, DPEA, C, P and Mg were analysed. In the presence of Pluronic F127 as a stabilizer NP with dimensions typically of 100-150 nm have been synthetized. Nanoparticles possess photophysical properties very different from molecules in THF. In most cases it is observed a widening and redshifting of the absorption and emission bands. In some cases the appearance of new emission bands characteristic of nanoparticles is observed. This shows that nanoprecipitation is effective for dispersing insoluble molecules in water.
Over time, some nanoparticles tend coalescing nanoparticles and precipitate, this is the case of DPA, but other chromophores such as P and Mg form stable suspensions for more than a week.
In Section 2, nanoparticles with two fluorophores have been analysed. In all nanoparticles, fluorescence of the donor is partially quenched, but only in DPA_P-NP it was observed sensitized emission of acceptor, confirming presence of energy transfer process. In the other cases, an electronic transfer process is happened. This result shows that nanoparticles dissipate absorbed light in heat and this makes them very promising for applications based on the photothermal effect.
In Section 3 have been studied nanoparticles of a single fluorophore mixed in water. Uv-Vis and fluorescence spectra show that such nanoparticles tend to exchange molecules. In this way, the

system is reorganized in mixed nanoparticles, where occur energy and electron transfer processes, already described in Section 2.

This exchange process, which leads to variations in the fluorescence signal can depend on environmental parameters (such as temperature and viscosity) and can be exploited for sensorial or diagnostic purposes.

6.7 Bibliography

1. Yoo, S. I.; Bae, S. H.; Kim, K.-S.; Sohn, B.-H., Nanostructures of diblock copolymer micelles for controlled fluorescence resonance energy transfer. *Soft Matter* **2009,** *5* (16), 2990-2996.
2. Lavis, L. D.; Raines, R. T., Bright ideas for chemical biology. *ACS chemical biology* **2008,** *3* (3), 142-155.
3. Bouchemal, K.; Briançon, S.; Perrier, E.; Fessi, H., Nano-emulsion formulation using spontaneous emulsification: solvent, oil and surfactant optimisation. *Int. J. Pharm.* **2004,** *280* (1-2), 241-251.
4. Basak, R.; Bandyopadhyay, R., Encapsulation of hydrophobic drugs in Pluronic F127 micelles: effects of drug hydrophobicity, solution temperature, and pH. *Langmuir* **2013,** *29* (13), 4350-4356.
5. Hornig, S.; Heinze, T.; Becer, C. R.; Schubert, U. S., Synthetic polymeric nanoparticles by nanoprecipitation. *J. Mater. Chem.* **2009,** *19* (23), 3838-3840.
6. Janczak, J.; Idemori, Y. M., Synthesis, crystal structure and characterisation of aquamagnesium phthalocyanine—MgPc (H2O). The origin of an intense near-IR absorption of magnesium phthalocyanine known as 'X-phase'. *Polyhedron* **2003,** *22* (9), 1167-1181.

Chapter 7: Near-infrared luminescent gold nanoclusters as biosensors

7.1 Introduction

Fluorescence, and more in general photoluminescence, is a powerful tool for investigating living organisms in real time and space, both in vivo and in vitro[1]. In the last decades, thanks to the advent of nanotechnology and nanochemistry, the use of ultra-bright nanoparticles, has been proposed as an innovative and advantageous alternative to molecular probes[2]. Gold nanoparticles have found wide spread in bioimaging[3] and nanomedicine[4] demonstrating high biocompatibility[5]. Nevertheless, the first investigators who observed the photoluminescence of gold nanoparticles reported photoluminescence quantum yield of the order of 0.1 % or lower[6], hence not suitable for fluorescence imaging. Improving the poor photoluminescence brightness of gold nanoparticles was a real challenge and involved a wide interdisciplinary scientific community including chemists, physicists, biologists and engineers. Although, achieving ultra-bright[7] gold nanoparticles, with features that make them actually superior to conventional fluorescent probe, is still challenging.

Photoluminescence is peculiar of small gold nanoparticles: roughly, only particles with a diameter below 2 nm show detectable light emission[8]. Nanoparticles of these sizes show discrete electronic states due to the strong quantum confinement effect[9] and present optical and electronic molecular-like properties. For these reasons they are specifically classified as gold nanoclusters in order to distinguish them from larger gold nanoparticles[3a, 4, 10]. Stabilization of gold nanoclusters in solution typically exploits surface functionalization with suitable organic ligands[11]. In order to achieve specific interaction and to produce protected nanoparticle high affinity of the ligand for the gold surface is required and organic thiolate are the first choice ligands[12]. The use of optimal thiolate ligands was a key strategy for the preparation of molecular like gold clusters with well-defined atomic composition[10b]. These atomically precise thiolate protected golds nanoclusters can be described with the general formula $Au_n(SR)_m$, where R is a generic organic residual.

Bottom-up (chemical) approach to gold nanoclusters has been recognized to guarantee a good control on particle size and mono-dispersity[10b,c,12]. Reduction of gold ionic species (e.g. AuIII in the form of $AuCl^{4-}$) in the presence of thiols as stabilizer had been first proposed by Brust and Shiffrin for the synthesis of gold nanoparticles in a two-phase liquid system using tetraoctylammonium bromide(TOAB) as a phase-transfer agent[13]. The groups of Whetten and

Murray greatly contributed to optimize the process in order to decrease the size of the particles and improve structural control[6, 14]. As schematized in Fig.7.1, in the first step (i) a large excess of thiol (molar ratio at least 3:1 with respect to gold) converts AuIII into AuI–SR polymers.

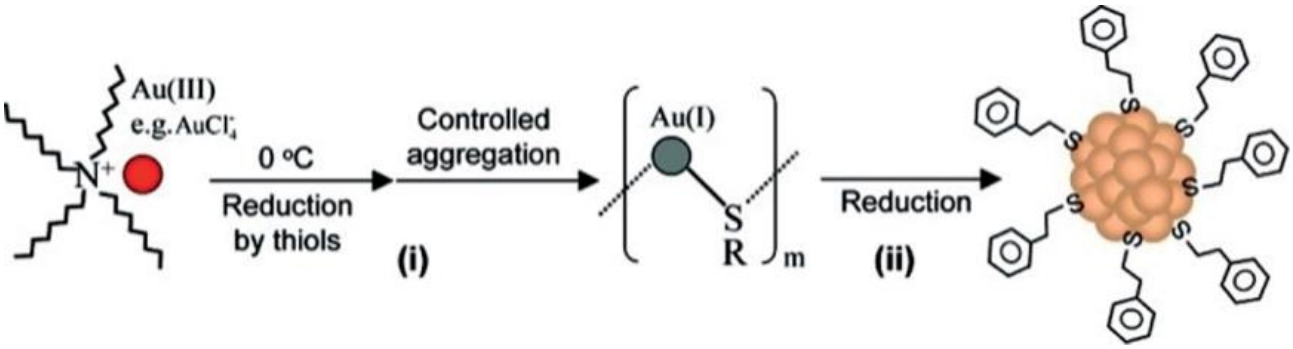

Fig.7.1 Scheme of the synthesis of gold nanoclusters. In the first stage (i) Au-thiolate oligomers are formed. In a second step (ii) the oligomers are reduced to give the gold nanoclusters [15].

We would like to stress that according to recent investigation these polymeric motifs are partially maintained in the final nanoclusters structure and they are considered to play a major role in determining the photoluminescence properties of the nanoclusters and in particular their photoluminescence quantum yield. AuI-thiolate polymers are hence reduced to give Au^0 using a large excess of reductant[15]. Despite such an excess of reducing agent the reaction is not complete and the presence of residual AuI atoms in the nanoclusters surface is fundamental both in conferring adequate chemical stability and in determining the optical and photoluminescence properties.

In the size-focusing phenomenon the first step, reduction of AuIII by excess thiol to form the AuI/SR polymeric inter-mediate, was done at a low temperature (e.g. 0 °C) rather than at room temperature. After addition of $NaBH_4$ a gradual growth of monodisperse Au25 nanoclusters from the size mixed product was observed (Fig.7.2).

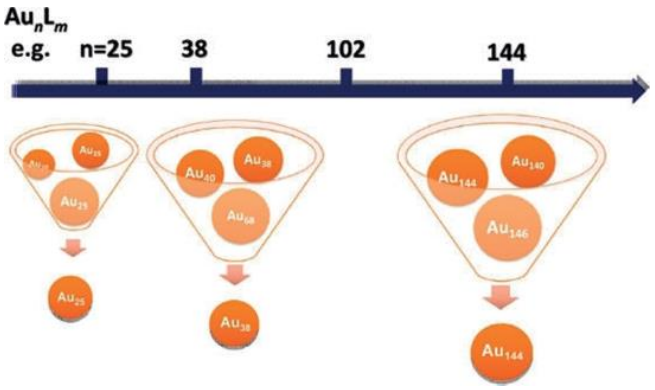

Fig.7.2 Schematization of the size focusing approach to the atomically controlled synthesis of gold nanoclusters.

This size-focusing growth process was found to be quite common (e.g., not limited by the type of thiol) and was demonstrated for other NC sizes [e.g. $Au_{38}(SR)_{24}$, $Au_{144}(SR)_{60}$][16].The

underlying principle of this size-focusing process is primarily related to the peculiar stability of certain sized $Au_n(SR)_m$ nanoclusters.

The use of mild reduction conditions has been proposed to achieve a better control on the size of gold nanoclusters. In particular carbon monoxide has been proposed as a mild reducing agent to control and tune gold nanoclusters size[17]. Reduction in alkaline conditions (NaOH) was also proposed as a size-control strategy in order to control the reducing activity of $NaBH_4$[18].

Differently from large nanoparticles (diameter larger than 2 nm, that show a typical broad surface plasmon resonance band at ca. 2.4 eV in the absorption spectrum)[19], gold nanoclusters present molecular-like transition arising from efficient quantum effect[10c]. The absorption spectra of series of nanoclusters have been recently reviewed.

The absorption spectrum of one of the most characterized and representative nanoclusters $Au_{25}(RS)_{18}$ is shown in Fig.7.3 where defined distinct absorption bands can be observed at 1.8, 2.75 and 3.1 eV.

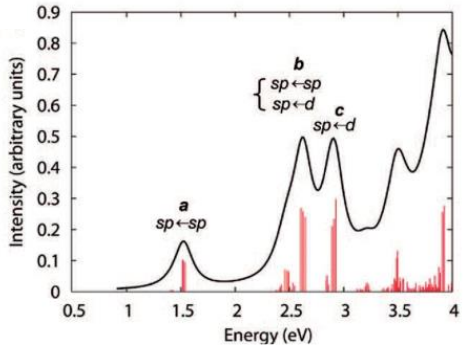

Fig.7.3 The theoretical absorption spectrum of $Au_{25}(SH)_{18}$. Peak assignments: peak a corresponds to 1.8 eV, observed peak b corresponds to 2.75 eV (observed), and peak c corresponds to 3.1 eV (observed)

Attribution of these transitions. Attribution of these transitions by Jim and co-workers was based on time-dependent density functional theory (TD-DFT) calculations[20] taking into account the structure obtained by X-ray crystallographic analysis. The calculated absorption spectrum matches quite satisfactory the experimental one. In particular, the experimental peak at 1.8 eV was interpreted essentially as an intraband (sp-sp) HOMO-to-LUMO transition. Moreover, the HOMO and LUMO derive mainly from the combination of atomic orbitals of the 13 gold atoms in the icosahedral core rather than the 12 surface gold atoms. As a consequence, the lowest energy optical absorption involves a transition localized on the Au_{13} core.

Independently on the size, the molar absorption coefficient[21] is of the order of $10^4 \cdot M^{-1}$ cm^{-1}. The position of the absorption peaks is, on the contrary, strongly size dependent and the lowest energy transition, in particular, it decreases its maximum wavelength upon decreasing the nanocluster size as expected for quantum effect.

For larger gold nanoclusters, as the ubiquitous $Au_{144}(SCH_2CH_2Ph)_{60}$[22] (that still exhibit a stepwise, multiple-band absorption spectrum, indicating quantum confinement of electrons in the particle) a molar extinction coefficient $4 \cdot 10^5$ M^{-1} cm^{-1} at 510 nm was reported. This value is considerably higher than what reported for smaller particles, nevertheless a significant contribution to light extinction due plasmon resonance as well as light scattering is expected considering the size of the nanoclusters and actual absorption coefficient is expected to be much less.

In bulk conductive metals, valence electrons are free to move in the lattice through the conduction band. In the case of gold nanoclusters, size of the metal starts to become comparable to the Fermi wavelength of an electron, and quantized electronic states[23] and energy levels start to emerge[24]. As a consequence, the most characteristic photoluminescence properties of gold nanoclusters can be interpreted in terms of molecular orbitals and transitions between electronic states, analogously to what happens in molecules. Both metal atoms and stabilizing ligands are expected to be involved in the electronic transition responsible for the photoluminescence emission to an extent that depends on their contribution to the HOMO–LUMO molecular orbitals. The typical core shell structure of the gold nanoclusters and the presence of staple-like motif suggested simplified interpretations where the emission is assumed to arise from a specific part of the nanoclusters.

Surface ligands have undoubtedly been proven to play a fundamental role in gold nanoclusters photoluminescence [25]. This emerges clearly in the work of Wang et al., which showed that gold nanoclusters ranging from Au_{11} to Au_{201} and protected by different ligands, showed similar NIR emissions (Fig.7.4), which did not scale accordingly to their number of atoms[26].

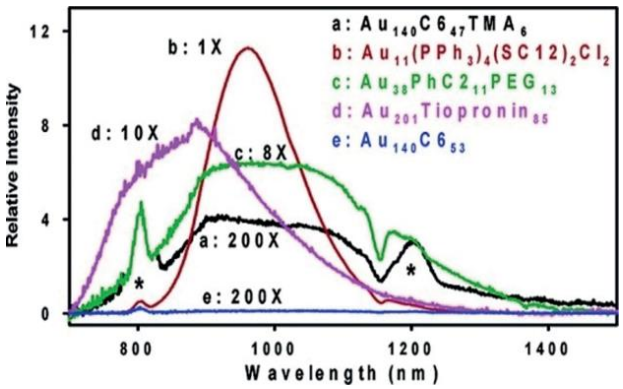

Fig.7.4 Gold nanoclusters with different core sizes and monolayers. C_6, C_{12},PhC_2, PEG, and PPh_3 represent hexanethiolate, dodecanethiolate, phenyl-ethanethiol, poly(ethylene glycol) (MW 350) thiolate, and triphenylphosphine, respectively

The same group reported that this NIR emission intensity linearly increases with the fraction of polar thiolate introduced on the clusters surface by ligand exchange (conserving core sizes). In particular, they showed that the photoluminescence enhancement was proportional to the

electron withdrawing capability of the ligand inserted and to the charge shift of the cluster core toward more positive values.

As discussed in the previous section, the effect of the nature of the stabilizing ligands on the photoluminescence properties of gold nanoclusters is well documented and generally accepted. This effect was partially attributed to the polarity of the ligands, but different authors suggested that strong electronic coupling between gold atoms and ligand molecules originates charge transfer states where electrons are photo-injected form the ligands to the metal core. According to Jin and co-workers, formation of the charge transfer state can occur according to two different mechanisms (Fig.7.5): (i) charge transfer from the ligands to the metal nanoparticle core through the gold–S bonds, and (ii) direct donation of delocalized electrons from electron-rich atoms or groups of the ligands to the metal core.

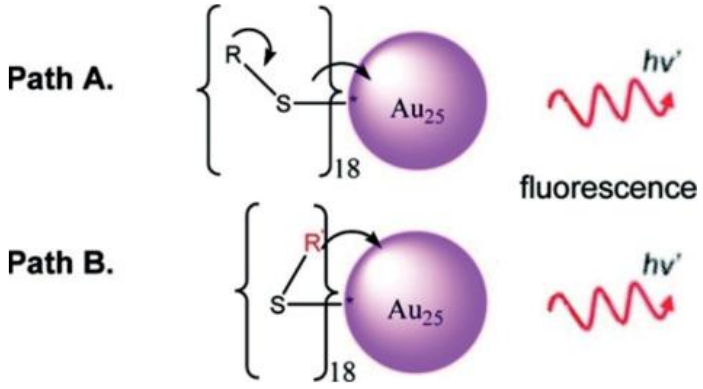

Fig.7.5 Mechanisms of formation of emissive LMCT states in Au NC. (A) charge transfer from the ligands to the metal nanoparticle core through the Au–S bonds, and (B) direct donation of delocalized electrons of electron-rich atoms or groups of the ligands to the metal core.

First reports about the photoluminescence of gold nanoclusters revealed very low photoluminescence quantum yield (typically below 0.1 %) and hence a brightness too low for practical application in bio-imaging and bio-sensing[27]. A big effort has been done by several research groups to enhance the brightness of gold nanoclusters mostly by improving the photoluminescence quantum yield.

Brightness of nanoprobes depends not only on the photoluminescence quantum yield but, strongly, on the efficiency of absorption of the excitation light (ε). Gold nanoclusters present a molar absorption coefficient ($\varepsilon \approx 10^4\ M^{-1}cm^{-1}$) which is about one order of magnitude lower than organic chromophores. In order to improve this feature, our and other groups proposed the design of hybrid structures that combine the photoluminescence properties of gold nanoclusters with the optical properties of organic dyes in order to enhance the brightness of the inorganic emitters. A considerable improvement of brightness can in fact be achieved by introducing ligands able to efficiently adsorb light (chromophores) and to transfer the excitation energy to the emitting gold core[28]. According to this strategy, Montalti group

prepared Au_{101} nanoclusters[29] stabilized with phosphine ligands terminated with a pyrene chromophores (Fig.7.6).

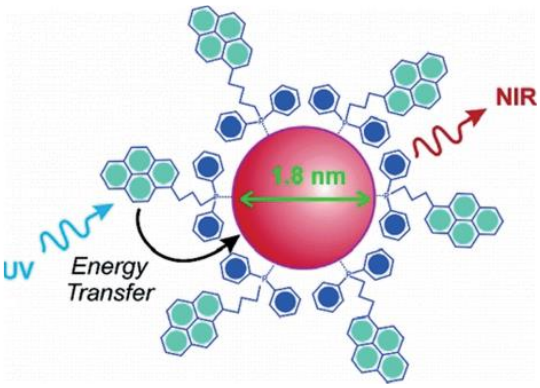

Fig.7.6 Scheme of a hybrid gold nanoparticles functionalized with pyrene chromophores. The ligands absorb the excitation light very efficiently and they transfer the excitation energy to the Au core producing sensitized emission. The light-harvesting process increases the NCs brightness.

Absorption spectra of nanoparticles are dominated by the contributions of the pyrene chromophores in the UV regions and are almost coincident with the absorption spectrum of the nanoclusters in the visible-NIR range. A partial broadening and bathochromic shift of the pyrene was observed upon binding to the nanoclusters. An increase of brightness of about one order of magnitude was detected upon excitation of the organic chromophores demonstrating that excitation energy absorbed by the pyrene was transferred with high efficiency (> 95 %) to the gold nanoclusters producing sensitized NIR emission (Fig.7.6). The occurrence of the efficient energy transfer process[30] was confirmed by the presence of the pyrene electronic transition peaks in the photoluminescence excitation spectrum of the gold NC. More detailed investigation revealed that the enhanced brightness was not only the effect of the energy transfer process from the pyrene ligand to the gold but that also a large increase of the photoluminescence quantum yield occurred because of the replacement of the simple triphenylphosphine with the pyrene terminated ligands.

More recently, Montalti group proposed a different strategy to turn on/off the photoluminescence of Au144 nanoclusters using as organic sensitizer a photoswitchable azobenzene derivative (Fig.7.7)[28b].

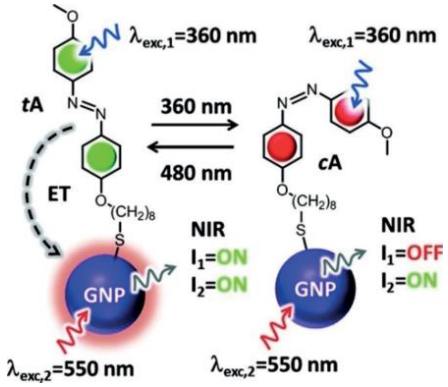

Fig.7.7 Chemical formula of the trans azobenzene tA and of its cisisomercA bound to gold nanoparticles (GNP). When the ligands are in the trans form (left, tAGNP, ON state) ET from tA to the GNP produces NIR-sensitized emission upon ligand excitation. Such contributions, owing to sensitization, are lost upon PI in cA covered NPs (right, cA-GNP, OFF state).

The conversion of the trans form of the ligand into the cis one took place almost quantitatively (> 95 %) with a quantum yield identical to the one measured for the same molecule free in solution (upon irradiation at 360 nm). Regeneration of 70 % of trans was, in turn, achieved by irradiation of cA-GNP at 480 nm.

Photophysical results confirmed the occurrence of an excitation energy transfer process from the ligands to the gold nanoclusters that produced sensitized near-infrared emission. Because of this process, the excitation efficiency of the gold core, upon excitation of the ligands, is much higher for the trans form than for the cis one (Fig.7.8).

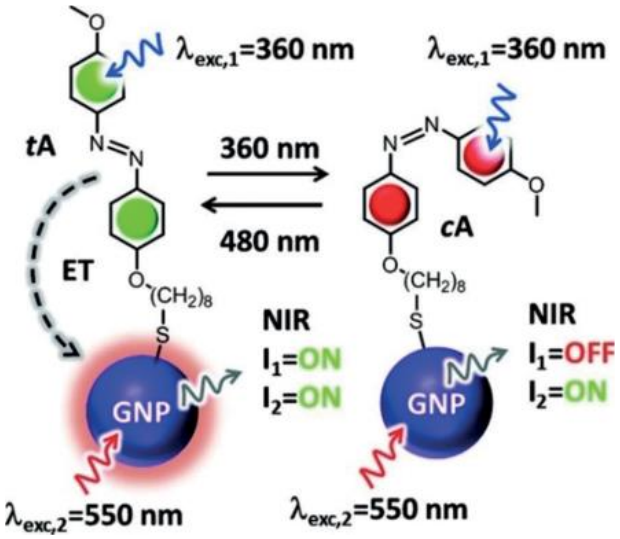

Fig.7.8 Chemical formula of the trans azobenzene tA and of its cisisomer cA bound to gold NP (GNP). When the ligands are in the trans form (left, tAGNP, ON state) ET from tA to the GNP produces NIR-sensitized emission upon ligand excitation. Such contributions, owing to sensitization, are lost upon PI in cA covered NPs (right, cA-GNP, OFF state).

Moreover, thanks to the energy transfer process the photoluminescence brightness of the gold nanoclusters is enhanced upon excitation of the ligands, both in the cis and trans form with respect to the bare nanoclusters. Interestingly, in these azobenzene functionalized gold nanoclusters, the photo-isomerization rate of the ligands was not affected by the interaction with the gold nanoclusters. This outcome demonstrated that excitation energy transfer to gold assists photo-isomerization, rather than competing with it. Recent developments in the design of photoluminescence gold nanoclusters demonstrated that several approaches permit to enhance the initially reported poor brightness of these nanoparticles. We believe that luminescent nanocluster will pave the road to hybrid ultra-bright nanoparticles that will match the best properties of organic and inorganic nanomaterials to give innovative photoluminescence probes for bio-applications.

7.2 Summary

In this chapter small gold nanoclusters functionalised with seven different kinds of thiol have been studied in order to investigate their ability to recognize and signal the presence of some important active pharmaceutical ingredients (API). Best results have been obtained with thiols 1 and 3 showed in Fig.7.9. These gold nanoclusters have been respectively called AuNCs-1 and AuNCs-3.

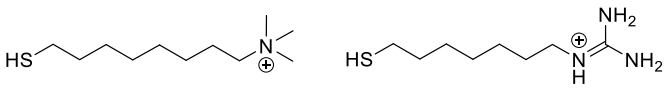

Fig.7.9 structure of thiols1(left) and 3(right) for coating gold nanoclusters

Gold nanocluster were characterized via UV-Vis absorption photoluminescence spectroscopy. They absorb in all UV-visible region and show emission in NIR region (Fig.7.10).

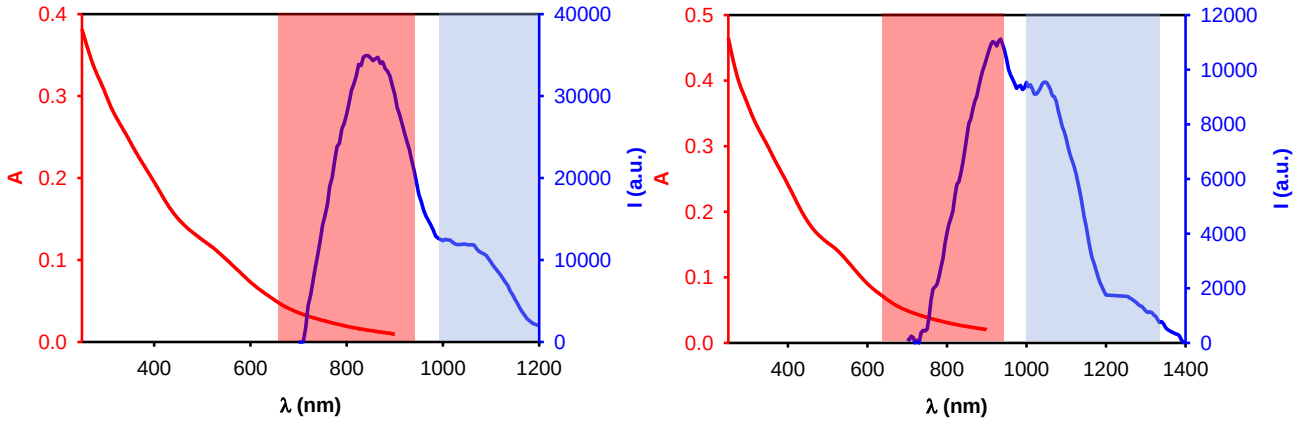

Fig.7.10 Photophysical properties of AuNCs-1 (left) and AuNCs-3 (right)

Gold nanocluster have been tested with API reported in Fig.7.11, that are some of most common commercial anti-inflammatory molecules.

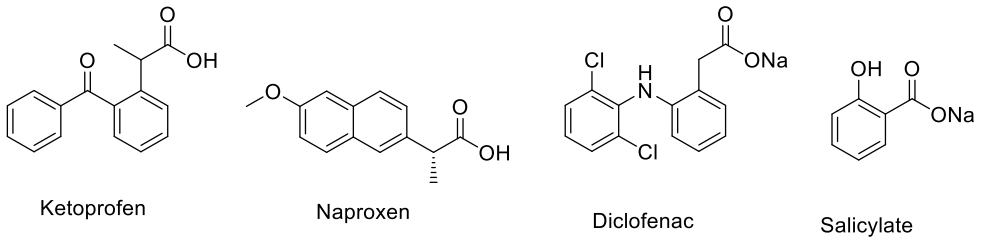

Fig.7.11 API structures

Experiments have been conducted in biological conditions at pH 7 (HEPES buffer in water) where ligands have a terminal quaternary nitrogen positively charged and API are dissociated and have a negative charge. The driving force of gold nanoclusters and amphiphilic organic anions interaction is a combination of hydrophobic effects due to the presence of an apolar portion of the substrate which can accommodate in the apolar monolayer alkyl layer of the nanoclusters, and the simultaneous ion-pairing interaction which involves the charged head

groups. This combination of effects provides selectivity and high affinity. A simple model to understand why the just described recognition process is expected to modify photophysical properties of gold nanoclusters takes into account two different mechanisms. The first mechanism considers the direct excitation energy and electron transfer processes involving API and gold nanoclusters upon binding. The second mechanism take into consideration the presence of positively charged API on gold nanoclusters surface that changes gold nanoclusters global charge distribution and hence influences their photophysical properties. We would like to stress that while the first mechanism is expected to affect the photoluminescence of both the API molecules and the gold NPs, the second one only modifies the gold emission. In Fig.7.12 are reported API photophysical properties. All of the molecules have an absorption band in the UV region and an emission in visible region. In order to discriminate which mechanisms of interaction between gold nanoclusters and API were involved, all the hybrid systems were exited at two different wavelengths: at 300 nm where API absorb, and both mechanisms can occur, and at 500 nm where API do not absorb and only the second mechanism can occur.

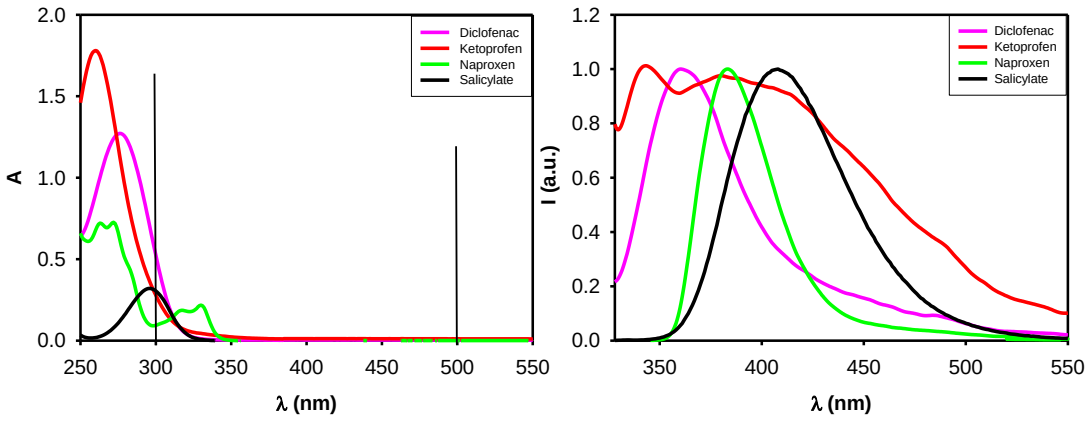

Fig.7.12 On the left: API absorption spectra. On the right: API emission spectra

In Fig.7.13 percentage variation of AuNCs-1NIR emission exited at 300 nm and at 500 nm as API concentration is increased are reported.

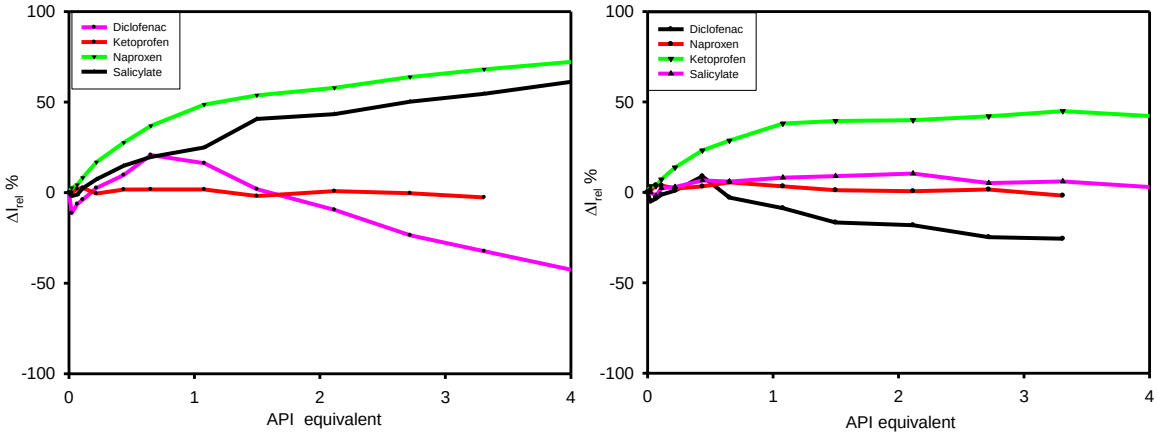

Fig.7.13 On the left: percentual variation of AuNCs-1 NIR emission exited at 300 nm; on the right:) percentual variation of AuNCs-1 NIR emission exited at 300 nm

Considering only most interesting trends, we can observe that in presence of Naproxen there is a considerable emission increase, almost 100%. Then, by comparing the response of the system excited at 300 nm and at 500 nm, we can deduce that both mechanisms discussed above contribute concurrently with the same importance.

Similarly, with salicylate it is possible observe an emission increase of about 100%. But in this case direct energy transfer from the drug molecules to gold nanoclusters is the only contribution. In fact, when the system is excited at 500 nm there are no significative AuNCs-1 emission changes.

In Fig.7.14 the percentual variation of AuNCs-3 NIR emission exited at 300 nm and at 500 nm as API concentration is increased are reported.

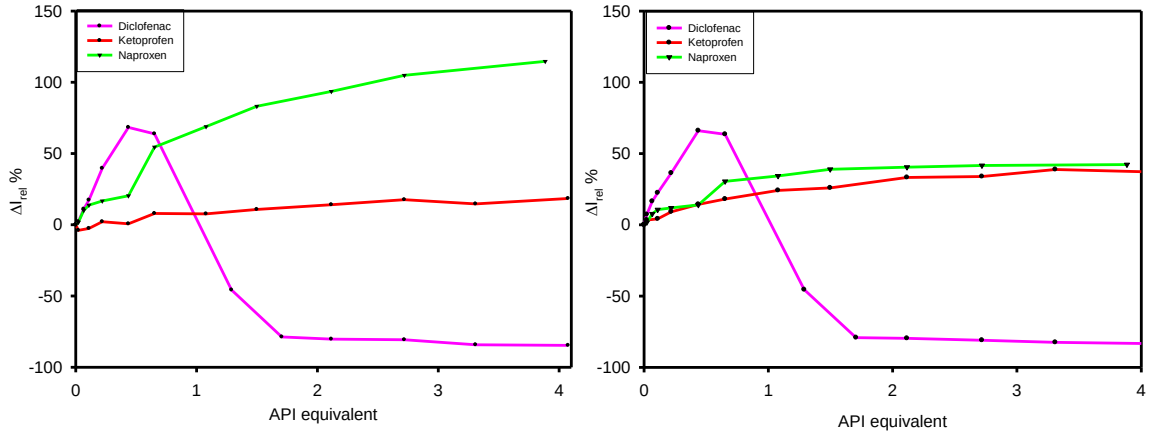

Fig.7.14 On the left: percentual variation of AuNCs-3 NIR emission exited at 300 nm; on the right:) percentual variation of AuNCs-3 NIR emission exited at 300 nm

In presence of Naproxen a huge enhancement of emission is observed, more than 100%. Then, by comparing the system response upon excitation at 300 nm and at 500 nm, we can say that both mechanisms occur concurrently giving similar contributions.

As shown in Fig.7.14, in presence of Diclofenac at the beginning AuNCs-3 emission increases but beyond a concentration threshold emission is totally quenched. This result suggests that a high concentration of Diclofenac on the surface of gold the formation of organic dimer or aggregates quenches any emission. In conclusion in this work have been developed a new class of photophysical API-sensors operating in biological conditions and active in the NIR spectral region where biological samples and tissues are more transparent and that is attracting a lot of attentions for bioimaging and sensing. Gold nanoclusters based sensors have showed a good selectivity towards specific drugs, demonstrating that these systems are potentially suitable as drug sensors.

7.3 Gold nanocluster synthesis

Monolayer protected gold nanoclusters have been prepared by Prof. Mancin at Department of Chemistry of University of Padova. Monolayer protected gold nanoclusters were prepared modifying a previously reported two-step procedure[31]. A solution of $HAuCl_4 \cdot 3H2O$ (50 mg, 0.127 mmol, 1 equiv) in water (2 mL) was extracted with a solution of tetraoctylammonium bromide (0.175 g, 0.318 mmol, 2.5 equiv) in N_2 purged toluene (125 mL). To the resulting reddish-orange organic solution dioctylamine (0.613 g, 2.539 mmol, 20 equiv) was added (the amount of dioctylamine was calculated in order to obtain 2 nm nanoparticles). The mixture is vigorously stirred under N_2 for 1,5 hours. During this period of time the color of the mixture fades. Then the solution is cooled at 0°C and a $NaBH_4$ solution (48.0 mg, 1.269 mmol, 10 equiv) in H_2O (1 mL) is then rapidly added. The color of the solution turns rapidly to black and after 1.5 hours of stirring at 0°C, the aqueous layer is removed. To the obtained nanoparticle solution, the desired thiol (0.254 mmol, 2 equiv) dissolved in 3 mL of ethyl acetate was rapidly added. The reaction mixture was stirred for 3 hours at 0°C. Then the solvent was evaporated and the resulting crude was purified. Gold nanocluster were dissolved in 5 ml of milliQ water and then washed 7 times with EtOAc. Then water was evaporated under reduced pressure and the resulting nanoparticles were purified by gel permeation chromatography with Sephadex G25. On the other hand, gold nanocluster were dissolved in the minimum amount of AcOEt and then precipitated with diethyl ether (2 times) and subsequently with petroleum ether (5 times). The resulting gold nanocluster were finally purified by gel permeation chromatography with Sephadex LH-20. The general formula of synthetized gold nanocluster is $Au_{144}(SR)_{60}$, where R is a generic organic residual. In Fig.7.15 are reported thiols chosen for coating gold nanoclusters.

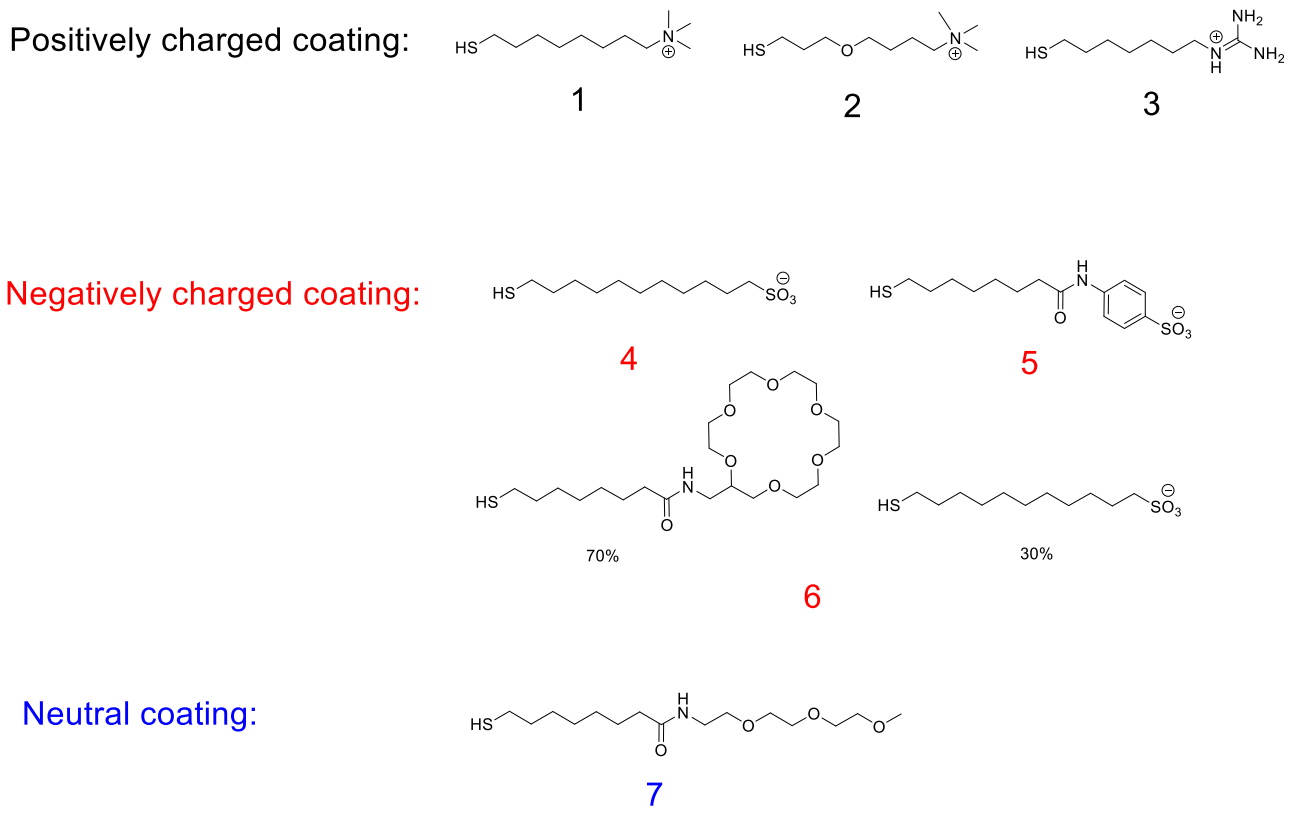

Fig.7.15 Thiols structure chosen for coating gold nanoclusters.

The selected thiols can be grouped in thiols positively, negatively charged or with a crown and neutral ether. The first group (with 1,2 and 3) it is supposed to interact with negatively charged substrates, indeed the second group (4,5 and 6) should interact with positively charged substrates or cations. Finally, 7 should not have a preferential interaction with the various substrates.

Gold nanoclusters have been called AuNCs-n where n is the number of thiols for coating.

7.4 Gold nanoclusters and fluorescein sodium salt

Gold nanoclusters have been tested with fluorescein sodium salt (F) (Fig.7.16), that is a well-known water soluble negatively charged.

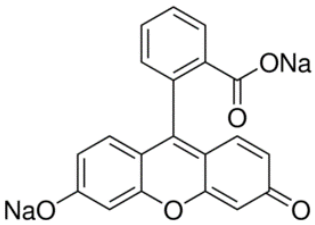

Fig.7.16 Fluorescein sodium salt structure

A water solutions of AuNCs-n (n=1,2,3,4,5,6, and 7) with a concentration of thiol of 20 mM and 0.33 mM of AuNCs has been prepared. From this solution 5 μL have been taken and added in

2.5 mL of a water solution of HEPES 0.01M. The final concentration of thiol (or binding site) is 40 μM and the final concentration of AuNCs is 0.67 μM. These solutions have been called AuNCs-n (n=1, 2, 3, 4, 5, 6, and 7).

A water solution of F with concentration 0.0022 M have been prepared. From this solution 5 μL have been taken and added in 2.5 mL of a water solution of HEPES 0.01M. The final concentration of F is 4 μM, this solution has been called F. Absorption spectrum of F is reported in Fig.7.17.

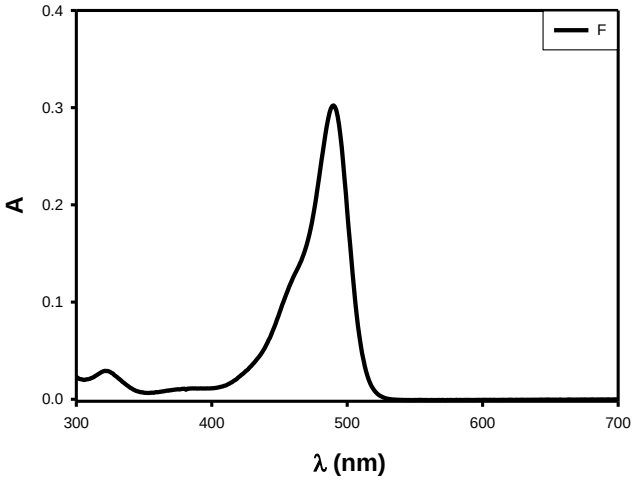

Fig.7.17 Absorption spectrum of F in water 0.0022M

A water solutions of AuNCs-n (n=1,2,3,4,5,6 and 7) with a concentration of thiol of 20 mM and 0.33 mM of AuNCs has been prepared. From this solution 5 μL have been taken and added in 2.5 mL of a water solution of HEPES 0.01M. The final concentration of thiol (or binding site) is 40 μM and the final concentration of AuNCs is 0.67 μM. Subsequently 5 μL of a water solution of F with concentration 0.0022 M have been added. The final concentration of F is 4 μM, with a ratio 1:10 with binding site. These solutions have been called AuNCs-n+F (n=1,2,3,4,5,6,7 and 8).

Molar extinction coefficient of AuNCs-1 is reported in Fig.7.18. The value along the whole spectrum is of the order of 10^5, which for this material is high. This is an advantage for obtain a high brightness.

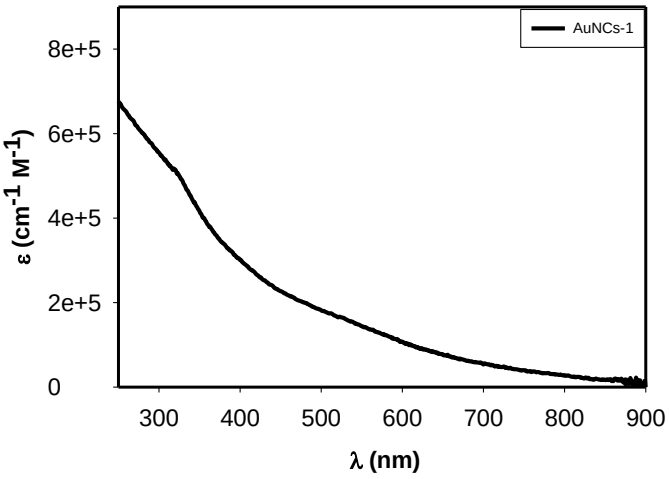

Fig.7.18 Molar extinction coefficient of AuNCs-1

In Fig.7.19 are reported absorption spectra of AuNCs-1 and AuNCs-2+F and emission spectra of F and AuNCs-1+F excited at 450 nm. It is clearly observed that in presence of AuNCs-1 emission of F is totally quenched and this suggests that there is interaction between F and AuNCs-1.

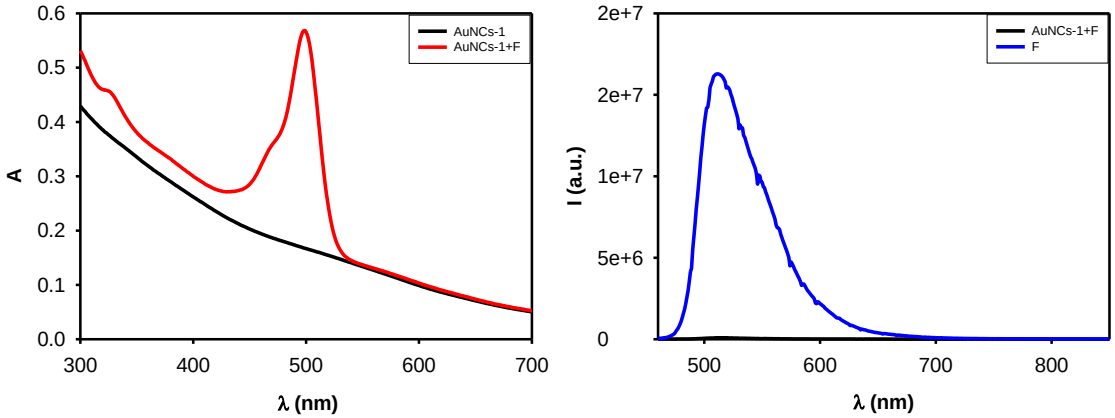

Fig.7.19 On the left: absorption spectra of AuNCs-1 (black line) and of AuNCs-1+F (red line). On the right: emission spectra of AuNCs-1+F (black line) and of F (blue line).

To demonstrate that AuNCs-1 quenches F by energy transfer, NIR emission spectra of AuNCs-1 and AuNCs-1+F have been obtained by exciting at 450 nm (Fig.7.20). Emission intensity is increased of almost 50% in presence of F, proving that energy transfer happens from F to AuNCs-1.

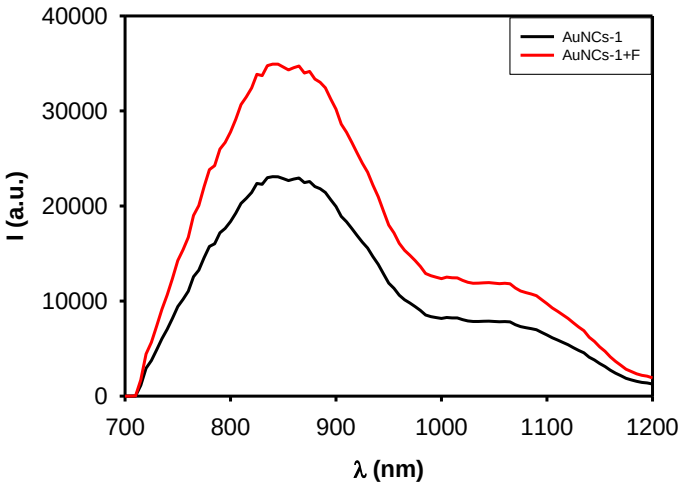

Fig.7.20 NIR emission spectra of AuNCs-1(black line) and of AuNCs-1+F (red line)

Molar extinction coefficient of AuNCs-2 is reported in Fig.7.21. The value along the whole spectrum is of the order of 10^5, which for this material is high. This is an advantage for obtain a high brightness.

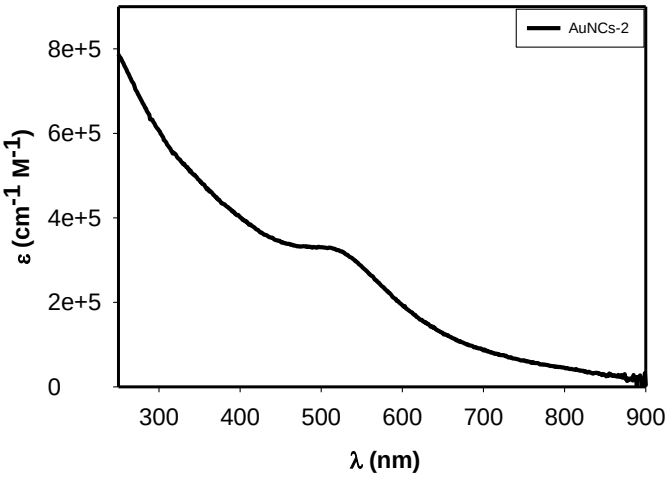

Fig.7.21 Molar extinction coefficient of AuNCs-2

In Fig.7.22 are reported absorption spectra of AuNCs-2 and AuNCs-2+F and emission spectra of F and AuNCs-2+F excited at 450 nm. It is observed that in presence of AuNCs-2 emission of F is partially quenched and this suggest that there is partial interaction between F and AuNCs-2.

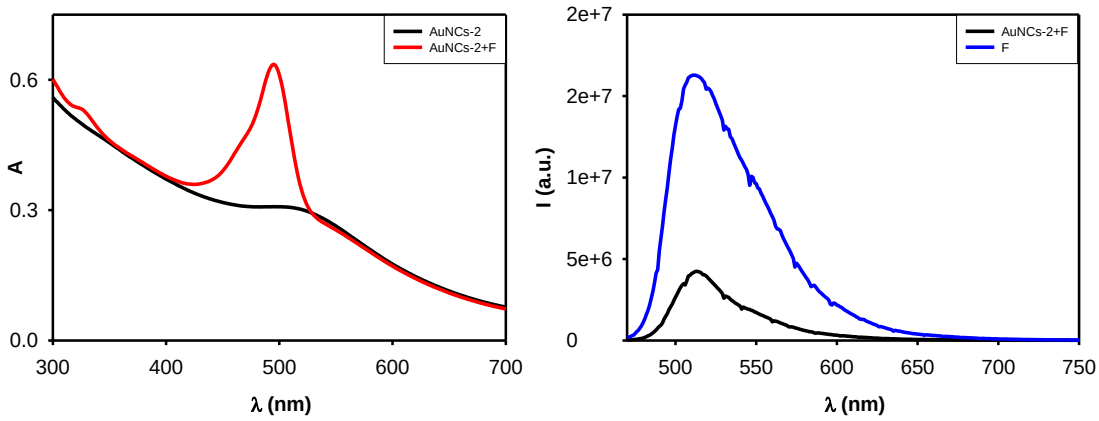

Fig.7.22 On the left: absorption spectra of AuNCs-2 (black line) and of AuNCs-2+F (red line). On the right: emission spectra of AuNCs-2+F (black line) and of F (blue line).

Molar extinction coefficient of AuNCs-3 is reported in Fig.7.23. The value along the whole spectrum is of the order of 10^5, which for this material is high.

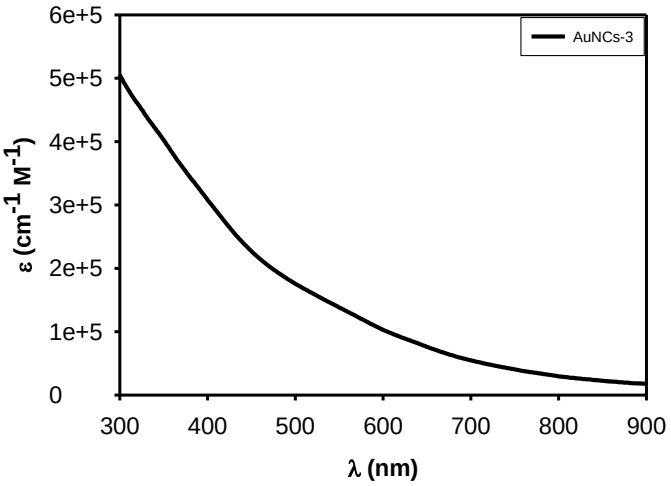

Fig.7.23 Molar extinction coefficient of AuNCs-3

In Fig.7.24 are reported absorption spectra of AuNCs-3 and AuNCs-3+F and emission spectra of F and AuNCs-3+F excited at 450 nm. It is observed that in presence of AuNCs-3 emission of F is quenched and this suggest that there is interaction between F and AuNCs-3.

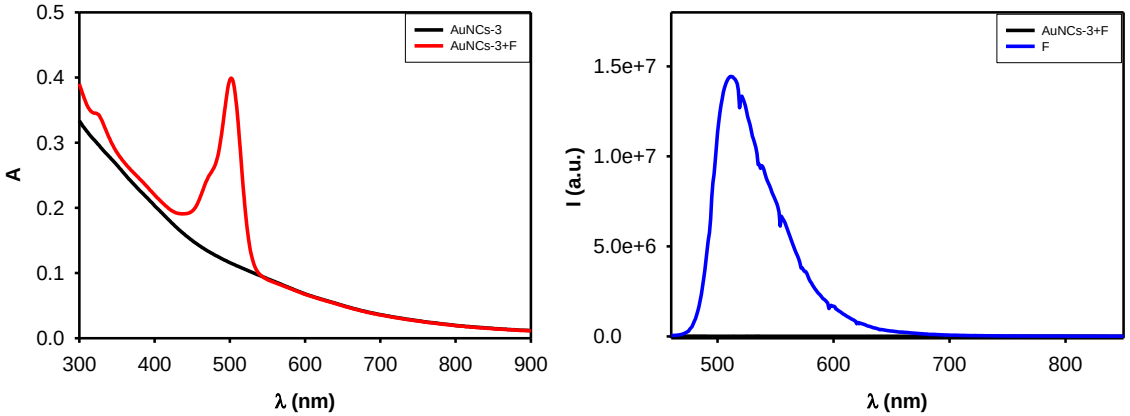

Fig.7.24 On the left: absorption spectra of AuNCs-3 (black line) and of AuNCs-3+F (red line). On the right: emission spectra of AuNCs-3+F (black line) and of F (blue line).

To demonstrate that AuNCs-3 quenches F by energy transfer, NIR emission spectra of AuNCs-3 and AuNCs-3+F have been obtained by exciting at 450 nm (Fig.7.25). Emission intensity is increased of almost 50% in presence of F, proving that energy transfer happens from F to AuNCs-3.

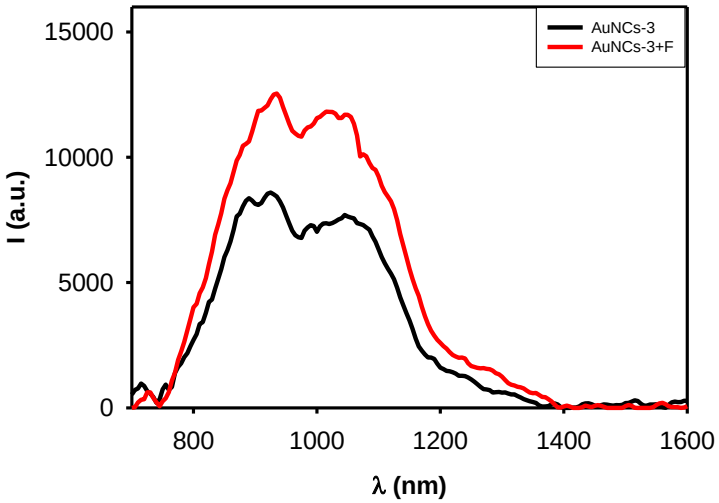

Fig.7.25 NIR emission spectra of AuNCs-3(black line) and of AuNCs-3+F (red line)

Molar extinction coefficient of AuNCs-4 is reported in Fig.7.26. The value along the whole spectrum is of the order of 10^5, which for this material is high. This is an advantage for obtain a high brightness.

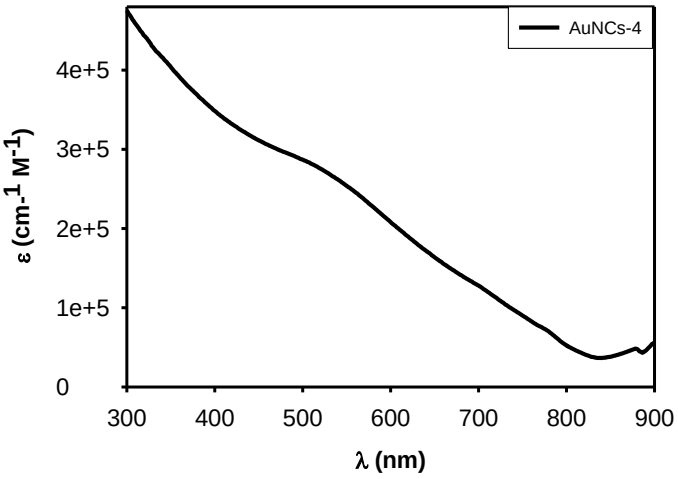

Fig.7.26 Molar extinction coefficient of AuNCs-4

In Fig.7.27 are reported absorption spectra of AuNCs-4 and AuNCs-4+F and emission spectra of F and AuNCs-4+F excited at 450 nm. It is observed that in presence of AuNCs-4 emission of F is partially quenched and this suggest that there is partial interaction between F and AuNCs-4. This is interesting because AuNCs-4 is not supposed interact with F. Indeed, they are both

negatively charged. However, quenching is smaller than the one of positively charged AuNCs, demonstrating that engineering coating permit to drive substrate interactions.

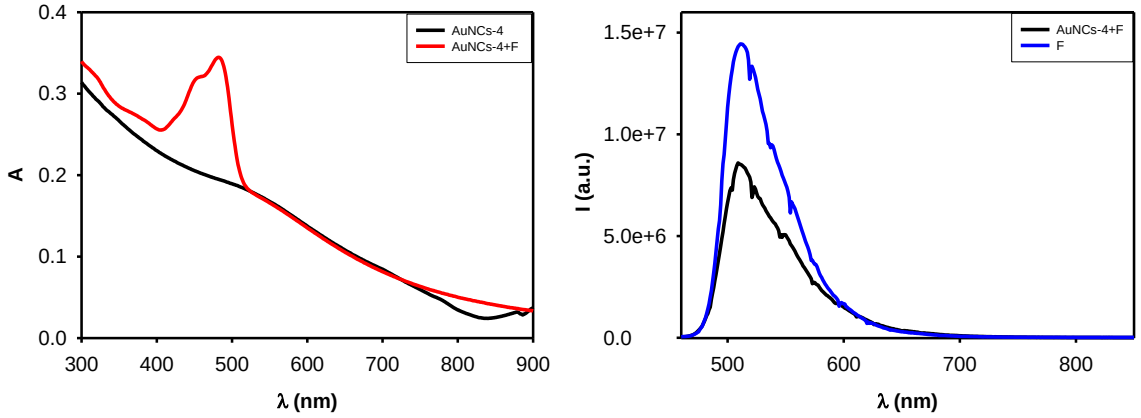

Fig.7.27 On the left: absorption spectra of AuNCs-4 (black line) and of AuNCs-4+F (red line). On the right: emission spectra of AuNCs-4+F (black line) and of F (blue line)

Molar extinction coefficient of AuNCs-5 is reported in Fig.7.28. The value along the whole spectrum is of the order of 10^5, which for this material is high. This is an advantage for obtain a high brightness.

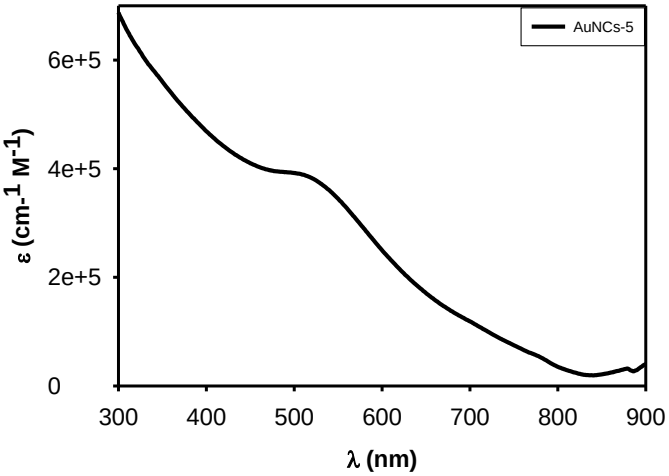

Fig.7.28 Molar extinction coefficient of AuNCs-5

In Fig.7.29 are reported absorption spectra of AuNCs5 and AuNCs-5+F. and emission spectra of F and AuNCs-5+F excited at 450 nm. It is observed that in presence of AuNCs-5 emission of F is partially quenched and this suggest that there is partial interaction between F and AuNCs-5. This is interesting because AuNCs-5 is not supposed interact with F. Indeed they are both negatively charged. However quenching is smaller than the one of positively charged AuNCs, demonstrating that engineering coating permit to drive substrate interactions.

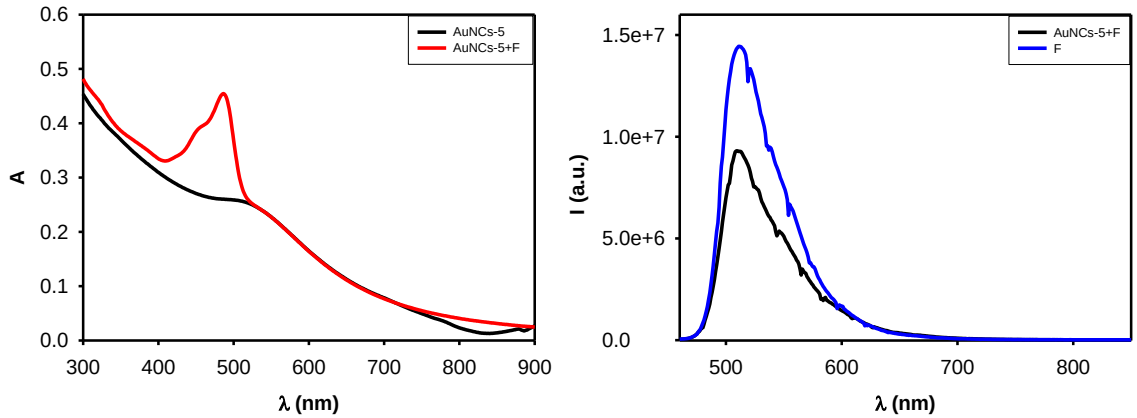

Fig.7.29 on the left: absorption spectra of AuNCs-5 (black line) and of AuNCs-5+F (red line). On the right: emission spectra of AuNCs-5+F (black line) and of F (blue line)

Molar extinction coefficient of AuNCs-6 is reported in Fig.7.30. The value along the whole spectrum is of the order of 10^5, which for this material is high and is useful to increase brightness.

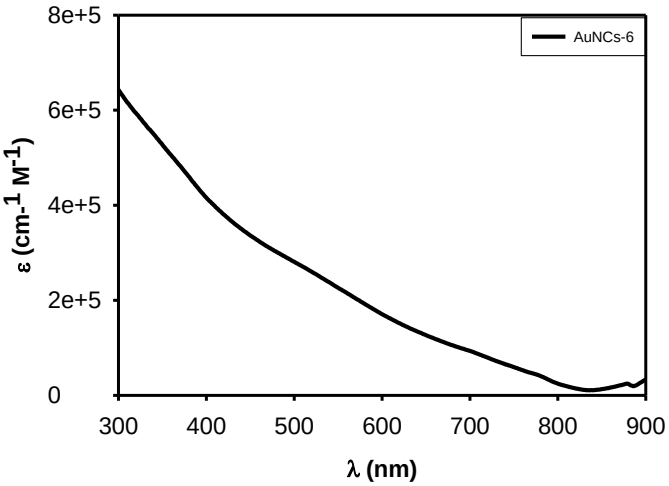

Fig.7.30 Molar extinction coefficient of AuNCs-6

In Fig.7.31 are reported absorption spectra of AuNCs-6 and AuNCs-6+Fand emission spectra of F and AuNCs-6+F excited at 450 nm. It is observed that in presence of AuNCs-6 emission of F is almost the same, suggesting that interaction between coating and AuNCs is limited, as we expected.

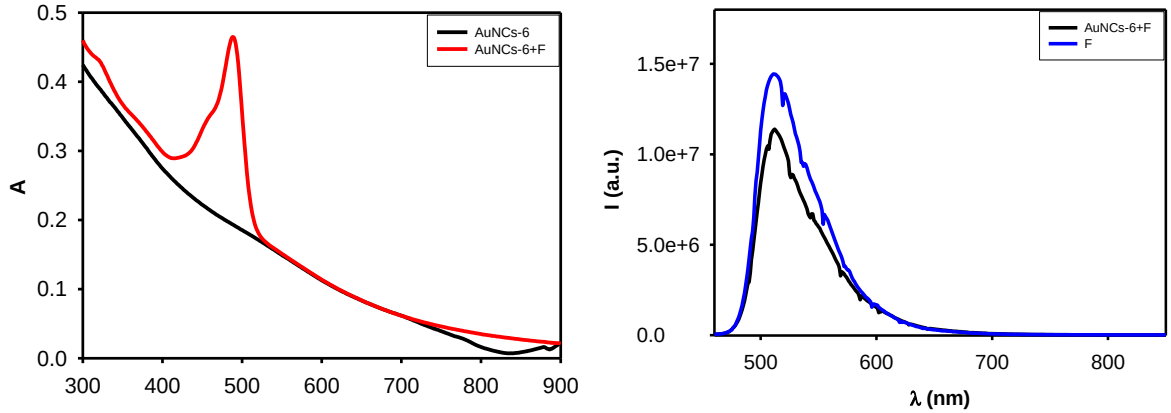

Fig.7.31 on the left: absorption spectra of AuNCs-6 (black line) and of AuNCs-6+F (red line). On the right: emission spectra of AuNCs-6+F (black line) and of F (blue line)

Molar extinction coefficient of AuNCs-7 is reported in Fig.7.32. The value along the whole spectrum is of the order of 10^5, which for this material is high. This is an advantage for obtain a high brightness.

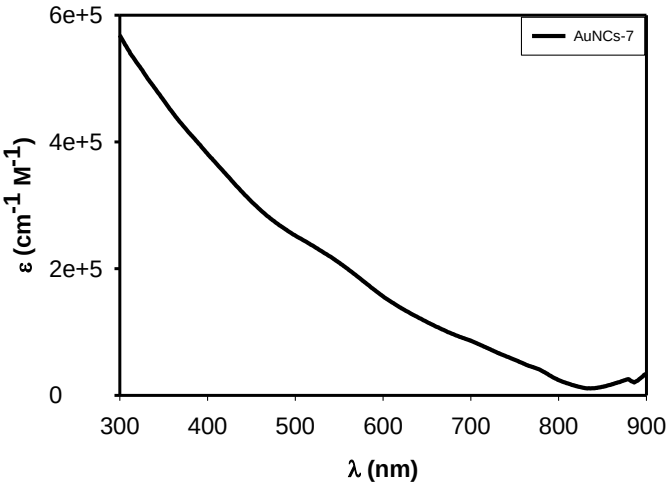

Fig.7.32 Molar extinction coefficient of AuNCs-7

In Fig.7.33 are reported absorption spectra of AuNCs-7 and AuNCs-7+F and emission spectra of F and AuNCs-7+F excited at 450 nm. It is observed that in presence of AuNCs-7 emission of F is almost the same, suggesting that interaction between coating and AuNCs is limited, as we expected.

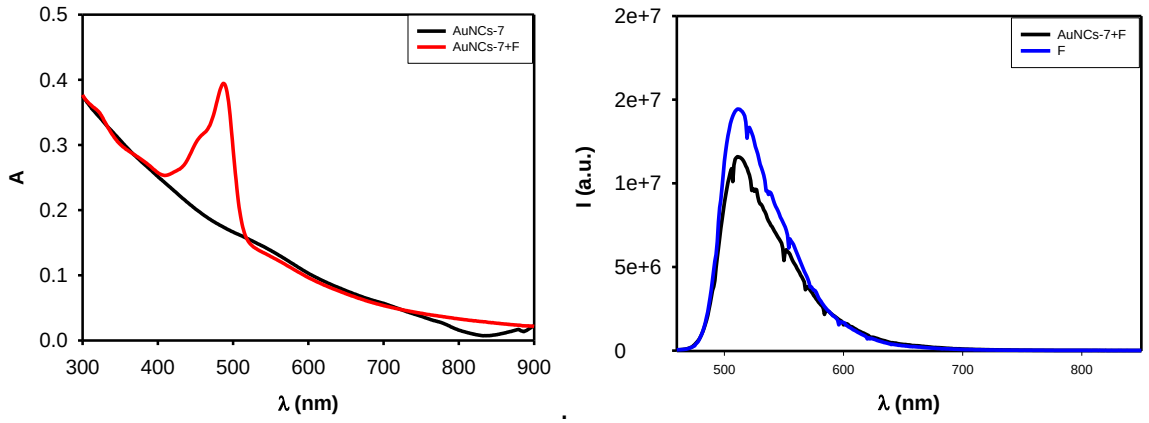

Fig.7.33 on the left: absorption spectra of AuNCs-7 (black line) and of AuNCs-7+F (red line). On the right: emission spectra of AuNCs-7+F (black line) and of F (blue line)

As expected, gold nanocluster coated with thiols positively charged have interacted more than the others with fluorescein sodium salt. In particular AuNCs-1 and AuNCs-3 have completely quenched fluorescein sodium salt, showing that interaction with negatively charged substrates is very favorite. For this reason, these gold nanoclusters have been tested with negatively charged active pharmaceutical ingredients (API).

7.5 AuNCs-1 and API

We have decided to test our positively charged nanoparticles with API reported in Fig.7.34, that are some of the most common commercial anti-inflammatory. In particular they are Naproxen (N), Diclofenac (D), Ketoprofen (K) and Salicylate (S).

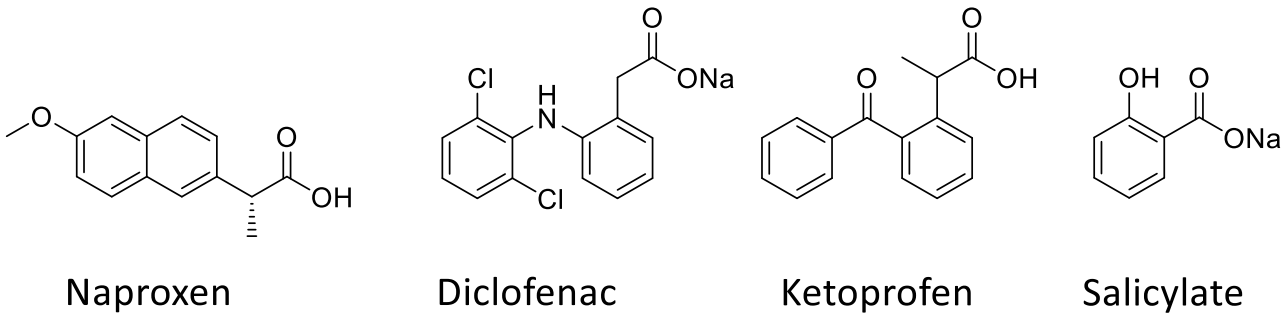

Fig.7.34 API structures

Tests have been conduced in biological conditions in water at pH 7 (HEPES buffer 0.01M), when these molecules are dissociated and have a negative charge.

The driving force of the interaction between gold nanoclusters and amphiphilic organic anions is a combination of the accommodation of the hydrophobic portion of the substrate in the alkyl portion of the monolayer and the simultaneous ion-pairing interaction with the head groups. This grants selectivity and high affinity. In Fig.7.35 photophysical properties of API are

reported. All of them have an absorption band in the UV region and an emission in visible region.

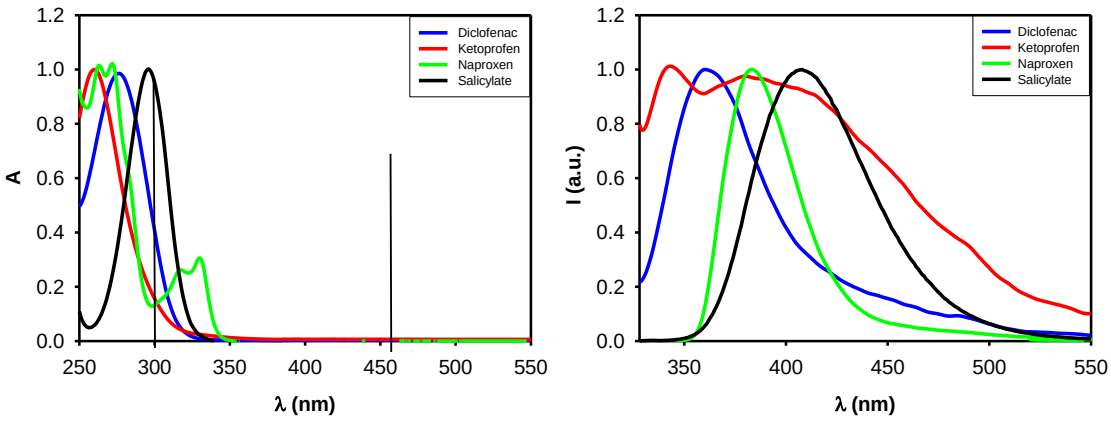

Fig.7.35 API photophysical properties. On the left: absorption spectra. On the right: emission spectra

The interaction between gold nanoclusters and API has been studied by photophysical means for monitor any possible changes in the photophysical properties of gold nanoparticles caused by API presence. The system can be simplified by approximating that API can modify photophysical properties of gold nanoclusters with two mechanisms. First mechanism: direct energy transfer from API to gold nanoclusters. Second mechanism: the presence of positively charged substrate on gold nanocluster surface changes the global charge distribution of gold nanocluster and this influences their photophysical properties. In order to discriminate which mechanism is activated by the interaction between nanoparticles and drugs, the system has been excited at two different wavelengths: at 300 nm where API absorb, and both mechanisms can occur, and at 500 nm where API do not absorb and only the second mechanism can occur.

7.5.1 AuNCs-1 and N

A water solutions of AuNCs-1with a concentration of thiol of 20 mM and of AuNCs of 0.33 mM has been prepared. From this solution 5 μL have been taken and added in 2.5 mL of a water solution of HEPES 0.01M. The final concentration of thiol (or binding site) is 40 μM and the final concentration of AuNCs is 0.67 μM. This solution has been called AuNCs-1.

A solution 1:1 H_2O:DMSO of N 0.0022 M has been prepared. Titration of AuNCs-1 with N has been carried out. In particular at AuNCs-1 have been added 0-1-3-5-10-20-30-50 -70-100-130-160-200 μL of N solution. In Fig.7.36 are reported absorption spectra of titration.

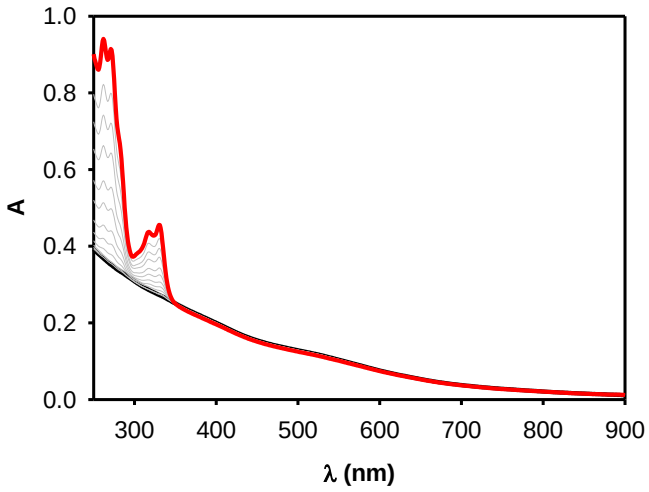

Fig.7.36 Absorption spectra of AuNCs-1 titrated with N

Emission spectra of system excited at 330 nm are reported in Fig.7.37a and of system excited at 500 nm are reported in Fig.7.37b.

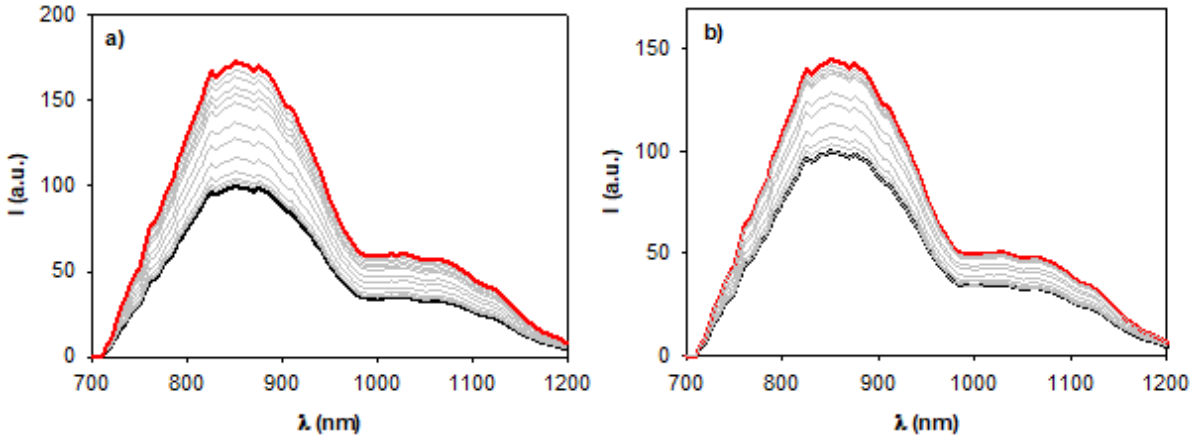

Fig.7.37 Emission spectra of AuNCs-1 titrated with N excited at 330 nm (a) and 500 nm (b)

Variation of area of emission spectra has been reported as function of N equivalent (calculated respect binding site concentration) (Fig.7.38).

The first thing that we can observe is that there is a considerable enhance of emission, almost 70%, when excited at 330 nm. Then, by comparing the answer of the system excited at 300 nm and at 500 nm, we can say that both mechanisms (energy transfer and polarity change effect) occur concurrently with the same importance.

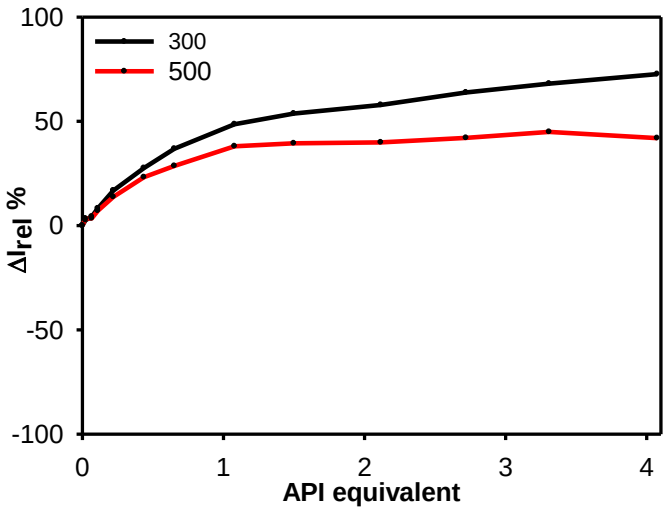

Fig.7.38 Variation of area of AuNCs-1 emission spectra as function of API equivalent

7.5.2 AuNCs-1 and D

A water solutions of AuNCs-1with a concentration of thiol of 20 mM and of AuNCs of 0.33 mM has been prepared. From this solution 5 μL have been taken and added in 2.5 mL of a water solution of HEPES 0.01M. The final concentration of thiol (or binding site) is 40 μM and the final concentration of AuNCs is 0.67 μM. This solution has been called AuNCs-1.

A water of D 0.0022 M has been prepared. Titration of AuNCs-1 with D has been carried out. In particular at AuNCs-1 have been added 0-1-3-5-10-20-30-50 -70-100-130-160-200 μL of D solution. In Fig.7.39 are reported absorption spectra of titration.

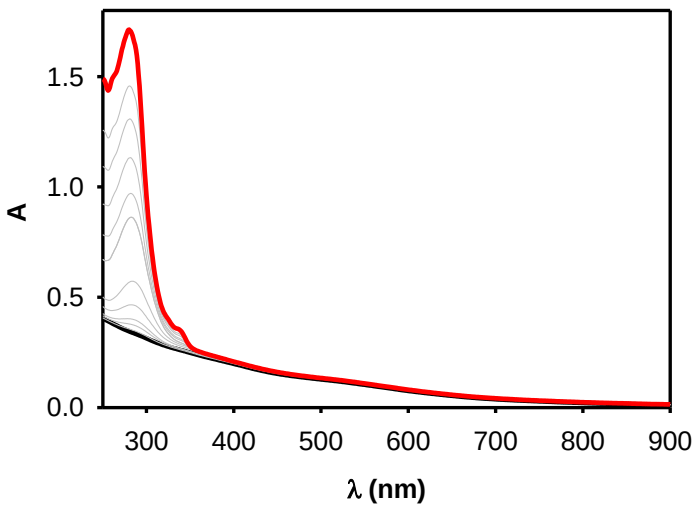

Fig.7.39 Absorption spectra of AuNCs-1 titrated with D

Emission spectra of system excited at 300 nm are reported in Fig.7.40a and of system excited at 500 nm are reported in Fig.7.40b.

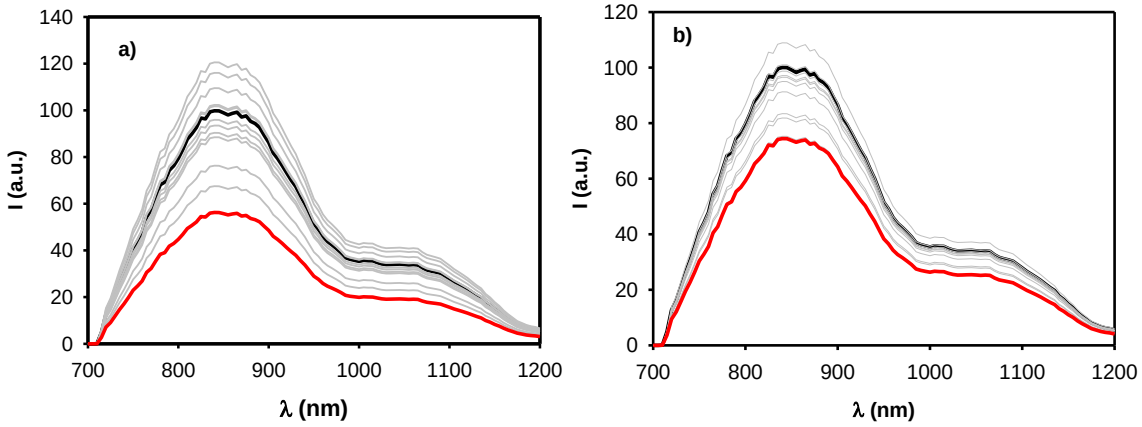

Fig.7.40 Emission spectra of AuNCs-1 titrated with D excited at 300 nm (a) and 500 nm (b)

Variation of area of emission spectra has been reported as function of D equivalent (calculated respect binding site concentration) (Fig.7.41).

This is the most curious trend. At the beginning is observed an increase in emission of AuNCs. But adding drug beyond a threshold emission is totally quenched. This indicates that over a certain concentration API aggregates are formed on the NP surface that quench any emission.

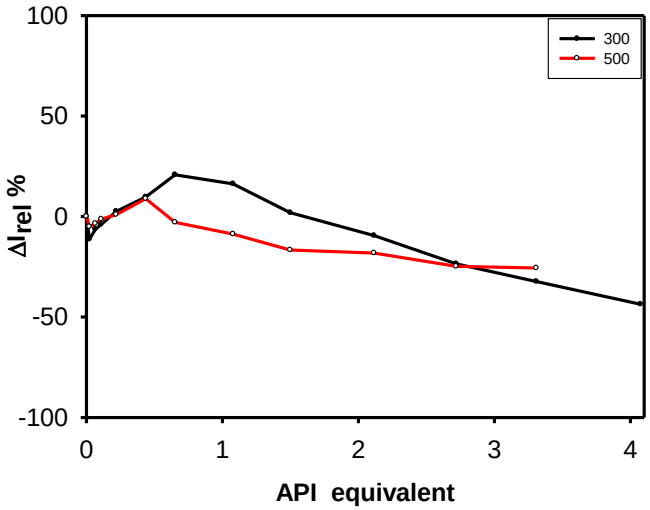

Fig.7.41 Variation of area of AuNCs-1 emission spectra as function of API equivalent

7.5.3 AuNCs-1 and K

A water solutions of AuNCs-1with a concentration of thiol of 20 mM and of AuNCs of 0.33 mM has been prepared. From this solution 5 μL have been taken and added in 2.5 mL of a water solution of HEPES 0.01M. The final concentration of thiol (or binding site) is 40 μM and the final concentration of AuNCs is 0.67 μM. This solution has been called AuNCs-1.

A solution 1:1 H_2O:DMSO of K 0.0022 M has been prepared. Titration of AuNCs-1 with K has been carried out. In particular at AuNCs-1 have been added 0-1-3-5-10-20-30-50 -70-100-130-160 μL of K solution. In Fig.7.42 are reported absorption spectra of titration.

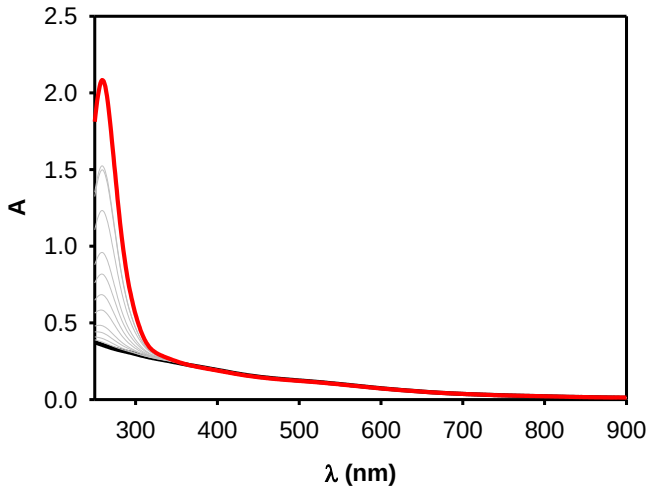

Fig.7.42 Absorption spectra of AuNCs-1 titrated with K

Emission spectra of system excited at 300 nm are reported in Fig.7.43a and of system excited at 500 nm are reported in Fig.7.43b.

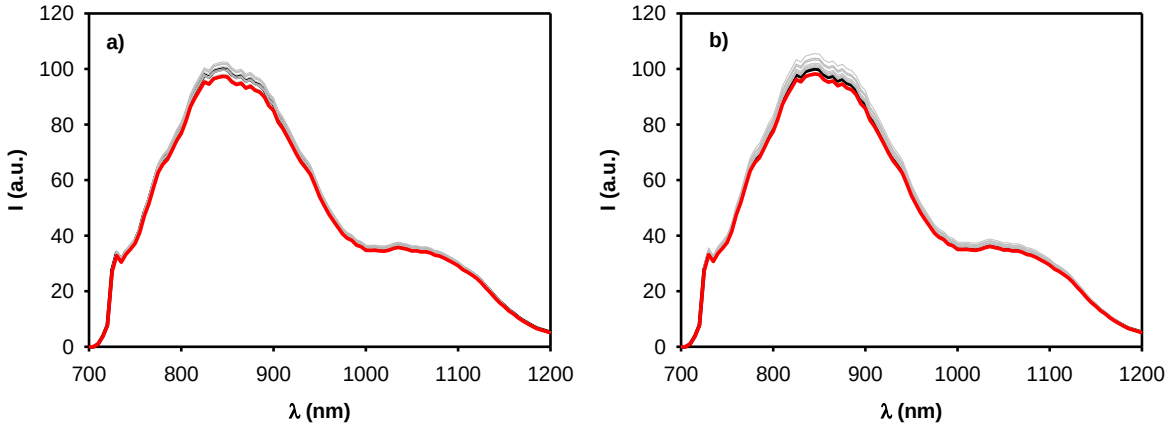

Fig.7.43 Emission spectra of AuNCs-1 titrated with K excited at 300 nm (a) and 500 nm (b)

Variation of area of emission spectra has been reported as function of K equivalent (calculated respect binding site concentration) (Fig.7.44).

It is observed that emission of AuNCs-1 do not changes in any case, both exciting at 300 nm or 500 nm. That means that there is no interaction between coating of AuNCs and K.

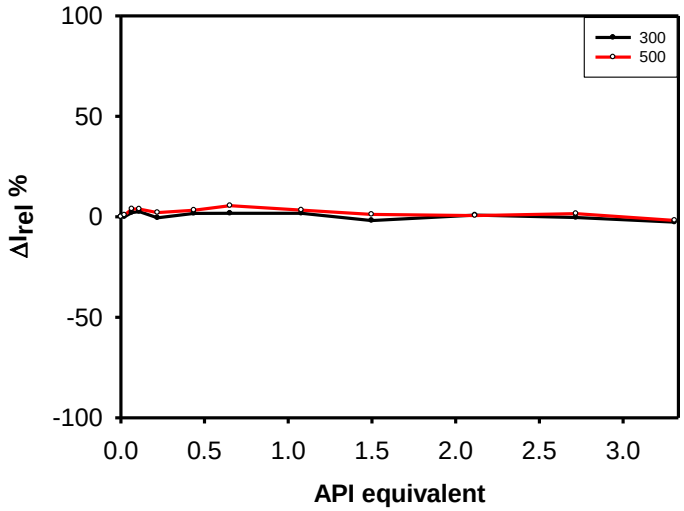

Fig.7.44 Variation of area of AuNCs-1 emission spectra as function of API equivalent

7.5.4 AuNCs-1 and S

A water solutions of AuNCs-1with a concentration of thiol of 20 mM and of AuNCs of 0.33 mM has been prepared. From this solution 5 μL have been taken and added in 2.5 mL of a water solution of HEPES 0.01M. The final concentration of thiol (or binding site) is 40 μM and the final concentration of AuNCs is 0.67 μM. This solution has been called AuNCs-1.

A water of S 0.0022 M has been prepared. Titration of AuNCs-1 with S has been carried out. In particular at AuNCs-1 have been added 0-1-3-5-10-20-30-50 -70-100-130-160-200 μL of S solution. In Fig.7.45 are reported absorption spectra of titration.

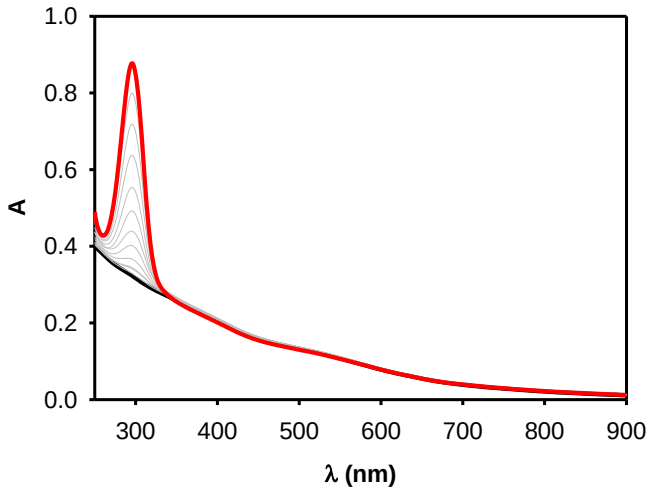

Fig.7.45 Absorption spectra of AuNCs-1 titrated with S

Emission spectra of system excited at 300 nm are reported in Fig.7.46a and of system excited at 500 nm are reported in Fig.7.46b. In this case is also possible observe an enhance of emission about 70%.

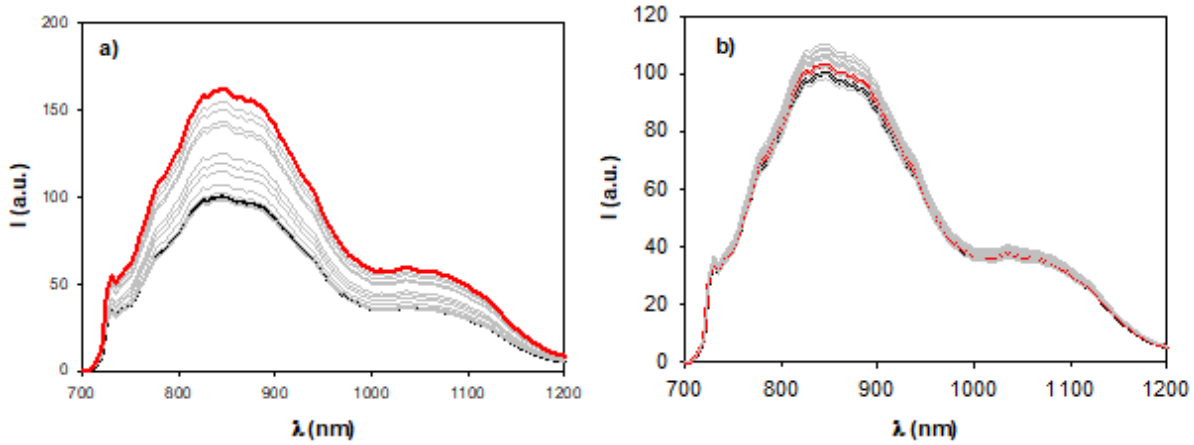

Fig.7.46 Emission spectra of AuNCs-1 titrated with S excited at 300 nm (a) and 500 nm (b)

Variation of area of emission spectra has been reported as function of S equivalent (calculated respect binding site concentration) (Fig.7.47).

But now is evident that the only contribution is the one of the direct energy transfers. In fact, when the system is excited at 500 nm no significative changes in emission of gold nanocluster are reported.

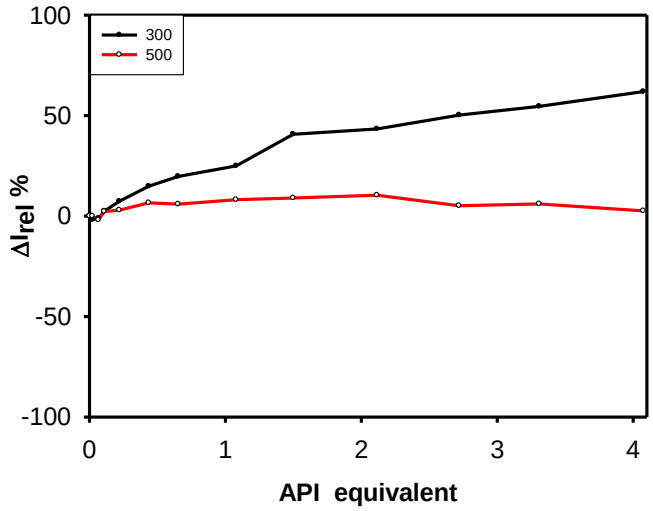

Fig.7.47 Variation of area of AuNCs-1 emission spectra as function of API equivalent

7.6 AuNCs-3 and API

7.6.1 AuNCs-3 and N

A water solutions of AuNCs-3 with a concentration of thiol of 20 mM and of AuNCs of 0.33 mM has been prepared. From this solution 5 μL have been taken and added in 2.5 mL of a water solution of HEPES 0.01M. The final concentration of thiol (or binding site) is 40 μM and the final concentration of AuNCs is 0.67 μM. This solution has been called AuNCs-3.

A solution 1:1 H_2O:DMSO of N 0.0022 M has been prepared. Titration of AuNCs-3 with N has been carried out. In particular at AuNCs-3 have been added 0-1-3-5-10-20-30-50 -70-100-130-160-200 μL of N solution. In Fig.7.48 are reported absorption spectra of titration.

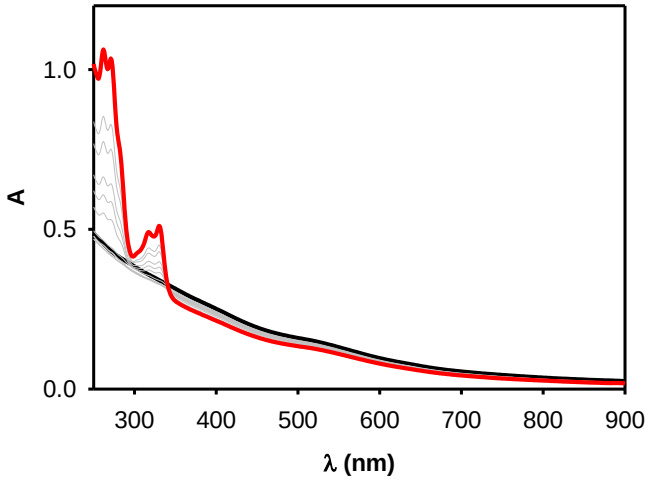

Fig.7.48 Absorption spectra of AuNCs-3 titrated with N

Emission spectra of system excited at 330 nm are reported in Fig.7.49a and of system excited at 500 nm are reported in Fig.7.49b.

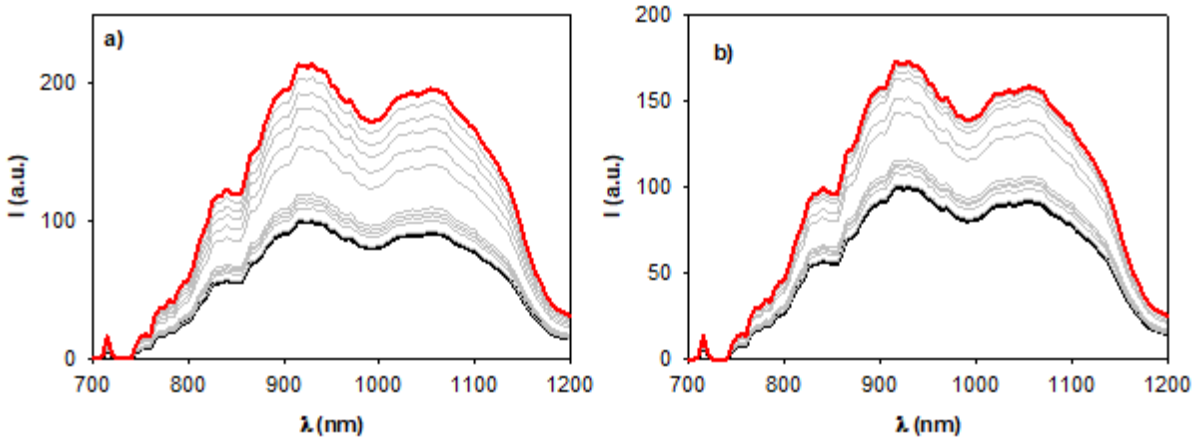

Fig.7.49 Emission spectra of AuNCs-3 titrated with N excited at 330 nm (a) and 500 nm (b)

Variation of area of emission spectra has been reported as function of N equivalent (calculated respect binding site concentration) (Fig.7.50). It is observed that there is a huge enhance of emission more than 100%. Then, by comparing the answer of the system excited at 330 nm and at 500 nm, we can say that both mechanisms occur concurrently with the almost same importance.

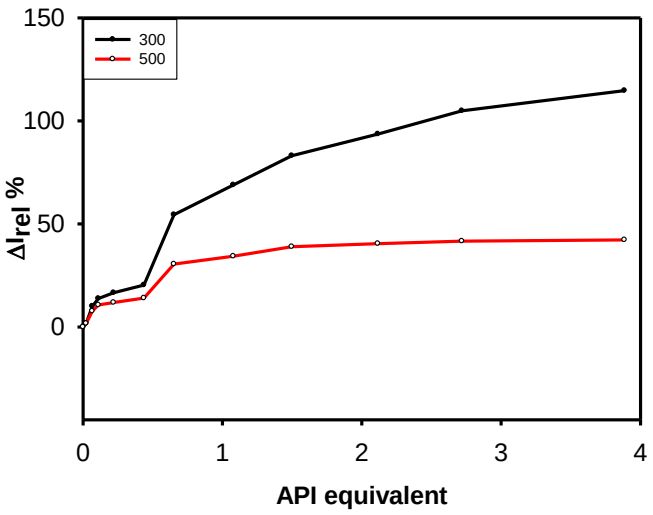

Fig.7.50 Variation of area of AuNCs-3 emission spectra as function of API equivalent

7.6.2 AuNCs-3 and D

A water solutions of AuNCs-3 with a concentration of thiol of 20 mM and of AuNCs of 0.33 mM has been prepared. From this solution 5 μL have been taken and added in 2.5 mL of a water solution of HEPES 0.01M. The final concentration of thiol (or binding site) is 40 μM and the final concentration of AuNCs is 0.67 μM. This solution has been called AuNCs-3.

A water of D 0.0022 M has been prepared. Titration of AuNCs-3 with D has been carried out. In particular at AuNCs-3 have been added 0-1-3-5-10-20-30-50 -70-100-130-160-200 μL of D solution. In Fig.7.51 are reported absorption spectra of titration.

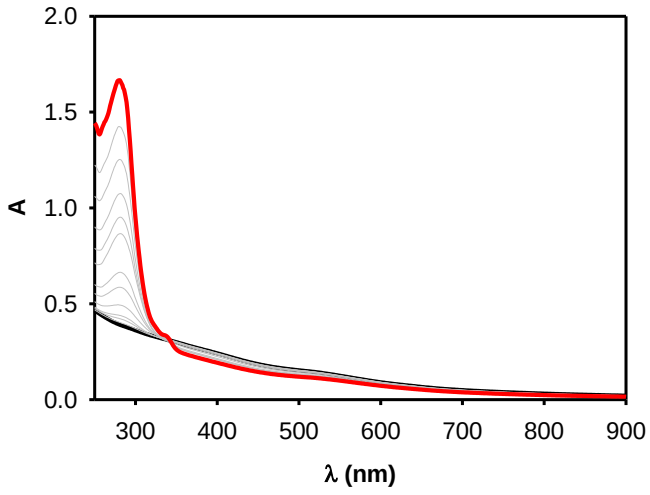

Fig.7.51 Absorption spectra of AuNCs-3 titrated with D

Emission spectra of system excited at 300 nm are reported in Fig.7.52a and of system excited at 500 nm are reported in Fig.7.52b. This is the most curious trend. At the beginning is observed

an increase in emission of nanoparticles. But adding drug beyond a threshold emission is totally quenched.

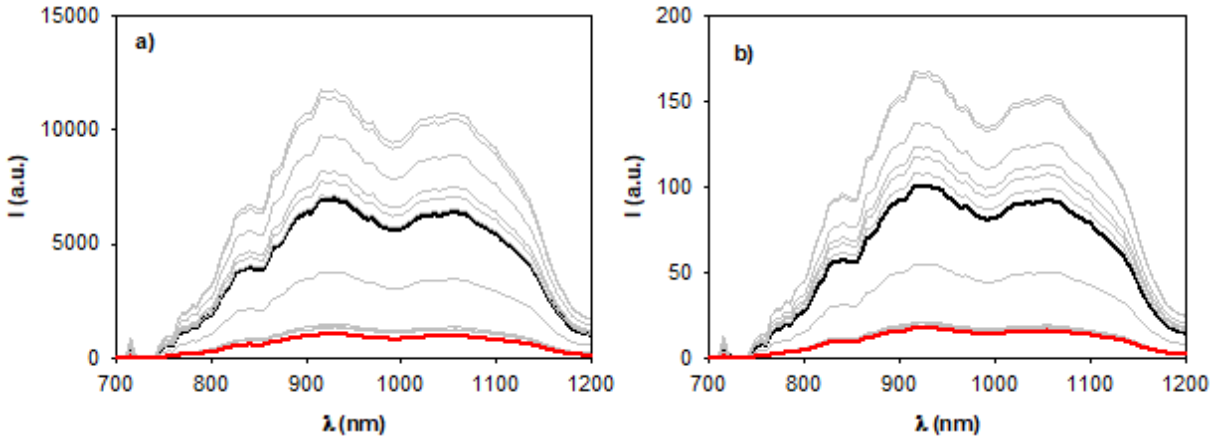

Fig.7.52 Emission spectra of AuNCs-3 titrated with D excited at 300 nm (a) and 500 nm (b)

Variation of area of emission spectra has been reported as function of N equivalent (calculated respect binding site concentration) (Fig.7.53).

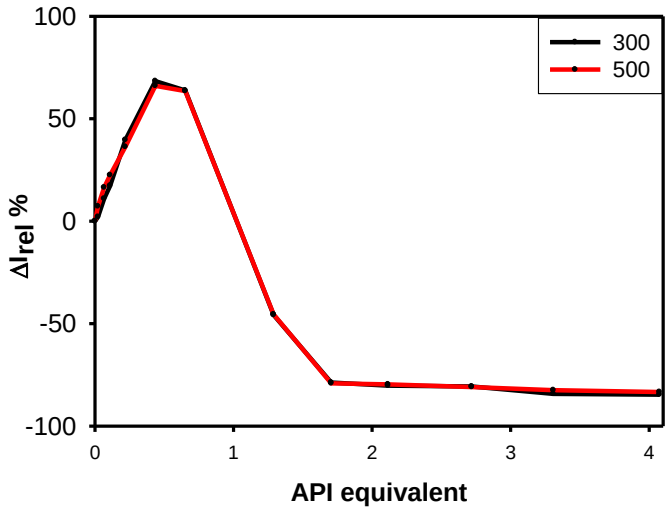

Fig.7.53 Variation of area of AuNCs-3 emission spectra as function of API equivalent

7.6.3 AuNCs-3 and K

A water solutions of AuNCs-3 with a concentration of thiol of 20 mM and of AuNCs of 0.33 mM has been prepared. From this solution 5 μL have been taken and added in 2.5 mL of a water solution of HEPES 0.01M. The final concentration of thiol (or binding site) is 40 μM and the final concentration of AuNCs is 0.67 μM. This solution has been called AuNCs-3.

A solution 1:1 H_2O:DMSO of K 0.0022 M has been prepared. Titration of AuNCs-3 with K has been carried out. In particular at AuNCs-3 have been added 0-1-3-5-10-20-30-50 -70-100-130-160-200 μL of K solution. In Fig.7.54 are reported absorption spectra of titration.

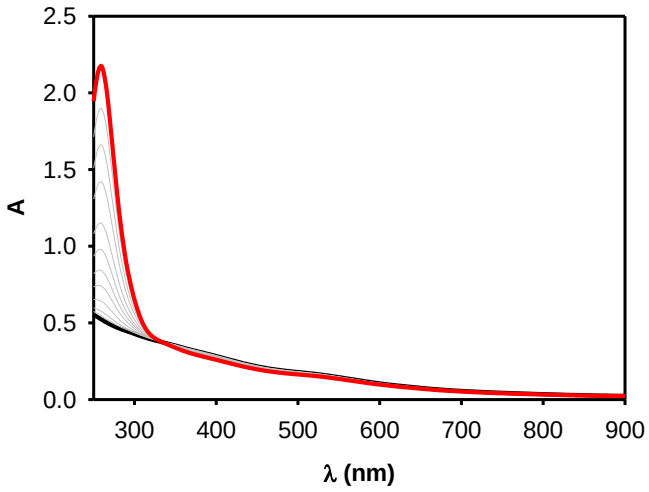

Fig.7.54 Absorption spectra of AuNCs-3 titrated with K

Emission spectra of system excited at 300 nm are reported in Fig.7.55a and of system excited at 500 nm are reported in Fig.7.55b.

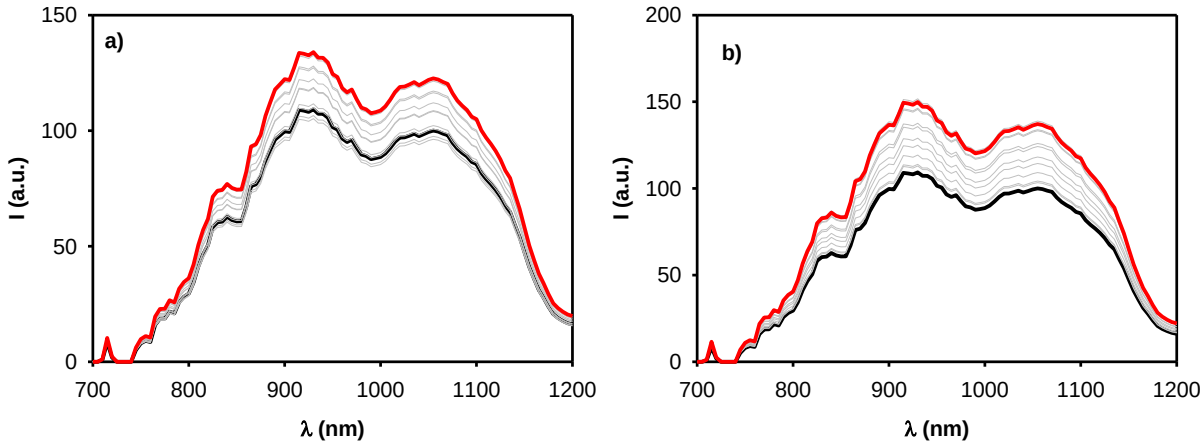

Fig.7.55 Emission spectra of AuNCs-3 titrated with K excited at 300 nm (a) and 500 nm (b)

Variation of area of emission spectra has been reported as function of K equivalent (calculated respect binding site concentration) (Fig.7.56).

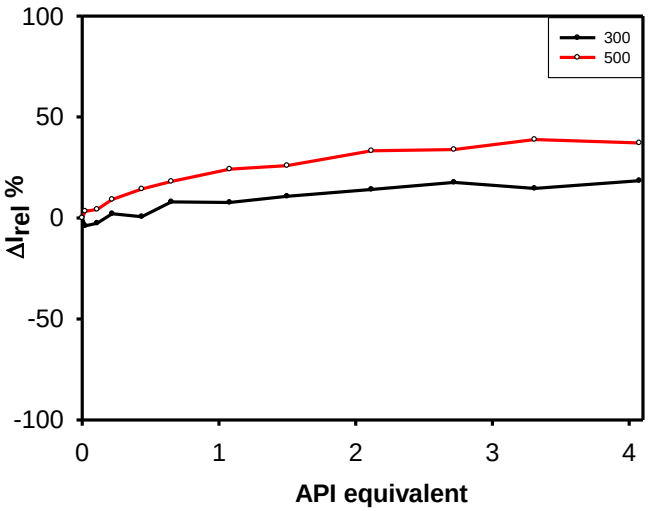

Fig.7.56 Variation of area of AuNCs-3 emission spectra as function of API equivalent

7.7 Conclusions

In this work a new class of photophysical system based on gold have been developed. In particular we focused on demonstrating that appropriate engineering of coating can tailor interaction between gold nanoclusters and substrate in order to achieve selectivity and sensibility. In the first part of the work we used fluorescein sodium salt, a fluorophore negatively charged in the working conditions (HEPES 0.01M). Gold nanoclusters coated with positively charged thiols have shown much higher affinity for fluorescein sodium salt, quenching its fluorescence. Most interesting results have been obtained for AuNCs-1 and AuNCs-3 and we demonstrate that energy transfer happens between fluorescein sodium salt and gold nanoclusters. Subsequently, AuNCs-1 and AuNCs-3 have been tested with API presents in commercial drugs. API have been chosen with amphiphilic structures. They have a negatively charged head and a lipophilic moiety. The driving force of the interaction between gold nanoclusters and amphiphilic organic anions is a combination of the accommodation of the hydrophobic portion of the substrate in the alkyl portion of the monolayer and the simultaneous ion-pairing interaction with the head groups. This grants selectivity and high affinity. Results demonstrate that there is interactions between gold nanoclusters and API. Moreover, API are able to influence gold nanoclusters emission with two mechanism. First mechanism: direct energy transfer from API to gold nanoclusters. Second mechanism: the presence of positively charged substrate on gold nanocluster surface changes the global charge distribution of gold nanocluster and this influences their photophysical properties. In order to discriminate which mechanism happens between nanoparticles and drugs, the system has been excited at two different wavelengths: at 300 nm where API absorb, and both mechanisms can occur, and at 500 nm where API do not absorb and only the second mechanism can occur. In

conclusion we demonstrate that gold nanoclusters are very promising as biological sensors, indeed they can be easily engineered to have specific interactions with selected substrates, they can work in biological conditions (water at pH 7) and they emit in in near infrared region where there is the biological window and for this reason is attracting a lot of attentions.

7.8 Bibliography

1. (a) Wu, Z.; Jin, R., On the ligand's role in the fluorescence of gold nanoclusters. *Nano Lett.* **2010,** *10* (7), 2568-2573; (b) Liang, H.; Zhang, X.-B.; Lv, Y.; Gong, L.; Wang, R.; Zhu, X.; Yang, R.; Tan, W., Functional DNA-containing nanomaterials: cellular applications in biosensing, imaging, and targeted therapy. *Acc. Chem. Res.* **2014,** *47* (6), 1891-1901; (c) Li, K.; Liu, B., Polymer-encapsulated organic nanoparticles for fluorescence and photoacoustic imaging. *Chem. Soc. Rev.* **2014,** *43* (18), 6570-6597; (d) Zhang, L.; Dong, W.-F.; Sun, H.-B., Multifunctional superparamagnetic iron oxide nanoparticles: design, synthesis and biomedical photonic applications. *Nanoscale* **2013,** *5* (17), 7664-7684.
2. (a) Zheng, Q.; Juette, M. F.; Jockusch, S.; Wasserman, M. R.; Zhou, Z.; Altman, R. B.; Blanchard, S. C., Ultra-stable organic fluorophores for single-molecule research. *Chem. Soc. Rev.* **2014,** *43* (4), 1044-1056; (b) Stennett, E. M.; Ciuba, M. A.; Levitus, M., Photophysical processes in single molecule organic fluorescent probes. *Chem. abbandono cani Soc. Rev.* **2014,** *43* (4), 1057-1075; (c) Blum, A. P.; Kammeyer, J. K.; Rush, A. M.; Callmann, C.E.; Hahn, M. E.; Gianneschi, N. C., Stimuli-responsive nanomaterials for biomedical applications. *J. Am. Chem. Soc.* **2015,** *137* (6), 2140-2154.
3. (a) Tao, Y.; Li, M.; Ren, J.; Qu, X., Metal nanoclusters: novel probes for diagnostic and therapeutic applications. *Chem. Soc. Rev.* **2015,** *44* (23), 8636-8663; (b) Chen, L.-Y.; Wang, C.-W.; Yuan, Z.; Chang, H.-T., Fluorescent gold nanoclusters: recent advances in sensing and imaging. *Anal. Chem.* **2014,** *87* (1), 216-229.
4. Yang, X.; Yang, M.; Pang, B.; Vara, M.; Xia, Y., Gold nanomaterials at work in biomedicine. *Chem. Rev.* **2015,** *115* (19), 10410-10488.
5. Tsoi, K. M.; MacParland, S. A.; Ma, X.-Z.; Spetzler, V. N.; Echeverri, J.; Ouyang, B.; Fadel, S. M.; Sykes, E. A.; Goldaracena, N.; Kaths, J. M., Mechanism of hard-nanomaterial clearance by the liver. *Nature materials* **2016,** *15* (11), 1212.
6. Huang, T.; Murray, R. W., Visible luminescence of water-soluble monolayer-protected gold clusters. *The Journal of Physical Chemistry B* **2001,** *105* (50), 12498-12502.
7. (a) Battistelli, G.; Cantelli, A.; Guidetti, G.; Manzi, J.; Montalti, M., Ultra-bright and stimuli-responsive fluorescent nanoparticles for bioimaging. *Wiley Interdisciplinary Reviews: Nanomedicine and Nanobiotechnology* **2016,** *8* (1), 139-150; (b) Reisch, A.; Klymchenko, A. S., Fluorescent polymer nanoparticles based on dyes: seeking brighter tools for bioimaging. *Small* **2016,** *12* (15), 1968-1992.
8. (a) Hesari, M.; Ding, Z., A grand avenue to Au nanocluster electrochemiluminescence. *Acc. Chem. Res.* **2017,** *50* (2), 218-230; (b) Wu, L.; Fang, W.; Chen, X., The photoluminescence mechanism of ultra-small gold clusters. *PCCP* **2016,** *18* (26), 17320-17325; (c) Weerawardene, K. D. M.; Aikens, C. M., Theoretical insights into the origin of photoluminescence of Au25 (SR) 18–nanoparticles. *J. Am. Chem. Soc.* **2016,** *138* (35), 11202-11210; (d) Gan, Z.; Lin, Y.; Luo, L.; Han, G.; Liu, W.; Liu, Z.; Yao, C.; Weng, L.; Liao, L.; Chen, J., Fluorescent Gold Nanoclusters with Interlocked Staples and a Fully Thiolate-Bound Kernel. *Angew. Chem. Int. Ed.* **2016,** *55* (38), 11567-11571.
9. Zeng, C.; Chen, Y.; Iida, K.; Nobusada, K.; Kirschbaum, K.; Lambright, K. J.; Jin, R., Gold quantum boxes: on the periodicities and the quantum confinement in the Au28, Au36, Au44, and Au52 magic series. *J. Am. Chem. Soc.* **2016,** *138* (12), 3950-3953.
10. (a) Lin, Y.-C.; Wu, T.; Lin, Y.-W., Fluorescence sensing of mercury (ii) and melamine in aqueous solutions through microwave-assisted synthesis of egg-white-protected gold nanoclusters. *Analytical methods* **2018,** *10* (14), 1624-1632; (b) Jin, R.; Zeng, C.; Zhou, M.; Chen, Y., Atomically precise colloidal metal nanoclusters and nanoparticles: fundamentals and opportunities. *Chem. Rev.* **2016,** *116* (18), 10346-10413; (c) Jin, R., Atomically precise metal nanoclusters: stable sizes and optical properties. *Nanoscale* **2015,** *7* (5), 1549-1565.

11. Chen, Y.; Liu, C.; Tang, Q.; Zeng, C.; Higaki, T.; Das, A.; Jiang, D.-e.; Rosi, N. L.; Jin, R., Isomerism in Au28 (SR) 20 nanocluster and stable structures. *J. Am. Chem. Soc.* **2016,** *138* (5), 1482-1485.
12. Jin, R., Quantum sized, thiolate-protected gold nanoclusters. *Nanoscale* **2010,** *2* (3), 343-362.
13. Brust, M.; Walker, M.; Bethell, D.; Schiffrin, D. J.; Whyman, R., Synthesis of thiol-derivatised gold nanoparticles in a two-phase liquid–liquid system. *J. Chem. Soc., Chem. Commun.* **1994,** (7), 801-802.
14. (a) Schaaff, T.; Shafigullin, M.; Khoury, J.; Vezmar, I.; Whetten, R.; Cullen, W.; First, P.; Gutierrez-Wing, C.; Ascensio, J.; Jose-Yacaman, M., Isolation of smaller nanocrystal Au molecules: robust quantum effects in optical spectra. *The Journal of Physical Chemistry B* **1997,** *101* (40), 7885-7891; (b) Schaaff, T. G.; Knight, G.; Shafigullin, M. N.; Borkman, R. F.; Whetten, R. L., Isolation and selected properties of a 10.4 kDa gold: glutathione cluster compound. *The Journal of Physical Chemistry B* **1998,** *102* (52), 10643-10646; (c) Heaven, M. W.; Dass, A.; White, P. S.; Holt, K. M.; Murray, R. W., Crystal structure of the gold nanoparticle [N (C8H17) 4][Au25 (SCH2CH2Ph) 18]. *J. Am. Chem. Soc.* **2008,** *130* (12), 3754-3755.
15. Zhu, M.; Lanni, E.; Garg, N.; Bier, M. E.; Jin, R., Kinetically controlled, high-yield synthesis of Au25 clusters. *J. Am. Chem. Soc.* **2008,** *130* (4), 1138-1139.
16. (a) Wu, Z.; Suhan, J.; Jin, R., One-pot synthesis of atomically monodisperse, thiol-functionalized Au 25 nanoclusters. *J. Mater. Chem.* **2009,** *19* (5), 622-626; (b) Jin, R.; Qian, H.; Wu, Z.; Zhu, Y.; Zhu, M.; Mohanty, A.; Garg, N., Size focusing: a methodology for synthesizing atomically precise gold nanoclusters. *The Journal of Physical Chemistry Letters* **2010,** *1* (19), 2903-2910.
17. Yu, Y.; Luo, Z.; Yu, Y.; Lee, J. Y.; Xie, J., Observation of cluster size growth in CO-directed synthesis of Au25 (SR) 18 nanoclusters. *ACS nano* **2012,** *6* (9), 7920-7927.
18. Yu, Y.; Luo, Z.; Chevrier, D. M.; Leong, D. T.; Zhang, P.; Jiang, D.-e.; Xie, J., Identification of a highly luminescent Au22 (SG) 18 nanocluster. *J. Am. Chem. Soc.* **2014,** *136* (4), 1246-1249.
19. (a) Montalti, M.; Prodi, L.; Zaccheroni, N.; Baxter, R.; Teobaldi, G.; Zerbetto, F., Kinetics of place-exchange reactions of thiols on gold nanoparticles. *Langmuir* **2003,** *19* (12), 5172-5174; (b) Amendola, V.; Pilot, R.; Frasconi, M.; Marago, O. M.; Iati, M. A., Surface plasmon resonance in gold nanoparticles: a review. *J. Phys.: Condens. Matter* **2017,** *29* (20), 203002.
20. Zhu, M.; Aikens, C. M.; Hollander, F. J.; Schatz, G. C.; Jin, R., Correlating the crystal structure of a thiol-protected Au25 cluster and optical properties. *J. Am. Chem. Soc.* **2008,** *130* (18), 5883-5885.
21. Wang, S.; Zhu, X.; Cao, T.; Zhu, M., A simple model for understanding the fluorescence behavior of Au 25 nanoclusters. *Nanoscale* **2014,** *6* (11), 5777-5781.
22. (a) Weissker, H.-C.; Escobar, H. B.; Thanthirige, V.; Kwak, K.; Lee, D.; Ramakrishna, G.; Whetten, R.; López-Lozano, X., Information on quantum states pervades the visible spectrum of the ubiquitous Au 144 (SR) 60 gold nanocluster. *Nat. Commun.* **2014,** *5*, 3785; (b) Zhou, C.; Sun, C.; Yu, M.; Qin, Y.; Wang, J.; Kim, M.; Zheng, J., Luminescent gold nanoparticles with mixed valence states generated from dissociation of polymeric Au (I) thiolates. *The Journal of Physical Chemistry C* **2010,** *114* (17), 7727-7732.
23. Zheng, J.; Zhou, C.; Yu, M.; Liu, J., Different sized luminescent gold nanoparticles. *Nanoscale* **2012,** *4* (14), 4073-4083.
24. Zheng, J.; Zhang, C.; Dickson, R. M., Highly fluorescent, water-soluble, size-tunable gold quantum dots. *Phys. Rev. Lett.* **2004,** *93* (7), 077402.
25. Crawford, S. E.; Andolina, C. M.; Smith, A. M.; Marbella, L. E.; Johnston, K. A.; Straney, P. J.; Hartmann, M. J.; Millstone, J. E., Ligand-mediated “turn on,” high quantum yield near-infrared emission in small gold nanoparticles. *J. Am. Chem. Soc.* **2015,** *137* (45), 14423-14429.
26. Wang, G.; Huang, T.; Murray, R. W.; Menard, L.; Nuzzo, R. G., Near-IR luminescence of monolayer-protected metal clusters. *J. Am. Chem. Soc.* **2005,** *127* (3), 812-813.
27. (a) Negishi, Y.; Nobusada, K.; Tsukuda, T., Glutathione-protected gold clusters revisited: Bridging the gap between gold (I)− thiolate complexes and thiolate-protected gold nanocrystals. *J. Am. Chem. Soc.* **2005,** *127* (14), 5261-5270; (b) Wang, G.; Guo, R.; Kalyuzhny, G.; Choi, J.-P.; Murray, R. W., NIR luminescence intensities increase linearly with proportion of polar thiolate ligands in protecting monolayers of Au38 and Au140 quantum dots. *The Journal of Physical Chemistry B* **2006,** *110* (41), 20282-20289; (c) Bigioni, T.; Whetten, R.; Dag, Ö., Near-infrared luminescence from small gold nanocrystals. *The Journal of Physical Chemistry B* **2000,** *104* (30), 6983-6986; (d) Link, S.; Beeby, A.; FitzGerald, S.; El-Sayed, M. A.; Schaaff, T. G.; Whetten, R. L., Visible to infrared luminescence from a 28-atom gold cluster. *The Journal of Physical Chemistry B* **2002,** *106* (13), 3410-3415.

28. (a) Montalti, M.; Zaccheroni, N.; Prodi, L.; O'Reilly, N.; James, S. L., Enhanced sensitized NIR luminescence from gold nanoparticles via energy transfer from surface-bound fluorophores. *J. Am. Chem. Soc.* **2007,** *129* (9), 2418-2419; (b) Bonacchi, S.; Cantelli, A.; Battistelli, G.; Guidetti, G.; Calvaresi, M.; Manzi, J.; Gabrielli, L.; Ramadori, F.; Gambarin, A.; Mancin, F., Photoswitchable NIR-Emitting Gold Nanoparticles. *Angew. Chem. Int. Ed.* **2016,** *55* (37), 11064-11068.
29. Weare, W. W.; Reed, S. M.; Warner, M. G.; Hutchison, J. E., Improved synthesis of small (d core≈ 1.5 nm) phosphine-stabilized gold nanoparticles. *J. Am. Chem. Soc.* **2000,** *122* (51), 12890-12891.
30. (a) Montalti, M.; Dolci, L. S.; Prodi, L.; Zaccheroni, N.; Stuart, M. C.; van Bommel, K. J.; Friggeri, A., Energy transfer from a fluorescent hydrogel to a hosted fluorophore. *Langmuir* **2006,** *22* (5), 2299-2303; (b) Bonacchi, S.; Rampazzo, E.; Montalti, M.; Prodi, L.; Zaccheroni, N.; Mancin, F.; Teolato, P., Amplified fluorescence response of chemosensors grafted onto silica nanoparticles. *Langmuir* **2008,** *24* (15), 8387-8392.
31. Salvia, M.-V.; Ramadori, F.; Springhetti, S.; Diez-Castellnou, M.; Perrone, B.; Rastrelli, F.; Mancin, F., Nanoparticle-assisted NMR detection of organic anions: from chemosensing to chromatography. *J. Am. Chem. Soc.* **2015,** *137* (2), 886-892.

Chapter 8: Polydopamine for radiation protection

8.1 Introduction

Melanin is an abundant and heterogeneous biopigment found ubiquitously in many livings being. It is present in bacteria, fungi and animals. There exist three major types of melanins: brown-to-black eumelanin, reddish-yellow pheomelanin and neuro melanin. In humans, melanin plays a key role in determining skin, eyes and hair color.

The abundance of eumelanin in the hair has a darker color, tending to brown or black. *Vice versa* if the pheomelanin prevails the color is red or blonde.

Mammalian melanocytes in the epidermis produce eumelanin and pheomelanin. The first steps in the synthesis of pigments are similar and under control of enzyme tyrosinase, which catalyse oxidation of tyrosine or 3,4-Dihydroxy-L-phenylalanine (L-DOPA) to DOPAquinone. Synthesis of eumelanin proceeds with later oxidation of DOPAquinone to L-dopachrome which tautomerises to form 5,6-dihydroxyindole-2-carboxylic acid (DHICA) aided by dopachrome tautomerase, or reaction proceeds spontaneously with decarboxylation to give mainly 5,6-dihydroxyindole (DHI). Oxidative polymerization of DHI and/or DHICA, carried out by tyrosinase-related protein 1, gives rise to the deposition of black insoluble eumelanin polymers. In the case of pheomelanin, the next step of biosynthesis involves cysteine which can bind in position 2 or 5 of the benzene ring. Subsequently, substrates are oxidized to cysteine-dopaquinones that cyclize in 1,4 benzothiazine intermediate. The latter polymerize producing pheomelanin.

The last one is neuromelanin, dark insoluble polymer pigment produced in specific populations of catecholaminergic neurons in the brain, where dopamine undergoes oxidation and cyclization that results in DHI, which polymerize and precipitate as neuromelanin. Humans have the largest amount of neuromelanin, which is present in lesser amounts in other primates, and totally absent in many other species.

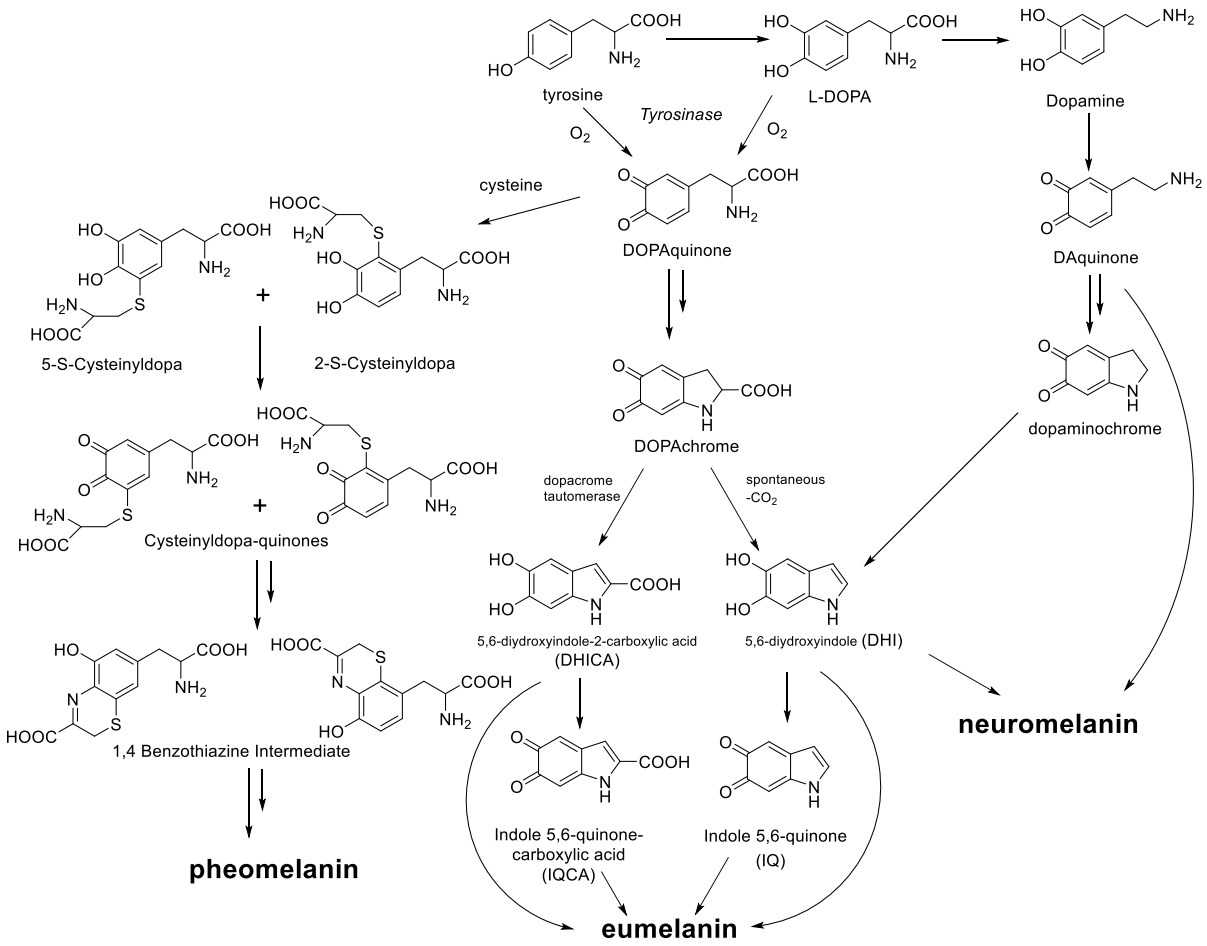

Fig.8.1 biological synthetic pathway of melanin[1]

Eumelanin and pheomelanin differ not only chemically but also in their physical properties. In fact, eumelanin plays an exemplary role as a radioprotector, thanks to its broad band absorption spectrum, its ability to convert 90% of absorbed light[2] and free radical scavenger into heat. On the other hand, pheomelanin is much less able to block UV energy and in fact may synergize with UV photons to promote free radical formation and carcinogenesis in the skin[3]. Consequently, research focused on eumelanin and its interesting properties. Despite the growing interest a fundamental obstacle still exists in this field: no complete structural elucidation of eumelanin is available to date. Indeed, they are macromolecular systems whose structure is still poorly understood. It is still uncertain how the constituent molecules organize and bond each other. This knowledge gap impedes attempts to discover the relationship between intrinsic properties and functions. Because of its amorphous nature and insolubility in all solvents it has been difficult to resolve the structure at molecular level. Despite obstacles, several clues have accumulated over the years. It is now widely accepted that molecular units of eumelanin are DHI, DHICA and their reduced forms.[4] These molecular units or monomers serve as the building blocks of eumelanin and in-plane oligomerize to form low molecular weight oligomers, called protomolecules[5] mainly tetramers or pentamers with porphyrin-like

structures[6] that tend to stack together due to strong out-of-plane noncovalent intermolecular interactions such as van der Waals and π−π interactions[7]. Stacked sheets of protomolecules weak interact to form onion-like nanostructures randomly oriented. Presence of amorphous supramolecular structure have been confirmed by TEM[8], Raman measurement[9], NMR solid-state study[10] and computational methods. Available information to date on the composition of eumelanin fail in expanding the peculiar properties that characterize these materials. It is therefore necessary to build a structure–property model that can fill this gap. The most characteristic and challenging behavior of eumelanin is the broad absorption spectrum in the UV and visible range, 700–200 nm. This behavior is central to some of its biological functions, such as the blocking of UV radiation, and is puzzling because it lacks any of the sharp features typical of other key biomolecules in the UV range[6c]. Best interpretation of eumelanin properties and characteristics is based on the model of chemical and geometric disorder. First there is chemical (or static) disorder of monomer involved in the polymerization process. Second electronic disorder relates to the distribution of redox states (i.e., catechol, semiquinone or quinone) within the oligomeric scaffolds. Then geometric (dynamic) disorder describes structural heterogeneity that comes from the broad range of possible aggregates generated by intermolecular interactions between oligomers that are in varied sizes and randomly oriented. Most advanced study conclude that eumelanin broadband absorption is not due simply to the overlap of static chromophore defined intrinsically by the conjugation length across the carbon frame but is also extrinsic in character resulting from aggregation-dependent intermolecular perturbations of the π-electron systems[6b, 7, 11]. The peaks in red and NIR region present most difficult interpretation. Excitonic interactions among the stacked eumelanin protomolecules may be responsible for the peaks at the lower-energy end of the spectra. The role of the excitonic couplings is suggested by the mix of stacked conjugated protomolecules and the short interlayer distance among them[2]. Thanks to broad band absorption spectrum eumelanin absorb UV and visible radiation. Melanin has been found have a relevant role in radioprotection. Survival rates of melanized and non-melanized fungi were evaluated under exposure to extremely high doses of gamma radiation. Results reported a significatively higher survival in melanized fungi and that radiation promoted growth of fungi. This attraction of fungi to radiation is called 'radiotropism'[12]

It was assumed that melanin pigments, participating in redox reactions, can perceive the energy of radiation and make it available for metabolic processes. The mechanism of eumelanin radioprotection involves quenching of ROS generated by the radiolysis of water and trapping high-energy electrons within eumelanin structure preventing harmful secondary ionizations[13]

A study demonstrated that irradiation of melanin resulted in melanin oxidation over time. Quinone moieties, present in melanin composition, are believed responsible for its redox behavior[14]. The radioprotective and antioxidant activities of melanin nanoparticles were investigated in mice in vivo and can protected mice against oxidative stress and DNA damage induced by ionizing radiation. Melanin nanoparticles appeared not produce tissue damage and may be considered as harmless antioxidant and antiradical compounds[15]. Melanin radioprotective ability have attracted a lot of interest by researchers. They could be exploited in space travel[16] in medical treatment, in tough environments. There are many sources in nature from which it is possible to extract melanin. Nevertheless, this operation has drawbacks. In fact, to date no extraction technique has been found that guarantees not to affect the properties of melanin in its natural environment. Therefore, researchers have sought alternative ways to obtain synthetic materials that reproduce the most interesting characteristics of melanin. Currently the best candidate is polydopamine (PDA), a black insoluble material produced by oxidative polymerization of dopamine under alkaline conditions. PDA shares chemical functionalities (i.e., catechol and nitrogen-containing groups) with natural eumelanin[17] and present similar features as broad band absorption spectrum, it is insoluble in almost all solvents, ability in metal chelation, free radical stable and semiconducting activity. Although, it is currently impossible to provide an accurate picture of eumelanin and PDA structure it is important stress that DHICA-derived units are absent as building blocks in PDA, for this reason PDA cannot be considered as synthetic melanin[4c]. The unique characteristics of melanin, conferring antioxidant and radio- and photo-protective properties, are mostly due to the presence of unpaired electrons in the structure that results in a stable free radical property[13]. We can suppose that increasing stable free radicals on melanin corresponds in increase the intrinsic free radical scavenging ability and consequently radioprotective effects. A simple strategy to achieve this goal is exploit nitroxide radical coupling (NRC) reactions obtained through bioinspired copolymerization of dopamine and a nitroxide functional dopamine derivative as monomers. A widely followed procedure to obtain functionalized adhesive precursor molecules is to use 3,4-dihydroxy-L-phenylalanine (L-DOPA) carrying a carboxylic acid moiety as a ligation point, which can be esterified or amidated for the introduction of the desired functionality. Thereby, the catecholamine unit is preserved, and thus, the ability to self-polymerize in a dopamine-like manner is maintained[18]. At the time that this thesis in written different studies with this interesting material are carried out to test its effective radiation protection properties. Together with the other considerable properties of melanin, there is the ability in ionic metal complexation. Gianneschi et all have been

developed an innovative prepolymerization doping strategy method for synthesis of Fe(III)−polydopamine complex nanoparticles. The results show that Fe(III)−catechol complexation, covalent bonding, and self-assembly take place simultaneously in the "polymerization" process[19]. Subsequently this strategy has been adapted for a large number of transition metal[20]. The presence of Fe(III) can contribute to increase the intrinsic melanin free radical scavenging ability, at the basis of radiation protection activity. Indeed, when Fe(III) meets a free electron it can catch it reducing at Fe(II). Then it appears interesting increase melanin radiation protection activity both increasing number of stable free radicals and introducing oxidative ion transition metal.

8.2 Summary

In this chapter we try to increase melanin radiation protection activity both increasing number of stable free radicals and introducing oxidative ion transition metal. We chose Fe(III) and Mn(III) to increase oxidative ability and Zn(II), that do not possess oxidative ability as reference. We used 4-amino-TEMPO to increase number of stable free radicals.

Reagents are presents with the sequent ratio: dopamine 3, Fe(III) 1, 4-amino-TEMPO 1.

Since scalability is a major issue in melanin preparation synthesis has been carried out first in small scale (Fe_T_PDAss) and then in a large scale (Fe_T_PDAls). Then we tried to increase iron concentration. We repeated reaction with the sequent ratio of reagents: dopamine 3, Fe(III) 2, 4-amino-TEMPO 1. Also, in this case synthesis has been carried out in small scale (Fe2_T_PDAss) and then in a large scale (Fe2_T_PDAls).

Then we used Mn(III). Reagents are presents with the sequent ratio: dopamine 2, Mn(III) 1, 4-amino-TEMPO 1. For starting, synthesis has been carried out in small scale (Mn_T_PDAss) and then in a large scale (Mn_T_PDAls).

Then we used Zn(II). Reagents are presents with the sequent ratio: dopamine 3, Zn(II) 1.5, 4-amino-TEMPO 1. For starting, synthesis has been carried out in small scale (Zn_T_PDAss). Unfortunately, it was not possible obtain this material in large scale. Then we tried to increase zinc concentration. We repeated reaction with the sequent ratio of reagents: dopamine 3, Zn(II) 3, 4-amino-TEMPO 1. Synthesis has been carried out in small scale (Zn2_T_PDAss) and then in a large scale (Zn2_T_PDAls).

All materials have been characterized by dynamic light scattering (DLS), transmission electron microscopy (TEM), energy dispersive spectroscopy (EDS), X-ray photoelectron spectroscopy (XPS), electron paramagnetic resonance (EPR) and inductively coupled plasma-atomic

emission spectrometry (ICP- AES). In conclusion DPPH assay was used to test antioxidant activity of nanoparticles.

8.3 Copolymerization of dopamine and nitroxide functional dopamine derivative (L-DOPA TEMPO)

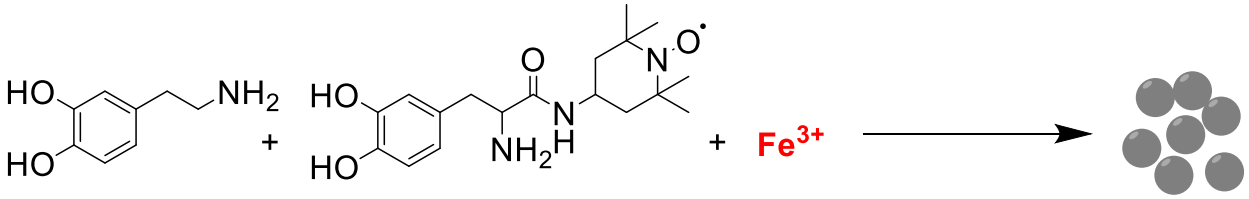

Fig.8.2 Synthesis of PDA NPs with Fe and L-DOPA TEMPO

In polymerization mechanisms of catecholamines, for example, dopamine (3,4-dihydroxyphenethylamine), many unknown passages are still present after years of study. However, it has now been established that the oxidation of the catechol group by atmospheric oxygen has a fundamental role. The resulting compounds are 5,6-dihydroxy indole and indole 5,6-quinone that start the polymerization process. The use of polymerizable catechol precursors for the introduction of targeted functional moieties is an efficient ligation technique. A widely followed procedure to obtain functionalized adhesive precursor molecules is to use 3,4-dihydroxy-L-phenylalanine (L-DOPA) carrying a carboxylic acid moiety as a ligation point, which can be esterified or amidated for the introduction of the desired functionality. Thereby, the catecholamine unit is preserved, and thus, the ability to self-polymerize in a dopamine-like manner is maintained[18b].

Herein, we used a functionalized L-DOPA monomer carrying a 4-amino-2,2,6,6-tetramethylpiperidine (4-amino-TEMPO) for introduction of TEMPO moiety.

The catechol-functionalized network of the nanoparticle acts as a scaffold for chelation of paramagnetic metal ions. A common approach to the preparation of metal-loaded PDA hybrid materials involves the synthesis of colloidal PDA nanoparticles, followed by doping with the appropriate metal salt. However, this methodology leads to limited metal loadings. Recently, prepolymerization strategies were reported for the preparation of Fe(III)-loaded dopamine nanoparticles in a single pot[19-20].

In the present case we have chosen to use the last approach starting from a solution of dopamine and iron with a 3:1 ratio. After many attempts to synthesize the desired material, an efficient NRC protocol in presence of iron was established. In a 50 mL flask dopamine hydrochloride (4.50 mg, 0.024 mmol) has been solubilized in 13 mL of water with iron chloride hexahydrate (2.04 mg, 0.0075 mmol) and solution was strongly stirred for one hour at room

temperature to allow the metal center coordination with dopamine catechol group. Then was added L-DOPA-TEMPO (2.52 mg, 0.0075 mmol) and Tris base (300 mg in 2 ml). It was observed that the solution colour immediately turned red, gradually turning black after 0.5 h. Solution was strongly stirred overnight. Resulting nanoparticles (Fe_LDT_PDA) were separated by centrifugation and washed three times with deionized water.

To understand how the presence of L-DOPA-TEMPO affect dopamine polymerization and resulting properties, dopamine nanoparticles without L-DOPA-TEMPO were synthetized with the same procedure (Fe_PDA).

The first investigation was carried out by measuring the polymerization kinetics by absorption in both cases.

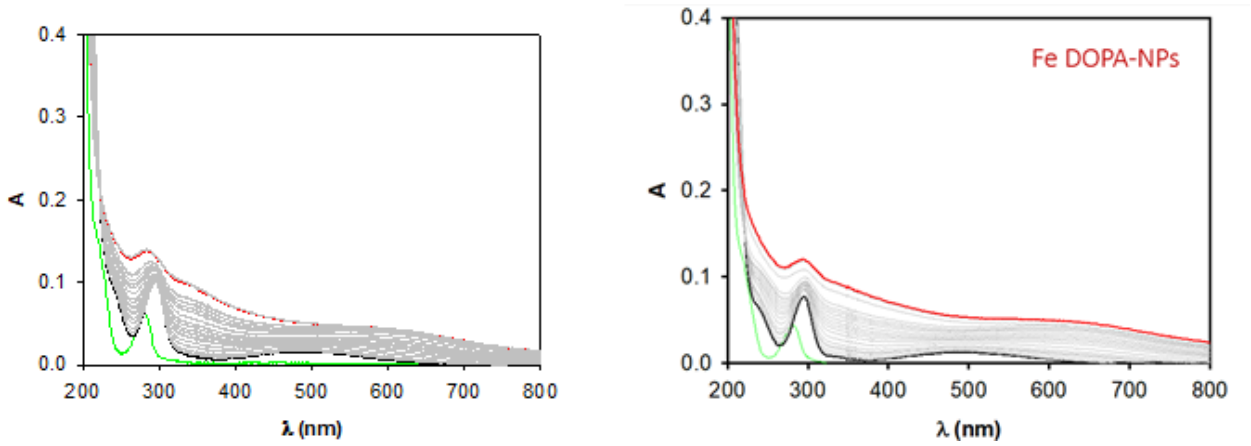

Fig. 8.3 on the left: absorption spectra of Fe_PDA at different time; on the right: absorption spectra of Fe_LDT_PDA at different time

In Fig.8.3 is reported dopamine and iron chloride spectrum (green line) with the spectrum collected after tris base was added (black line). Subsequently different spectra have been collected at different time (grey lines) and the last one was collected after 27 hours (last one in red).

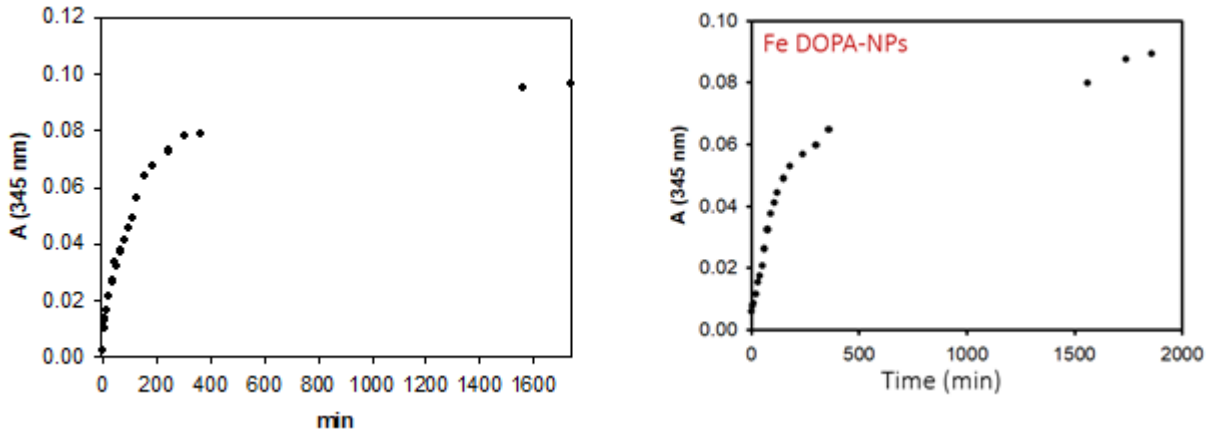

Fig.8.4 on the left: Fe_PDA absorbance at 345 nm at differet time;on the right: Fe_LDT_PDA absorbance at 345 nm at different time

In Fig.8.4 is reported absorbance at 345 nm at different time. Absorbance at 345 nm has been chosen as probe, because in other regions of spectrum there are different trends that can disturb the signal. At 280 nm there is the peak ok of dopamine that is disappearing, but intensity does not change significantly because of polymerization process increase the ground. Moreover, in presence of L-DOPA-TEMPO it is observed that the maximum shifts to blue during polymerization.

Size and morphology of nanoparticles were investigated by transmission electron microscopy (TEM). TEM grids were prepared by diluting solution in ethanol (5 μL in 20 μL) and depositing small (2 μL) aliquots of resulting sample onto grids (Formvar stabilized with carbon (5–10 nm) on 400 copper mesh, Ted Pella Inc.) that had previously been glow.

In Fig.8.5 are reported images of nanoparticles of Fe_LDT_PDA (first line) and Fe_PDA (second line).

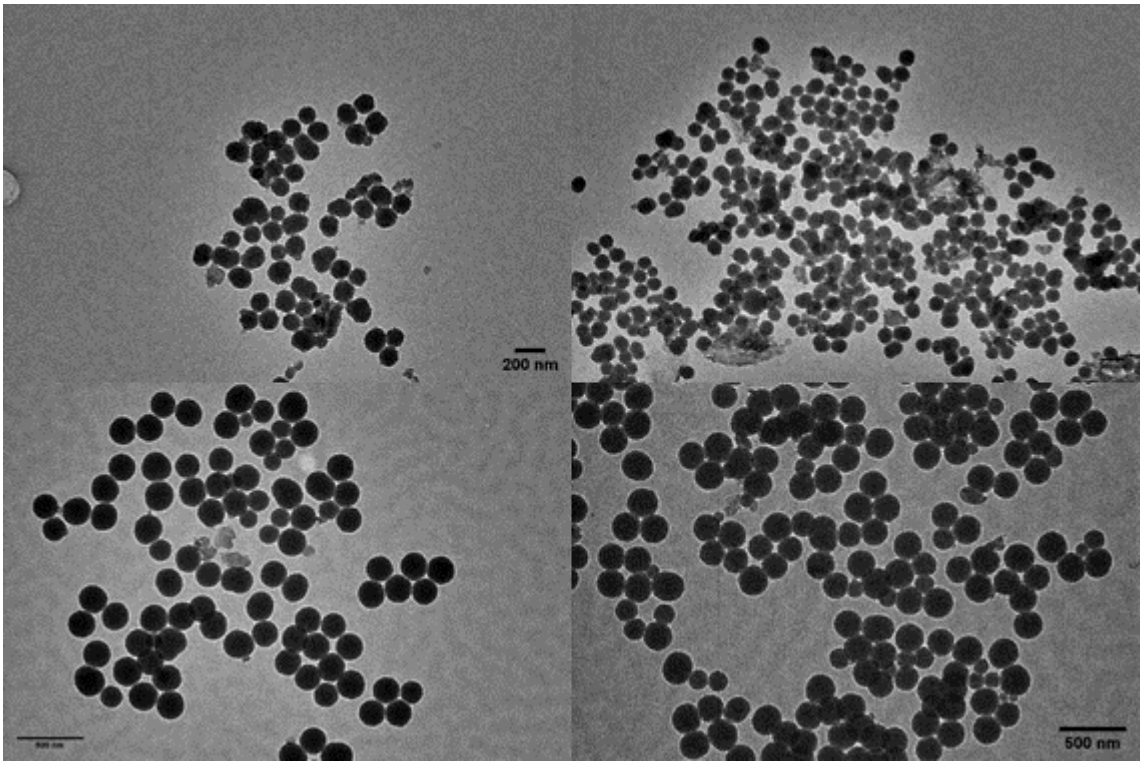

Fig.8.5 first line: Fe_LDT_PDA TEM images; second line: Fe_PDA TEM images

Fe_LDT_PDA nanoparticles have a spherical shape with a homogeneous diameter 172±16nm and Fe_PDA nanoparticles diameter of 207±46 nm.

EDS (energy dispersive spectroscopy) analysis have performed to proof presence of iron ions inside both nanoparticles.

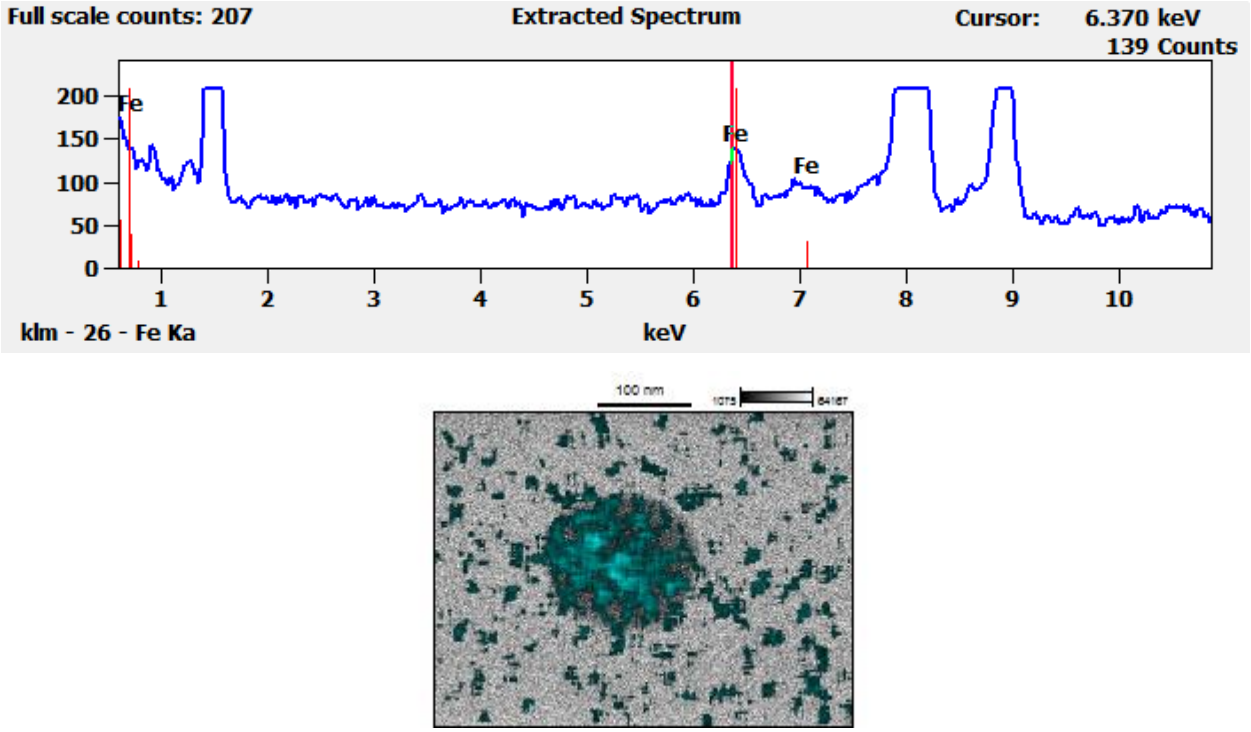

Fig.8.6 EDS results for Fe_LDT_PDA

In Fig.8.6 has been reported results of EDS signals for iron in sample Fe_LDT_PDA. It can be observed that its presence is confirmed by the high number of counts (139) and that origin of signal is concentrated in nanoparticles.

Comparable results are obtained for sample Fe_PDA as shown in Fig.8.7.

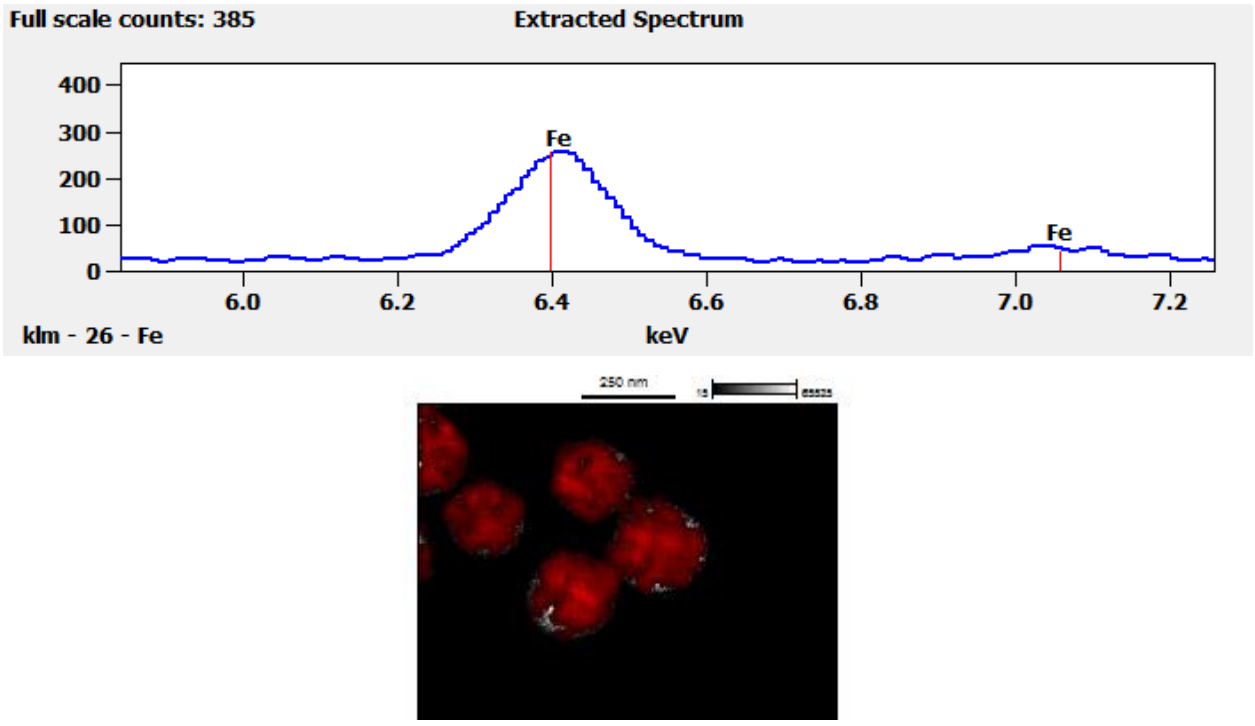

Fig.8 7 EDS results for Fe_PDA

Further evidence of iron presence has been obtained by X-ray photoelectron spectroscopy (XPS), which also provides quantitative information on the composition of nanoparticles.

Table 8.1 XPS Elemental analysis of Fe_PDA and Fe_LDT_PDA

Name	**Peak BE** Fe_PDA	**Atomic %** Fe_PDA	**Peak BE** Fe_LDT_PDA	**Atomic %** Fe_LDT_PDA
C1s	284.655	63.15	284.566	65.35
N1s	399.622	8.37	399.579	8.72
O1s	531.373	26.26	531.445	24.35
Fe2p	711.265	2.22	711.166	1.57

In Table8.1 are shown XPS results for both samples. Iron is present in a similar percentage 2.22% (without L-DOPA-TEMPO) and 1.57 (without L-DOPA-TEMPO) and this demonstrate that presence of L-DOPA-TEMPO do not interferes with iron uptake. Another interesting result is the difference in percentage of carbon and oxygen (respectively 63.15% and 26.26% without L-DOPA-TEMPO; 65.35% and 24.35 % with L-DOPA-TEMPO). This is an indirect evidence of the presence of L-DOPA-TEMPO. Indeed, atomic composition of dopamine (without hydrogen) is 8 carbons (72 %), 2 oxygens (18 %) and 1 nitrogen (9 %). Atomic composition of L-DOPA-TEMPO is 18 carbons (75 %), 4 oxygens (16%) and 2 nitrogen atoms (8%). In L-DOPA-TEMPO carbon percentage is a little bit higher than in dopamine and oxygen percentage is a little bit lower, as results from XPS analysis.

8.4 Copolymerization of dopamine and 4-amino-TEMPO

Unfortunately, synthesis of Fe_LDT_PDA is not completely reproducible and it does not work on large scale. Moreover, synthesis of L-DOPA-TEMPO is time demanding and gives the product in low yield. For this reason, it was necessary to find an innovative approach.

As mentioned above, presence of catechol groups is fundamental for polymerization process, but when it is started it is not clear what happens. It is possible, for example, that dopamine, which has not turned into 5,6-dihydroxy indole or indole 5,6-quinone, binds covalently to polydopamine via the amino group. This means that maybe catechol group is not indispensable

for participating in the polymerization process and it is possible carries out nitroxide radical coupling reaction, just exploiting amine group of TEMPO.

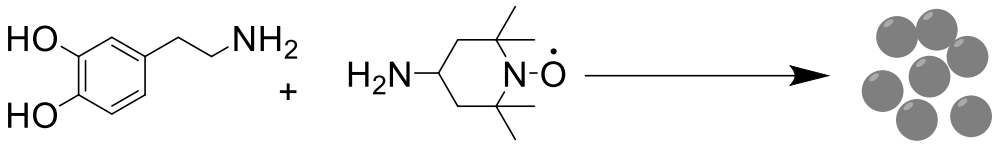

Fig.8 8 Synthesis of PDA NPs with 4-amino-TEMPO

As proof of concept polydopamine nanoparticles (T_PDA) have been synthetized with TEMPO with the following procedure: in a 50 mL flask dopamine hydrochloride (40 mg, 0.211 mmol) has been solubilized in 11 mL of water and 2 mL of ethanol with 4-amino-tempo (12 mg; 0.07 mmol) and 63 μL of NH_4OH have been added. Solution was strongly stirred overnight. Resulting nanoparticles were separated by centrifugation and washed three times with deionized water. To understand how the presence TEMPO affect dopamine polymerization and resulting properties, dopamine nanoparticles without TEMPO were synthetized with the same procedure (PDA).

Size of nanoparticles was investigated by DLS: hydrodynamic diameter of T_PDA is 544 nm with 0.1 PDI and the one of PDA results 250 nm with 0.0 PDI.

Morphology of nanoparticles was investigated by TEM. TEM grids were prepared following the procedure described above.

In Fig.8.9 are reported images of nanoparticles T_PDA (first line) and PDA (second line).

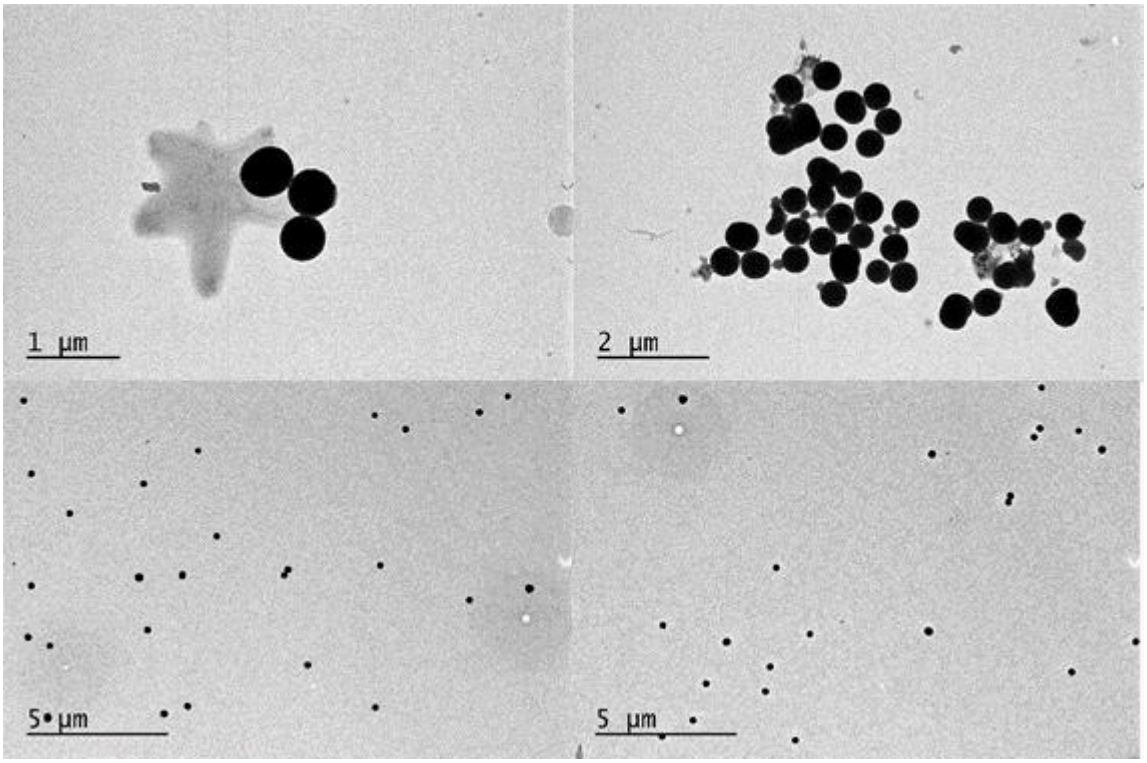

Fig.8.9 TEM images of T_PDA (first line); TEM images of PDA (second line)

T_PDA nanoparticles have a spherical shape with a homogeneous diameter of 498±45 nm and PDA nanoparticles have a diameter of 241±27 nm. Such a large difference in size is indirect evidence that TEMPO intervened during the polymerization process.

Presence of TEMPO free radical has been confirmed by EPR (Electron Paramagnetic Resonance) analysis on nanoparticles. In Fig.8.10 is reported EPR spectrum of a water solution of T_PDA 2.5 mg/mL collected in a range of 328-345 mT with a power of 20.0 mW and a speed of 120.0 s

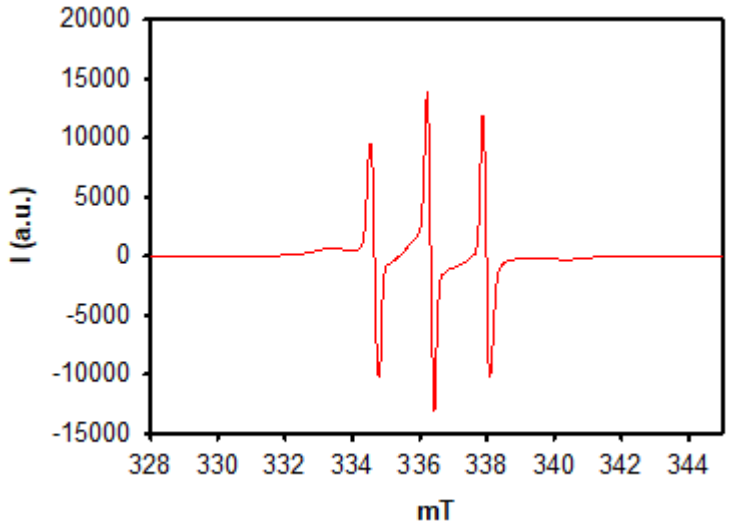

Fig.8.10 EPR analysis of T_PDA

It is clearly visible the characteristic signal of TEMPO radical with three peaks at 334.6, 336.3 and 338.0 mT. There are also two small and broad peaks at 333.34 and 340.25 mT. Signals of TEMPO overlap the one of melanin that cannot be detected in these conditions.

Next step is to synthesize new polydopamine nanoparticles with TEMPO and transition metals. For the first attempt iron was chosen.

8.5 Copolymerization of dopamine and 4-amino-TEMPO and $FeCl_3$

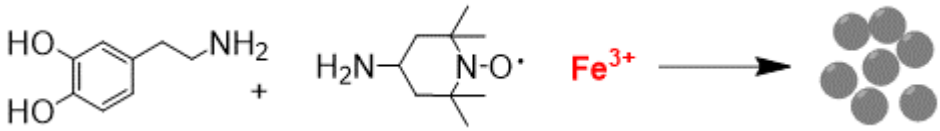

Fig.8.11 Synthesis of PDA nanoparticles with Fe and 4-amino-TEMPO

The following procedure was developed (Fe_T_PDAss): in a 500 mL flask dopamine hydrochloride (10.4 mg, 0.055 mmol) has been solubilized in 100 mL of water with iron chloride hexahydrate (4.7 mg, 0.017mmol) and solution was strongly stirred for one hour at room temperature to allow the metal center coordination with dopamine catechol group. Then was added TEMPO (2.9 mg,0.017mmol) and 4.6 mL of Tris base (1500 mg/5mL). It was

observed that the solution colour immediately turned red, gradually turning black after 0.5 h. Solution was strongly stirred overnight. Resulting nanoparticles were separated by centrifugation and washed three times with deionized water.

The hydrodynamic diameter measured by DLS is 307 nm with 0.1 PDI.

Size and morphology of Fe_T_PDAss nanoparticles were investigated by TEM. TEM grids were prepared following the procedure described above. In Fig.8.12 are reported images of nanoparticles.

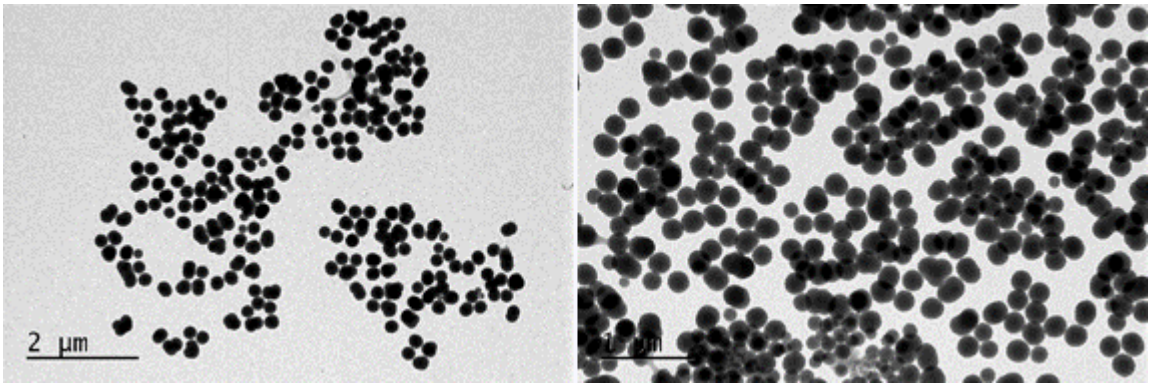

Fig.8.12 TEM images of Fe_T_PDAss

These nanoparticles have a spherical shape with a homogeneous diameter of 227±19 nm.

Resonance) analysis on nanoparticles.

EDS analysis have performed to proof presence of iron ions inside Fe_T_PDAss nanoparticles.

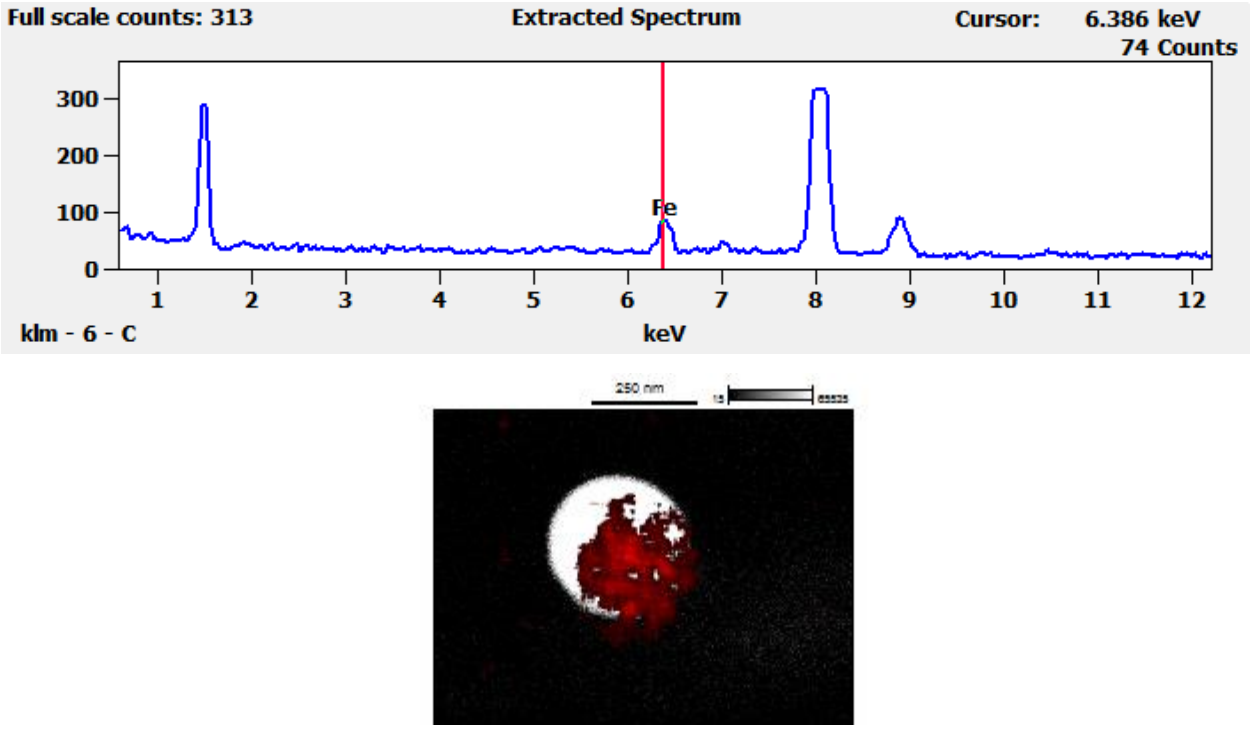

Fig.8.13 EDS results for Fe_T_PDAss:

In Fig.8.13 has been reported results of EDS signals for iron in sample Fe_T_PDAss. It can be observed that its presence is confirmed, and that origin of signal is concentrated in nanoparticles.

Further evidence of iron presence has been obtained by XPS as shown in Table8.2.

Table 8.2 XPS elemental analysis of Fe_T_PDAss

Name	**Peak BE** Fe_T_PDAss	**Atomic %** Fe_T_PDAss
C1s	284.65	65.59
N1s	399.497	9.01
O1s	531.363	23.25
Fe2p	711.099	2.15

We note that the percentage of iron present in these last nanoparticles is very similar to that of the nanoparticles previously studied (Fe_PDA and Fe_LDT_PDA).

After obtaining these very positive preliminary results, to demonstrate the efficacy and reproducibility of the synthetic protocol developed, the synthesis was repeated on the larger scale (40 mg of dopamine) three time (Fe_T_PDAls **a**, **b**, **c**).

The resulting nanoparticles were analyzed separately via DLS. Their hydrodynamic diameter is respectively for Fe_T_PDAls **a**, **b**, **c**: 224 nm with 0.1 PDI, 232 nm with 0.1 PDI and 245 nm with 0.2 PDI.

Size and morphology of nanoparticles were investigated by TEM. TEM grids were prepared following the procedure described above. In Fig.8.14 are reported images of nanoparticles Fe_T_PDAls **a** (a), Fe_T_PDAls **b** (b) and Fe_T_PDAls **c** (c).

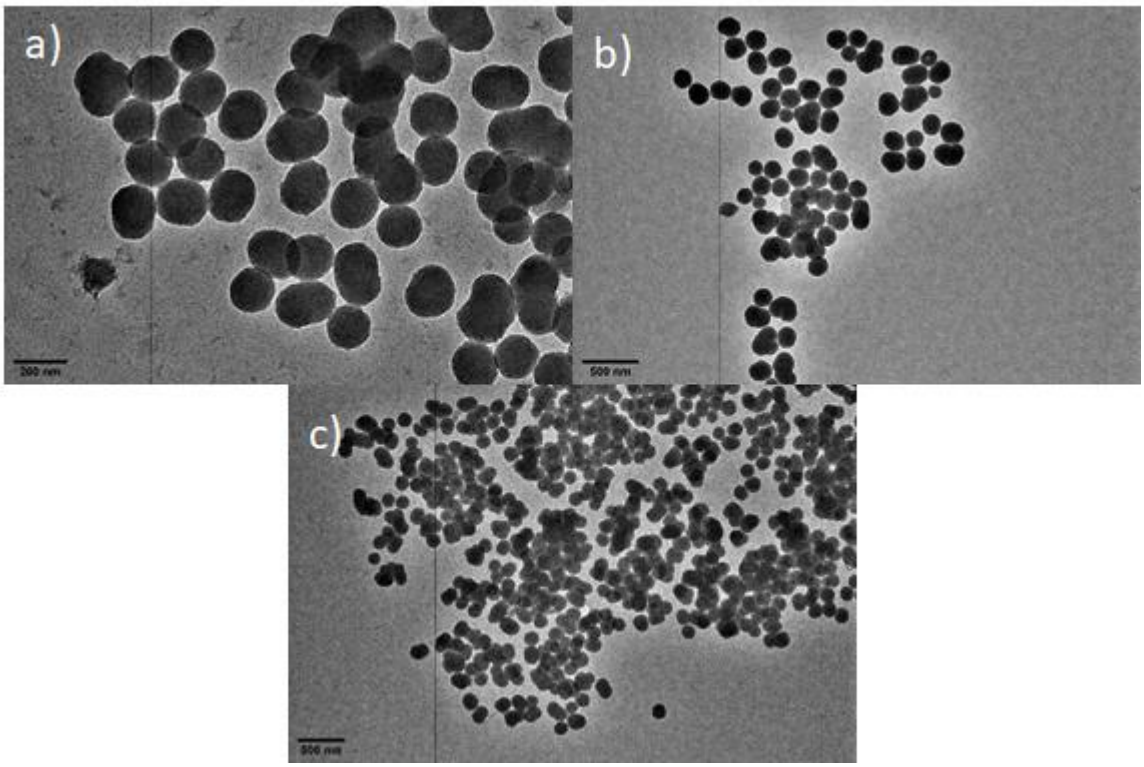

*Fig.8.14 TEM images of Fe_T_PDAls **a** (a); Fe_T_PDAls **b** (b) and Fe_T_PDAls **c** (c);*

These nanoparticles have a spherical shape with a homogeneous diameter respectively of 174±16 nm, 171±24 nm and 154 ±18 nm. These morphological data demonstrate that synthesis is reproducible also on large scale. In Fig.8.15 is reported molar extinction coefficient of Fe_T_PDAls nanoparticles as cm^{-1} (mg/mL). It is necessary adopt these these units of measurement, although they are improper, because it is not possibly knowing polydopamine molar concentration.

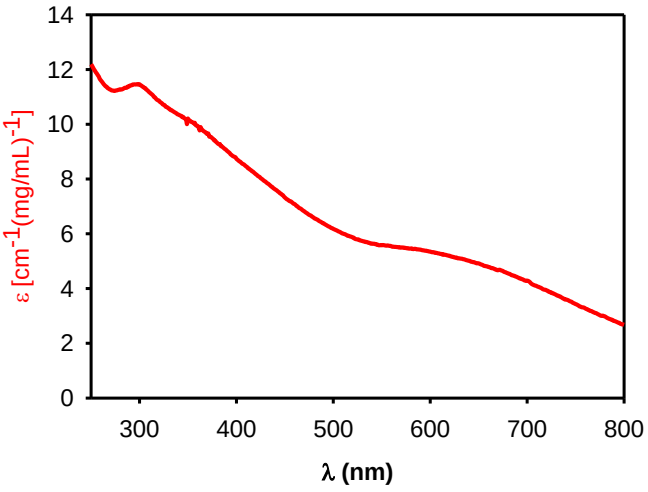

Fig.8.15 Molar extinction coefficient of Fe_T_PDAls

To evaluate how iron uptake varies in different samples of nanoparticles have been collected inductively coupled plasma atomic emission spectroscopy (ICP-AES) measurement of Fe_T_PDAls **a**, **b**, **c** that present respectively 7.24 %, 13.35% and 13.34% (wt) of iron.

Presence of TEMPO free radical has been confirmed by analysis on nanoparticles. In Fig.8.16 is reported EPR spectrum of a water solution of Fe_T_PDAls **a** 2.5 mg/mL collected in a range of 328-345 mT with a power of 20.0 mW and a speed of 120.0 s

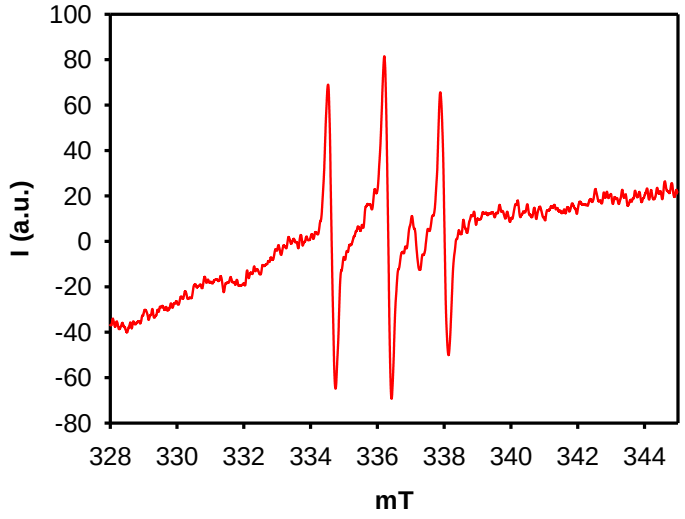

*Fig.8.16 EPR signal of Fe_T_PDAls **a***

It is visible the characteristic signal of TEMPO radical with three peaks at 334.6, 336.3 and 338.0 mT. Signals are not very intense because of presence of Fe(III). Signals of TEMPO overlap the one of melanin that cannot be clearly detected in these conditions.

The next step is trying to incorporate a higher iron percentage in polydopamine nanoparticles doubling iron concentration.

To achieve this goal different conditions have been screened. In particular we focused on tris base concentration because pH plays a central role in dopamine polymerization and Fe(III)$Cl_3 \cdot 6H_2O$ in a Lewis acid. That means that a mayor concentration of tris base is needed to obtain the desired basic conditions. By the way, it is important do not exceed with base, because too alkaline pH cause destruction of catechol group. Here reported tested conditions (respectively Fe2_T_PDAss **a**, **b**, **c**, **d**). In a 10 mL flask dopamine hydrochloride (1.04 mg) has been solubilized in 3 mL of water with iron chloride hexahydrate (0.94 mg) and solution was strongly stirred for one hour at room temperature to allow the metal center coordination with dopamine catechol group. Then was added TEMPO (0.29 mg) and for **a** 0.55 mL of Tris base (1500 mg/5mL), for **b** 0.64 mL, for **c** 0.73 mL and for **d** 0.82 mL. It was observed that the solution colour immediately turned red, gradually turning black after 0.5 h. Solution was strongly stirred overnight. Resulting nanoparticles were separated by centrifugation and

washed three times with deionized water. Size and morphology of nanoparticles were investigated by TEM. The flask with best results is Fe2_T_PDAss **a**.

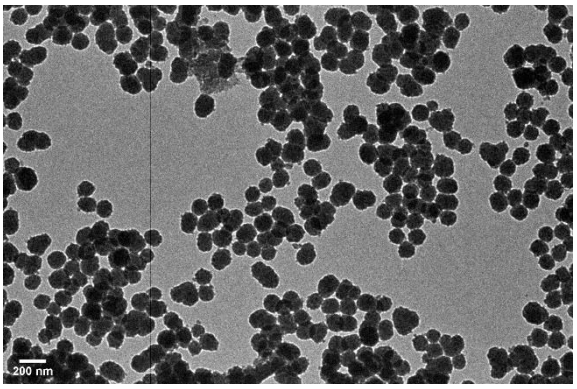

*Fig.8.17 TEM images of Fe2_T_PDAss **a***

These nanoparticles have a spherical shape with a homogeneous diameter of 124±16nm.

After obtaining these preliminary results, to demonstrate the efficacy and reproducibility of the synthetic protocol developed, the synthesis was repeated on the larger scale (35 mg of dopamine) three time (Fe2_T_PDAls **a**, **b**, **c**). The resulting nanoparticles were analyzed separately via DLS. Their hydrodynamic diameter is respectively for Fe2_T_PDAls **a**, **b**, **c**: 259 nm with 0.1 PDI, 268 nm with 0.1 PDI and 242 nm with 0.1 PDI.

Size and morphology of nanoparticles were investigated by TEM. TEM grids were prepared following the procedure described above. In Fig.8.18 are reported images of nanoparticles Fe2_T_PDAls **a** (a), Fe2_T_PDAls **b** (b) and Fe2_T_PDAls **c** (c).

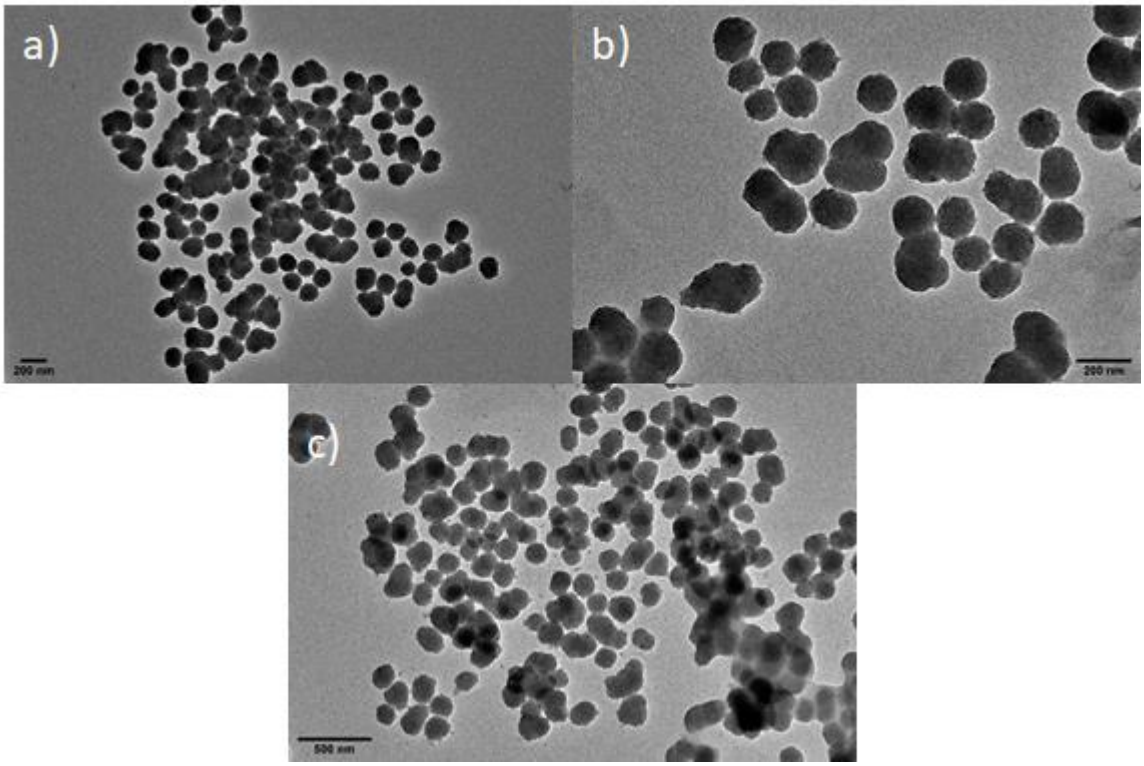

*Fig.8.18 TEM images of Fe2_T_PDAls **a** (a); Fe2_T_PDAls **b** (b); Fe2_T_PDAls **c** (c);*

These nanoparticles have a spherical shape with a homogeneous diameter respectively of 144±19 nm, 158±21 nm and 152±21 nm. Presence of TEMPO free radical has been confirmed by analysis on nanoparticles. In Fig.8.19 is reported EPR spectrum of a water solution of Fe2_T_PDAls **a** 2.5 mg/mL collected in a range of 328-345 mT with a power of 20.0 mW and a speed of 120.0 s

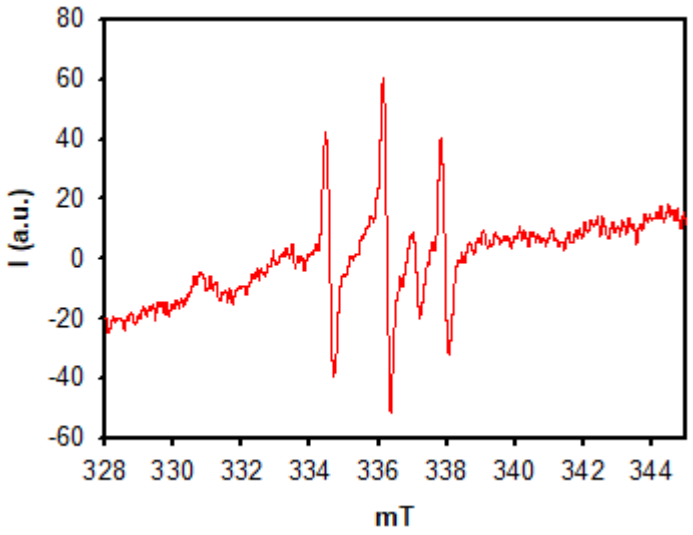

*Fig.8.19 EPR signal of Fe2_T_PDAls **a***

It is visible the characteristic signal of TEMPO radical with three peaks at 334.6, 336.3 and 338.0 mT. Signals are not very intense because of presence of Fe(III). Signals of TEMPO overlap the one of melanin that cannot be clearly detected in these conditions.

EDS analysis have performed to proof presence of iron ions inside Fe2_T_PDAls nanoparticles.

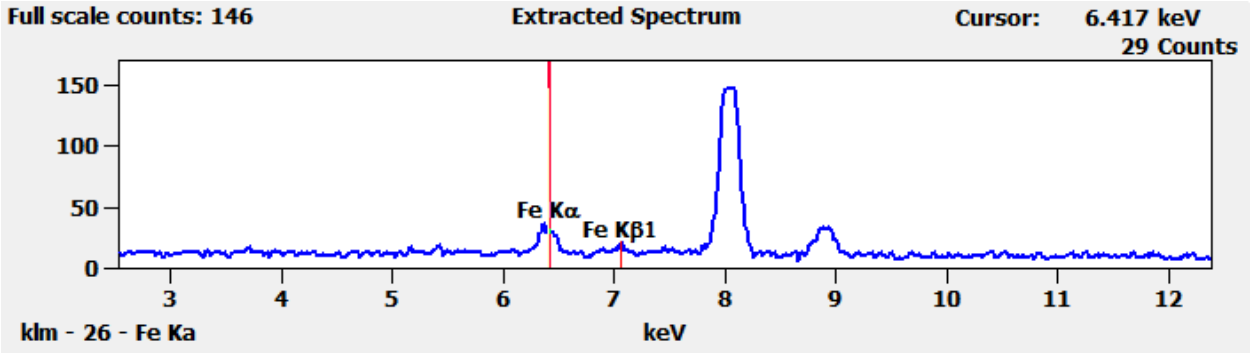

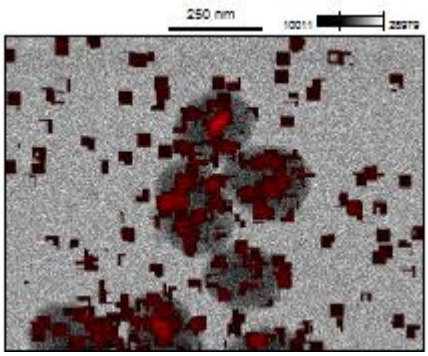

*Fig.8.20 EDS results for Fe2_T_PDAls **a***

In Fig.8.20 has been reported results of EDS signals for iron in sample Fe2_T_PDAls **a**. It can be observed that its presence is confirmed, and that origin of signal is concentrated in nanoparticles.

Further evidence of iron presence has been obtained by XPS as shown in Table 8.3.

*Table 8.3 XPS elemental analysis of Fe2_T_PDAls **a***

Name	**Peak BE** Fe2_T_PDAls **a**	**Atomic %** Fe2_T_PDAls **a**
C1s	284.187	60.59
N1s	399.088	8.23
O1s	530.693	26.88
Fe2p	710.729	4.29

We note that the percentage of iron present in Fe2_T_PDAls **a** nanoparticles is the double of the one of the nanoparticles previously studied (Fe_T_PDAss).

In Fig.8.21 is reported molar extinction coefficient of Fe2_T_PDAls nanoparticles as cm^{-1} $(mg/mL)^{-1}$.

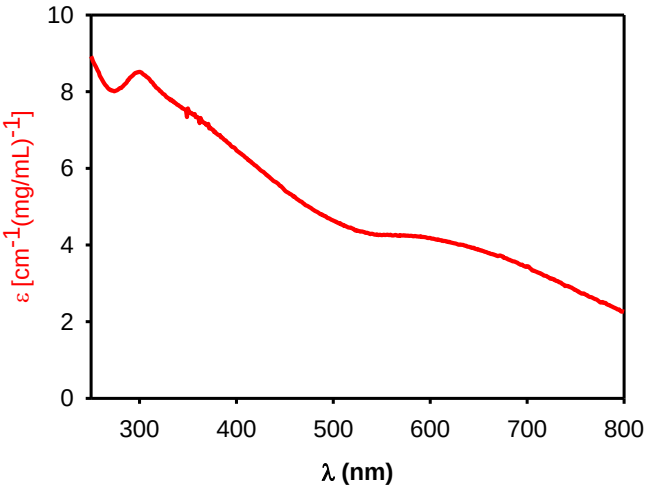

Fig.8.21 Molar extinction coefficient of Fe2_T_PDAls

To evaluate how iron uptake varies in different samples of nanoparticles have been collected ICP-AES measurement of Fe2_T_PDAls **a**, **b**, **c** that present respectively 11.07 %, 19.88 % and

13.60% (wt) of iron. Unfortunately, we were able to double the iron concentration only in one sample.

8.6 Copolymerization of dopamine and 4-amino-TEMPO and $Mn(Ac)_3$

Having obtained such interesting results for iron, we decided to try functionalizing the nanoparticles with other transition metals and we started by testing manganese(III).

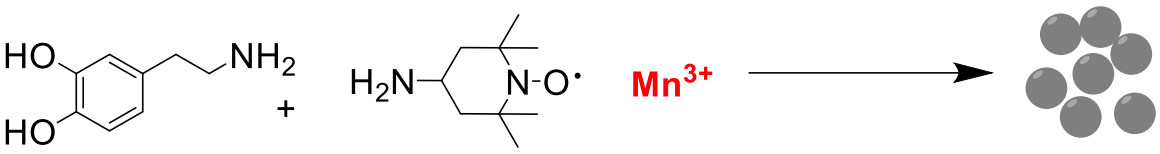

Fig.8.22 Synthesis of PDA nanoparticles with manganese and 2-amino-TEMPO

Synthetic procedure was developed based on synthesis reported in literature: in a 50 mL flask dopamine hydrochloride (3.51 mg, 0.018 mmol) has been solubilized in 27 mL of water with manganese(III)acetate dihydrate (2.47 mg, 0.009 mmol) and solution was strongly stirred for one hour at room temperature to allow the metal center coordination with dopamine catechol group. Then was added TEMPO (1.2 mg, 0.007 mmol) and 1.4 mL of Tris base (300 mg/5mL). It was observed that the solution colour immediately turned orange, gradually turning black after 0.5 h. Solution was strongly stirred overnight. Resulting nanoparticles (Mn_T_PDAss) were separated by centrifugation and washed three times with deionized water.

The hydrodynamic diameter measured by DLS is 207 nm with 0.1 PDI.

Size and morphology of nanoparticles were investigated by TEM.

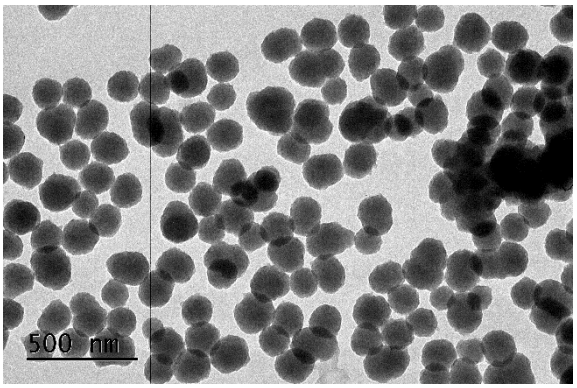

Fig.8.23 TEM images of Mn_T_PDAss

These nanoparticles have a spherical shape with a homogeneous diameter of 145±16nm.

EDS analysis have performed to proof presence of manganese ions inside Mn_T_PDAss nanoparticles.

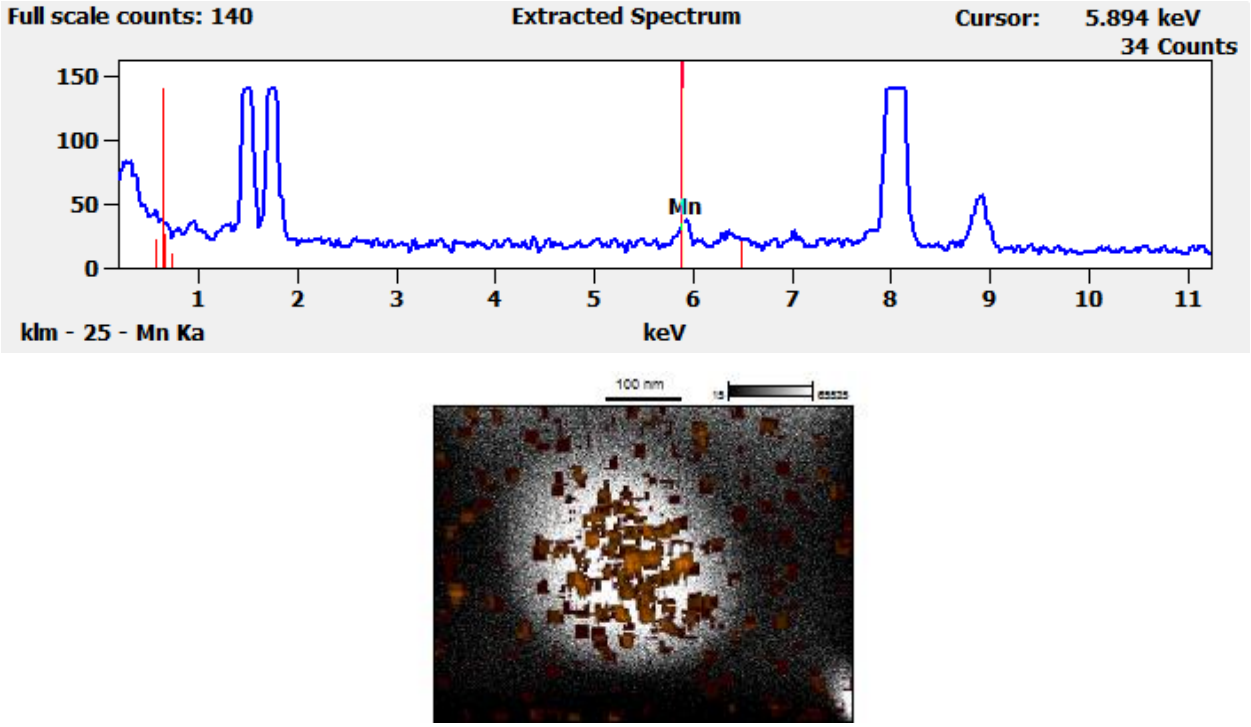

Fig.8.24 EDS results for Mn_T_PDAss

In Fig.8.24 has been reported results of EDS signals for manganese in sample Mn_T_PDAss. It can be observed that its presence is confirmed, and that origin of signal is concentrated in nanoparticles.

Further evidence of manganese presence has been obtained by XPS as shown in Table8.4.

Table 8.4 XPS elemental analysis of Mn_T_PDAss

Name	**Peak BE** Mn_T_PDAsl	**Atomic %** Mn_T_PDAsl
C1s	284.693	59.97
N1s	399.400	8.90
O1s	531.951	29.72
Mn2p	641.053	1.41

After obtaining these preliminary results, to demonstrate the efficacy and reproducibility of the synthetic protocol developed, the synthesis was repeated on the larger scale (20 mg of dopamine) three time (Mn_T_PDAls **a**, **b**, **c**).

The resulting nanoparticles were analyzed via DLS. Their hydrodynamic diameter is respectively for Mn_T_PDAls **a**, **b**, **c**: 242 nm with 0.1 PDI, 255 nm with 0.1 PDI and 59 nm with 0.1 PDI. Last data is on disagreement with other results.

Size and morphology of nanoparticles were investigated by TEM. TEM grids were prepared following the procedure described above. In Fig.8.25 are reported images of nanoparticles Mn_T_PDAls **a** (a), Mn_T_PDAls **b** (b) and Mn_T_PDAls **c** (c).

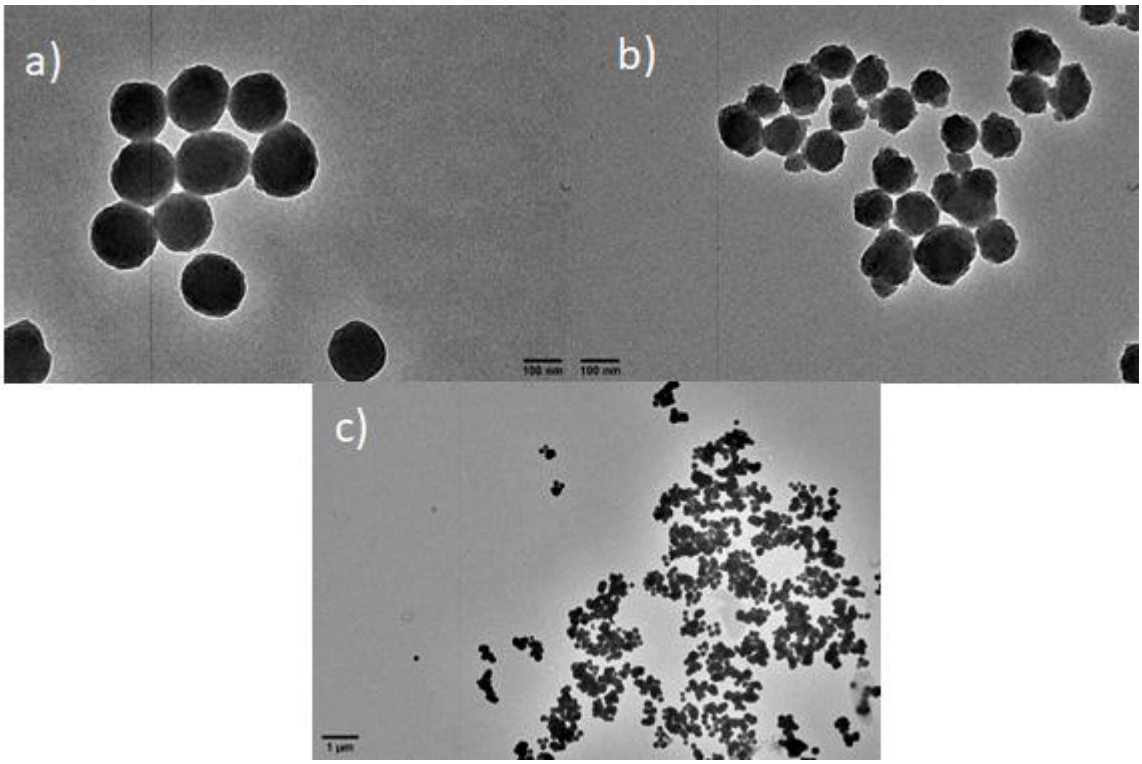

*Fig.8.25 TEM images of Mn_T_PDAls **a** (a); Mn_T_PDAls **b** (b); Mn_T_PDAls **c** (c);*

Sample Mn_T_PDAls **a** and **b** have a spherical shape with a homogeneous diameter respectively of 169±15 nm and 109±19 nm. In Mn_T_PDAls **c** it is possible see that there are large and unregular aggregate that may have distorted results on DLS. Such bad morphology could due to something that went wrong during stirring and probably it is a casual problem of sample Mn_T_PDAls **c** and not a limitation of synthetic procedure. That is, morphological data demonstrate that synthesis is reproducible also on large scale.

In Fig.8.26 is reported molar extinction coefficient of Mn_T_PDAls nanoparticles as cm^{-1} $(mg/mL)^{-1}$.

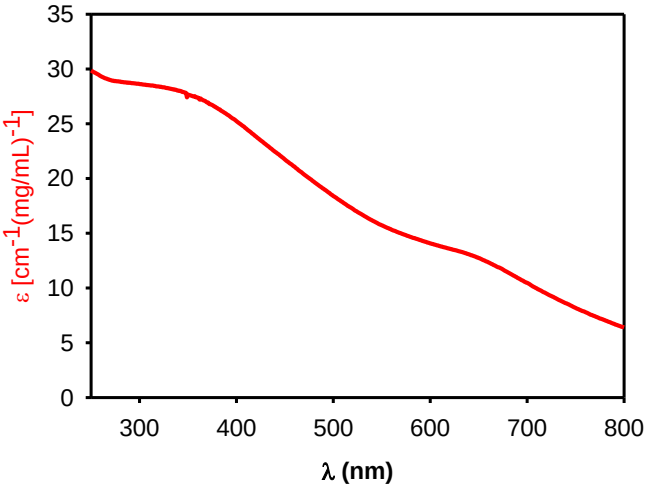

Fig.8.26 Molar extinction coefficient of Mn_T_PDAls

To evaluate how manganese uptake varies in different samples of nanoparticles have been collected inductively coupled plasma atomic emission spectroscopy (ICP-AES) measurement of Mn_T_PDAls **a**, **b**, **c** that present respectively 11.64 %, 8.89% and 9.36% (wt) of manganese. Presence of TEMPO free radical has been confirmed by analysis on nanoparticles. In Fig.8.27 is reported EPR spectrum of a water solution of Mn_T_PDAls **a** 2.5 mg/mL collected in a range of 300-380 mT with a power of 20.0 mW and a speed of 180.0 s

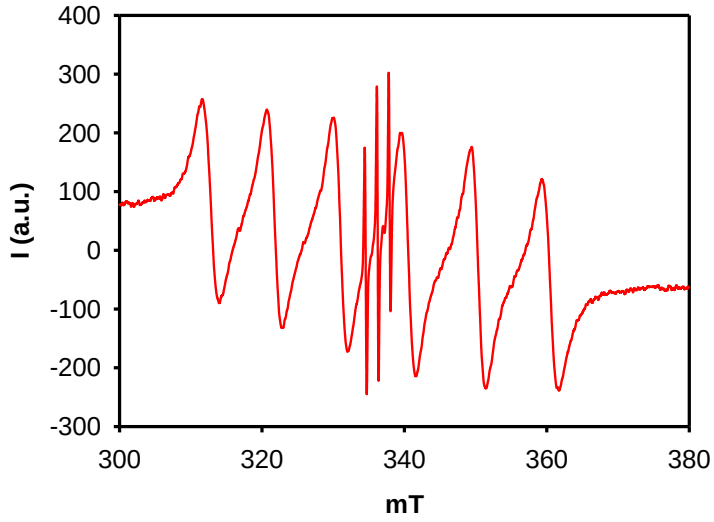

*Fig.8.27 EPR signals of Mn_T_PDAls **a***

It is visible the characteristic signal of TEMPO radical with three peaks at 334.6, 336.3 and 338.0 mT overloaded with characteristic. Signals are not very intense because of presence of Mn(III). Signals of TEMPO overlap the one of melanin that cannot be clearly detected in these conditions. As for the particles loaded with iron, also in this case we tried to increase the presence of manganese, but it was not possible to find a synthesis to obtain this material.

8.7 Copolymerization of dopamine and 4-amino-TEMPO and $ZnCl_2$

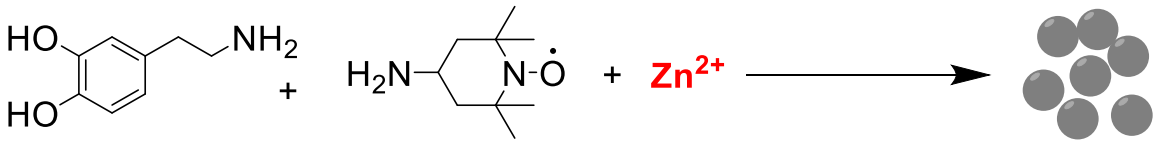

Fig.8.28 Synthesis of PDA nanoparticles with Zn and 4-amino-TEMPO

The last metal that has been tested is zinc. Also, in this case, the synthesis of nanoparticles was adapted on what is reported in the literature. in a 100 mL flask dopamine hydrochloride (8.34 mg, 0.044 mmol) has been solubilized in 20 mL of water with zinc chloride (3 mg, 0.022 mmol) and solution was strongly stirred for one hour at room temperature to allow the metal center coordination with dopamine catechol group. Then was added TEMPO (2.5 mg, 0.014 mmol) and 10 mL of Tris base (300 mg/5mL). Solution was strongly stirred overnight. Resulting nanoparticles (Zn_T_PDAss) were separated by centrifugation and washed three times with deionized water. The hydrodynamic diameter measured by DLS is 198 nm with 0.1 PDI. Size and morphology of nanoparticles were investigated by TEM.

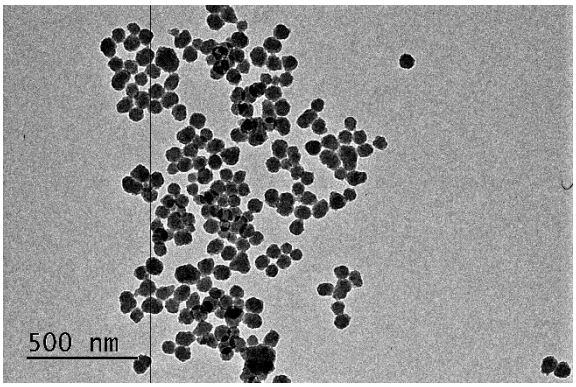

Fig.8.29 TEM images of Zn_T_PDAss

These nanoparticles have a spherical shape with a homogeneous diameter of 63±6 nm.

EDS analysis have performed to proof presence of zinc ions inside Zn_T_PDAss nanoparticles.

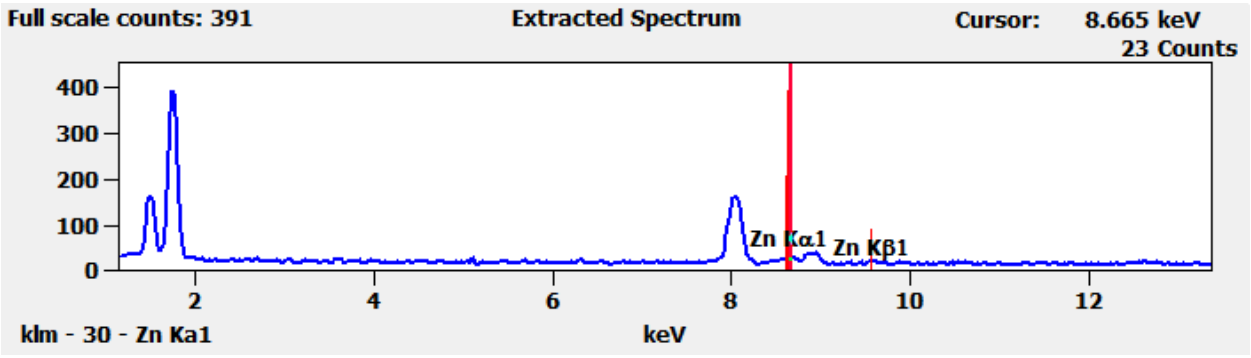

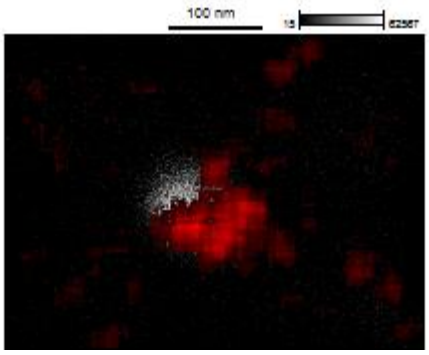

Fig.8.30 EDS results for Zn_T_PDAss:

In Fig.8.30 has been reported results of EDS signals for zinc in sample Zn_T_PDAss. It can be observed that its presence is confirmed, and that origin of signal is concentrated in nanoparticles.

Further evidence of zinc presence has been obtained by XPS as shown in Table8.5.

Table 8.5 XPS elemental analysis of Zn_T_PDAss

Name	**Peak BE** Zn_T_PDAss	**Atomic %** Zn_T_PDAss
C1s	284.478	59.70
N1s	399.385	11.3
O1s	531.525	26.38
Zn2p	1021.691	2.62

After obtaining these preliminary results, to demonstrate the efficacy and reproducibility of the synthetic protocol developed, the synthesis was repeated on the larger scale (40 mg of dopamine) three time.

Unfortunately, in this case the large-scale synthesis proved ineffective and very often the yield was too low or even no material was obtained.

Despite this failure, we still tried to synthetize nanoparticles with more zinc. The first attempt was simply to double the amount of zinc added and the result was very positive (Zn2_T_PDAss). Size and morphology of nanoparticles were investigated by TEM.

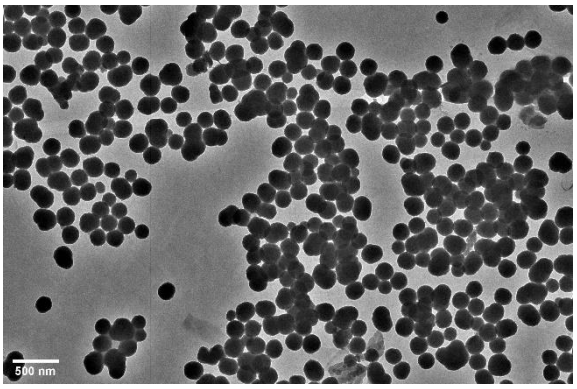

Fig.8 31 TEM images of Zn2_T_PDAss

These nanoparticles have a spherical shape with a homogeneous diameter of 192±20 nm.

To prove efficacy and reproducibility of the synthetic protocol developed, the synthesis was repeated on the larger scale three time (Zn2_T_PDAls **a**, **b**, **c**). In a 500 mL flask dopamine hydrochloride (41.75 mg) has been solubilized in 100 mL of water with zinc chloride (30 mg) and solution was strongly stirred for one hour at room temperature to allow the metal center coordination with dopamine catechol group. Then was added TEMPO (12.5 mg) and 50 mL of Tris base (300 mg/5mL). Solution was strongly stirred overnight. Resulting nanoparticles were separated by centrifugation and washed three times with deionized water.

Their hydrodynamic diameter is respectively for Zn2_T_PDAls **a**, **b**: 373 nm with 0.1 PDI and 327 nm with 0.1 PDI. For sample Zn2_T_PDAls · it was not possible obtain DLS data.

Size and morphology of nanoparticles were investigated by TEM.

In Fig.8.32 are reported images of nanoparticles Zn2_T_PDAls **a** (a), Zn2_T_PDAls **b** (b) and Zn2_T_PDAls **c** (c).

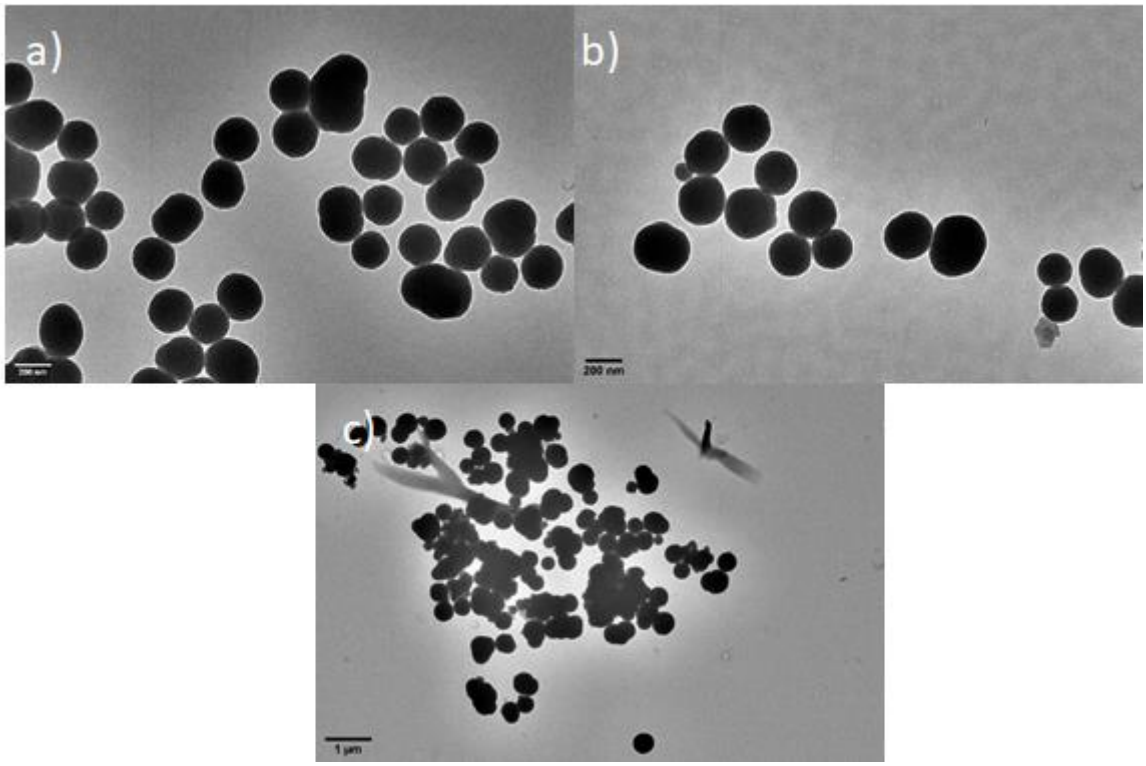

*Fig.8.32 TEM images of Zn2_T_PDAls **a** (a); Zn2_T_PDAls **b** (b); Zn2_T_PDAls **c** (c);*

Sample Zn2_T_PDAls **a** and **b** have a spherical shape with a homogeneous diameter respectively of 233±27 nm and 247±28 nm. In Zn2_T_PDAls **c** it is possible see that there are large and unregular aggregate that may have distorted results on DLS. Such bad morphology could due to something that went wrong during stirring and probably it is a casual problem of sample Zn2_T_PDAls **c** and not a limitation of synthetic procedure. That is, morphological data demonstrate that synthesis is reproducible also on large scale.

EDS analysis have performed to proof presence of zinc ions inside Zn2_T_PDAls **a** nanoparticles.

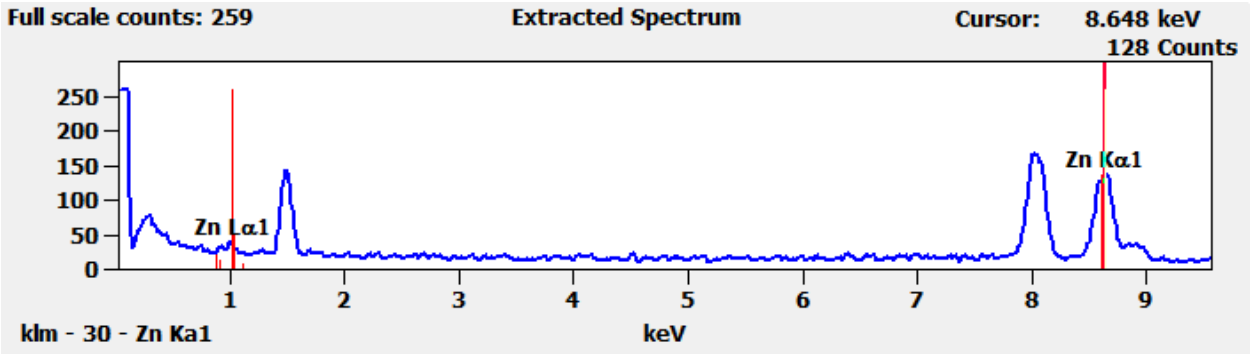

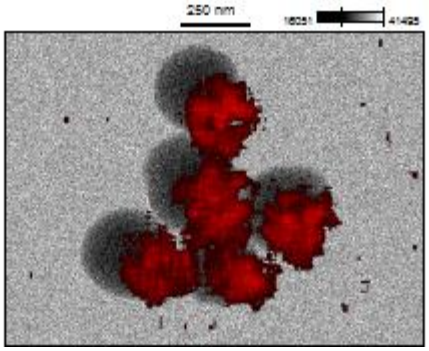

*Fig.8.33 EDS results of Zn2_T_PDAls **a***

In Fig.8.33 has been reported results of EDS signals for zinc in sample Zn2_T_PDAls **a**. It can be observed that its presence is confirmed, and that origin of signal is concentrated in nanoparticles.

Further evidence of zinc presence has been obtained by XPS as shown in Table 8.6.

*Table 8. 6 XPS elemental analysis of Zn2_T_PDAls **a***

Name	**Peak BE** Zn2_T_PDAls **a**	**Atomic %** Zn2_T_PDAls **a**
C1s	284.066	60.83
N1s	398.964	6.58
O1s	531.254	28.43
Zn2p	1021.921	4.16

We note that the percentage of zinc present in Zn2_T_PDAls **a** nanoparticles is the double of the one of the nanoparticles previously studied (Zn_T_PDAss).

In Fig.8.34 is reported molar extinction coefficient of Zn2_T_PDAls nanoparticles as cm^{-1} $(mg/mL)^{-1}$.

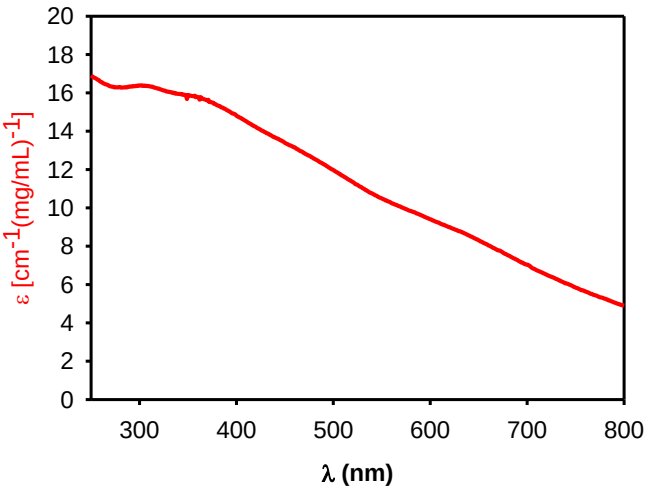

Fig.8.34 molar extinction coefficient of Zn2_T_PDAls

To evaluate how zinc uptake varies in different samples of nanoparticles have been collected ICP-AES measurement of Zn2_T_PDAls **a**, **b**, **c** that present respectively 13.74 %, 25.04 % and 20.86% (wt) of zinc.

Presence of TEMPO free radical has been confirmed by analysis on nanoparticles. In Fig.8.35 is reported EPR spectrum of a water solution of Zn2_T_PDAls **a** 2.5 mg/mL collected in a range of 328-345 mT with a power of 20.0 mW and a speed of 120.0 s

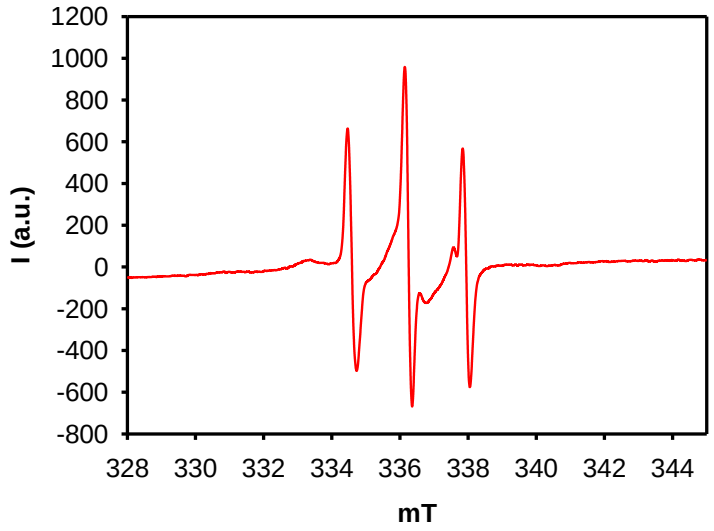

*Fig.8.35 EPR signals of Zn2_T_PDAls **a***

It is clearly visible the characteristic signal of TEMPO radical with three peaks at 334.6, 336.3 and 338.0 mT. There are also two small and broad peaks at 333.34 and 340.25 mT. Signals of TEMPO overlap the one of melanin that cannot be detected in these conditions.

8.8 DPPH Test

The potential antioxidant activity of synthesized melanin-like nanoparticles was evaluated by 2,2-diphenyl-1- picrylhydrazyl (DPPH) radical-scavenging assay according to the literature method[21].

Here we report results for polydopamine nanoparticles (PDA), polydopamine nanoparticles and TEMPO radical (T_PDA), polydopamine nanoparticles with iron (Fe_PDA), Fe_T_PDAls **a** and Fe2_T_PDAls **a**.

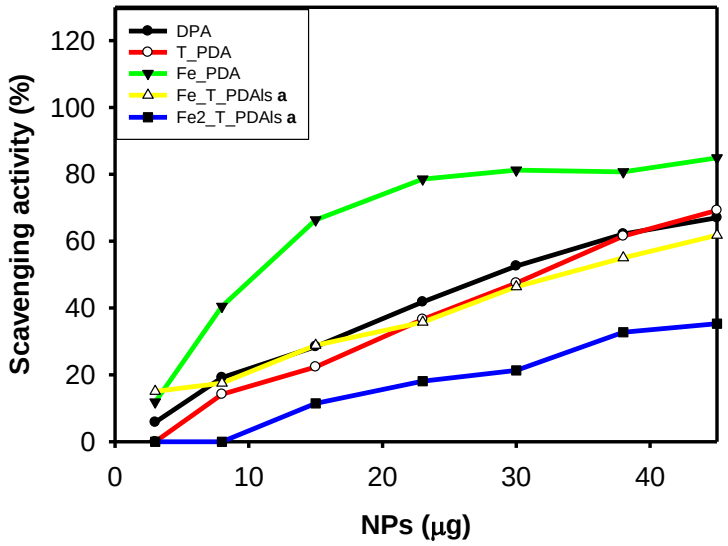

*Fig.8.36 DPPH test for free radical scavenger activity. Black line PDA; Red line: T_PDA; Green line: Fe_PDA; yellow line: Fe_T_PDAls **a**; blue line: Fe2_T_PDAls **a**.*

Results show that free radical scavenging activity is not increased by presence of TEMPO radical or iron ions. Indeed, Fe_PDA is the only sample with high scavenging activity, but probably this is due to small nanoparticles side (70nm) and not to iron presence.

Here we report results for polydopamine nanoparticles (PDA), polydopamine nanoparticles and TEMPO radical (T_PDA), polydopamine nanoparticles with manganese (Mn_PDA) and Mn_T_PDAls **a**.

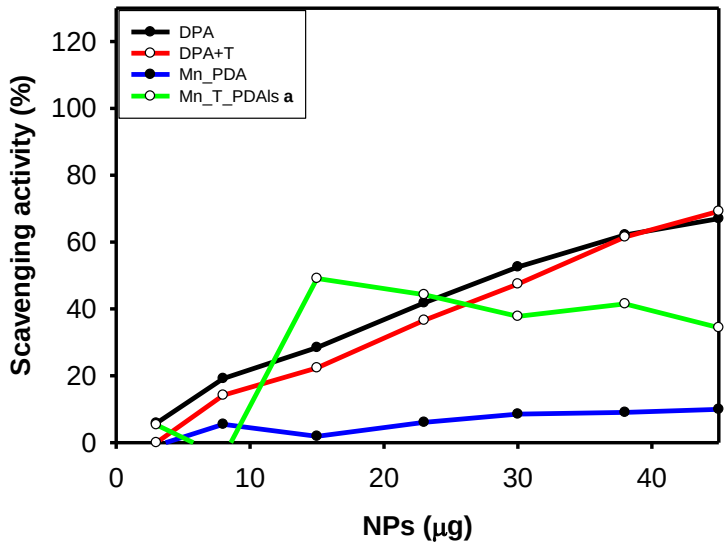

*Fig.8.37 DPPH test for free radical scavenger activity. Black line PDA; Red line: T_PDA; Blue line: Mn_PDA; green line: Mn_T_DPAls **a***

Results show that free radical scavenging activity is not increased by presence of TEMPO radical or manganese ions.

Here we report results for polydopamine nanoparticles (PDA), polydopamine nanoparticles and TEMPO radical (T_PDA), polydopamine nanoparticles with zinc (Zn_PDA) and Zn2_T_PDAls **a**.

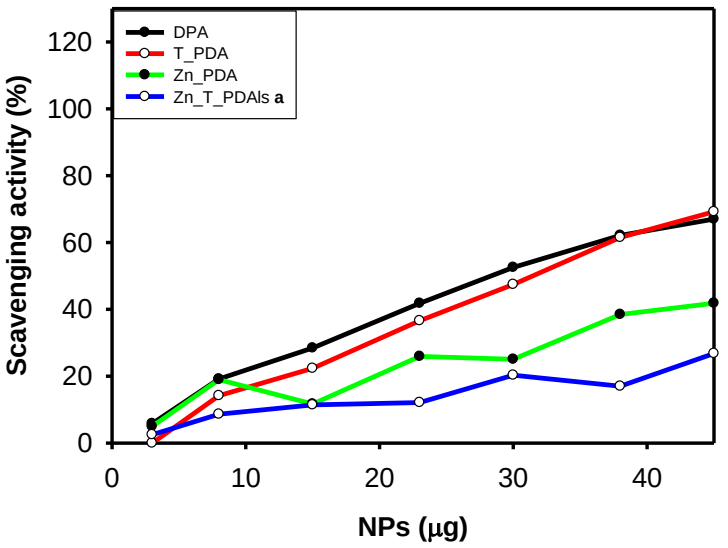

*Fig.8.38 DPPH test for free radical scavenger activity. Black line PDA; Red line:T_ PDA; green line: Zn_PDA with zinc; blue line: Zn2_T_PDAls **a**.*

8.9 Conclusions

Experimental results clearly demonstrate that several different radicals species can be efficiently incorporated in melanin nanoparticles. Hence the synthesis of the material was successful as demonstrated in particular by EPR measurements. Demonstrating the actual enhanced radioprotective activity of these new NPs is beyond the objective of this thesis, Nevertheless DPPH experiment failed in confirming that free radical scavenging activity is increased by presence of TEMPO radical or zinc ions.

Although I would like to stress that beside DPPH experiment are very convenient and easy to perform, they cannot be considered as conclusive. and future applcability of the new NPs to radioprotection cannot be ruled out. Moreover, PDA-Mn nanoparticles promise to be good contrast agents both for magnetic resonance imaging (MRI) and electron paramagnetic resonance imaging (EPRI). This is in agreement with results by Gianneschi et al. who have reported that presence of manganese in PDA nanoparticles permit them to act as MRI probes[20]. Now we added free radical TEMPO that present most of required properties to be chosen as EPRI probe[22].

8.10 Bibliography

1. (a) Chang, T.-S., An Updated Review of Tyrosinase Inhibitors. *International journal of molecular sciences* **2009,** *10*, 2440-75; (b) Hałdys, K.; Latajka, R., Thiosemicarbazones with tyrosinase inhibitory activity. *MedChemComm* **2019,** *10* (3), 378-389; (c) Mousavi, S. M.; Zarei, M.; Hashemi, S. A., Polydopamine for Biomedical Application and Drug Delivery System. *Medicinal Chemistry* **2018,** *08*.
2. Chen, C.-T.; Chuang, C.; Cao, J.; Ball, V.; Ruch, D.; Buehler, M. J., Excitonic effects from geometric order and disorder explain broadband optical absorption in eumelanin. *Nat. Commun.* **2014,** *5*, 3859.
3. Holcomb, N. C.; Bautista, R.-M.; Jarrett, S. G.; Carter, K. M.; Gober, M. K.; D'Orazio, J. A., cAMP-mediated regulation of melanocyte genomic instability: A melanoma-preventive strategy. *Advances in protein chemistry and structural biology* **2019,** *115*, 247-295.
4. (a) Lambert, C.; Chacon, J. N.; Chedekel, M. R.; Land, E. J.; Riley, P. A.; Thompson, A.; Truscott, T. G., A pulse radiolysis investigation of the oxidation of indolic melanin precursors: evidence for indolequinones and subsequent intermediates. *Biochimica et Biophysica Acta (BBA)-General Subjects* **1989,** *993* (1), 12-20; (b) Pezzella, A.; Panzella, L.; Natangelo, A.; Arzillo, M.; Napolitano, A.; d'Ischia, M., 5, 6-Dihydroxyindole Tetramers with "Anomalous" Interunit Bonding Patterns by Oxidative Coupling of 5, 5 ', 6, 6 '-Tetrahydroxy-2, 7 '-biindolyl: Emerging Complexities on the Way toward an Improved Model of Eumelanin Buildup. *The Journal of organic chemistry* **2007,** *72* (24), 9225-9230; (c) Chen, C.-T.; Martin-Martinez, F. J.; Jung, G. S.; Buehler, M. J., Polydopamine and eumelanin molecular structures investigated with ab initio calculations. *Chemical science* **2017,** *8* (2), 1631-1641.
5. Panzella, L.; Pezzella, A.; Napolitano, A.; d'Ischia, M., The First 5, 6-Dihydroxyindole Tetramer by Oxidation of 5, 5 ', 6, 6 '-Tetrahydroxy-2, 4 '-biindolyl and an Unexpected Issue of Positional Reactivity en Route to Eumelanin-Related Polymers. *Org. Lett.* **2007,** *9* (7), 1411-1414.

6. (a) Kim, Y. J.; Khetan, A.; Wu, W.; Chun, S. E.; Viswanathan, V.; Whitacre, J. F.; Bettinger, C. J., Evidence of Porphyrin-Like Structures in Natural Melanin Pigments Using Electrochemical Fingerprinting. *Adv. Mater.* **2016,** *28* (16), 3173-3180; (b) Meng, S.; Kaxiras, E., Theoretical models of eumelanin protomolecules and their optical properties. *Biophys. J.* **2008,** *94* (6), 2095-2105; (c) Kaxiras, E.; Tsolakidis, A.; Zonios, G.; Meng, S., Structural model of eumelanin. *Phys. Rev. Lett.* **2006,** *97* (21), 218102.
7. d'Ischia, M.; Napolitano, A.; Ball, V.; Chen, C.-T.; Buehler, M. J., Polydopamine and eumelanin: From structure–property relationships to a unified tailoring strategy. *Acc. Chem. Res.* **2014,** *47* (12), 3541-3550.
8. Watt, A. A.; Bothma, J. P.; Meredith, P., The supramolecular structure of melanin. *Soft Matter* **2009,** *5* (19), 3754-3760.
9. Yu, X.; Fan, H.; Liu, Y.; Shi, Z.; Jin, Z., Characterization of carbonized polydopamine nanoparticles suggests ordered supramolecular structure of polydopamine. *Langmuir* **2014,** *30* (19), 5497-5505.
10. Cîrcu, M.; Filip, C., Closer to the polydopamine structure: new insights from a combined 13 C/1 H/2 H solid-state NMR study on deuterated samples. *Polymer Chemistry* **2018,** *9* (24), 3379-3387.
11. Ascione, L.; Pezzella, A.; Ambrogi, V.; Carfagna, C.; d'Ischia, M., Intermolecular π-Electron Perturbations Generate Extrinsic Visible Contributions to Eumelanin Black Chromophore in Model Polymers with Interrupted Interring Conjugation. *Photochem. Photobiol.* **2013,** *89* (2), 314-318.
12. (a) Dadachova, E.; Casadevall, A., Ionizing radiation: how fungi cope, adapt, and exploit with the help of melanin. *Curr. Opin. Microbiol.* **2008,** *11* (6), 525-531; (b) Pacelli, C.; Bryan, R. A.; Onofri, S.; Selbmann, L.; Zucconi, L.; Shuryak, I.; Dadachova, E., Survival and redox activity of Friedmanniomyces endolithicus, an Antarctic endemic black meristematic fungus, after gamma rays exposure. *Fungal biology* **2018,** *122* (12), 1222-1227.
13. Gessler, N.; Egorova, A.; Belozerskaia, T., Melanin pigments of fungi under extreme environmental conditions (review). *Prikl. Biokhim. Mikrobiol.* **2014,** *50* (2), 125-134.
14. Turick, C. E.; Ekechukwu, A. A.; Milliken, C. E.; Casadevall, A.; Dadachova, E., Gamma radiation interacts with melanin to alter its oxidation–reduction potential and results in electric current production. *Bioelectrochemistry* **2011,** *82* (1), 69-73.
15. Rageh, M. M.; El-Gebaly, R. H., Melanin nanoparticles: antioxidant activities and effects on γ-ray-induced DNA damage in the mouse. *Mutation Research/Genetic Toxicology and Environmental Mutagenesis* **2018,** *828*, 15-22.
16. Cordero, R. J., Melanin for space travel radioprotection. *Environ. Microbiol.* **2017,** *19* (7), 2529-2532.
17. Lee, H.; Dellatore, S. M.; Miller, W. M.; Messersmith, P. B., Mussel-inspired surface chemistry for multifunctional coatings. *Science* **2007,** *318* (5849), 426-430.
18. (a) Woehlk, H.; Lauer, A.; Trouillet, V.; Welle, A.; Barner, L.; Blinco, J. P.; Fairfull-Smith, K. E.; Barner-Kowollik, C., Dynamic Nitroxide Functional Materials. *Chemistry–A European Journal* **2018,** *24* (71), 18873-18879; (b) Woehlk, H.; Steinkoenig, J.; Lang, C.; Goldmann, A. S.; Barner, L.; Blinco, J. P.; Fairfull-Smith, K. E.; Barner-Kowollik, C., Oxidative polymerization of catecholamines: structural access by high-resolution mass spectrometry. *Polymer Chemistry* **2017,** *8* (20), 3050-3055.
19. Li, Y.; Xie, Y.; Wang, Z.; Zang, N.; Carniato, F.; Huang, Y.; Andolina, C. M.; Parent, L. R.; Ditri, T. B.; Walter, E. D., Structure and function of iron-loaded synthetic melanin. *ACS nano* **2016,** *10* (11), 10186-10194.
20. Wang, Z.; Xie, Y.; Li, Y.; Huang, Y.; Parent, L. R.; Ditri, T.; Zang, N.; Rinehart, J. D.; Gianneschi, N. C., Tunable, metal-loaded polydopamine nanoparticles analyzed by magnetometry. *Chem. Mater.* **2017,** *29* (19), 8195-8201.

21. Ju, K.-Y.; Lee, Y.; Lee, S.; Park, S. B.; Lee, J.-K., Bioinspired polymerization of dopamine to generate melanin-like nanoparticles having an excellent free-radical-scavenging property. *Biomacromolecules* **2011,** *12* (3), 625-632.
22. (a) Matsumoto, K.-i.; Subramanian, S.; Murugesan, R.; Mitchell, J. B.; Krishna, M. C., Spatially resolved biologic information from in vivo EPRI, OMRI, and MRI. *Antioxidants & redox signaling* **2007,** *9* (8), 1125-1142; (b) Hyodo, F.; Matsumoto, S.; Devasahayam, N.; Dharmaraj, C.; Subramanian, S.; Mitchell, J. B.; Krishna, M. C., Pulsed EPR imaging of nitroxides in mice. *J. Magn. Reson.* **2009,** *197* (2), 181-185; (c) Matsumoto, K. i.; Subramanian, S.; Devasahayam, N.; Aravalluvan, T.; Murugesan, R.; Cook, J. A.; Mitchell, J. B.; Krishna, M. C., Electron paramagnetic resonance imaging of tumor hypoxia: enhanced spatial and temporal resolution for in vivo pO2 determination. *Magnetic Resonance in Medicine: An Official Journal of the International Society for Magnetic Resonance in Medicine* **2006,** *55* (5), 1157-1163.

Chapter 9: Conclusions

In this thesis have been synthesized nanomaterials with different strategies. In chapter four we have found an innovative synthetic cheap, fast and green way for PBI amine derivates. PBI derivates have been functionalized with polar chains that makes them both water soluble and pH sensitive. They have been tested at different concentration and different pH. PIPER3 has given best results responding to concentration, pH and ionic strength in a unique way. It was also possible discriminate two different aggregations with monomer-dimer model and isodesmic model. Low pH favour dimer formation, on the other hand at higher pH larger aggregates are preferred. This spread new light on the intriguing mechanisms of self-organization of molecular unit in water environment.

In chapter five we found that molecular design is fundamental in driving self-assembly and it determines the stability of self-assembled nanoparticles. In fact, starting from molecule NBD-Ph that does not form stable nanoparticles upon nanoprecipitation in physiological conditions we introduced minor structural modification to give species NBD-PhM and NBD-PhOM. Nanoprecipitation of these new molecules leads indeed to the formation of very stable nanoparticles. Unfortunately the quantum yield of molecule NBD-PhOM, which is already low in the non-aggregated form, further decreases upon assembly in the nanoparticles. As a result, the brightness of NBD-PhOM nanoparticles is about two orders of magnitude lower than the one of NBD-PhM nanoparticles. Such a difference is so relevant that while NBD-PhM nanoparticles can be clearly tracked at the single nanoparticle level in solution at very low concentration by fluorescence microscopy, NBD-PhOM nanoparticles cannot be observed with the same technique.

Most interestingly, the brightness of NBD-PhM nanoparticles could be estimated to be about six orders of magnitude higher than an NBD water soluble derivative used as reference. These results demonstrate that rational design of the molecular precursor is fundamental for producing stable and strongly bright nanoparticles by self-assembly.

Cellular experiments proved that NBD-PhM nanoparticles are suitable to be used as fluorescent contrast agents for bioimaging, also thanks to their good biocompatibility. We believe that our approach can be extended to other molecules and surfactants in order to tune the excitation/emission wavelength as well as the nanoparticles size.

In chapter six the aim of the present work was synthesis and characterization of new molecular nanoparticles potentially useful in the diagnostic and therapeutic field (optical imaging, photoacoustic imaging and photoacoustic therapy, photothermal therapy and photodynamic).

Molecular nanoparticles were synthesized using different chromophores (DPA, DPEA, C, P, Mg) with similar chemical-physical characteristics to allow aggregation in aqueous solution. Molecular nanoparticle were synthesized by the nanoprecipitation method (section 1, 2, and 3) to obtain nanoparticles containing a single chromophore (section 1), nanoparticles containing two chromophores, acceptor and a donor (section 2) and systems consisting of two types of nanoparticles containing one the donor and the other the acceptor (section 3).

In section 1 the properties of molecular nanoparticles obtained from DPA, DPEA, C, P and Mg were analysed. In presence of Pluronic F127 as a stabilizer, nanoparticles with dimensions typically of 100-150 nm have been synthetized. Nanoparticles possess photophysical properties very different from molecules in THF. In most cases it is observed a widening and red-shifting of the absorption and emission bands. In some cases, the appearance of new emission bands characteristic of nanoparticles is observed. This shows that nanoprecipitation is effective for dispersing insoluble molecules in water and that this very simple and quite general synthetic approach can be exploited to achieve water compatible and stable nanoparticles with tailored spectral feature

Over time in fact only some nanoparticles undergo coalescence (this is the case of DPA), while other very interesting chromophores such as P and Mg form durable stable suspensions.

In section 2, self-assembled nanoparticles containing two different fluorophores (a potential excitation energy donor and a potential excitation energy acceptor) have been prepared and analysed. In all nanoparticles, fluorescence of the donor is totally or partially quenched by the acceptor, and in DPA_P-NP it was observed sensitized emission of acceptor, confirming presence of energy transfer process. Thanks to this feature these nanoparticles possessed a broad pseudo-Stokes shift suitable for highly sensitive detection in bioimaging. In the other cases, electronic transfer processes happened. This result was also very interesting since it demonstrated that nanoparticles dissipate absorbed light in heat, and this makes them very promising for applications based on the photothermal effect.

In section 3 the effect of mixing of different nanoparticles made by a single fluorophore in water was investigated. Uv-Vis and fluorescence spectra showed that depending on their nature such nanoparticles tend to exchange molecules or not. These results demonstrate that surprisingly, in the case of some specific molecules self-assembled nanoparticles are very stable although molecular components are to covalently bound. In other cases, nanoparticles reorganized in mixed nanoparticles, where energy and electron transfer processes occurred. Also, this exchange process is very interesting since it can be exploited for sensorial or diagnostic

purposes, considered that it leads to variations in the fluorescence signal can depend on environmental parameters (such as temperature and viscosity) it.

In chapter seven a new class of photophysical system based on gold have been developed. These gold NP show a very interesting photoluminescence in the NIR region a window more transparent and suitable for optical detection in biological samples. In this work we focused on demonstrate that appropriate engineering of coating can tailor interaction between gold nanoclusters and substrate in order to achieve selectivity and sensibility on sensing application. In the first part of the work we demonstrated that photoluminescence brightness of gold NPs can be strongly enhanced by sensitization using organic molecules as light harvesting antenna. In particular we used fluorescein sodium salt, a fluorophore negatively charged at physiological pH (HEPES 0.01M). Gold nanoclusters coated with positively charged thiols have shown much higher affinity for fluorescein sodium salt, quenching its fluorescence. Most interesting results have been obtained for AuNCs-1 and AuNCs-3 and we demonstrate that energy transfer happens between fluorescein sodium salt and gold nanoclusters producing a strongly enhanced luminescence signal of the gold nanoparticles upon excitation of the organic antenna. This was an important step forward in the development of new bright gold based NIR nano-emitters.

Subsequently, AuNCs-1 and AuNCs-3 have been tested as luminescent sensors for very diffused API presents in commercial drugs. API have been chosen with amphiphilic structures. They have a negatively charged head and a lipophilic moiety. The driving force of the interaction between gold nanoclusters and amphiphilic organic anions is a combination of the accommodation of the hydrophobic portion of the substrate in the alkyl portion of the monolayer and the simultaneous ion-pairing interaction with the head groups. This grants selectivity and high affinity. Results demonstrate that there is interactions between gold nanoclusters and API. Moreover, API are able to influence gold nanoclusters emission with two mechanism. The first mechanism involves the direct energy transfer from API to gold nanoclusters. The second mechanism results from changes of polarity on the nanocluster surface: the presence of charged molecules adsorbed on gold nanocluster surface changes the global charge distribution of gold nanocluster and this influences their photophysical properties. In order to discriminate which mechanism modified the properties of the nanoparticles upon recognition of the drug molecules, the system has been excited at two different wavelengths: at 300 nm where API absorb, and both mechanisms can contribute, and at 500 nm where API do not absorb and only the second mechanism can occur. In conclusion we demonstrate that gold nanoclusters are very interesting biological sensors, indeed they can be easily engineered to have specific interactions with selected substrates, they can work in

biological conditions (water at pH 7) and they emit in in near infrared region where there is the biological window and for this reason is attracting a lot of attentions.

In chapter eight we clearly demonstrate that several different radicals species can be efficiently incorporated in melanin nanoparticles in view of the preparation of better performant chemical screens for radiation. Demonstrating the actual enhanced radioprotective activity of these new nanoparticles was beyond the objective of this thesis, nevertheless EPR revealed the presence of a high amount of free radicals with potential scavenging activity. Although DPPH experiment did not confirm any enhanced protective action the application of these new nanoparticles to radioprotection cannot be ruled out.

Moreover DPA-Mn nanoparticles promise to be good contrast agents both for magnetic resonance imaging (MRI) and electron paramagnetic resonance imaging (EPRI). This is in agreement with results by Gianneschi

In conclusion nanoparticles have proven to be applicable in numerous high-profile fields as bioimaging, environmental and pharmaceutical sensors. We believe there is still much to be discovered about nanoparticles potential and applications. For this reason, we are sure that in the coming years the study of these fascinating and surprising materials will continue revealing unpredicted properties and applications.